Kinetic Simulation of Ion Propulsion Systems

Inauguraldissertation

zur

Erlangung des akademischen Grades eines

doctor rerum naturalium (Dr. rer. nat.)

an der Mathematisch-Naturwissenschaftlichen Fakulät

der

Ernst-Moritz-Arndt Universität Greifswald

vorgelegt von

Julia Duras

geboren am 21. Mai 1985

in Berlin, Deutschland

Greifswald, den 05. April 2018

Dekan:	Prof. Dr. Werner Weitschies
1. Gutachter:	Prof. Dr. Ralf Schneider
2. Gutachter:	Prof. Dr. Akiyoshi Hatayama
Tag der Disputation:	24. August 2018

Abstract

Ion thrusters are Electric Propulsion systems used for satellites and space missions. Within this work, the High Efficient Multistage Plasma Thruster (HEMP-T), patented by the THALES group, is investigated. It relies on plasma production by magnetised electrons. Since the confined plasma in the thruster channel is non-Maxwellian, the near-field plume plasma is as well. Therefore, the Particle-In-Cell method combined with a Monte-Carlo Collision model (PIC-MCC) is used to model both regions. In order to increase the simulated near-field plume region, a non-equidistant grid is utilised, motivated by the lower plasma density in the plume. To minimise artificial self-forces at grid points bordered by cells of different size a modified method for the electric field calculation was developed in this thesis. In order to investigate the outer plume region, where electric field and collisions are negligible, a ray-tracing Monte-Carlo model is used. With these simulation methods, two main questions are addressed in this work.

What are the basic mechanisms for plasma confinement, plasma-wall-interaction and thrust generation?
For the HEMP-T the plasma is confined by magnetic fields in the thruster channel, generated by cylindrical permanent magnets with opposite polarity. Due to different Hall parameters, electrons are magnetised, while ions are not. Therefore, the dominating electron transport is parallel to the magnetic field lines. In the narrow cusp regions, the magnetic mirror effect reduces the electron flux towards the wall and confines the electrons like in a magnetic bottle. At the anode, propellant gas streams into the thruster channel, which gets ionised by the electrons creating the plasma. As a result of the electron oscillation between the two cusp regions, ionisation of the propellant gas is efficient.
The magnetic field configuration of the HEMP-T also influences the plasma potential inside the thruster channel. Close to the symmetry axis, the mainly axial magnetic field results in a flat potential. At the inner wall, the field configuration reduces the plasma wall interaction to only the narrow cusp regions. Here, the floating potential of the dielectric channel wall and its plasma sheath result in a rather low radial potential drop compared to the applied anode potential. As a result, the electric potential is rather flat and impinging ions at the thruster channel wall have energies below the sputter threshold energy of the wall material. Therefore, no sputtering appears at the dielectric wall. At the thruster exit the confinement by the magnetic field is weakened and the potential drops with nearly the full anode voltage. The resulting electric field accelerates the generated ions into the plume and generate the thrust, but they are also able to sputter surfaces. During terrestrial testing, sputtering

at vacuum vessel walls leads to the production of impurities. The amount of back-flux towards the channel exit is determined by the sputter yield of the vacuum chamber wall. A large distance between thruster exit and vessel wall reduces the back-flux and smooths the pattern of deposition inside the thruster channel. Dependent on their material, the evolving deposited layers can get conductive, modify by this the potential distribution and reduce the thrust.

For the HEMP-T, ions are mainly generated at high potential close to the applied anode potential. Therefore, the accelerated ions producing the thrust gain the maximum energy as observed in experiment. Ions emitted from the thruster into different angles in the plume contribute mainly to the ion current at angles between 30° and 90°. They mainly originate from ionisation at the thruster exit. The resulting angular distribution of the ejected ion current is close to the one of the experiment, slightly shifted by about ten degrees to higher emission angles. In front of the thruster exit, electrons are trapped by electrostatics forces. This enhanced density allows ionisation and an additional electron density structure establishes.

What are possible physics based ideas for optimisation of an ion thruster?

An optimised thruster should have a high ionisation rate inside the thruster channel, low erosion and an ion angular distribution with small contributions at high angles for minimised thruster satellite interactions. In experiments, the HEMP-T satisfies already quite nicely these requests. In the simulations, low erosion inside the thruster channel and angular ion distributions close to the experimental data are demonstrated. However, the ionisation efficiency is lower and radial ion losses are larger than in experiment. A possible explanation of these differences is an underestimated transport perpendicular to the magnetic field lines, well known for magnetised plasmas.

A successful example for an optimisation using numerical simulations is the reduction of back-flux of sputtered impurities during terrestrial experiments by an improved set-up of the vacuum vessel. The implementation of baffles reduces the back-flux towards the thruster exit and therefore deposition inside the channel. These improvements were successfully implemented in the experiment and showed a reduction of artefacts during long time measurements. This leads to a stable performance, as it is expected in space.

Contents

1. Summary

1.1. Introduction

Ion thrusters are Electric Propulsion (EP) systems used for satellites and space missions. For the thrust production they utilise electrothermal, electrostatic, or electromagnetic forces to accelerate an ionised propellant. Since the 1980's these systems are getting more and more important especially for commercial space missions [Hoskins et al., 2013].

During a propulsion phase the satellite gains velocity due to the momentum change $\frac{\mathrm{d}p}{\mathrm{d}t}$, produced by the emitted propellant and loss of weight. Typically, the exhaust velocity is assumed to be constant. That means that the thrust T of the propulsion system is given by the exhaust velocity v_{ex} of the emitted propellant and the consumption of the propellant mass m_p.

$$T = -\frac{\mathrm{d}p}{\mathrm{d}t} = -v_{ex}\frac{\mathrm{d}m_p}{\mathrm{d}t} \quad . \tag{1.1}$$

In order to reduce costs of space missions, mass reduction and efficiency of the propulsion system are important. For a demanded thrust, reduction of propellant can be achieved by a higher exit velocity, as can be seen by Equation 1.1. Traditionally, Chemical Propulsion (CP) systems are used as satellite engines. They obtain their energy from an exothermic reaction of fuel and oxidiser which generates a heated propellant. By a nozzle, the thermal energy of the reactants is transferred into kinetic energy. The propellant gets accelerated. Despite an optimised design of the nozzle geometry or the physics of the gas expansion, the maximum exhaust velocity is about 3 km/s, limited by the energy stored within the chemical bonds of the propellant [Messerschmid and Fasoulas, 2009]. A higher v_{ex} can be obtained by acceleration of charged particles with electric fields. This is the basic idea of plasma based electric propulsion systems. Operational bounds of the space mission limit the power for the thruster system and therefore the applied electric field. This limits the acceleration

of the ionised propellants to velocities of some 10 km/s. Compared to chemical propulsion this exhaust velocity is much higher, resulting in a lower propellant consumption $\frac{\mathrm{d}m_p}{\mathrm{d}t}$ for a given thrust. Within the operational limits, this gives a produced thrust in the range of mN to N instead of several N to kN for CP systems [Messerschmid and Fasoulas, 2009]. However, due to the absence of friction within space, the thrust adds up over the time and produces a change in momentum

$$\Delta p = \int -T \, \mathrm{d}t \ . \tag{1.2}$$

While the traditional systems accelerate to high speed very rapidly, electric propulsion systems need longer time to reach the same change in velocity in space. CP and EP are suited for different kind of missions and the choice of the propulsion type is strongly determined by the demands.

Typical applications for EP are manoeuvres of orbit rising and station keeping. During the orbit rising, the space craft is carried from its position to another orbit, while within a station keeping manoeuvre forces like gravity of surrounding planets or radiation pressure have to be compensated. The low propellant consumption can be used to reduce the spacecraft launch mass which gains cost reductions. Therefore, nowadays (2013) about 70 % of EP in operation are mounted on commercial satellites [Hoskins et al., 2013]. But also for non-commercial missions EP is used for controlling and positioning. An example is the "Gravity field and steady-state Ocean Circulation Explorer" (GOCE) mission [ESA, nd]. It exceeded the planned mission time of 20 months by about one year, until it ran out of propellant [Dreissigacker, 2013]. The high efficiency enables also missions of long duration such as the deep space missions "Deep Space 1" [Rayman, nd] and "Dawn" [Wise, nd]. Here, EP systems were used as the main propulsion engines.

The most straight forward concept of an EP system is the gridded ion thruster, developed in the early 1960's at the National Aeronautics and Space Administration (NASA) [Hoskins et al., 2013]. Inside a discharge chamber, called as thruster channel, a plasma is generated by ionisation of a propellant gas. At the thruster exit, the produced ions are getting accelerated electrically by biased grids. Outside the thruster channel the neutraliser is placed. It is an electron source which prevents the satellite from charging by the accelerated ions from the thruster. For this propulsion system, separation of ionisation in the chamber and acceleration in the grid system gives the possibility of independent optimisation of the two processes and therefore of the whole thruster, which is a big advantage of this concept.

During several experimental missions gridded ion thrusters demonstrated functionality with produced thrusts in the range of several mN [Sovey et al., 2001]. However, plasma wall interactions lead to erosion of the accelerating grid system which reduced the thruster lifetime [Sovey et al., 2001],[Boyd, 2005]. In order to overcome this limit, grid-less thruster types were developed. Ideally, also the separation of ionisation and acceleration should be kept to allow easy optimisation.

For all thruster types, the ultimate question in the field of development is the optimisation in terms of a higher thrust at high efficiency, a longer lifetime of the thruster and a minimised interaction with the satellite. For a given input power, a better efficiency of the thruster can be reached by a higher ionisation rate. This requires a reduction of discharge losses and erosion of thruster components. A better efficiency should increase production of ions in the thruster channel and leads therefore to a higher emitted ion current and a higher thrust. For a given ion density, an increase in thrust is also gained by higher energy of the emitted ions directing out of the thruster channel. Since most thruster types produce a cone of emitted ions its cone angle has to be minimised. This is a key problem of optimisation. In order to reduce erosion of the thruster as well as of satellite components, the impingement of high energetic ions or neutrals have to be reduced. A minimised erosion of the thruster enables a stable performance and leads to a longer lifetime. For a minimised erosion of the satellite components, e.g. the solar panels, especially the spatial distribution of the accelerated ions is crucial.

For these technical optimisations a knowledge of the following basic physics is of importance.

Plasma physics of ionisation and acceleration: To understand the ionisation process a microscopic view of the charged particle confinement in a plasma is useful. In most of the current ion thruster types, an applied magnetic field plays an important role. Since the electron gyro radius is much smaller than the system dimensions, the electrons follow the magnetic field and electron confinement can be reached by the magnetic field configuration, e.g. by a magnetic bottle. Due to quasi neutrality, ions are following the electrons, the plasma is confined. Along with the self-consistent developing electric field of the plasma the Lorentz force can be used to trap electrons and therefore the plasma inside the thruster channel. For an efficient ionisation process another important process is electron heating, e.g. by high energetic source electrons or by capacitive heating. The ionised propellant is accelerated by an electric field, which is either generated by the plasma potential gradient

or by an applied electric potential. This gives the spatial as well as the energy distribution of the emitted ions producing the thrust of the EP system. In the plume region, charge exchange collisions with non ionised propellant atoms and surface charges of the satellite further influence these distributions.

Plasma-wall-interactions: Inside the thruster channel plasma wall interactions are of importance since they lead to discharge losses and therefore are able to reduce the ionisation efficiency. Also changes of the channel geometry are determined by plasma wall interactions like erosion, re-deposition or evaporation. These changes are able to reduce the thruster performance and lifetime. In the plume an understanding of plasma wall interactions at satellite surfaces is of importance. Here, the accelerated ions produce thrust but are also able to sputter. Especially erosion of solar panels have to be avoided since this can reduce mission time. In the plume, charge exchange collisions of the accelerated ions with non-ionised propellant atoms lead to ions of lower energy with trajectories of wider angle than the cone angle. This transport of momentum forms a side wing in the plume plasma, resulting in plasma interactions with satellite surfaces. For terrestrial experiments, also interactions with the vacuum vessel walls are of interest.

These physics topics result in two main questions addressed in this work.

- **What are the basic mechanisms for plasma confinement, plasma-wall-interaction and thrust generation?**
- **What are possible physics based ideas for optimisation of an ion thruster?**

The system used for studying these questions is the High Efficient Multistage Plasma Thruster (HEMP-T) [Kornfeld et al., 1999]. Experimental measurements of this thruster type mainly quantify the emitted ions. Frequently used methods are Retarding Potential Analyser (RPA) to detect current and energy distribution of ions and optical spectroscopy methods like Laser Induced Fluorescence (LIF) to measure ion velocity and temperature. Additionally, thrust balance to quantify the produced thrust, pressure sensors to measure neutral density and 3D Langmuir probes to evaluate electron density and temperature profiles are used.
In contrast to the plume, experimental measurements of the channel plasma is more challenging due to the difficult access to the plasma. The size of typically used Langmuir probes is in the range of the channel radius. Therefore, measurements of the channel result in a dramatic change of the system. Also, optical spectroscopy, as non-invasive methods, have

problems since their line of sight is mainly axial. This results in measurement of plasma properties integrated over line of sight. Indirect evaluations of the channel plasma are done with thermal elements embedded in channel walls. Conclusions about high energetic ions can also be drawn by the measurement of the surface evolution.
Due to the lack of experimental measurements, a model of the channel physics need to be developed to understand principles of the channel plasma. Although analytic models can explain the basic physics aspects, detailed numerical simulations are needed to quantify the plasma properties such as evolution of potentials, densities and particle velocities. Since channel and plume plasma are interlinked, simulation of the thruster channel must be extended to the plume region. Where experimental data are available, comparison allows the validation of the simulated model.

Within this cumulative thesis, simulations will be used to study channel and plume physics and to address the above mentioned questions. The thesis articles will be indicated by the references [I] - [VII].
In the next chapter, the physics of the HEMP-T system will be discussed. Fundamental mechanisms will be described and typical plasma parameters will be provided. Due to an electron-electron collision mean free path larger than the system dimensions, electrons in the thruster channel are non-Maxwellian. In addition the applied magnetic field prevents them from thermalisation and the plasma is in a non-equilibrium state. The electron behaviour in such a plasma is characterised by the electron velocity distribution function, which needs to be described by a kinetic model.
A common kinetic simulation method, used in the field of plasma physics is the Particle-In-Cell (PIC) method. A detailed description of the utilised code will be given. In general, the PIC method has the disadvantage of high computational costs. To be able to obtain a realistic thruster model, it is combined with a similarity scaling and a non-equidistant grid. The similarity scaling allows the simulation of a smaller system and to map it into the size of the experimental device following analytic scaling laws. A non-equidistant grid is used to extend the simulation domain of the plume. Combining this grid with the standard calculation scheme for the electric field produces artificial self-forces due to the spatially non-equal distributed values of the electric potential. Therefore, a calculation scheme to minimise these artefacts at the change of cell sizes is given and evaluated. For a larger plume domain, a less costly ray-tracing Monte-Carlo method is used for a simplified plume model.
With these tools, it is possible to simulate the HEMP-T self-consistently. The investigation of the plasma physics will be separated into two regions: thruster channel and plume. It will

provide a detailed understanding of the integral plasma scenario. The simulation gives an insight into plasma quantities and plasma wall interactions in the thruster channel. Here, the main mechanisms for ionisation, discharge losses and ion extraction can be identified. For a compact quantification an integral flux balance is evaluated.
To analyse plume physics a large simulated plume region is needed, which will be shown by sensitivity studies. Since the main objective for optimisation is the ion acceleration, the ion physics will be discussed in detail. To overcome the size limit of the simulation domain, the concept of a transfer function is introduced. As a consequence of plasma wall interactions at vacuum vessel walls, sputtered impurities are generated. A fraction of these particles are emitted towards the thruster exit and are able to produce deposited layers inside the channel. The resulting modification of surface properties can lead to changes of the thruster performance. The presented simulations of this problem allow to develop concepts to reduce these effects.
Finally, the results are summarised and an outlook will be given.

1.2. The High Efficient Multistage Plasma Thruster

The ion thruster studied within this work is the High Efficient Multistage Plasma Thruster (HEMP-T). It was patented by the THALES group in 1999 [Kornfeld et al., 1999] and works as an electrostatic thruster with a cross-field discharge. Xenon gas is used as propellant. A detailed description of the HEMP-T can be found in [Koch et al., 2011] and [Kornfeld et al., 2007].

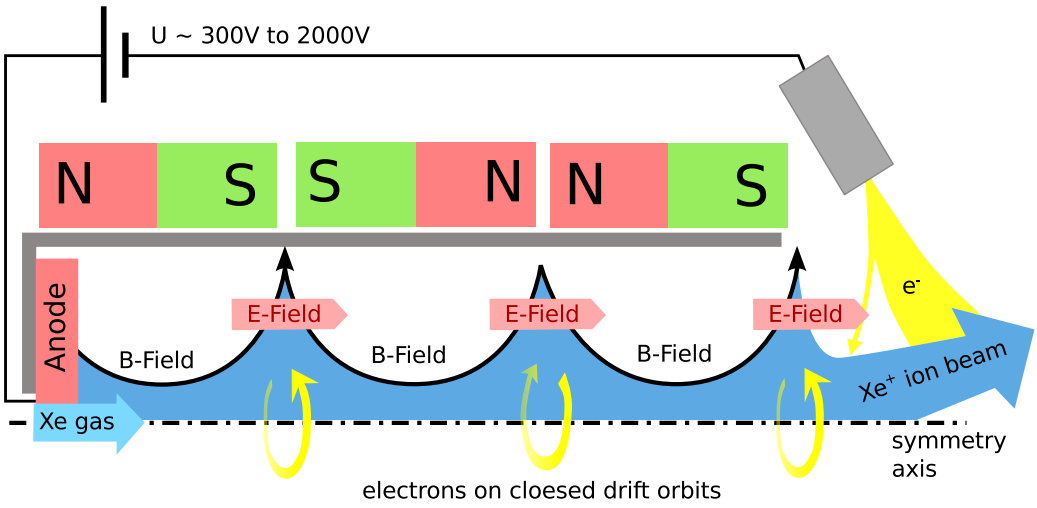

Figure 1.1.: Scheme of HEMP-like thrusters [III].

Thruster channel length and radius	$L = 5.1\,\mathrm{cm}$	$R = 0.9\,\mathrm{cm}$
Anode discharge voltage	$U_a = 500\,\mathrm{V}$	
Average magnetic induction	$B = 0.1\,\mathrm{T}$	
Neutral density	$n_n = 10^{21} - 10^{19}\,\mathrm{m}^{-3}$	
Electron and ion density	$n_e = 10^{18}\,\mathrm{m}^{-3}$	$n_i = 10^{18}\,\mathrm{m}^{-3}$
Electron and ion temperature	$T_e = 2\,\mathrm{eV}$	$T_i = 4\,\mathrm{eV}$
Electron and Ion Larmor radius	$r_{L,e} = 47.6\,\mu\mathrm{m}$	$r_{L,i} = 1.7\,\mathrm{cm}$
Electron and ion Hall parameter	$\omega_{c,e}/\nu_{e-e} = 18.7$	$\omega_{c,i}/\nu_{i-i} = 0.5$

Table 1.1.: Operational parameters of the HEMP-T model DM3a thruster channel.

A schematic view of the HEMP-T concept is shown in Figure 1.1. It consists of a rotational symmetric discharge channel with an anode and an exhaust of propellant at the bottom of the channel. The discharge channel is surrounded by axially magnetised permanent magnet rings with opposite magnetisation. Inside the thruster channel a dielectric wall is facing the plasma. Outside the thruster channel a hollow cathode neutraliser is placed. It provides neutralises the out-going ion beam. The permanent magnets generate a magnetic field which points mainly in axial direction especially in the channel region close to the symmetry axis. In the cusp regions, the magnetic field next to the channel wall is mostly directed in radial direction. For all HEMP-T models geometrical size and magnetic induction is chosen such that the Larmor radius of the electrons $r_{L,e}$ is much smaller than the radius of the discharge channel, while for the ions it is larger ($r_{L,e} \ll R < r_{L,i}$). Due to different Hall parameter, electrons in the thruster channel are magnetised while ions are not. As an example, Figure 1.1 shows a thruster model with four cusps, an anode cusp, two inner cusp and an exit cusp. Within this work, the HEMP-T model DM3a [Kornfeld et al., 2003, Koch et al., 2003] is investigated, which contains only three cusp regions. In addition to the described scheme, it has a grounded metal pole piece, placed at the thruster exit. Its most important operational parameters are given in Table 1.1. Further plasma properties can be found in appendix A.1.

To understand the operational principle of a HEMP-T, it is helpful to analyse the electron transport in the different regions. Source electrons are emitted by the neutraliser in the thruster plume. They are getting attracted by the anode potential and move towards the thruster channel. In the exit cusp region, the radial magnetic field guides the magnetised electrons towards the channel wall. The magnetic field configuration builds up a magnetic mirror and the electrons are getting reflected before they reach the channel wall. A sketch of a reflecting particle trajectory is shown in Figure 1.2. The point of reflection depends

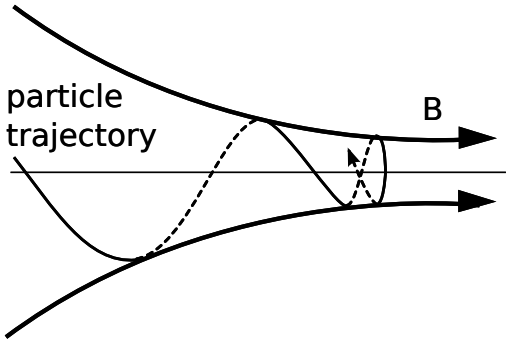

Figure 1.2.: The magnetic mirror effect.

on the energy of the particles and only highly energetic particles are able to overcome the barrier and reach the channel wall. In addition to the reflection of the magnetised electrons, electric and magnetic fields are perpendicular in the exit cusp region. This induces a $\vec{E} \times \vec{B}$-drift which leads to a poloidal movement of the electrons, indicated in Figure 1.1 by yellow arrows. As a result of these two effects electrons are getting trapped in the exit cusp and the strong radial magnetic field in this region prevents electrons to stream further down the thruster channel towards the anode. Only few electrons can escape either by collisional or anomalous diffusion. Anomalous diffusion denotes non collisional transport of magnetised particles across magnetic field lines. It is typically caused by turbulence in the electric field. For low collisional plasmas as used for the HEMP-T, Bohm diffusion [Bohm et al., 1949] can be of importance [Lieberman and Lichtenberg, 2005]. Only by these two transport processes electrons are able to pass the exit cusp. Then they are getting trapped in the next cusp region. This process goes on, until the electrons get lost at the anode or at the dielectric channel wall.
Within this transport path, electrons can ionise propellant gas, which produce ions and further electrons. Especially in the thruster channel, where the neutral density is higher than in the plume, this process builds up a plasma. Here, the electron confinement increases the efficiency of the ionisation process. The corresponding electric potential is flat, determined by the anode discharge voltage U_a and the very large parallel transport of electrons along the fieldlines, especially close to the axis, where the fieldlines are mostly axial. At the thruster exit, the potential drops and the produced ions in the channel are accelerated into the plume, which generates thrust.
With the help of kinetic simulations of the HEMP-T model DM3a it is possible to give a detailed description of the mechanisms in the channel region in section 1.4.

While in the thruster channel the plasma is confined by the magnetised electrons, the

unbounded plume region is characterised by ions accelerated out of the channel and electrons accelerated towards the exit. This results, in decreasing plasma densities with increasing distance to the channel exit. While at the thruster exit the plasma density is in the range of $n_e = n_i = 1 \times 10^{18}\,\mathrm{m}^{-3}$, at 5 cm far from the exit, where the accelerated ions reach a temperature of $T_i \approx U_a$, the plasma density in in the range of $1 \times 10^{14}\,\mathrm{m}^{-3}$. Due to these different plasma properties, channel and plume physics are operating on different time and length scales. More detailed plasma parameters can be found in appendix A.1. These differences have to be taken into account for ion thruster simulations, as will be shown in section 1.5.

In the appendix A.2 a short discussion of the most important collisions of the HEMP thruster channel region can be found. It shows that most of the mean free paths of the charged particles are in the range of or even larger than the channel length. That means, electrons and ions are not following a Maxwellian velocity distribution. In the plume, the decreasing plasma densities lead to an increase in the collision mean free paths, which are larger than the plume dimension. Therefore, also the plume plasma is non-Maxwellian and a kinetic simulation method has to be used for both regions. Due to the coupling by the ejected ions and the attracted source electrons, a HEMP-T simulation has to contain both regions.

For comparison of the HEMP-T, the Hall-effect thruster [Turner, 2006] is used within this thesis. It is a widely used ion thruster of similar concept, consisting of a ring shaped channel with an anode at the channel bottom. In the plume a neutralising electron source is placed, which generates an axial electric field. Contrary to the HEMP thruster, the magnetic field is radially inside the whole channel. Therefore, the resulting $E \times B$-drift confines the electrons all along the channel length, generating a poloidal Hall current. This leads to an efficient ionisation of the propellant, injected at the channel bottom, and confines the plasma inside the thruster channel. The generated ions are accelerated into the plume by the developing potential drop.
These two ion thruster concepts relay on electromagnetic confinement of a plasma, which allows a continuous operation. Beside this, pulsed ion thruster concepts are also possible. One example is the cathode arc thruster [Neumann et al., 2009], where electromagnetic force is mainly used to direct the ejected current. It is a rather new thruster concept, where during a pulse of several microseconds an electric arc is generated inside a thruster channel. It consists of a ring shaped anode and a circular cathode. During the pulse, the generated arc ablates the cathode. The eroded material is ionised in the high current

arc discharge, which creates a plasma inside the channel. Due to the negative cathode potential, electrons are accelerated out of the channel and an applied magnetic field guides them into mainly axial direction. In order to sustain quasi-neutrality, channel ions are following, which generates thrust. As could been shown by kinetic simulations the author contributes to [I], the interaction of the arc beam with the background plasma results in a plasma-beam-instability. It leads to ejection of electron blobs and therefore to a fluctuating thrust, as it is visible in experiments. This strong thrust fluctuation, which increases the thrust, is beneficial for the operational characteristics of the cathode arc thruster. Such a study provides a deeper understanding of the underlying physics.

With the basic understanding gained from this, simulation models suitable for different purposes can be developed, as will be given in the next chapter.

1.3. Kinetic simulation methods

As described in the previous chapter, a simulation model of the HEMP thruster physics has to be kinetic. Kinetic simulation methods solve the Boltzmann equation. It describes the collective motion of a large number of particles of the same species s

$$\left.\frac{\partial f}{\partial t}\right|_{coll} = \frac{\partial f}{\partial t} + \vec{v}_s \frac{\partial f}{\partial \vec{x}_s} + \frac{\vec{F}}{m_s}\frac{\partial f}{\partial \vec{v}_s} \quad \Rightarrow^{operator}_{notation} \quad \hat{J}f = \frac{\partial f}{\partial t} - \hat{D}f \quad , \tag{1.3}$$

where $f = f(t, \vec{x}_s, \vec{v}_s)$ is the particles distribution function in space $\vec{x}_s$ and velocity $\vec{v}_s$ at the time t and m_s is the particle mass [Lieberman and Lichtenberg, 2005]. It describes the change of the distribution in time influenced by forces $\vec{F}$ as well as by collisions between the particles, given by the collision operator $\hat{J}$ at the left hand side. In the case of no collisions, the Boltzmann equation reduces to the Vlaslov equation.
A typical approach for kinetic simulations is its linearisation. For small time steps Δt, the plasma properties, given by the distribution function f, can be calculated for the time $t+\Delta t$ from the the previous state $f(t+\Delta t) = f(t) + \Delta t \frac{\partial f(t)}{\partial t}$. Replacing the time derivative in the operator notation of the Boltzmann equation gives after factorisation

$$f(t+\Delta t) = (1 + \Delta t\hat{J})(1 + \Delta t\hat{D})f(t) + O(\Delta t^2) \quad . \tag{1.4}$$

It shows the possibility of splitting the calculation of particle motion into two parts: one determined by collisions processes $(1 + \Delta t\hat{J})$ and the other one $(1 + \Delta t\hat{D})$ by forces and

the particle velocities [Bird, 1994]. Therefore, within kinetic simulations these two parts are typically realised with different methods and the collective behaviours of a plasma is calculated within cycles, each representing a small time step Δt.

One method to calculate the Vlaslov part of the Boltzmann equation is the Particle-In-Cell (PIC) method. A description of this method will be given in subsection 1.3.1. Within this work, it is applied to investigate the channel and the near field plume plasma. In order to represent the collisional processes, it is combined with a Monte-Carlo Collision (MCC) model. Afterwards, in subsection 1.3.2, a collision-less kinetic model is described. It will be used for the plume region, in order to investigate the back-flux of impurities by sputtering ions at vacuum vessel walls.

1.3.1. The Particle-In-Cell method with Monte-Carlo Collisions

For the HEMP-T channel physics, electromagnetic interactions as well as collision processes are of importance. These two processes can be well simulated with the Particle-In-Cell method combined with a Monte-Carlo Collision model (PIC-MCC).

The simulation of the HEMP thruster started with the work of K. Matyash et al., see [Matyash et al., 2009] and [Matyash et al., 2010]. For the channel, magnetic field, plasma potential and particle distributions are rotational symmetric. This allows to reduce the three-dimensional problem to a two-dimensional one. But since for collisional interactions all directions of the velocity vector are of importance, velocities are simulated in 3D, while positions are simulated in 2D. Since the applied magnetic field is dominant in comparison to the induced magnetic field, the ion thruster physics is electrostatic. Therefore, the chosen HEMP-T model is electrostatic as well. Within this thesis the PIC-MCC method, as given in [Tskhakaya et al., 2007], [Matyash et al., 2010] and [III], was used. Further descriptions can be found in the author's contributions [II], [IV] and [V]. In Figure 1.3, a chart of one cycle is shown, which will be shortly described.

To calculate the electromagnetic interaction of each particle in a plasma consisting of N_p particles with all other, N_p^2 interactions have to be calculated. Even for a low density plasma of about $N_p = 10^7$ simulated particles these calculations are too time consuming. Therefore, the electrostatic PIC method calculates the potential and the electric field on a spatial grid (**Integration of field equations on the grid**), based on the charges of super-particles, mapped on the grid points (**Charge weighting**). These super-particles, each representing

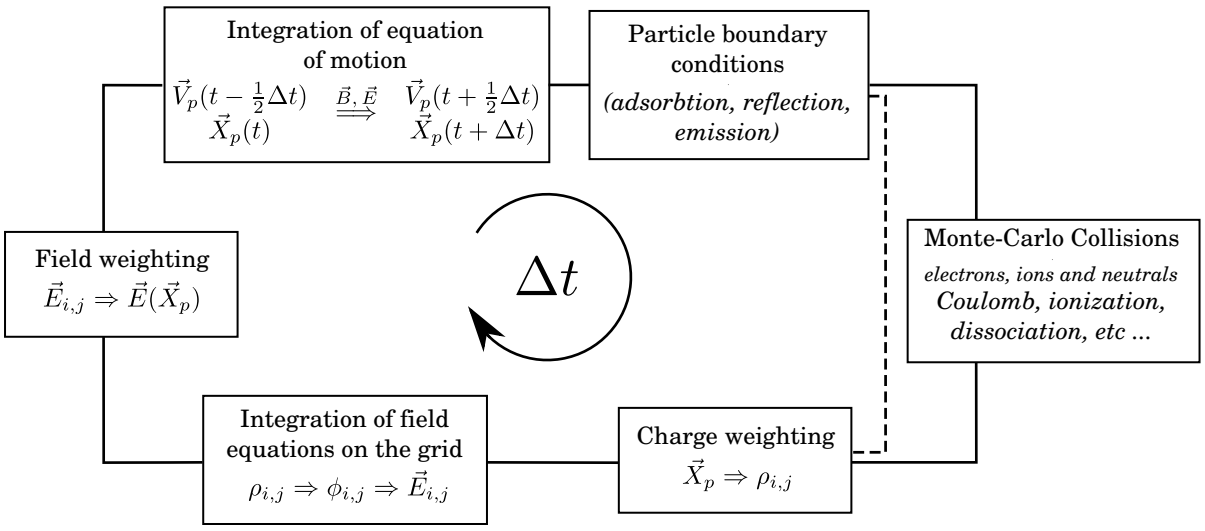

Figure 1.3.: Chart of a cycle of the electrostatic PIC-MCC code. The index p denotes a particle quantity in continuous space, while i, j indicates a quantity at a discreet grid point.

a number of physical particles, are moved according to the calculated fields (**Integration of equation of motion**) which are mapped from the grid points to the particle positions (**Field weighting**). This gives the new particle positions and velocities, which are compared with the positions of the thruster model walls (**Particle boundary conditions**). In order to calculate the time evolution of the plasma this PIC-cycle is repeated.

The resolution of such a simulation is given by the mesh size of the spatial grid Δx and the time step of the PIC-cycle Δt. That means interactions smaller than Δx and faster than Δt are unresolved. Therefore, space and time discretisation have to be chosen according to the smallest length and time scale to be resolved. In this work the spatial resolution is chosen to be in the range of the electron Debye length $\lambda_{D,e}$, which is the screening length of the Debye-Hückel potential, $\Delta x = 1.3 \cdot \lambda_{D,e}$. For the time step a high accuracy of the particle pusher is ensured by $\Delta t = 0.2/\omega_{p,e}$ [Birdsall and Langdon, 1985], where $\omega_{p,e}$ denotes the plasma frequency. These parameters satisfy the Courant-Friedrichs-Lewy condition $v \cdot \Delta t \leq \Delta x$ and ensures therefore the convergence of the system of partial differential equations [Courant et al., 1967].

Within the HEMP-T model the kinetics of electrons and Xenon ions is followed. In order to be as self-consistent as possible, also the kinetics of the neutral propellant atoms are followed within the PIC-MCC simulations of this work. Since neutrals are not effected by electromagnetic fields, for this specie the PIC-cycle reduces to the integration of equation of motion.

For the collisional interactions a MCC model (**Monte-Carlo Collisions**) is integrated into

the PIC-cycle. It approximates the interaction by hard sphere collisions between superparticles. For the HEMP thruster physics the most important collisional process are collisions with neutral Xenon atoms. Therefore, the HEMP-T model used within this work includes: electron neutral elastic collisions, ionisation, neutral excitation by electrons, ion-neutral momentum transfer, ion-neutral charge exchange as well as elastic neutral-neutral collisions. Also electron electron Coulomb collisions are included, although they are not of importance for the DM3a HEMP-T due to their large mean free path, compared to the system size. As given by the Courant-Friedrichs-Lewy condition, each particle does not cross more than one cell during one time step. Therefore, collisions are taking place only between particles of the same cell. The colliding pairs of particles are sampled statistically according to the probability calculated from the collision cross sections. Afterwards, within the collision routine, rotation of the velocity vectors around an isotropic distributed angle is calculated, while the particle position is unchanged. This Monte-Carlo routine is similar to the one published by Vahedi [Vahedi et al., 1993]. Inelastic collisions are realised by an approximated friction term. A detailed description of the used collision routines can be found in [Matyash, 2003],[Bronold et al., 2007] and [Tskhakaya et al., 2007].

Although, PIC simulations are very accurate for plasma physics, they have the disadvantage of being very computationally costly. Here, the main reason is the demanded resolution in time and space. One method to reduce the computational time is the application of a similarity scaling [Taccogna et al., 2005], [Szabo et al., 2000], [Liu et al., 2010]. All similarity scaling methods have to preserve the important physical characteristics of the simulated system. For the HEMP thruster these are: magnetic confinement and collisions with neutrals. Within this work, scaling of the simulated system size L and the simulated time t is applied, similar to [Taccogna et al., 2005]. It preserves the electron Hall parameter $\beta_{Hall} = m_e v_{e,\perp}/(eBL)$, the Knudsen number $\mathrm{Kn} = \lambda_n/L$ and by this the particle velocity $v = L/t$. The resulting scaling laws are given in the appendix A.3. This scaling preserves the physics of the plasma volume inside the thruster channel. Since the Debye length stays constant, plasma sheaths at walls are not preserved and the scaling is violated if surface processes get important. In general a down scaling of a system leads to a higher influence of wall processes. For a plasma sheath the thickness can be estimated as $d \approx 10 \cdot \lambda_{D,e}$, which results for the DM3a HEMP-T in $d \approx 0.1\,\mathrm{mm}$. Within this work the HEMP thruster is scaled down by a factor of ten. This reduces the channel radius to 9 mm, which is about ten times larger than the plasma sheath thickness. Therefore, wall processes does not dominate the channel plasma in the down-scaled system, although the influence of wall processes is larger than in the real-size system. This similarity scaling reduces the number of cells of the

2D grid by a factor of 100 and therefore the computational costs of the PIC simulation.

In section 1.4 and section 1.5 of this work, the PIC-MCC method is used to build up a HEMP-T simulation model to investigate the channel and plume plasma. As motivated in the previous chapter, both regions have to be integrated within one simulation. Due to the smaller length scales, the applicable similarity scaling is bounded by the channel physics. Therefore, only a small region of the near-field plume can be included. As shown in previous simulations [Matyash et al., 2009], [Matyash et al., 2010], this domain size is able to represent the channel physics well, but gives artefacts in the density distributions in the plume. For a proper representation of the near-field plume a larger simulation domain is needed, which results in higher computational costs. A method, which over-comes this problem, is the reduction in the number of cells by using a non-equidistant grid. Due to the out-streaming characteristic in the plume and therefore the much smaller plasma densities the electron Debye length is larger than in the channel. That means, for PIC simulation of ion thrusters the resolution of the grid can be much lower in the plume than in the the channel region. But as has been shown in the author's publication [II], Particle-In-Cell simulations with non-equidistant grids lead to self-forces. These are generated if the standard two-point central difference scheme is used to calculate the electric field at a grid point where cells of different size meet. While the solution of the Poison equation is correct for a non-equidistant grid, the standard electric field calculation is inaccurate. This can be seen by the test case of one test particle, placed in a one-dimensional grid. In Figure 1.4, the potential ϕ of this scenario is shown. At the left hand side the electric field E_p at the particle position X_p is

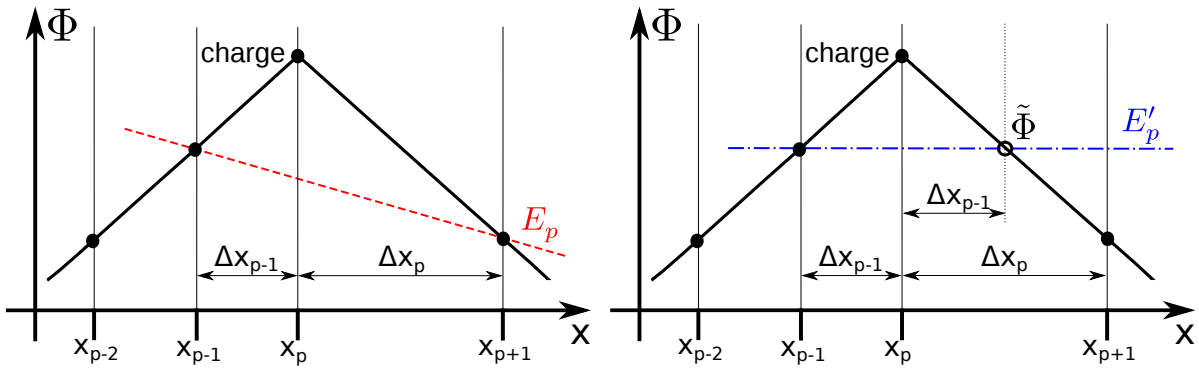

(a) Standard calculation scheme (b) Modified calculation scheme

Figure 1.4.: Calculation schemes of the electric field E for one charged particles located at X_p, in a non-equidistant grid with a change of cell size $\Delta x_{p-1} \neq \Delta x_p$ [II].

shown as the gradient of the red line, calculated from $\Phi(X_{p-1})$ and $\Phi(X_{p+1})$ by the standard two-point central difference scheme. But although, no external forces are included in this test case, the calculated electric field is not zero $E_p \neq 0\,\mathrm{V}$. As a result, the particle experi-

ence an artificial self-force if it is located at the border between two cells of different sizes. In order to conserve momentum by reducing this artificial force, an improved calculation of the electric field at the point of changing cell size is proposed in the author's publication [II]. Instead of using the potential at the grid point X_{p+1} a potential $\tilde{\Phi}$ is utilised. It is interpolated from the neighbouring grid points to the position $X_p + \Delta x_{p-1}$ and therefore restores the equidistant spacing of the grid, as sketched in Figure 1.4 (b). To calculate the electric field at the point X_p, this interpolation is included in the general two-point scheme. It reduces the artificial forces and the particle in the test scenario feels no electric field $E'_p = 0\,\mathrm{V}$. This allows the usage of a non-equidistant grid in PIC simulations.
Since for the interpolation a linear potential profile is assumed within the cells, in more realistic systems with high number of particles self-forces are not totally diminished. Therefore, in this work grid coarsening is done only in the plume region, where electric fields are low and so artificial forces. Within this work, a coarsening factor of two is applied when using this technique. As can be found in [IV] and [V], this allows a larger domain size with a simulated plume volume of about five times larger than before at equal computational costs.

1.3.2. The ray-tracing Monte-Carlo model

Beside the investigation of the HEMP thruster channel and the near field plume, also the kinetics of sputtered impurities is a topic of this thesis. These impurities are a consequence of plasma wall interactions in large vacuum vessels, the ion thruster is placed in during experimental test campaigns on Earth. These vessels are typically much larger than the investigated thruster. To study the back-flux of impurities towards the thruster exit, a three dimensional ray-tracing Monte-Carlo model was developed in the publications [III] and [VI] of this thesis. The idea is to sample the distribution of ions ejected by the thruster by the Monte-Carlo method, with respect to energies, angles and species and to follow their trajectories by the ray-tracing method.

Within the presented work here, distributions of an example ion thruster is used similar to those published for the SPT-100 Hall-effect thruster [King, 1998]. The distribution of the ejected mean energy [King, 1998] is shown in Figure 1.5 (a). The fraction of Xe^{2+} to Xe^{+} ions with respect to the emission angle θ is taken arbitrarily. It is used with the ion current

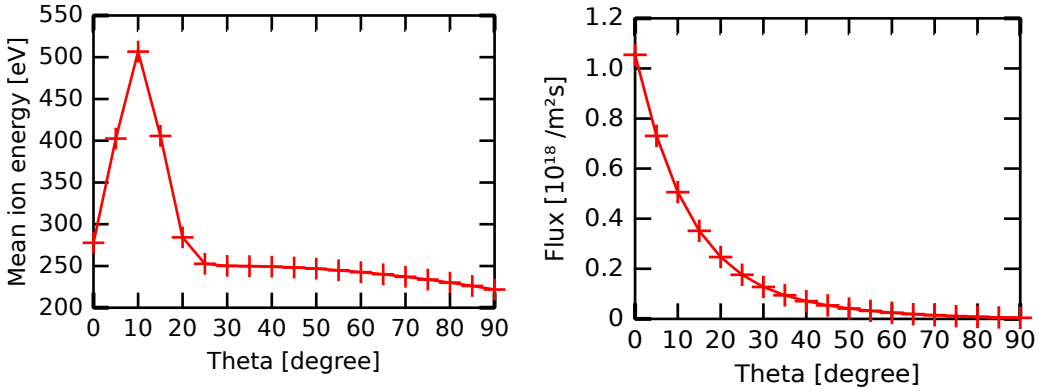

(a) Mean ion energy E(θ) (b) Flux density $\Gamma(\theta)$

Figure 1.5.: Sampled Xenon ion distributions, similar to the Hall-effect thruster SPT-100 [VI].

density $j(\theta)$ to calculate the flux density

$$\Gamma(\theta) = \frac{j(\theta)}{e \cdot (1 + f^{em}(\theta))} \quad , \tag{1.5}$$

with e the elementary charge and $f^{em}(\theta)$ the fraction of double charged ions. The resulting distribution is shown in Figure 1.5 (b). It shows that the ejected Xenon ions have a mean emission angle of zero degree. In polar direction an uniform distribution is used. These three distributions are used for the Monte-Carlo method to sample the ejected ions of the example thruster. To reduce computational time, instead of real particles, super particles are used.

Since the particle densities in the vacuum vessel are very low, the collision term of the Boltzmann equation is neglected. To solve the Vlaslov equation, a ray tracing method is used. It is valid, since in the outer plume region electric and magnetic fields are negligible and the sampled particles are moving along rays according to their source distribution. The place of impingement of the primary source ions at the vessel wall is therefore directly calculated. Here, the high energetic ions, ejected by the thruster are able to sputter the wall. The corresponding sputter yield is taken from binary collision cascade simulations by the SDTrimSP code [Eckstein et al., 2007]. During operation of the thruster, ions with energies larger than the sputter threshold create micro roughness on the thruster surfaces. Due to shadowing, this micro-roughness modifies the real angle of incidence, effectively reducing its range to values between 20° and 50°. For this angular range, sputter yields vary only slightly with angle. Therefore, we assume sputter yields to depend only on the energy of the impinging ions.

From the sputtering ions, the distribution of the emitted impurities can be calculated. Due

to the micro roughness of the wall material, they are assumed to obey a cosine law for their angular distribution [Eckstein, 1991]. To ensure a better statistic, each sputtering ion produces a bunch of sputtered particles, which are sampled by the Monte-Carlo method. Since the goal of this model is to investigate the back-flux of impurities towards the thruster exit, only particles with this direction are followed in the simulation. The back-flux is collected inside a hollow cylinder, representing a simplified ion thruster.
In [Kalentev et al., 2013] this model has been successfully validated with an analytic calculation of the back-flux.
According to the author's publication [VI], results of the back-flux simulation for different test set-ups will be be shown in subsection 1.5.4. The resulting modification of surface properties will be discussed and concepts to reduce these effects will be given.

After the description of the simulation methods, the physics of the HEMP thruster channel and plume region is discussed in the following two chapters.

1.4. Physics of the HEMP thruster channel

The motivation of this thesis is the optimisation of the HEMP-T with respect to thrust, efficiency and lifetime. Therefore, key roles are the physics of ionisation, ion extraction and plasma wall interaction. As will be shown within this chapter, these physics properties result for the DM3a thruster in an efficient ionisation of the propellant and low erosion inside the thruster channel.

As has been introduced in section 1.2, electrons in the HEMP-T channel are oscillating between two cusp regions, guided by the magnetic field. Beside scattering by collisions, transport across magnetic field lines occurs due to anomalous diffusion. In order to represent this 3D effect in the 2d3v PIC-MCC model an effective anomalous transport coefficient was used for a random walk model in the velocity space [III]. This model represents a Bohm like diffusion, where the transport coefficient D scales with the electron temperature T_e and the inverse of the magnetic induction $D \propto T_e/B$. The value of the diffusion coefficient was deduced from a self-consistent 3D simulation [III]. Especially in the cusp regions, this process plays an important role for the filling of the thruster channel, since it enables electrons to stream towards the anode.
At the anode propellant is injected. The trapped electrons in the channel ionise the neutral Xenon gas. In order to reach quasi-neutrality, the produced ions follow the electron

distribution and a channel plasma is building up. The corresponding density distributions of electrons and singly ionised Xenon ions are given in Figure 1.6. They are shown for the

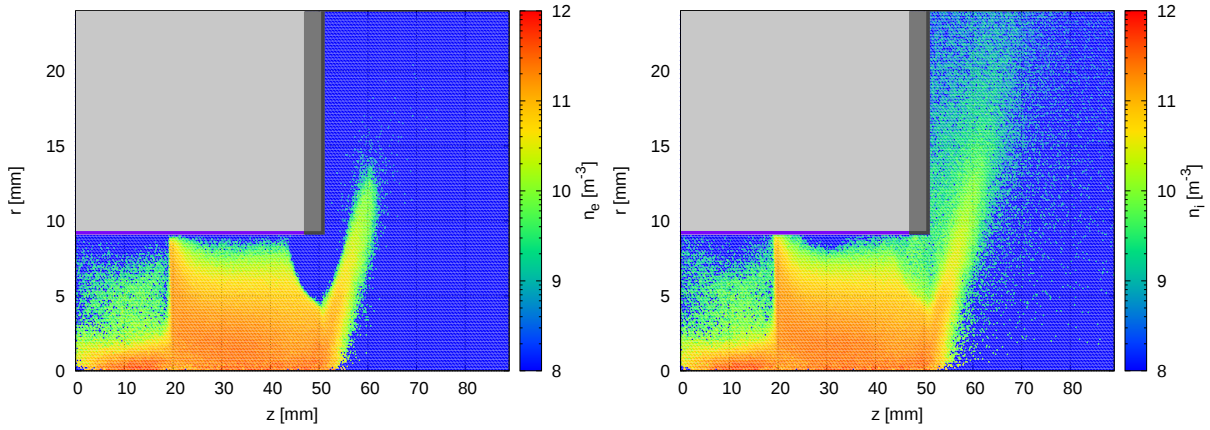

(a) Electrons (b) Single charged Xenon ions

Figure 1.6.: Density distributions in the channel and the near field plume, derived from [III].

computational domain, which contains the thruster channel of the DM3a ($0\,\text{mm} \leq r \leq 9\,\text{mm}$ and $z \leq 51\,\text{mm}$) and the near field plume ($z > 51\,\text{mm}$). Due to electron magnetisation, the dominating electron transport is parallel to the magnetic field lines, which builds up a characteristic density distribution. In the channel, clearly two regions can be distinguished. Due to electron trapping, high plasma densities in the second magnetic bottle between the inner cusp ($z = 21\,\text{mm}$) and the exit cusp ($z = 50\,\text{mm}$) are visible. In the first magnetic bottle electrons are less confined and getting lost at the anode ($z = 0\,\text{mm}$). This results in a lower electron density in this region and also in a lower ion density. In the central cusp the radial guidance of the electrons is clearly visible by the high plasma density. Since the injected electron current of the neutraliser, which is a hollow cathode, is low, its impact on the electron density can not be identified.

Close to the symmetry axis of the thruster channel, the mainly axial magnetic field combined with the very large parallel electron transport results in a flat potential. Only in the narrow cusp regions, where the field lines intersect the channel wall, the electron transport parallel to the magnetic field leads to plasma wall interactions. All over the channel, electrons and ions are in contact with the inner channel wall, which mainly consists of a dielectric. But due to the guidance of the magnetic field, the overall electron wall contact is reduced. Therefore, impinging ions at the dielectric channel wall build up a positive surface charge. The resulting surface potential is in the range of the plasma potential, which gives a low electric field also in radial direction. The overall channel potential is flat and its value is determined by the applied anode voltage $U_a = 500\,\text{V}$, as can be clearly seen by the simulation result in Figure 1.7. It also shows the potential drop inside the dielectric channel wall as well as

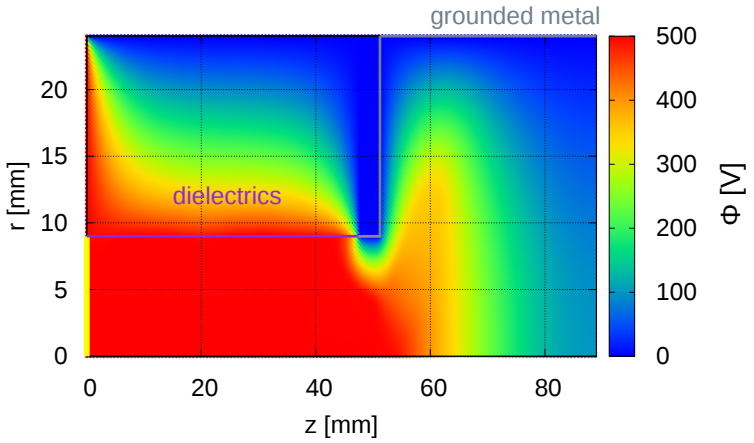

Figure 1.7.: Potential in the thruster channel and the near field plume [III].

the grounded pole piece mounted at the thruster exit. This grounded wall leads to a radial drop of the channel potential, which focuses the electrons at the channel axis. Therefore, no electron wall contact appears in this region, although the magnetic field guides them into radial direction. This electron focusing also affects the ion density distribution.
In summary, the channel plasma is confined by the magnetic field configuration, acting on the magnetised electrons and therefore also on the ions. It is characterised by a flat electric potential, driven by the anode voltage. Therefore, the electric field in the thruster channel is rather low. As a consequence, also the $\vec{E} \times \vec{B}$-drift in the cusp-regions is rather low. That means, for the HEMP thruster the plasma is confined by the magnetic field structure and not by a Hall current, as it is the case for the Hall-effect thruster.

Further investigation of the published results, gives more insight into the electron kinetics and therefore to the ionisation process. In Figure 1.7 also the potential drop at the thruster exit into the plume region is visible. This drop accelerates primary source electrons, injected by the neutraliser, towards the channel. Close to the exit, where the field strength is high enough, the magnetic field configuration guides these electrons. The exit cusp allows them to enter the thruster channel only close to the thruster symmetry axis. As can be seen by the distribution of the electron mean energy given in Figure 1.8, these high energetic electrons are guided by the field lines along the thruster axis into the central cusp region. Due to collisions, the mean energy decreases with increasing distance to the thruster exit. In the cusp regions, the magnetic mirror effect reflects low energy electrons and the electron mean energy rises towards the channel wall. Due to the higher electron energy diffusion perpendicular to the magnetic field lines increases. This leads to a transport of highly energetic electrons from the second to the first magnetic bottle. All along their trajectories, collisions lead to scattering, which results in a decreasing electron temperature perpendicu-

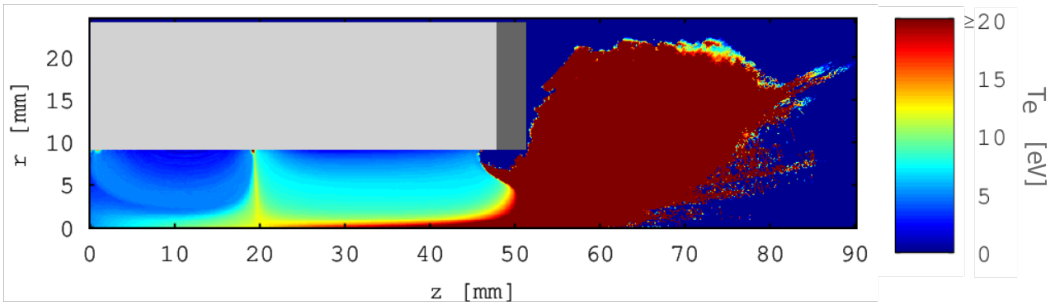

Figure 1.8.: Electron mean energy distribution, restricted to energies lower than 20 eV.

lar the magnetic field lines. Similar to other laboratory plasmas, the mean electron energy in the thruster channel is in the range of $1 - 8\,\mathrm{eV}$, while also electrons above 10 eV are existing. While Figure 1.8 the mean electron energy for each cell can be seen, in Figure 1.9 full electron energy distribution functions are given for three axial positions in the channel. It shows a non-Maxwellian characteristic, where also electrons with an energy higher than 10 eV are present. The electron-electron mean free path is larger than the channel length

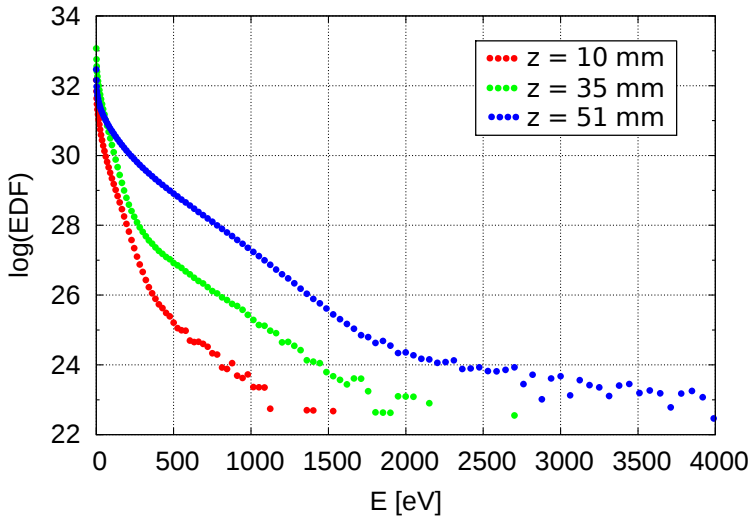

Figure 1.9.: Electron energy distribution function (EDF) at different axial positions accumulated over the channel radius, derived from [III].

therefore electrons are not thermalised and the logarithmic plot of the distribution function is not linear. A comparison of the electron distribution functions at different axial positions shows the decreasing electron energy downstream the thruster channel, caused by collisions. In [III] also the axial velocity distributions of ions and neutral propellant atoms are published. For the propellant neutrals the normal distribution around $v_z = 0\,\mathrm{m/s}$ indicates a thermal behaviour. In contrast, the non-normal distribution for the Xenon ions demonstrate the non-Maxwellian character in the thruster channel. This corresponds to the discussion of the collisions in section 1.2. The non-Maxwellian characteristics of the channel plasma determines the need of a kinetic method to simulate the HEMP thruster.

While for the HEMP thruster the mean electron energy is in the range of $1 - 8\,\mathrm{eV}$, the threshold energy of single ionisation in a Xenon gas is $\mathcal{E}_{thr}^{INZ} = 12.13\,\mathrm{eV}$ [Hayashi, 2003]. That means, ionisation takes place only by high energy electrons from the tail of the energy distribution. This is evident from the distribution of ionisation collisions, given in Figure 1.10, which correlates with the distribution of highly energetic electrons. The ionisation

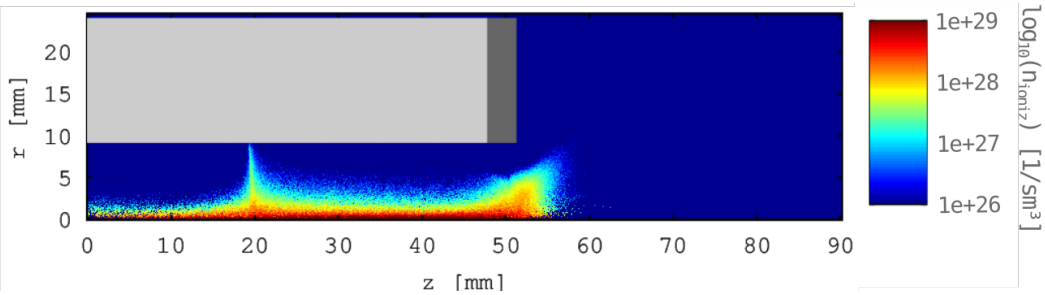

Figure 1.10.: Density distribution of single ionisation collisions.

of propellant atoms mainly takes place at the axis and in the cusp regions. Due to the trapping of electrons in the magnetic bottles, the ionisation rate is increased. The limited radial extension of ionisation at the exit cusp is caused by the grounded pole piece, focusing electrons at the symmetry axis. Also ionisation in front of the exit can be seen. Here, the neutral density is not as low as in the outer plume region and the electron energy is high due to acceleration by the potential drop. The good electron confinement of the HEMP-T leads to an efficient ionisation of the propellant.
For a better understanding of the low discharge losses as well as the low channel erosion, a discussion of the plasma wall interactions is given in the following.

Within the channel, the plasma wall contact is determined by the magnetic field configuration. In most of the channel wall regions, the electron flux is axial, only in the narrow cusps it is guided towards the surface. In the following, plasma wall interactions in the cusps, in the regions in between, at the pole piece and in the anode regions are discussed separately. In the cusp regions, the magnetic mirror effect reduces the flux, but highly energetic electrons are able to overcome the barrier and reach the dielectric channel wall. Since the ions are following, a classical plasma sheath is developing, with equal current densities at the surface $j_e = j_i$ and a resulting potential drop of $\Delta\Phi \approx -k_B T_e/(e)\ln(\sqrt{m_i/(2m_e)}) = -21\,\mathrm{V}$ towards the dielectric wall [Lieberman and Lichtenberg, 2005]. Impinging electrons can induce secondary electron emission (SEE). This cools the channel electrons, since the re-emitted particles have low energy. These additional negative charges in front of the wall lead to a further reduction of the radial potential drop in the cusp region. This reduces the mean energy of the impinging ions to $\mathcal{E}_i < 15\,\mathrm{eV}$ [Matyash et al., 2010]. To prevent

the surfaces from sputtering by these ions, Boron Nitrite ceramics is used for the dielectric channel wall. Under Xenon ion bombardment, it has a sputter threshold of $\mathcal{E}_{thr}^{sput} \approx 50\,\mathrm{eV}$ [Gamero-Castano and Katz, 2005], which is higher than the mean ion energy. Therefore, the erosion of the dielectric channel wall should not be a constraint in the lifetime of the thruster. Besides performance, this is an important parameter for space missions.
Between the cusp regions, no plasma sheath is building up, since the magnetic field is mainly parallel to the channel wall. That means, the overall flux towards the dielectric channel wall is reduced and appears only in the central cusp region [Matyash et al., 2010].
At the exit the grounded metal set the plasma bulk potential drop to zero, as can be seen in Figure 1.7. This causes a strong electric field. Although the magnetic field configuration in the exit cusp points radially towards the pole piece, the electric field reflects the electrons and therefore focuses the plasma to the symmetry axis. But the negative potential drop also results in a flux of ions towards the grounded wall.
At the anode, the magnetic field configuration is similar to the cusp regions. Due to the mainly axial field at the symmetry axis, electron wall interaction is strong. But at higher radial positions, the field lines are bounded in radial directions, which reduces the electron flux towards the anode with increasing radial position. Due to the anode potential, nearly no ions impinge and the flux is dominated by electrons.
In summary, the plasma wall contact of the HEMP-T is minimised with practically no erosion inside the thruster channel. Experimental measurements showed after a 1200 h test run, erosion of less than $5\,\mu$m in the cusp regions [Koch et al., 2011]. Therefore, lifetime is expected to be $> 10\,000$ h and could be shown for 7532 h [Lazurenko et al., 2012].
Another plasma wall interaction in the channel is deposition. As will be shown in the next section, this can appear by impurities generated during terrestrial testing within vacuum chambers.

As can be deduced by these discussions, the plasma confinement depends on the area of intersection between channel wall and magnetic field lines. The smaller the area, the more electrons are reflected by the magnetic mirror effect. This is due to the stronger magnetic field gradient affecting the electrons. A minimised area of intersection can be reached by a channel wall close to the permanent magnets. Therefore, for optimisation of the HEMP-T magnetic field and channel geometry have to be adjusted in order to reduce discharge losses.
The plasma volume of the channel plays a role for the performance of a HEMP thruster. Surely, a large volume ensures a large amount of generated ions, but due to limited strength of permanent magnets, confinement decreases with the increasing channel radius. On the other side, a small channel radius increases the influence of the plasma sheath on the channel

plasma and therefore reduces the volume of confinement. An example of such a HEMP thruster configuration can be found in the publication the author contributes to [VII]. While the DM3a thruster aims at mN thrust, the μ-HEMP is developed for a thrust production in the range of some micro-Newtons. In this case, the channel volume is reduced by much smaller channel radii down to scales comparable to the thickness of the plasma sheath [VII].

From the different plasma wall interactions, the global current flux balance can be understood. Generation of doubly charged Xenon ions Xe^{2+} is also included in the simulation, complimentary done to the published results. Due to a lower ionisation rate the fraction of Xe^{2+} is about 2% of the singly charged ones. Therefore, the principal plasma physics of the HEMP-T is not affected and the articles of this thesis only follow the kinetics of singly charged ions Xe^{+}. But for the production of thrust, such a small fraction of Xe^{2+} is of importance since these ions are accelerated to twice the energy of the singly charged ones. In Figure 1.11, the integral current flux balance is sketched. It gives the current of the three species towards the different parts of the channel wall as well as out of the thruster channel. As expected, it shows the emittance of ions into the plume, indicated by a positive

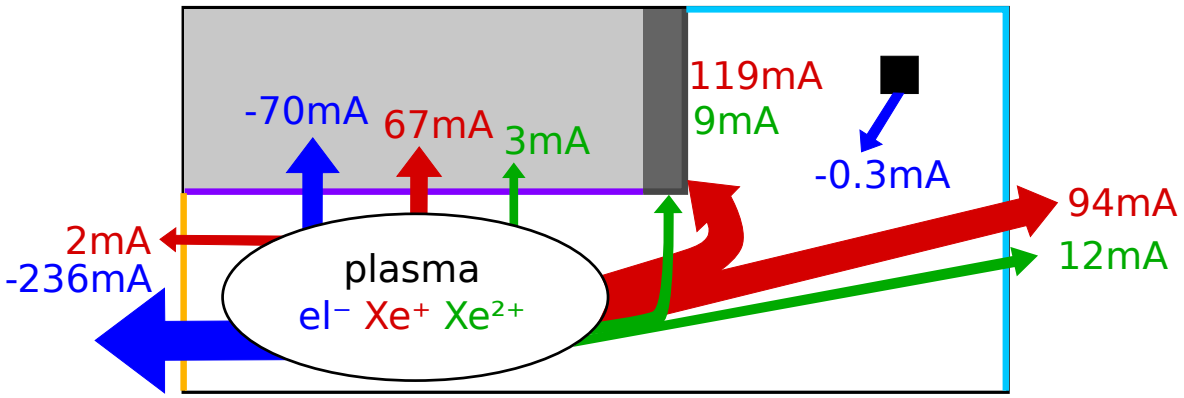

Figure 1.11.: Integral current balance of the DM3a HEMP-T by the flux of electrons (blue), singly (red) and doubly charged ions (green) towards the anode (orange), the dielectric channel wall (violet), the pole piece (gray) and out of the domain (light blue).

current at the right hand side domain boundary. This is the main goal of an ion thruster. To sustain the quasi-neutrality of the channel plasma also electrons have to get lost from the discharge. Due to the potential drop at the thruster exit, this takes place inside the channel. As discussed before, at the dielectric channel wall the flux is reduced to the narrow cusp regions. Therefore, the main loss of electrons appears at the anode, as shown by the size of the blue arrows. Here, the net current of electrons and ions is $I_{anode} = -234\,\mathrm{mA}$, where the negative sign indicates a current driven by electrons. Due to the dielectric sheath

in the cusps also ions are getting lost at the dielectric wall and the total net current is zero $I_{diel} = 0\,\text{mA}$. Therefore, the same amount of I_{anode} has to be ejected as positive current from the channel plasma. For the simulation, this current is partitioned into two parts, where one part is ejected into the plume $I_{plume} = +106\,\text{mA}$ and the other one impinges at the grounded pole piece $I_{pole} = +128\,\text{mA}$. This gives an overall ion current of $+234\,\text{mA}$ ejected from the channel plasma. In Figure 1.11, the electron source current I_{source}, injected by the neutraliser is indicated by a black box in the plume. In short, the sum of the outgoing current corresponds to the incoming current $I_{anode} + I_{diel} + I_{pole} + I_{plume} = I_{source}$. The source current is conserved, which shows the validation of the simulation.
For this specific simulation, the source current is much lower compared to the out streaming currents. This shows the high amplification of source electrons within the plasma of the DM3a HEMP thruster. The production of an ion current of 234 mA by a source of 0.3 mA electrons is possible by a long lifetime of electrons. For the HEMP-T, this is ensured by a good electron confinement and therefore low discharge losses. In experiment, this good electron confinement is implied by the fact, that the thruster performance is practically not influenced by switching of the neutraliser [Kornfeld et al., 2003].
Although, the electron amplification is high, the ionisation efficiency is much lower than in experiment. It is calculated as $\mu = I_{plume}/(q_e \cdot Q_{prop})$, where q_e is the elementary charge and Q_{prop} the flux of the propellant source. Within the simulation a source of $Q_{prop} = 12.5\,\text{sccm}$ was used, which results in $\mu = 11.8\,\%$. For similar propellant sources, experiments reached an ionisation efficiency in the range of $70\% - 90\%$ [Kornfeld et al., 2003], [Koch et al., 2011]. A likely reason for the much lower ionisation efficiency than in the experiment is a lower volume of ionisation due to an underestimated electron transport perpendicular to the magnetic field lines.

Since the channel and plume plasma of the HEMP-T are coupled, the production of ions is also influenced by the plume plasma physics. This will be discussed in the next chapter.

1.5. Plume physics

For ion thrusters, channel and plume plasma are coupled. The channel plasma ejects ions into the plume, which influences the plume potential. Their trajectories are given by the potential gradient at the thruster exit and the angle of emittance determines the produced thrust. But also in the plume the ion trajectories are influenced by electric fields and collisions and changes therefore the thrust. On the other side, the channel plasma relies on electrons provided by the plume to hold on the ionisation process. A change of the electron distribution in the near-field plume can modify the ionisation rate inside the thruster channel and therefore the thruster efficiency. Within the plume these electrons are affected by the potential and by the magnetic field of the thruster. This gives a rather complex interaction between plasma densities, potential and magnetic field.

The coupling of the two regions is driven by plasma. Therefore, the channel plume interaction takes place mainly in the near-field plume region, where the neutraliser provides electrons. For an integrated HEMP-T model including a reasonable plume size, a non-equidistant grid was used. In order to reduce artificial self-forces it was combined with a corrected electric field calculation at the change of cell size, as described in subsection 1.3.1. But as will be discussed in subsection 1.5.1, this integrated model has a computational problem in equilibration of the plume plasma, which leads to non quasi-neutrality in parts of the plume region. In order to obtain an electric field comparable to the experiment, special domain set-ups are used. In subsection 1.5.2 the physics of electrons in the near-field plume and its impact on the channel plasma is investigated. In subsection 1.5.3 the physics of the accelerated ions is studied with respect to the angular ion distributions. From these distributions the produced thrust is calculated.
In the outer plume region, the coupling to the channel plasma is reduced. A topic of interest in this region is sputtering of surfaces by the accelerated ions. Especially within experimental measurements in vacuum vessels, the produced sputter impurities can redeposit inside the thruster channel and influence the channel plasma. Details will be given in subsection 1.5.4.

1.5.1. Computational problems

Within a model of channel and plume plasma, the larger time scale of the plume makes it difficult to reach a steady state of the simulation. Due to the out streaming characteristic

of the plume, the ion density is decreasing with distance to the thruster itself. In order to sustain the potential drop at the HEMP-T exit and therefore the ion acceleration, also the electron density has to be low. Since the electron density is reduced in the plume, collisional transport is very weak and expansion of the electron distribution is slow. In the near-field plume this process is further delayed by the guidance of the magnetic field, which results in an overall equilibration time scale of about some seconds. But the high computational costs of the used PIC-MCC model allows only simulated system times in the range of µs. Therefore, in the simulation presented here, nearly no electrons are present in most of the plume regions while ions are. This can be seen in Figure 1.6 in the previous chapter. As a result, the simulated plume is partially non quasi-neutral, which is an artefact and does not appear in reality.
In addition to the long equilibration time scale, the neutraliser in most of the simulations of this work are only used as a primary source of the channel plasma. During operation in space, the main task of the neutraliser is to fill the plume with electrons and neutralise the plume plasma in order to prevent satellite surfaces from electrostatic charging. But due to the long equilibration time this process is not possible to be reproduced with the time consuming PIC-MCC method. On the other hand, terrestrial experiments of the DM3a HEMP thruster showed a stable operation without a neutraliser [Kornfeld et al., 2003]. This might indicates, a quasi-neutral plume is not critical for the thruster physics and the approach of a primary electron source is reasonable. Therefore, in the publications of this work an electron source current much lower than the ejected ion current was injected, which results in a non quasi-neutral plume plasma.

Du to the low plasma densities, the plume potential Φ_{plume} is not screened from the potential set at the domain boundaries. Therefore, the evolving Φ_{plume} is sensitive to the boundary conditions and thus also to the domain size. Corresponding to space condition or a grounded vacuum chamber, typically a Dirichlet boundary condition with $\Phi = 0\,\mathrm{V}$ is set. Here, a change of the domain size stretches and shrinks the plume potential. This can lead to an electric field with different direction than in the experiment and therefore to to different charged particle trajectories. Beside the size also the aspect ratio of the simulated plume region is of importance and can lead to a non-isogonal deformation. Such an example can be seen in Figure 1.12, where the change of the domain size stretches the potential drop in the plume. Due to the slowly decreasing Φ_{plume} also a von Neumann condition with $\vec{E} = 0\,\mathrm{V}$ can be chosen. This boundary condition is used in Figure 1.12 at the axial plume boundary. It corresponds to an enlargement of the domain and therefore deforms Φ_{plume} as well.

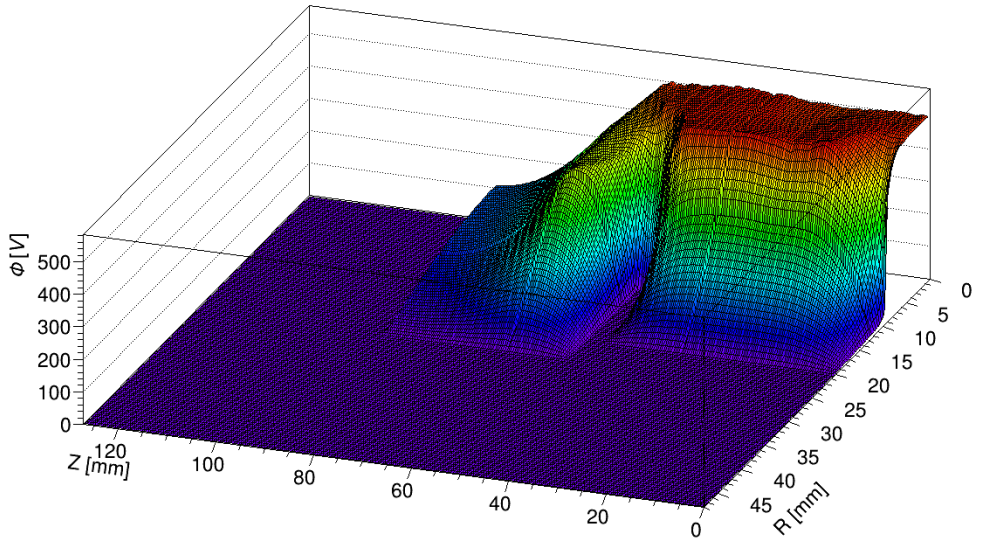

(a) Small domain

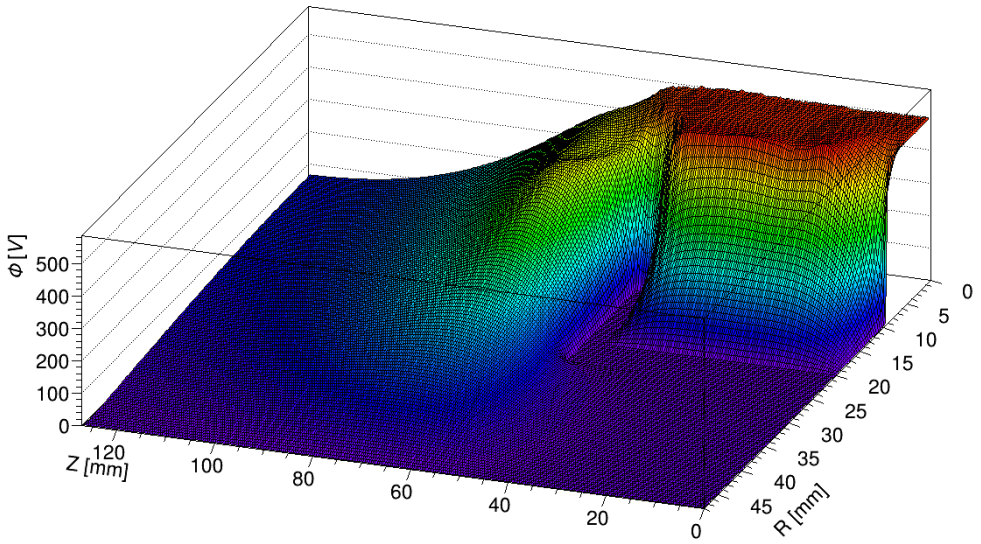

(b) Large domain

Figure 1.12.: Influence of the domain size on a potential solution of the DM3a HEMP-T model [III].

In order to reduce artefacts by stretching and shrinking the electric field in the plume, a domain size less sensitive to the change of the axial boundary condition was chosen. The resulting potential is shown in Figure 1.13. It has a plume aspect ratio of roughly 76.2 mm/50.0 mm $\approx$ 1.5, which is close to the one in the ULAN vacuum chamber of the THALES group [Harmann et al., 2007], where the DM3a HEMP thruster is typically measured in. This results in an isogonal shrunk plume potential in the simulation and therefore in ion trajectories close to the experiment. In order to decrease the calculation time, also a smaller domain size with a von Neuman boundary condition was used in [IV]. It gives nearly the same electric field as for the large domain used in the author's publication [V] and therefore comparable results for the direction of the accelerated ions.

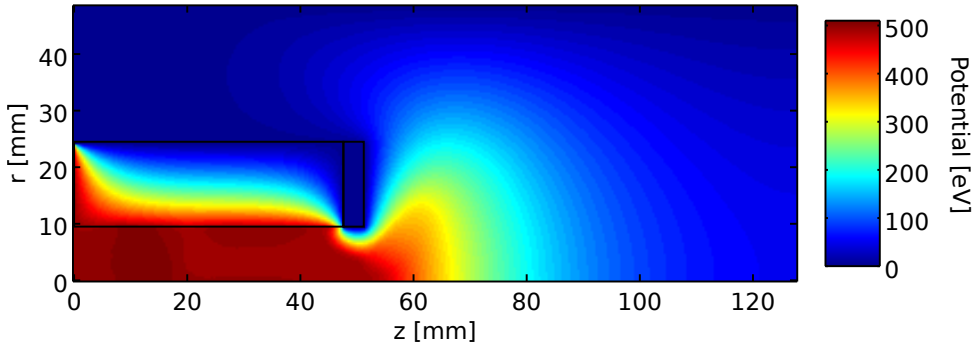

Figure 1.13.: Potential of the simulation domain used in [V].

With the chosen domain size the physics of electrons and ions in the near-field plume can be studied in the following sections.

1.5.2. Physics of plume electrons

Electrons of the plume are attracted by the anode potential and therefore getting accelerated towards the channel exit. Close to the thruster, in the near field plume, the electron movement is additionally influenced by the magnetic field. As investigated in the author's publication [V], in front of the thruster exit its impact is quite strong. This can be seen by the small influence of different electron source positions on the electron distribution in the plume. The resulting electron densities, given in logarithmic scale in Figure 1.14, show no significant changes. Especially in front of the thruster exit the combination of the mag-

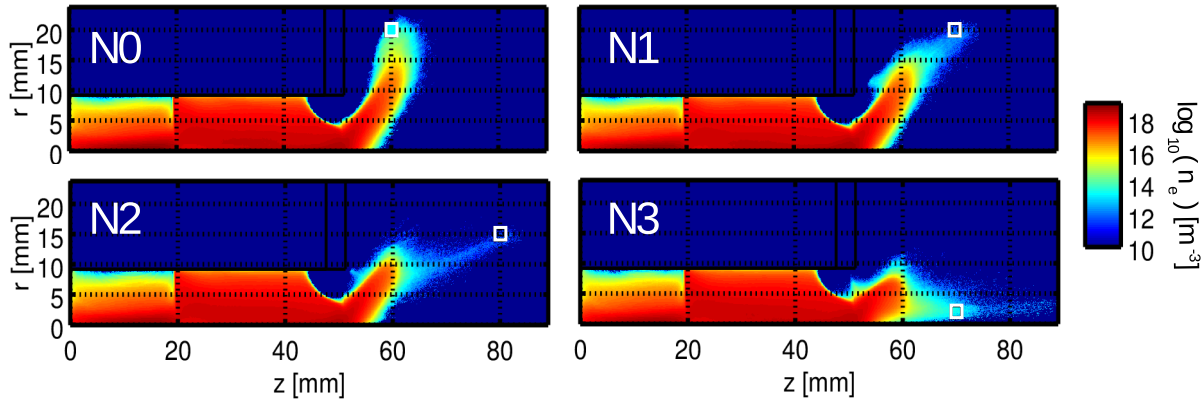

Figure 1.14.: Electron density in logarithmic scale for four different source positions (N0 - N3), indicated by a white box [V].

netic and electric field results in electron trajectories oscillating in an electric well. The magnetised electrons are trapped and build up a characteristic spatial distribution, which is nearly independent of the place of injection. This oscillating behaviour can also be found

for other magnetic field configurations, as for example the μ-HEMP thruster [VII]. Only for a source position close to the symmetry axis the electron plume density changes, see N3 in Figure 1.14. Here, close to the symmetry axis, the magnetic field points directly towards the anode and axial plume electrons can directly enter the thruster channel.

While in the simulations mentioned before, the electron source is situated close to the thruster exit, in experimental set-ups the neutraliser is mounted at larger radial positions. Here, the injected electrons also experience a drift velocity pointing downstream the thruster channel. This results in less magnetised source electrons, which can produce a broader electron distribution in the plume. To study the influence of low magnetised source electrons, a beam-like electron source situated in a further outside plume region was investigated in [V]. As can be seen in Figure 1.15, the electron density in the plume is more extended which also affects the potential. It results in a more pronounced ion beam. This is a much more

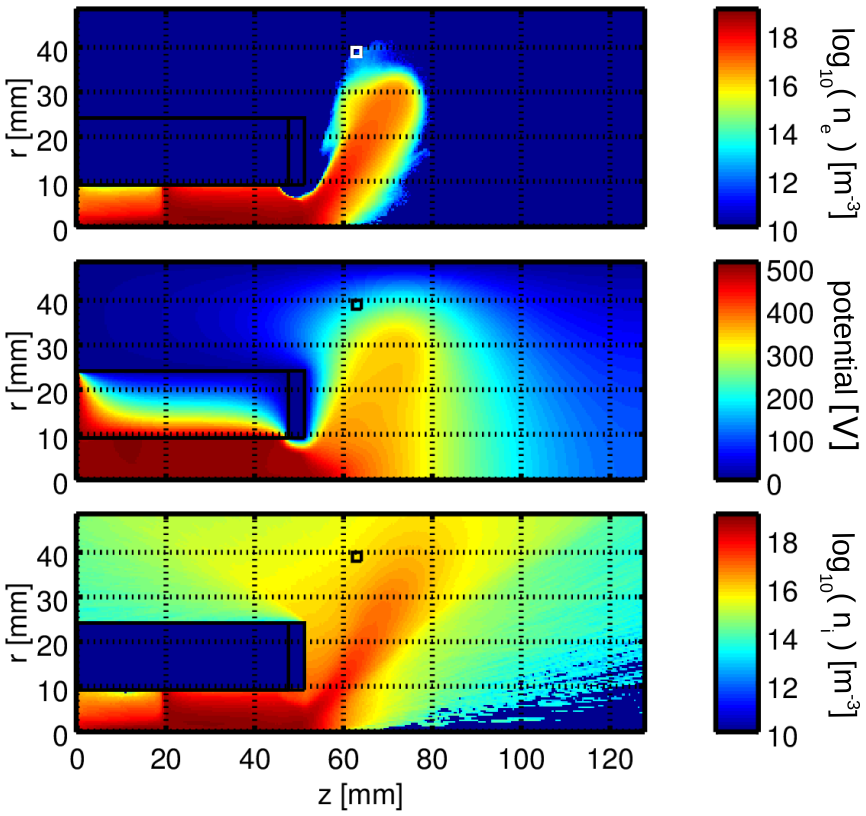

Figure 1.15.: Electron density (top), potential (central) and ion density (bottom) for a beam-like electron source directed away from the thruster [V]. The source position is indicated by a white, respectively a black box.

realistic scenario compared with experiment since the neutraliser not only supplies electrons to fill the thruster channel but also neutralises the plume plasma.

The changes in the plume plasma also affects the channel. Comparison of the electron distribution in Figure 1.14 and Figure 1.15 shows a higher electron density in the channel of

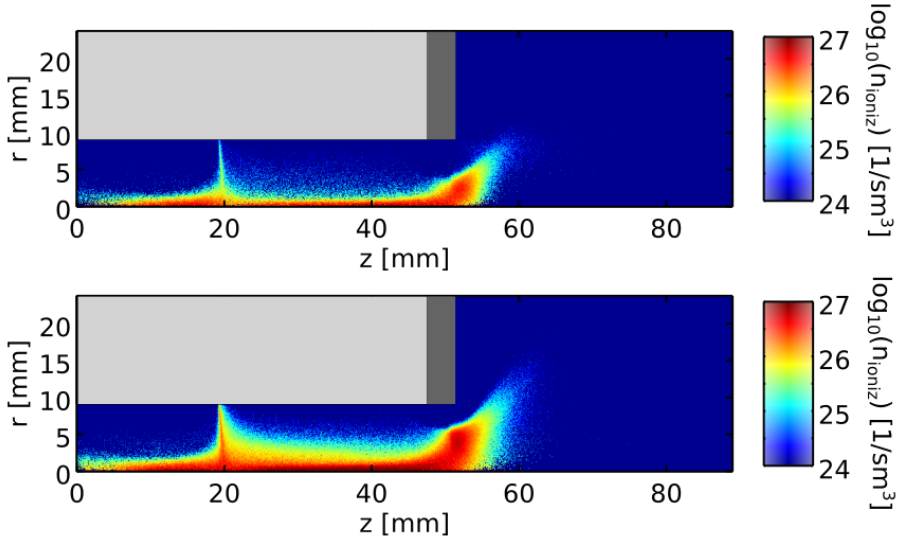

Figure 1.16.: Ionisation rate in logarithmic scale for the thermal electron source at position N2 (top) and the beam-like electron source (bottom).

the later. As a result, the ionisation rate is increased, as can be seen in Figure 1.16. It produces more electrons, which further increase the electron density and therefore the ionisation rate. This non-linear process is crucial for the ion thruster performance and depends on the ability of plume electrons to enter the HEMP-T and remain in the thruster channel. As a consequence of the higher ionisation rate, more ions are exhausted into the plume, which changes the plume potential and therefore the plume electrons. This gives a rather complex interaction of channel and plume plasma and shows the need of a simultaneous simulation of both regions. Due to the large time scale of collisional electron transport in the plume the expansion of the electron cloud towards symmetry axis is not yet saturated. As a result the potential drop is expected to be stretched in axial directions and the ionisation inside the channel further increase.

1.5.3. Physics of accelerated ions

The physics of the accelerated ions in the plume is of high interest, since it determines the thrust. The thrust production is mainly given by their angular current and energy distributions. Within the plume, these distributions are modified by the electric potential and collisional effects. They play an important role in optimisation of the thruster performance. It is also one of the few experimental parameters which can be used for validation of the simulation. The angular ion distributions in current and energy will be discussed in the

following. It allows the calculation of the produced thrust.

In experiment, angular ion distributions of current and energy are typically measured by a Retarding Potential Analyser (RPA). They are placed at about a few tens of centimetres to few meters distance from the thruster exit. For the definition of the ejection angle, the thruster is assumed as a point source positioned with $r = 0\,\mathrm{mm}$ in the thruster exit plane. Although the usage of a non-equidistant grid reduces the cost of calculation, the possible simulation domain is much smaller than a few tens of centimetres. Therefore, these distribution functions are diagnosed along the plume domain boundary, a few centimetre from the thruster exit. For a comparison of the experimental ion distributions with the simulation, the physics appearing within the space between the different positions of measurements has to be taken into account. For this transfer of information a mapping routine, called transfer function was proposed in the author's publication [IV]. Especially for small domains with von Neumann boundary conditions it has an impact on the angular ion energy distribution. Here, the plume potential has not yet decayed to zero at the surface of measurement and the potential energy of the detected ions have to be taken into account. In Figure 1.17, a comparison of the corrected and uncorrected angular ion energy distributions can be found for an example of a simulation domain with a von Neumann condition at the axial boundary. The energy distribution of ejected ions is mainly determined by the potential the ions are

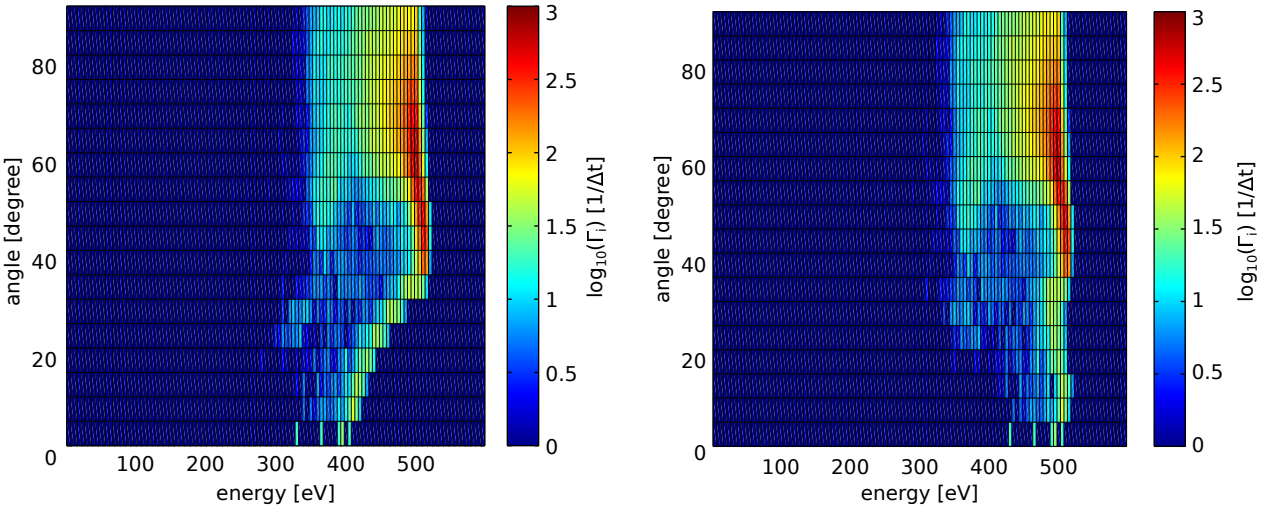

(a) Detected (b) Mapped

Figure 1.17.: Detected angular ion energy distribution of the ion particle flux Γ_i (a) in logarithmic scale and mapped to the detector position (b). The simulation has a von Neumann boundary condition at the axial domain boundary [IV].

generated at. Therefore, most of the detected ions in Figure 1.17 have an energy close to the anode potential $U_a = 500\,\mathrm{V}$. This observation agrees very well with the experimental

measurements, for example in [Koch et al., 2011], and leads to the deduction of a nearly constant potential in the regions of ionisation.
But the energy distribution of the plume ions is also influenced by charge exchange collisions with residual propellant gas which lead to high energetic neutrals and low energetic ions. In comparison with experimental data these low energetic ions are missing in the simulation. While inside the thruster channel the mean free path of charge-exchange collisions is smaller than the channel length, the decreasing neutral density increases it to about 1 m. This distance is much larger than the size of the simulated plume, which results in less collisions than in the experiment. Therefore, the low energetic ions are under represented in the angular ion energy distribution of the simulation.

For the amount of produced thrust, not only the energy distribution of the ejected ions is of importance but also the angular current distribution. As shown in the author's work [IV], a dependency of the place of ionisation and the detected angle exists. The different origins of the ejected ions lead to two different peaks in the angular current distribution. In Figure 1.18 the ionisation distribution for two example angles of 40° and 60° is shown. The

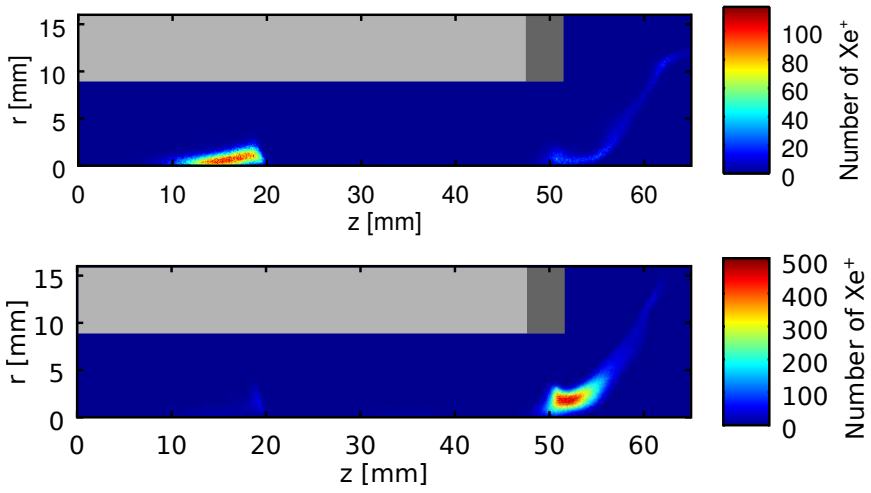

Figure 1.18.: Ionisation distribution for ions detected at the diagnostic surface at $40° \pm 2.5°$ (top) and $60° \pm 2.5°$ (bottom). In light Gray the dielectric channel wall and in dark Gray the grounded pole piece are sketched [IV].

corresponding angular current distribution is shown in Figure 1.19, indicated in blue. While for angles between 30° and 50°, ions are mainly generated inside the thruster channel, for angles larger than 55° the exit cusp is the place of birth. For angles below 30° both cusp regions contribute.

In Figure 1.19 also the angular current distribution measured by experiment at a larger distance [Kornfeld et al., 2003] is shown in red. Between the diagnostic surface in the sim-

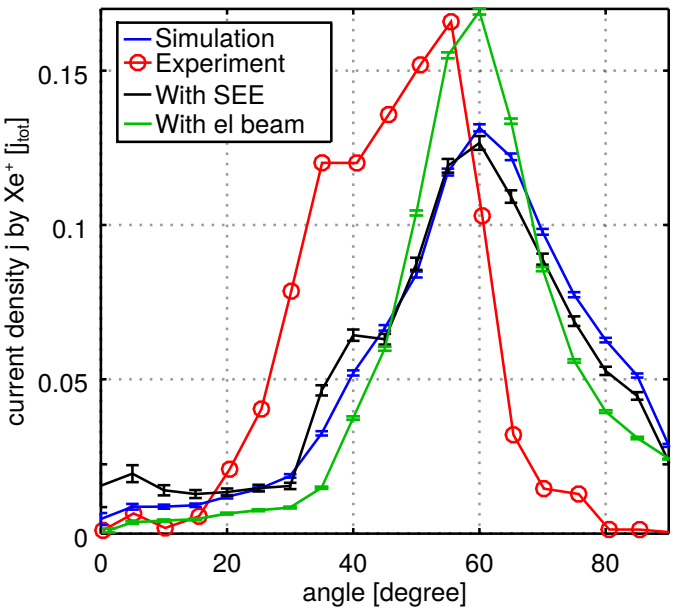

Figure 1.19.: Angular distribution of current density j by singly charged Xenon ions relative to the total current density j_{tot}, according to [IV] and [V].

ulation and the place of the RPA in the experiment, the plume potential can be estimated as decaying linearly. Therefore, a direct flight can be assumed for the ejected ions and the angular current distribution can be directly compared with the experimental data. For the measured as well as for the simulated angular current distributions, the two components according to the two regions of ionisation can be distinguished. In order to investigate the influence of experimental conditions which does not appear in space, in [IV] the effect of secondary electron emission from the vessel walls during terrestrial testing was studied. The resulting angular current distribution, is given by the black line in Figure 1.19. It shows a more pronounced peak at 40°, similar to the experimental measurement. The angular ion current distribution given as a green line in Figure 1.19 corresponds to the simulation of the beam-like electron source, introduced in subsection 1.5.2. The more realistic source provides additional electrons to neutralise the plume plasma, which develops a pronounced ion beam.

By comparison of the different simulation results, a stable angular ion current distribution is visible. This is caused by the trapped electrons in front of the thruster exit. The electron density structure in front of the exit drives the lagging of the electric potential into the plume and a bending of the electric field. Although the angular current distribution is close to the experiment, still a discrepancy of about ten degrees is seen.

In the experiment, the thruster is mounted on a thrust balance, which measures the thrust T. In the simulation T can be calculated by the angular distributions of the ejected ions.

While Equation 1.1 gives just an approximation of the produced thrust, a calculation, based on the ejected ion current I_{plume} and ion energy distribution $\mathcal{E}_{plume}$, gives a more accurate result. For each ion specie i the thrust can be calculated by

$$T^i = \int \mathrm{d}\mathcal{E}^i_{plume} \int \mathrm{d}\alpha \sqrt{\frac{2\,\mathcal{E}^i_{plume}(\alpha)}{m_i}}\,\cos(\alpha)\,\frac{m_i\,I^i_{plume}\big(\mathcal{E}^i_{plume}\,(\alpha)\big)}{q_i}\ , \tag{1.6}$$

where α is the angle of emission, q_i the charge and m_i are the mass of the corresponding ion species. This gives the total thrust $T = T^{Xe^+} + T^{Xe^{2+}} = 1.51\,\mathrm{mN} + 0.14\,\mathrm{mN} = 1.65\,\mathrm{mN}$. It is much lower than in experiments, where thrusts of $12 - 43\,\mathrm{mN}$ were measured for the DM3a HEMP thruster [Koch et al., 2003]. The main reasons for this is the low ionisation efficiency.

It might be caused by an underestimated electron transport across magnetic field lines, induced by turbulence in the electric field. The importance of this transport is indicated by measurements of Hall-effect thrusters, e.g. in [Janes and Lowder, 1966]. Within the PIC-MCC simulations of this thesis, this three dimensional effect is approximated by an anomalous diffusion coefficient which might not be accurate enough. For an increased anomalous transport, the region of high energetic electrons in the channel would be larger. Therefore, the volume of ionisation increases and thus the total amount of ions ejected by the channel plasma. As seen by the analysis of ion origins, this would also increase the low angle contribution of the angular ion distributions, which would reduce the amount of ions getting lost at the metal wall. A higher consumption of propellant inside the channel also leads to less residual neutrals at the thruster exit and therefore to less ionisation in this region. Due to less plasma in front of the thruster exit, the potential drop would be shifted into the channel creating an accelerating electric field with more axial direction. As an overall result, the total amount of ion current would get higher and the angular distribution would get shifted towards lower angles. Therefore, a better adoption of the anomalous diffusion coefficient would lead to a simulated angular current distribution and a thrust closer to the experiment. For a self-consistent simulation of this effect, a three dimensional PIC-MCC simulation of channel and plume plasma would be necessary. But due to the high computational costs, such a simulation is not applicable. Therefore, it is difficult to give predictive results for here used simulation method.

Also the similarity scaling might lead to a smaller ionisation inside the thruster channel. Since the applied similarity scaling does not scale the plasma sheath, the transport towards the channel walls might be higher than in the experiment. This reduces the plasma confinement and therefore the ionisation efficiency. For the chosen similarity factor this effect is

expected to be small, because the sheath still stays quite small compared with the channel size.

Beside the production of thrust also the impact of ions on surfaces in the plume regions, e.g. solar panels, is of high interest for the design of space missions. During terrestrial measurement, sputtering by these highly energetic ions can influence the channel plasma. Therefore, the next section deals with plasma wall interactions in the plume region.

1.5.4. Plasma wall interaction

Plasma wall interaction in the plume means interaction with satellite components or during terrestrial testing with experimental facilities. For spacecrafts, a serious problem is electrostatic charging, since it leads to electrical discharges. These discharges are able to produce transients in signal lines or power distribution lines. Also overloading of power circuits and therefore failures in power units can be caused by electrical discharges [Francis, 1982]. One cause for surface charging is ion impingement. Therefore, a neutralizer is placed in the plume, which provides a reservoir of electrons. Near satellite surfaces, these mobile particles are attracted by the developing wall potential and compensate the positive charge.
Another ion wall interaction is sputtering. Within terrestrial tests of all types of ion thrusters, sputtering in the plume can appear at vessel walls. This can produce impurities in the plume plasma, which are able to get back towards the thruster exit and build up co-deposited layers. These layers can change the optimized channel geometry and therefore the thruster performance, as has been seen within test-campaigns of the HEMP-T [Genovese et al., 2011] and other ion thruster concepts, e.g. the grid thruster NEXT [Shastry et al., 2013]. For this reason, a reduced back-flux is important to minimise artefacts in terrestrial measurements. A detailed study of the back-flux of an example ion thruster is given in the author's publications [III] and [VI] as well as in the conference proceeding [Duras et al., 2013]. These results will be summarised in the following.

To calculate the back-flux towards the thruster exit generated by sputtered particles at the vessel walls a ray-tracing Monte-Carlo model, described in subsection 1.3.2, was used. It approximates the far field thruster plume by an ideal vacuum with no electric fields. From an ion distribution ejected by the thruster the sputtered impurities and the resulting back-flux towards the thruster channel is calculated.
Within terrestrial evaluations of ion thrusters, typically two experimental set-ups are investigated. For a precise measurements of performance, the so called "performance test"

set-up is used. Here, one thruster is placed in the center of the vessel cross section. In order to be closer to the application in space also the performance of a cluster of four thrusters with only one operating thruster is measured. This "end-to-end test" set-up is a typical scenario for satellite station-keeping. In both cases, a characteristic pattern of impurities is entering the thruster channel exit. It is determined by a combination of the mean ion energy distribution of the emitted ions, the sputter yield of the vessel material, the cosine distribution of the sputtered impurities and the geometry of the vacuum vessel. Inside the thruster channel, this back-flux leads for the performance test set-up to a re-deposition symmetric in poloidal direction and decreasing with channel length [VI]. In the case of the end-to-end test set-up the non-centralised ion source causes an ion flux towards the vessel walls which is not equally distributed in poloidal direction. This disturbed symmetry is overlaying with the distribution of the sputtered impurities at the vessel walls. As a result, areas of high and low re-deposition inside the thruster channel are formed. Due to the different position inside the vessel, these deposition patterns are different for the four thruster channels [VI]. The back-flux towards the thruster exit can be reduced by using a larger vacuum vessel. Since the distance between vessel wall and ion thruster is longer, the solid angle to reach the thruster exit is smaller and therefore the fraction of flux coming back to the thruster channel is less. This also smooths the deposition patterns inside the channel [VI].
Another strategy to reduce the deposition inside an ion thruster is to reduce the source of emitted impurities. This can be done by choosing a wall material with a low sputter yield. For ion bombardment of $300eV$ Xenon, the commonly used wall material Aluminium has a sputter yield of $Y_{Al} = 0.45$ [Rosenberg and Wehner, 1962]. The most promising material for a reduction of the secondary source is Carbon, since it has a sputter yield of $Y_c = 0.08$ for the same conditions [Rosenberg and Wehner, 1962]. In experiments those Carbon walls are frequently realized by Carbon-coated tiles. The simulated back-flux of Carbon coated walls is significantly reduced in comparison to Aluminium [Duras et al., 2013]. But ventilation of the vacuum vessel generate a reservoir of Hydro-Carbons at the vessel walls, which will produce re-deposited Hydro-Carbon layers inside the thruster channel. These layers can get conductive depending on their thickness. Hence, electron leak current over the channel wall towards the anode increases. This decreases the ion current and thus the thrust. The result is a different performance of the thruster in the vessel compared to the one in space. Using metal walls instead of Carbon, the rates of physical sputtering are larger, but the evaporation at hot channel parts, namely the cusp regions, will prevent deposition of a continuously layer overall the channel wall and hence an electron leak current [III]. This effect has been observed and investigated during endurance testing of HEMP-T [Genovese et al., 2011]. It

also showed a clear decrease of thrust due to graphite tiles in the vacuum vessel, while for Aluminium coated walls the thrust stays stable.
A third strategy to overcome re-deposited layers is the implementation of baffles inside the vacuum vessel. Its operational principle is shown in Figure 1.20. Due to micro roughness of

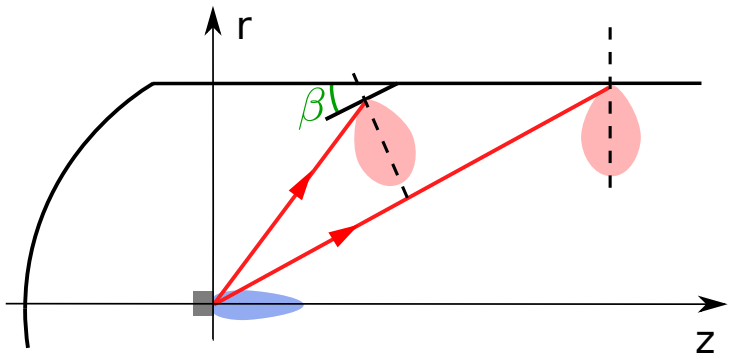

Figure 1.20.: Operational principle of a baffle to reduce the amount of back scattered particles towards the thruster channel, derived from [III].

wall surfaces, the distribution function of the sputtered particles follows a cosine function [Eckstein, 1991], sketched in light red. Its orientation, shown as dashed line, is mainly vertical to the surface, but nearly independent on the incident angle of the accelerated particles. For a tilted baffle, open towards the thruster, this cosine distribution results in a reduced amount of back-scatted particle towards the thruster channel. Here, the tilting angle and the distance between two baffles influences the total back-flux and therefore re-deposition inside the thruster channel. For example an angle of $\beta = 15°$ the back-flux towards the thruster channel can be reduced by 70 % [Duras et al., 2013]. Also the distance between the mounted baffles is of importance. This was shown for an angle of $\beta = 20°$ in [III], where the back-flux was reduced by $40\,\% - 66\,\%$. Because of these findings, these baffles were implemented in the Areospazio test facility [Monetti et al., 2017].

This model gives just a first estimates for the back-flux of sputtered impurities towards the thruster exit and the resulting re-deposition inside the channel. Effects like secondary electron emission at vessel walls, which influences the plume potential, collisions of propellant ions with residual gas, regions of magnetised electrons in the plume and changes in the thruster potential due to re-deposited layers inside the channel are not considered. They can be included in next modelling steps, which could clarify more precisely how terrestrial conditions influence the thrust measurements. Determining these artefacts is also of importance for the validation of the PIC-MCC simulation, since only few comparable parameters are accessible. This model can also be used to compute the ion flux towards satellite surfaces or solar panels. But here, surface charges might have a high impact on the

ion kinetics, therefore the ray-tracing Monte-Carlo model can give only a first estimate. For a more precise quantification a kinetic simulation of the full plasma has to be done.

1.6. Conclusions

In this work, kinetic simulations of ion propulsion systems were performed. This was done for the High Efficient Multistage Plasma Thruster HEMP-T patented by the THALES group [Kornfeld et al., 1999], which also performed the experiments.

The ion propulsion system HEMP-T relies on plasma production with magnetised electrons. The electron collision mean free paths are larger than the channel dimensions, which leads to a non-Maxwellian plasma. Therefore, kinetic simulation methods are needed for the simulation of the HEMP-T acceleration channel. In this work, the PIC-MCC method was used for this purpose. It requires a temporal resolution determined by the electron plasma frequency and a spatial resolution determined by the electron Debye length. The HEMP-T consists of the channel region with high plasma density and a plume region where the density is decreasing with the distance to the thruster exit. Therefore, the Debye length is strongly varying from some tens of micrometres to some centimetres. For an instantaneous simulation of both regions, the spatial resolution has to be chosen according to the smallest Debye length. This results for a domains size of $25\,\mathrm{mm} \times 90\,\mathrm{mm}$ in a grid of about 10^7 cells. The high number of cells can be reduced by similarity scaling of the system, which reduces the size of the simulated thruster while magnetic confinement, Knudsen number and particle velocity are preserved. This scaling preserves the physics of the plasma volume and is violated, if surface processes get important. Therefore its application is limited and the number of cells can only be reduced to about 10^5. For the PIC-MCC method used within this thesis, the calculation time for solving the Poisson equation is the most time consuming part. The high spatial resolution needed for the HEMP-T makes the simulation very costly. In order to increase the simulated near-field plume region, a non-equidistant grid was introduced in this work. It is motivated by the larger Debye length in the plume. In the standard PIC method a non-equidistant grid produces artificial self-forces, if a particle crosses cells with different sizes. To overcome this limit, a more accurate method was developed in this thesis. A modified calculation of the electric field at positions with cell size change minimises the error. Coarsening the grid in the plume, where only small space charge exists, allows to simulate the whole plasma dynamics within some centimetres.
For length scales of one metre and beyond, the PIC-MCC method is not applicable due to

the run-time limitations mentioned before. Since in this region electric and magnetic fields as well as collisions can be neglected, a ray-tracing Monte-Carlo model was developed and applied to simulate the outer plume region.
These simulation techniques allowed a detailed study of the physics of the HEMP thruster and an answer to the main research questions of this work.

What are the basic mechanisms for plasma confinement, plasma-wall-interaction and thrust generation?

The HEMP-T is characterised by a non-Maxwellian plasma confined in the thruster channel by a magnetic field. The magnetic field is generated by cylindrical permanent magnets with opposite polarity, see Figure 1.21. This leads to mainly axial field lines close to the

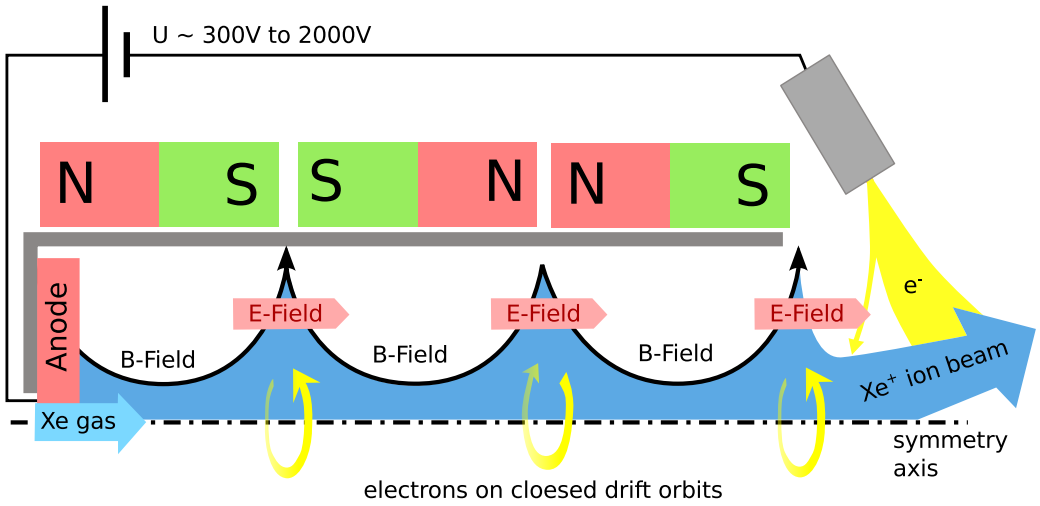

Figure 1.21.: Scheme of HEMP-like thrusters [III].

thruster symmetry axis and so called cusp regions, where the dominant direction is radial. These cusp regions are locations where the magnetic cylinders face each other. In the thruster channel, the Larmor radii of the electrons are small compared to the channel dimensions, in contrast to the ions. Due to different Hall parameters, electrons are magnetised, while ions are not. Therefore, the dominating electron transport is parallel to the magnetic field lines. Close to the symmetry axis of the thruster channel, the mainly axial magnetic field results in a flat potential. Only in the narrow cusp regions, where the field lines intersect the channel wall, the electron transport parallel to the magnetic field leads to plasma wall interactions. The magnetic mirror effect in the cusps reduces the electron flux towards the wall and confines the electrons like in a magnetic bottle. Ions are following the electrons due to quasi-neutrality and therefore discharge losses mainly take place in the cusp regions. For low losses and therefore a good confinement, the area of intersection

between channel wall and magnetic field lines has to be minimised. The lower the area of intersection, the more electrons are reflected by the magnetic mirror effect, because more of the magnetic field gradient affects the electrons.
At the anode, propellant gas streams into the thruster channel, which gets ionised by the electrons creating the plasma. As a result of the magnetic field configuration, electrons are oscillating between the two cusp regions, which forms a magnetic bottle. This electron trapping leads to an increased and efficient ionisation of the propellant gas. Due to reflection of low energetic electrons by the magnetic mirror effect, the electron mean energy rises in the cusps. At the exit cusp, high energetic electrons accelerated by the plume potential enter the thruster channel. These hot electrons determine the ionisation region by transport parallel to the magnetic field. Electron transport perpendicular to the magnetic field lines, e.g. by collisions, increase this volume. Compared to the experiment, the simulations show a much lower ionisation efficiency of the in streaming neutral gas, which indicates a too low ionisation volume compared with the experiment. A possible explanation of this difference is an underestimated transport perpendicular to the magnetic field lines. The inclusion of additional turbulent transport, well known for magnetised plasmas, will increase the ionisation volume.
The magnetic field configuration of the HEMP-T reduces the plasma wall interaction to only the narrow cusp regions. Here, the floating potential of the dielectric channel wall and its plasma sheath result in a rather low radial potential drop compared to the applied anode potential. Only high energy electrons, which are not reflected by the magnetic mirror, can overcome this drop and impinge at the channel wall. Here they produce secondary electrons, which are re-emitted into the plasma volume. These additional negative charges in front of the wall lead to a further reduction of the radial potential drop in the cusp region. As a result, impinging ions at the thruster channel wall are accelerated by the potential drop. Their energies are below the sputter threshold energy of the wall material. Therefore, no sputtering appears and the channel wall is not eroded. At the thruster exit the confinement by the magnetic field is weakened and strong losses of electrons appear. Here, the channel potential drops with nearly the full anode voltage and accelerates the generated ions into the plume. Outside the thruster channel, these energetic ions are able to sputter surfaces in the whole plume. This leads to the production of impurities at vessel walls during terrestrial testing in vacuum vessels. As has been shown in this thesis, a fraction of these impurities generate a flux towards the channel exit and lead to re-deposition inside the thruster channel. The amount of back-flux is determined by the sputter yield of the vacuum chamber wall. Therefore, compared with Aluminium walls Carbon coated walls should significantly

reduce the back-flux due to the smaller sputter yield of Carbon compared to Aluminium. A large distance between thruster exit and vessel wall reduces the amount of back-flux and smooths the pattern of deposition inside the thruster channel. The evolving deposited layers can get conductive. This can change the channel potential and the thruster operation.
The thrust of the HEMP-T is generated by the acceleration of ions. It is influenced by three factors: the amount of ejected ion current, the energy of these ions and their angular distributions. As has been shown in this thesis, ions are mainly generated at high potential close to the applied anode potential. Therefore, the accelerated ions producing the thrust gain the maximum energy. This is also observed experimentally. Also, the angular distribution of the ejected ion current is close to the one of the experiment, slightly shifted by about ten degrees to higher emission angles. Ions emitted from the thruster into different angles in the plume contribute mainly to the ion current at angles between 30° and 90°. They mainly originate from ionisation at the thruster exit. In front of the thruster exit, electrons are trapped by electrostatics forces. This enhanced density allows ionisation and an additional electron density structure establishes, which is also influenced by the magnetic field shape in the near field plume. This density structure drives the lagging of the electric potential into the plume and a bending of the electric field. As a result, the ejected ions are mainly accelerated into angles larger then 55°. Ions not generated at the exit cusps, but in the central cusps are mostly getting lost at the grounded pole piece at the thruster exit. Only a small fraction passes the exit cusp close to the thruster symmetry axis and therefore contribute to the lower angles of the angular ion distribution in the plume. Due to this self-sustained mechanism, simulations with different electron source locations show practically no difference of the ion angular distribution. Beside the energy of the ejected ions and the angular distribution of the ion current also the total amount of ion current influences the thrust production. The loss of ions at the grounded pole piece reduces the amount of ejected beam current and therefore the produced thrust.

In summary, HEMP-T is an efficient grid thruster with minimised erosion but with a potential characteristics similar to a grid thruster. This makes it highly attractive for space missions.

What are possible physics based ideas for optimisation of an ion thruster?

An optimised thruster should have a high ionisation rate inside the thruster channel, low erosion and an ion angular distribution with small contributions at high angles for minimised thruster satellite interactions. In experiments, the HEMP-T satisfies already quite nicely

these requests. Also the simulation contained in this thesis demonstrate the low erosion inside the thruster channel. However, in the simulations ion losses at the pole piece reduce the thrust production. The main reason for these high losses is the underestimated electron transport perpendicular to the magnetic field lines. A higher transport increases the volume of ionisation inside the thruster channel. An increased ionisation rate reduces the amount of residual propellant at the thruster exit. Therefore the ionisation in this region is reduced and the plasma density is decreasing. The potential drop moves back into the anode direction and the electric field gets steeper and more axially oriented. This reduces the loss of ions at the pole piece and a higher ion current is ejected into smaller angles. This scenario is well known from experiment. To use numerical simulations for the optimisation of the HEMP-T, the simulated values have to get closer to the experiment. Here, the position of the potential drop at the thruster exit is crucial for the angular ion distribution and the total amount of ejected ion current. It is closely linked with realistic radial transport, probably driven by turbulence. Optimisation of the magnetic field configuration at the thruster exit is able to optimise the electron distribution in front of the thruster exit and therefore the position of the potential drop.
A successful example for an optimisation using numerical simulations is the reduction of back-flux of sputtered impurities during terrestrial experiments by an improved set-up of the vacuum vessel. The implementation of baffles reduces the back-flux towards the thruster exit and therefore re-deposition. Since the distribution of the sputtered particles is normal to the emitting wall, implementation of baffles with normals pointing away from the thruster reduces the amount of sputtered back-flux reaching the thruster. Also, the material choice for the vessel walls could be optimised. The implementation of Carbon-coated tiles have the disadvantage of producing Hydro-Carbon layers during ventilation. Sputtering of these tiles lead to deposition of Hydro-Carbons inside the thruster channel. Due to a lower evaporation energy, the usage of Aluminium walls reduces deposition in the regions of plasma wall interaction at the hot cusps, although the sputter yield of Aluminium is larger. These improvements were successfully implemented in the experiment and showed a reduction of artefacts during long time measurements. This leads to a stable performance, as it is expected in space.

This work presented here, show that simulations in combination with experimental measurements are a useful tool to get a better physical understanding and hopefully support an improved design. A close collaboration between both disciplines is necessary to obtain good results with relevance for basic physics understanding and engineering applications. Unfortunately, the simulation results indicate that the HEMP thruster is not only charac-

terised by classical transport and the additional turbulent transport needs to be quantified with parametric studies. This will allow a successful combination of experiment and simulation in the design process of new thruster models to minimise the number of expensive prototypes.

2 Thesis articles

Author Contributions

Article [I]: Lüskow, K. F., Neumann, P. R. C., Bandelow, G., Duras, J., Kahnfeld, D., Kemnitz, S., Matthias, P., Matyash, K., and Schneider, R. (2018). Particle-in-cell simulation of the cathodic arc thruster. Physics of Plasmas, 25(1):013508
All authors carved out the problem, outlined the calculation, and determined the scope of the article. K. Lüskow and R. Schneider performed the analytic calculation. K. Lüskow performed the numerical calculation, based on numerical developments by S. Kemnitz, G. Bandelow, J. Duras and D. Kahnfeld. The manuscript was written by K. Lüskow, R. Schneider and D. Konigorski and was edited by all authors.

Article [II]: Duras, J., Matyash, K., Tskhakaya, D., Kalentev, O., and Schneider, R. (2014). Self-force in 1d electrostatic particle-in-cell codes for nonequidistant grids. Contributions to Plasma Physics, 54(8):697–711
All authors carved out the problem, outlined the calculation, and determined the scope of the article. K. Matyash and D. Tskhakaya performed the analytic calculation. J. Duras performed the numerical calculation, based on numerical developments by K. Mayash and O. Kalentev. The manuscript was written and was edited by all authors.

Article [III]: Kalentev, O., Matyash, K., Duras, J., Lüskow, K. F., Schneider, R. E., Koch, N., and Schirra, M. (2014). Electrostatic ion thrusters - towards predictive modeling. Contributions to Plasma Physics, 54(2):235–248
All authors carved out the problem, outlined the calculation, and determined the scope of the article. O. Kalentev, K. Matyash, J. Duras and K Lüskow performed the numerical calculation. The manuscript was written by O. Kalentev, K. Matyash, J. Duras and R. Schneider and was edited by all authors.

Article [IV]: Duras, J., Kahnfeld, D., Bandelow, G., Kemnitz, S., Lüskow, K., Matthias, P., Koch, N., and Schneider, R. (2017). Ion angular distribution simulation of the highly efficient multistage plasma thruster. Journal of Plasma Physics, 83
All authors carved out the problem, outlined the calculation, and determined the scope of the article. D. Kahnfeld performed the analytic calculation. J. Duras performed the numerical calculation, based on numerical developments by D. Kahnfeld, G. Bandelow, S. Kemnitz, K. Lüskow and P. Matthias. The manuscript was written by J. Duras, D. Kahnfeld, N. Koch and R. Schneider and was edited by all authors.

Article [V]: Duras, J., Schneider, R., Kalentev, O., Kemnitz, S., Matyash, K., Koch, N., Lüskow, K., Kahnfeld, D., and Bandelow, G. (2016). Influence of electron source on the near field plume in a multistage plasma thruster. Plasma Physics and Technology, 3(3):126–130
All authors carved out the problem, outlined the calculation, and determined the scope of the article. J. Duras performed the numerical calculation, based on numerical developments by O. Kalentev, S. Kemnitz, K. Matyash, K. Lüskow, D. Kahnfeld and G. Bandelow. The manuscript was written by J. Duras, R. Schneider and N. Koch and was edited by all authors.

Article [VI]: Duras, J., Kalentev, O., Schneider, R., Matyash, K., Lüskow, K., and Geiser, J. (2015). Monte-carlo re-deposition model during terrestrial measurements of ion thrusters. Acta Polytechnica, 55(1):7–13
All authors carved out the problem, outlined the calculation, and determined the scope of the article. J. Duras performed the analytic and numerical calculations, based on the numerical development by O. Kalentev, K. Matyash, K. Lüskow and J. Geiser. The manuscript was written by J. Duras and R. Schneider and was edited by all authors.

Article [VII]: Brandt, T., Schneider, R., Duras, J., Kahnfeld, D., Hay, F. G., Kersten, H., Jensen, J., and Braxmaier, C. (2016). Particle-in-cell simulation of a down-scaled hemp thruster. Transaction of the Japan Society for Aeronautical and Space Sciences, Aerospace Technology Japan, 14(ists30):Pb_235–Pb_242
All authors carved out the problem, outlined the calculation, and determined the scope of the article. T. Brandt performed the analytic calculation. T. Brand, D. Kahnfeld and J. Duras performed the numerical calculation. The manuscript was written by T. Brand and R. Schneider and was edited by all authors.

Confirmed:

_____ Greifswald, April 05, 2018

(Prof. Dr. Ralf Schneider)

_____ Greifswald, April 05, 2018

(Julia Duras)

PHYSICS OF PLASMAS **25**, 013508 (2018)

Particle-in-cell simulation of the cathodic arc thruster

Karl Felix Lüskow,[1,a)] Patrick R. C. Neumann,[2,b)] Gunnar Bandelow,[1] Julia Duras,[3] Daniel Kahnfeld,[1] Stefan Kemnitz,[4] Paul Matthias,[1] Konstantin Matyash,[1] and Ralf Schneider[1]

[1]*Institute of Physics, Ernst-Moritz-Arndt University of Greifswald, 17489 Greifswald, Germany*
[2]*Neumann Space Pty Ltd., 41 Wood Avenue, Brompton 5007, South Australia, Australia*
[3]*Department of Applied Mathematics, Physics and Humanities, Nuremberger Institute of Technology, 90489 Nuremberg, Germany*
[4]*Institute of Computer Science, University of Rostock, 18059 Rostock, Germany*

(Received 7 November 2017; accepted 26 December 2017; published online 12 January 2018)

The cathodic arc thruster is a newly developed electric propulsion system. It provides a stream of ions with very high velocities from a solid conducting cathode. This high ion velocity in combination with a high ionization fraction makes the cathodic arc thruster attractive for spacecraft propulsion. In the past, a record-high specific impulse was measured for such thrusters. The thruster uses a voltage of −220 V at the cathode for several microseconds, producing plasma from the cathode material which then streams out of the thruster producing thrust. In this work, a two-dimensional axial-symmetric particle-in-cell code with Monte-Carlo collisions is used to simulate the plasma of a cathodic arc thruster with a simplified wall model for the initial triggering of the arc. The work concentrates on the plasma transport and aims not at a self-consistent description of the arc, including plasma-wall interaction, e.g., description of the erosion and surface heating. The interaction of the arc beam with the background plasma results in a plasma-beam instability. Due to this instability charge separation can be detected that leads to large electric fields. By this electric field, plasma particles are accelerated and contribute to the thrust. *Published by AIP Publishing.*
https://doi.org/10.1063/1.5012584

I. INTRODUCTION

Cathodic arc thrusters are a new development that could permit the delivery of far higher mass fractions to destination orbits due to their high specific impulse.[1] The eroded material from a conducting cathode is ejected by a striking electrical arc between the anode and cathode.[2] Due to its high current discharge, this material is ionized and plasma is accelerated away from the cathode surface.[3] Previous studies measured extremely high ion velocities for such pulsed cathodic arc thrusters. Measurements of erosion rates have confirmed that these thrusters can operate highly efficient.[1,2,4,5]

In order to get deeper insight into the underlying physics, simulations are perfectly suited.[6] Results of simulations can support the experimental development by providing a basic understanding of the system. Due to the non-Maxwellian character of cathodic arc thrusters, a fully kinetic plasma description is needed. Plasma particles have no chance to maxwellize, due to strong magnetic fields, very fast electrons from the initial arc and, in consequence, mean free paths longer than the device dimension. Particle-In-Cell with Monte-Carlo collisions (PIC-MCC) is a widely used kinetic method to simulate a plasma and is used in this work to study the time-dependent behavior of a cathodic arc thruster.

II. BASICS

Pulsed cathodic arcs are high current, low voltage discharges at low pressure that ablate and ionize the cathode material and then accelerate that material away from the cathode surface in small regions known as cathode spots.[7] This results in a highly ionized quasi-neutral plasma being ejected from the cathode and directed downstream at high velocity.[4] Devices of this type are used for ion implantation and surface modification in industry, in applications ranging from the creation of hard films on the surface of tools to altering the bioactivity of polymer surfaces.[5,8] An application which has been of interest in recent years is that of spacecraft propulsion, where the high ion velocity implies that a flight-rated pulsed arc thruster could operate at specific impulses far greater than current technologies.[1,9,10] The design of experimental systems should be informed by high fidelity simulations that run at conditions experienced in laboratory experiments, so that simulation results can be verified using experimental results.[6] This work presents simulations of the cathodic arc plasma undertaken using PIC-MCC to guide the development of a pulsed arc thruster system.

III. SIMULATION METHOD

The well-established electrostatic Particle-In-Cell method is combined with Monte Carlo collisions (PIC-MCC). PIC-MCC provides time-dependent information about all microscopic and macroscopic parameters of a plasma. In particular, physical entities like potential, densities of all species, temperatures, and velocity distribution functions can be calculated. For further information about the PIC-MCC method itself, several reviews can be found.[11,12]

The idea behind PIC is to follow the so-called superparticles where one super-particle represents a certain

[a)]lueskow@physik.uni-greifswald.de
[b)]patrick@neumannspace.com

number of physical particles. Due to the same mass-to-charge ratio as a single particle, the super-particle follows the same trajectory as the single particle. The electrostatic electric field is calculated self-consistently by using a Poisson solver on an equidistant rectangular grid. The electrostatic approximation can be used here, because the magnetic fields generated from the electric plasma currents can be neglected compared with the self-consistent electric fields or background magnetic fields (e.g., from coils) acting in the Lorentz force. Collisions between particles are simulated using Monte Carlo collision algorithms. This is valid as long as the collision term in the kinetic equation can be linearized in time, which is valid for the small time steps used in PIC. This allows implementing all relevant types of collisions like electron-neutral elastic, ionization, excitation, Coulomb collisions, neutral-neutral, and charge exchange collisions. Neutrals are treated the same way as plasma particles, but due to their zero charge they experience no electric forces. This is equivalent for the neutral transport to a DSMC (Direct Simulation Monte Carlo) description.

The two-dimensional cylinder symmetric domain used in this study consists of 150 cells in radial and 400 cells in axial direction. To resolve the collision dynamics correctly, all three dimensions in velocity space are resolved. Using a cell size of $dr = 1\,\text{mm}$ leads to a domain size of $15\,\text{cm} \times 40\,\text{cm}$. This guarantees to resolve the shortest length-scale of the system, namely, the Debye scale. A time step of $dt = 10^{-12}\,\text{s}$ is chosen in order to resolve the fastest time-scale of the system, namely the plasma frequency. Due to slower velocities of ions and neutrals compared to electrons, a sub-cycling can be used for both species. This means that neutrals and ions are pushed only every two hundredth time step. A similar ansatz can be followed for collisions. According to the collision, frequency collisions are performed only every tenth time step.

The magnetic field created by the magnetic coils is calculated using the finite element solver FEMM.[13] A plot of the magnetic field lines including the position of magnetic coils, anode, cathode, cathodic mount, and a trigger pin is shown in Fig. 1. To improve the numerical performance, the size of the system is scaled down by a self-similarity factor of 100 applying a scaling which preserves the ratios of length to gyroradii and mean free path. Consequently, all densities and the magnetic field are multiplied by this factor. By using this scaling, one ensures the correct physical behaviour of the scaled system compared to the real one.[14] The similarity scaling is motivated by the one of Taccogna *et al.*[15]

The potential at all outer boundaries of the domain is set to zero voltage and all particles get absorbed. Also, the anode is grounded, whereas at the cathode a pulsed potential

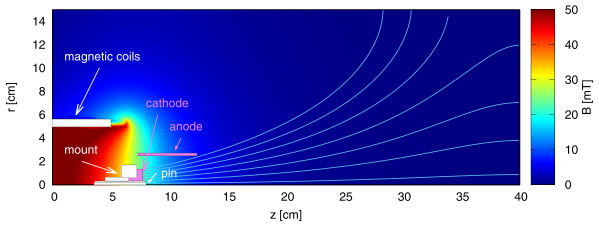

FIG. 1. Magnetic field and simulation domain.

boundary condition is applied. For the pulse lengths of $1.7\,\mu\text{s}$ $-220\,\text{V}$ is set at the cathode and electrons are injected into the system at the trigger pin. The voltage of $-220\,\text{V}$ is chosen according to the experiment of Neumann Space, but the simulation allows every other voltage as a boundary condition. When the pulse has ended there is a cool-down phase of $0.5\,\mu\text{s}$. During this phase, the cathode is at ground potential and the electron injection is turned off. Afterwards, $-220\,\text{V}$ is applied again and the injection source is turned on again. During the injection phase, fast electrons of about 20 eV are injected at the pin. This mimics the initial arc phase, which is not included self-consistently in the simulation. Electrons move then towards the cathode. If an electron hits the cathode, there is a probability of 1% to sputter a neutral from the cathodic surface according to the approach of Timko *et al.*[16]

As discussed in experimental reviews about arcs,[17,18] one of the most uncertain physics aspects is the triggering mechanism. Several different mechanisms had been proposed for this like thermionic electron emission, photoinduced ionization, sputtering, evaporation, and oxide removal.[19–22] It is still not clear which processes are active for certain conditions. Therefore, and to hold this part of the simulation as simple as possible, the approach of Timko *et al.* is used as the initial trigger for the simulations of arc discharges[16] in this paper. Timko *et al.*[16] were able to reproduce the observed currents. All plasma transport processes resulting from this initial trigger are simulated self-consistently in the code. Further effects in the cathode spot are neglected, e.g., ion emission.[17] Ion emission would contribute mostly to the surface heating which is not included in the model. Ions emitted from the surface will not contribute to the plasma because they experience the sheath in front of the wall and will be redeposited on the cathode delivering additional cathode heating. This paper describes the dynamics of the plasma in the thruster channel. Therefore, the approach for the physics at the cathode is chosen rather simplistic. If one wants to model the dynamics of the arc itself including effects like dynamical cathode spots, other timescales than here would be of interest and a molecular dynamic description is needed like in Ref. 23. In Ref. 17, the equilibration time for a cathodic arc is given as typically larger than $1\,\mu\text{s}$. In the system analyzed here, the typical pulse length is a few milliseconds and the arc is not fully developed in terms of densities and currents. This dynamic behavior requires a kinetic description of the system, because equilibration is not reached. The electron density stays below $10^{12}\,\text{cm}^{-3}$. Therefore, electrostatic Particle-in-Cell calculations are appropriate and possible for this system.

These neutrals can be ionized by other fast electrons and ions are created. Every impinging ion that reach the cathode can emit a new neutral. Neutrals that are sputtered from the surface are injected into the system with Maxwell distributed velocities, assuming room temperature.

Electrons are magnetized and stream along the magnetic field lines towards the exit of the thruster. Ions follow electrons due to quasi-neutrality in the plasma and contribute to the thrust. At the end of the pulse after $1.7\,\mu\text{s}$, all plasma particles left the thruster producing maximum thrust. Only neutrals remain in the thruster as an inventory for higher ionization during the next pulse. After about 4–5 pulses, a

quasi-steady state is reached, because the dynamic relaxation process of the neutrals has saturated and the whole thruster is filled up with neutrals.

IV. RESULTS

The large benefit of a PIC simulation is that it allows diagnosing all macroscopic and microscopic quantities time-dependently. Figure 2 shows the behavior of electron and ion densities. The number of super-particles in the system is shown at the top of this figure, left side for electrons and right side for ions. One can see that the number of electrons fluctuates strongly after a short ramp-up phase, whereas the ion number increases continuously and remains afterwards relatively constant until the end of the pulse. Electrons have a very small mass compared to ions; therefore, their dynamic response to changes is much faster. Heavy ions are slow and experience only the time-averaged electric field, like already discussed in detail for radio-frequency plasmas.[24]

The strong fluctuations in the number of electrons are also visible in the different snapshots of the electron density during a pulse, which are shown on the left side of Fig. 2. First, electrons starting from the pin fill up the thruster and by following the magnetic field lines they form a small plume after the exit of the thruster. Ions are created near the cathode and a small plasma builds up (a) during the first 0.3 μs. Therefore, the number of electrons and ions increases monotonically. The plasma density inside the thruster increases especially near the cathode where ions are injected. At time (b), which is after 0.3 μs first fluctuations in the electron density show up and a blob of electrons is separated from the bulk plasma at the thruster exit around $z = 15$ cm. Afterwards, fluctuations in the electron density begin to increase. Similar to a plasma gun, regions with higher electron density form, separate and are sent out of the thruster (c). After each release of electrons, the plasma reaches a minimum in electron density, whereas the ion density increases further (d). Ions are slower and do not react as fast as electrons. Therefore, electrons are stronger influenced by fluctuations. Electron density builds up again until a critical density is reached. When this limit is reached, new blobs of electrons form and leave the thruster. The electron blobs now get so large that even ions are carried with them due to quasi-neutrality and one can detect small ion blobs (e), too. At this point, the fluctuations have grown so strong that several blobs leave close to the axis with a high frequency, visible at axial positions 20 and 28 cm. After 1.7 μs, the end of the pulse is reached and the anode potential is set to zero Volts. In the plots of super-particle numbers at the top of Fig. 2, this is visible in a strong decrease of the particle numbers of both plasma species. The plasma collapses and only neutrals remain in the thruster channel. For the start of the next pulse, the remaining neutrals act as an inventory for ionization. Therefore, the plasma builds up faster, fluctuations are getting even stronger and the thrust is higher than in the first pulse. After about 4–5 pulses, one reaches a quasi-steady state, because the whole thruster is pre-filled with neutrals.

The fluctuations increase in size and frequency, characteristic of a plasma instability. This instability is responsible for the dynamics of the thruster described before. To identify the underlying effect responsible for these fluctuations, a phase space analysis for electrons is shown in Fig. 3. The plots show the phase space of velocity in axial direction v_z as a function of axial position z.

The six plots are snapshots of the phase space taken at the same time as the density snapshots discussed before. In the first plot (a), the thruster fills up with electrons. Beyond the exit of the thruster, which is located at $z = 15$ cm, fast electrons leave the thruster with velocities larger than 10^7 m/s. At time step (b), first fluctuations occur in the density. In the phase space plot first eddies appear, characteristic of a plasma-beam instability. There are fast beam electrons with about 1.4×10^7 m/s and background electrons from the plasma in the thruster channel. Considering the densities of beam and plasma electrons, following Birdsall[11] one can estimate the ratio $R = n_b/n_p \propto \omega_{pb}/\omega_{pp} \approx 0.01$. This is typical of a plasma-beam instability with a weak beam and a cold plasma.[11,25,26] Taking into account $R = 0.01$ and following the calculations of Birdsall,[11] the instability frequency can be estimated as $\omega = 0.93\omega_p = 0.93\sqrt{\frac{n_e e^2}{\epsilon_0 m_e}}$. Using an average electron density near the cathode of $n_e \approx 10^{15}\,\mathrm{m}^{-3}$, an instability frequency of $1.8 \times 10^9\,\mathrm{s}^{-1}$ is obtained. This analytical result is similar to the frequency of the emitted electron blobs that one can see at time step (c), namely $10^9\,\mathrm{s}^{-1}$. Three regions of trapped electrons with low energies are visible. Also, three blobs of very fast electrons appear that will leave the thruster during the next time steps. In the fourth plot (d), the instability has reached its maximum, producing also a maximum in the velocity of electrons leaving the thruster. The inventory of electrons in the thruster has to build up again, which is reached in the next time step (e). The phase space plot shows slow trapped electrons in the thruster and also some very fast blobs of electrons that leave the thruster. At timestep (f), the potential is shut down and the bulk plasma leaves the thruster, too.

After identifying the beam-plasma instability, one can explain now the electron blobs dynamics that contribute to the thrust. It is well known that the plasma-beam instability is linked with a time-varying potential, which is shown in Fig. 4. The time steps for the potential plots are the same as for density and phase space.

In the first plot (a), the potential builds up, in plot (b) first potential gradients establish beyond the exit of the thruster, which creates electric fields in the plume. These potential gradients get larger in (c), where for the first time positive potential values are detected. The steep potential gradients that are built up now enlarge the electric fields up to about 10 kV/m. Following the simple model of Birdsall,[11] the electric field E is calculated as

$$\frac{1}{4}\epsilon_0 E^2 = 4 m_b n_b v_0 \Delta v \;\Rightarrow\; E \approx 4 \times 10^4\,\mathrm{kV/m}. \qquad (1)$$

This calculated electric field has the same order of magnitude as the electric field obtained in the simulation. In (d),

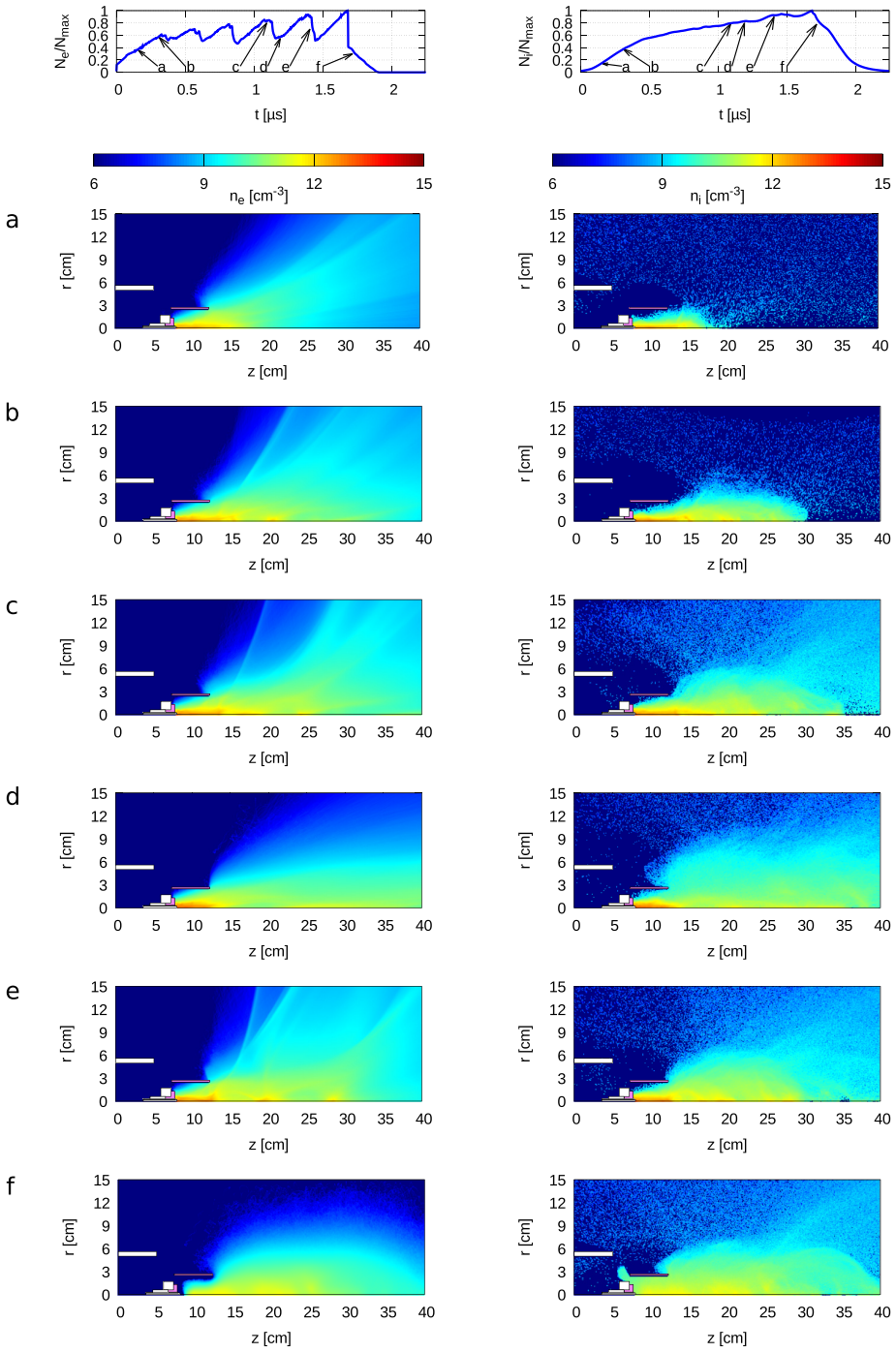

FIG. 2. Electron (left) and ion (right) densities for different time steps during a typical pulse.

the plasma loads again and the potential is again relatively constant with only small gradients. At time step (e), one large potential gradient builds up, the charge separation gets larger resulting in strong electric fields of more than 10 kV/m. The dynamics in the plume region is covered by the Poisson equation. Plasma dynamics determines the charge separation and by this the creation of electric fields. Charge separation is possible due to the higher mobility of electrons compared to ions. On longer timescales, quasi-neutrality of plasma will be reached, but for short timescales very high electric fields occur. These very high electric fields accelerate electrons to high velocities, which contribute to the thrust. In (f), the potential at the cathode is turned off, so that only a positive plasma potential remains. Very fast, all plasma particles leave the thruster and the potential approaches zero before starting with the next pulse. The resulting thrust of a complete run with four pulses is shown in Fig. 5.

The simulated thrust is diagnosed by collecting all particles leaving the thruster and their directed momentum in axial direction. This models the measurement from a pendulum thrust stand. The thrust is diagnosed at the end of the anode, where the thruster exit is located. It shows a pulsed and fluctuating characteristic as shown in Fig. 5 due to the mechanisms discussed before. The thrust in the simulation

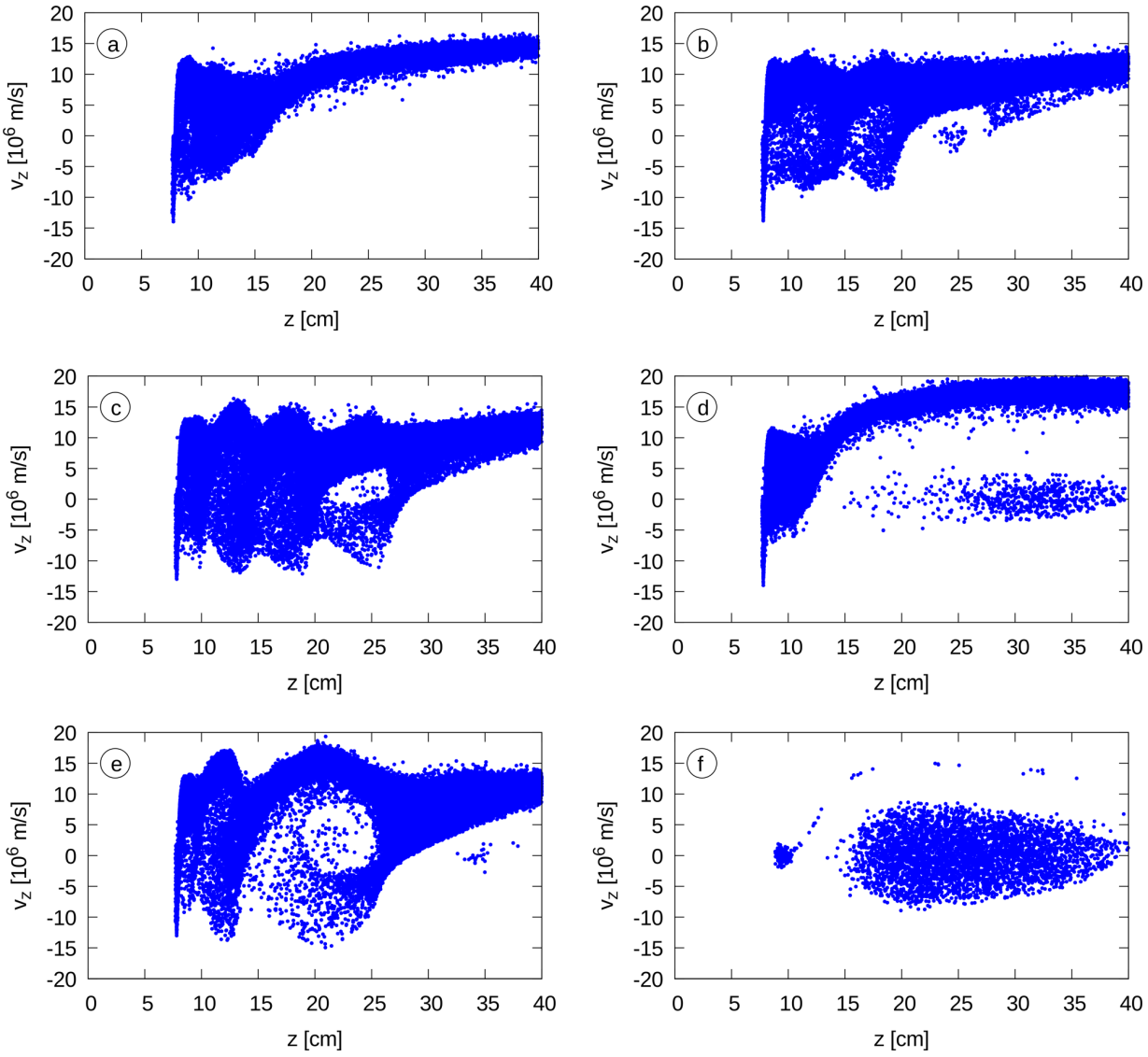

FIG. 3. Phase space of axial velocity as a function of axial position for electrons at different time steps for one pulse.

and in the experiment is of the order of 2 N. Experimentally such thrust values were reached for the same scenarios with currents of about 1 kA. This results in 0.2 mN/A.

V. DISCUSSION

The plasma dynamics in the simulation is similar to the experimentally observed one of cathodic arcs.[2,27,28] In the experiments, a narrow plasma beam appears as in the simulations. A narrow beam results in a high thrust efficiency due to a better directed stream. In addition, the interaction with other spacecraft components is minimized by a narrow beam. Comparing electron and ion density in the simulation, one can see a higher electron density in the plume. This gives a net electron current as measured in the experiment, not only due to the higher density, but due to the higher electron mobility.[29] This electron current is necessary to sustain the arc discharge experimentally, as it creates the conductive path for the capacitors driving the arc to discharge through the plasma, depositing energy into the plasma while generating more ionized species.[7] A net electron current is a helpful feature since it mitigates spacecraft charging issues due to charge expulsion.[30] Since ion and Hall effect thrusters are designed to extract and accelerate ions from a discharge plasma, they must also neutralize the exhaust stream; otherwise, the spacecraft would become more negatively charged until the ions return to the spacecraft, thus imparting no momentum. Since there is a net electron current, the spacecraft will gain a positive charge, which environmental electrons should be able to neutralize easily.[31] Thus, there is no need for charge neutralization systems, which will reduce system complexity, mass and failure modes in operational systems.

The calculated thrust in the simulation is in the region of a few Newton, due to the amount of current being modeled. As in the experiment the thrust is pulsed, with the thrust being dominated by ion production. The simulations described here simulate the action of individual cathode spots, while

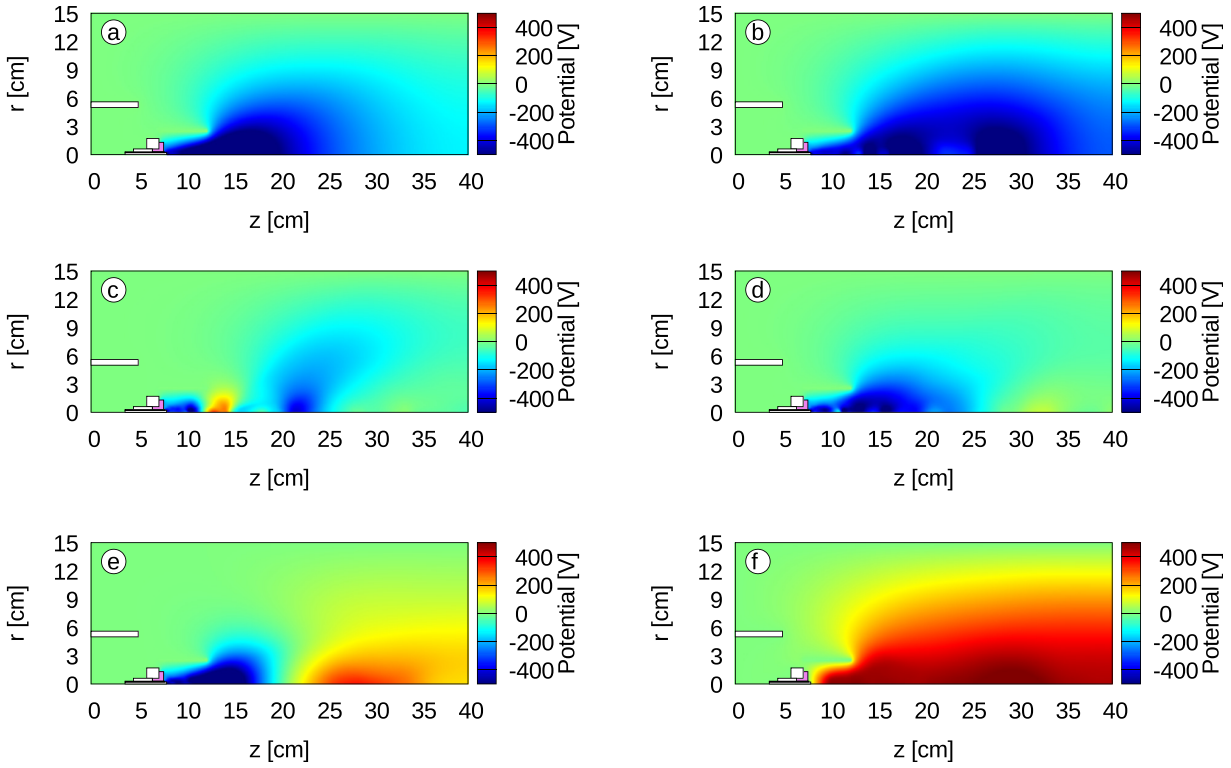

FIG. 4. Plasma potential for different time steps during a typical pulse.

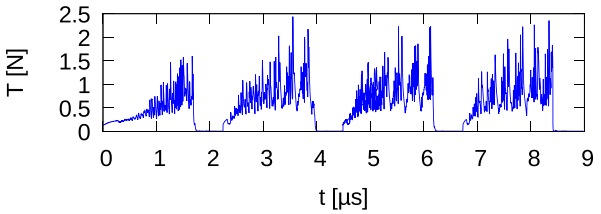

FIG. 5. Simulated thrust created by all species.

experiments with high current pulsed arcs tend to produce several tens of cathode spots; empirically, some 60…80 A of cathode current is carried by each cathode spot, and cathode current can peak at several kiloamps.[7] The actions of the various cathode spots reinforce each other, and so experimental generation of average thrusts on the order of Newtons is common.[1,2]

VI. CONCLUSIONS AND OUTLOOK

PIC simulations are widely accepted for plasma simulations; in particular, they are well-suited for simulations of electric thrusters. In this study, the PIC method was used to simulate the plasma dynamics of a pulsed cathodic arc thruster with a simplified wall model. This pulsed cathodic arc thruster was developed by Neumann Space. The simulation is able to reproduce basic features of the plasma observed in the cathodic arc thruster. Experimental diagnostics show similar results to the simulation, especially the strongly fluctuating currents and thrust. Analyzing in the simulation the phase space of the electrons, these fluctuations can be explained by a plasma-beam-instability. The strong fluctuations are beneficial for the operational characteristics of the arc thruster by increasing the thrust. In the future, PIC simulations can be used to study modified magnetic field configurations and their impact on the predicted performance of the arc thruster. To improve the code technically, the rather simplistic model of the surface model can be extended using a strategy as derived by Timko *et al.*[23]

The use of simulations to guide the experimental investigations is invaluable, as it permits a more rapid iteration and testing of prototypes while demonstrating which designs may not be worth exploring. The union of insights from simulation and data from experiment results in better science and engineering than either can do alone.

[1]P. R. C. Neumann, M. Bilek, and D. R. McKenzie, "A centre-triggered magnesium fuelled cathodic arc thruster uses sublimation to deliver a record high specific impulse," Appl. Phys. Lett. **109**, 094101 (2016).
[2]P. R. C. Neumann, M. M. M. Bilek, R. N. Tarrant, and D. R. McKenzie, "A pulsed cathodic arc spacecraft propulsion system," Plasma Sources Sci. Technol. **18**, 045005 (2009).
[3]J. Daalder, "Cathode spots and vacuum arcs," Phys. B: Condens. Matter **104**, 91–106 (1981).
[4]G. Y. Yushkov, A. Anders, E. M. Oks, and I. G. Brown, "Ion velocities in vacuum arc plasmas," J. Appl. Phys. **88**, 5618–5622 (2000).
[5]M. Bilek, D. McKenzie, and R. Powles, "Treatment of polymeric biomaterials by ion implantation," in *Biomaterials and Surface Modification* (Research Signpost, Kerala, 2007).
[6]O. Kalentev, K. Matyash, J. Duras, K. F. Lüskow, R. Schneider, N. Koch, and M. Schirra, "Electrostatic ion thrusters - towards predictive modeling," Contrib. Plasma Phys. **54**, 235–248 (2014).
[7]E. Hantzsche, "Mysteries of the arc cathode spot: A retrospective glance," IEEE Trans. Plasma Sci. **31**, 799–808 (2003).
[8]R. Fu, S. Kwok, P. Chen, P. Yang, R. Ngai, X. Tian, and P. Chu, "Surface modification of cemented carbide using plasma nitriding and metal ion

implantation," Surf. Coat. Technol. **196**, 150–154 (2005); in 13th International Conference on Surface Modification of Materials by Ion Beams (2005).
[9]P. R. C. Neumann, M. M. M. Bilek, and D. R. Mackenzie, "Optimising ion production in pulsed refractory and non-refractory cathodic arcs," in *Proceedings of the 12th Asia Pacific Physics Conference (APPC12)* (JPS Conference Proceedings, 2014), Vol. 1, p. 015059.
[10]J. E. Polk, M. J. Sekerak, J. K. Ziemer, J. Schein, N. Qi, and A. Anders, "A theoretical analysis of vacuum arc thruster and vacuum arc ion thruster performance," IEEE Trans. Plasma Sci. **36**, 2167–2179 (2008).
[11]L. Birdsall, *Plasma Physics via Computer Simulation* (CRC Press, 2004).
[12]D. Tskhakaya, K. Matyash, R. Schneider, and F. Taccogna, "The particle-in-cell method," Contrib. Plasma Phys. **47**, 563–594 (2007).
[13]D. Meeker, "Finite element method magnetics," FEMM **4**, 32 (2010).
[14]K. F. Lüskow, S. Kemnitz, G. Bandelow, J. Duras, D. Kahnfeld, P. Matthias, R. Schneider, and D. Konigorski, "Electrostatic particle-in-cell simulation of heat flux mitigation using magnetic fields," J. Plasma Phys. **82**, 595820502 (2016).
[15]F. Taccogna, S. Longo, M. Capitelli, and R. Schneider, "Self-similarity in hall plasma discharges: Applications to particle models," Phys. Plasmas **12**, 053502 (2005).
[16]H. Timko, F. Djurabekova, K. Nordlund, L. Costelle, K. Matyash, R. Schneider, A. Toerklep, G. Arnau-Izquierdo, A. Descoeudres, S. Calatroni, M. Taborelli, and W. Wuensch, "Mechanism of surface modification in the plasma-surface interaction in electrical arcs," Phys. Rev. B **81**, 184109 (2010).
[17]B. Jüttner, "Cathode spots of electric arcs," J. Phys. D: Appl. Phys. **34**, R103 (2001).
[18]B. E. Djakov and R. Holmes, "Cathode spot structure and dynamics in low-current vacuum arcs," J. Phys. D: Appl. Phys. **7**, 569 (1974).
[19]G. Mesyats, *Cathode Phenomena in a Vacuum Discharge: The Breakdown, the Spark, and the Arc* (Nauka, Moscow, 2000).
[20]R. Behrisch and K. Wittmaack, *Sputtering by Particle Bombardment* (Springer, Berlin, 1981), Vol. 1.
[21]J. Rager, A. Flaig, G. Schneider, T. Kaiser, F. Soldera, and F. Mücklich, "Oxidation damage of spark plug electrodes," Adv. Eng. Mater. **7**, 633–640 (2005).
[22]A. Anders, S. Anders, M. A. Gundersen, and A. M. Martsinovskii, "Self-sustained self-sputtering: A possible mechanism for the superdense glow phase of a pseudospark," IEEE Trans. Plasma Sci. **23**, 275–282 (1995).
[23]H. Timko, K. Ness Sjobak, L. Mether, S. Calatroni, F. Djurabekova, K. Matyash, K. Nordlund, R. Schneider, and W. Wuensch, "From field emission to vacuum arc ignition: A new tool for simulating copper vacuum arcs," Contrib. Plasma Phys. **55**, 299–314 (2015).
[24]J. Meichsner, M. Schmidt, R. Schneider, and H.-E. Wagner, *Nonthermal Plasma Chemistry and Physics* (CRC Press, 2012).
[25]A. B. Mikhailovskii, *Theory of Plasma Instabilities: Instabilities of a Homogeneous Plasma* (Consultants Bureau, 1974), Vol. 1.
[26]A. Akhiezer and Y. B. Fainberg, "On the interaction of a charged particle beam with electron plasma," Doklady Acad. Nauk SSSR **69**, 555–556 (1949).
[27]R. Sanginés, M. M. M. Bilek, and D. R. McKenzie, "Optimizing filter efficiency in pulsed cathodic vacuum arcs operating at high currents," Plasma Sources Sci. Technol. **18**, 045007 (2009).
[28]L. Ryves, D. R. McKenzie, and M. M. M. Bilek, "Cathode-spot dynamics in a high-current pulsed arc: A noise study," IEEE Trans. Plasma Sci. **37**, 365–368 (2009).
[29]J. Schein, N. Qi, R. Binder, M. Krishnan, J. K. Ziemer, J. E. Polk, and A. Anders, "Inductive energy storage driven vacuum arc thruster," Rev. Sci. Instrum. **73**, 925–927 (2002).
[30]D. M. Goebel and I. Katz, *Fundamentals of Electric Propulsion: Ion and Hall Thrusters* (John Wiley & Sons, 2008), Vol. 1.
[31]M. Tajmar, "Electric propulsion plasma simulations and influence on spacecraft charging," J. Spacecr. Rockets **39**, 886–893 (2002).

Contributions to Plasma Physics, 19/11/2013

Self-force in 1D electrostatic Particle-in-Cell codes for non-equidistant grids

J.Duras[1,*], **K.Matyash**[2,**], **D.Tskhakaya**[3,4,***], **O.Kalentev**[1,†], and **R.Schneider**[1,‡]

[1] Institute of Physics, Ernst-Moritz-Arndt University of Greifswald, Felix-Hausdorff-Str. 6, D-17487 Greifswald, Germany
[2] Computing Centre, Ernst-Moritz-Arndt University of Greifswald, Felix-Hausdorff-Str. 12, D-17489 Greifswald, Germany
[3] Association Euratom-ÖAW, Institute of Applied Physics, TU Wien, A-1040 Vienna, Austria
[4] Permanent address: Andronikashvili Institute of Physics, 0177 Tbilisi, Georgia

Abstract: Effects of non-equidistant grids on momentum conservation is studied for simple test cases of an electrostatic 1D PIC code. The aim is to reduce the errors in energy and momentum conservation. Assuming an exact Poisson solver is assumed and only numerical errors for the particle mover are analysed. For the standard electric field calculation using a central-difference scheme, generation of artificial electric fields at the particle position are generated in the case when the particle is situated next to a change of cell size change. This is sufficient to destroy momentum conservation. To reduce this error A modified electric field calculation scheme is derived to reduce this error. Independent of the calculation scheme additional fake forces in a two-particle system are found which results in an error in the total kinetic energy of the system. This contribution is shown to be negligible for many particle systems. To test the accuracy of the two electric field calculation schemes numerical tests are done to compare with an equidistant grid set-up. All tests show an improved behaviour of momentum conservation and total kinetic energy for the modified calculation scheme of the electric field.

1 Introduction

Particle-in-Cell (PIC) codes are standard tools for plasma simulations [1]. They follow the kinetics of charged particles in a system and to calculate the fields self-consistently on a spatial grid in order to reduce the computational costs. The accuracy of this method is determined, among others, by the grid cell size. The grid has to resolve locally the smallest length scale. Usually, this is the electron Debye length. In addition, special geometries of physical boundaries can require a finer grid in order to resolve boundaries accurately. These restrictions of the cell size strongly limits the computationally possible size of the simulation domain.

To simulate larger domains orto resolve special geometries different mesh generation strategies, like Boundary-Fitted Coordinates (BFC) [2] or Adaptive Mesh Refinement (AMR) [3], have been used. However, these methods are not without problems. Non-uniform grids often lead to non-trivial interpolation functions [4] and a strong change in cell size can cause non-physical effects, for example self-forces. Therefore, many of these applied methods are not momentum conserving.

A first approach for an electrostatic PIC code with a non-uniform grid, avoiding self-forces was given by Fichtl [5]. Colella et al. had made some effort to estimate the error caused by a non-equidistant grid [6].

In this paper momentum and kinetic energy conservation for a 1D electrostatic PIC code using non-equidistant grids is analysed. Such conservation is equivalent to the non-existence of self-forces and correct inter-particle interactions. The outline of the paper is as follows: After a short description of the general PIC cycle, constraints

* Corresponding author E-mail: duarsj@uni-greifswald.de.
** E-mail: knm@ipp.mpg.de.
*** E-mail: david.tskhakaya@uibk.ac.at.
† E-mail: okalenty@ipp.mpg.de.
‡ E-mail: schneider@uni-greifswald.de.

for momentum conservation, weighting function and Green's function are derived for non-uniform grids. In the the following is shown that even for an exact Poisson solver the calculation scheme for the electric field can introduce errors destroying momentum conservation. For simplicity a system of a single particle in a 1D electrostatic PIC code is destroying. It will be shown, that for a non-equidistant grid, the two-point central difference scheme used for the electric field calculation generates self-forces. to minimize this non-physical force, a modified electric field calculation is presented. For the modified field calculation, as well as for the conservative one, the error in the total kinetic energy is derived. Since PIC is not conserving energy, this derivation is done to prove that no additional forces are appearing. Within single-particle and two-particle set-ups total kinetic energy and momentum conservation are tested numerically and compared with an equidistant grid case.

2 General scheme of electrostatic PIC

The Particle-in-Cell method calculates the time evolution of a plasma in so-called PIC cycles, where potential and electric field are calculated at grid points. based on the electric field calculated from the charges of the pseudo particles, representing a bunch of physical particles. These are pushed using the electric field calculated before. The simplest grid is an equidistant grid, where each cell has the same quadratic size $\Delta\mathbf{x} = (\Delta x, \Delta x, \Delta x)^T$. A non-equidistant grid has cells with different size $\Delta\mathbf{x}_i \neq \Delta\mathbf{x}_j$, where $\Delta\mathbf{x}_i = (\Delta x_i, \Delta y_i, \Delta z_i)^T$, but not necessarily for each cell.

To solve the Poisson equation the charge density is needed at the grid points. For a system with $i = 0, ..., N_g$ grid points, the charge density is calculated as

$$\rho_i = \frac{q_i}{\nu_i} \,, \tag{1}$$

where ν_i is the corresponding cell volume and q_i the collective charge assigned to the grid point. For this "grid point charge", a weighting function W interpolates the particle charge Q_p from the particle position $\mathbf{X}_p$ to the grid point position $\mathbf{x}_i$

$$q_i = \sum_{p=1}^{N_p} Q_p \cdot W(\mathbf{X}_p, \mathbf{x}_i) \,. \tag{2}$$

N_p is the number of charged particles in the system. With the resulting charge density ρ_i on the grid, the electric field given by the field equation

$$\nabla \cdot \mathbf{E} = \frac{1}{\varepsilon_0}\rho \,, \tag{3}$$

can be calculated on the grid. In PIC codes, this is done in two steps. At first, the Poisson equation

$$\nabla^2\phi = -\frac{1}{\varepsilon_0}\rho \tag{4}$$

is solved numerically for the electric potential ϕ_i at the grid points x_i. Afterwards, the electric field at the grid point E_i is calculated by

$$\mathbf{E} = -\nabla\phi \,, \tag{5}$$

to solve the equation of motion for each pseudo particle $p = 1, ..., N_p$

$$\dot{\mathbf{V}}_p = \frac{Q_p}{m_p}(\mathbf{E}(\mathbf{X}_p) + \mathbf{V}_p \times \mathbf{B})$$

located in the domain, with mass m_p and velocity $\mathbf{V}_p$. For simplicity we consider a constant magnetic field $\mathbf{B}$. The electric field values $\mathbf{E}(\mathbf{X}_p)$ have to be interpolated from grid points to particle positions $\mathbf{X}_p$. This is done by a weighting function W'

$$\mathbf{E}(\mathbf{X}_p) = \sum_{i=0}^{N_g} \mathbf{E}_i \cdot W'(\mathbf{X}_p, \mathbf{x}_i) \,. \tag{6}$$

This defines the current velocity of the particle $\mathbf{V}_p = \mathbf{V}_p(t)$ and allows to calculate the a new position of the particle at the next time step $\mathbf{X}_p(t + \Delta t) = \mathbf{X}_p(t) + \mathbf{V}_p(t) \cdot \Delta t$. The equation of motion is solved with the so-called pusher. Boundary conditions of the domain have to be taken into account. At the end of the PIC cycle, collisions can be introduced by Monte Carlo methods. For the next time step, the particle charges need to be interpolated on the grid points and the PIC cycle is repeated.

To analyse the total numerical error of a complete PIC cycle, one has to derive the overall error in the forces $\mathbf{F}(\mathbf{X}_p) = Q_p\mathbf{E}(\mathbf{X}_p)$ acting on each particle. This is determined by weighting functions, Poisson Solver and particle pusher. These different contributions interact with each other and therefore have to fulfil both individually and in their combination conservation of charge, energy and momentum conservation [1].

In this paper the performance and the interaction of the different numerical contributions with respect to the generation of a non-physical self-force will be investigated. For a better understanding of the problem, a 1D system is considered.

2.1 Momentum conservation

Momentum conservation in PIC is determined by Newton's third law of motion. The force F_{12} acting on a charged particle labelled 1, generated by the electric field of a charged particle labelled 2 has to act opposite to the force F_{21} acting on particle 2 generated by the electric field of particle 1

$$F_{12} = -F_{21} \ . \tag{7}$$

With the help of a discrete Green's function $\hat{g}(x_i, x_k)$, defined at grid points $i, k = 0, ..., N_g$, the electric field can be expressed as

$$E_i = \frac{1}{\varepsilon_0} \sum_{k=0}^{N_g} \hat{g}(x_i, x_k) q_k \ , \tag{8}$$

as given by Hockney [1]. The Green's function element $\hat{g}(x_i, x_k) = g_{ik}$ corresponds to the electric field at the grid point x_i generated by the charge corresponding to the grid point x_k. Therefore, the force on particle 1, located at spatial coordinate X_1, due to particle 2 at spatial coordinate X_2, is given by Equ. 2, 6 and 8 as

$$F_{12} = \frac{Q_2 Q_1}{\varepsilon_0} \sum_{i,k} W(X_2, x_i,) \hat{g}(x_i, x_k) W'(X_1, x_k) \ . \tag{9}$$

Vice versa, the force on particle 2, generated by particle 1 is

$$F_{21} = \frac{Q_1 Q_2}{\varepsilon_0} \sum_{i,k} W(X_1, x_k) \hat{g}(x_k, x_i) W'(X_2, x_i) \ . \tag{10}$$

The special case of an equidistant grid can be found in [1]. To fulfil Equ. 7, two constraints have to be fulfilled. The first is to have the same weighting function for assigning the charge from the particles onto the grid (W) and to interpolate the electric field from the grid back to the particles' positions (W'):

$$W(x, y) = W'(x, y). \tag{11}$$

The second constraint is the antisymmetry of the Green's function

$$\hat{g}(x_i, x_k) = -\hat{g}(x_k, x_i) \quad \forall i, k \ . \tag{12}$$

In this paper the influence of a non-equidistant grid on the antisymmetry of the Green's function is studied. Therefore, condition Equ. 11 is assumed to be fulfilled.

3 Error in Green's function

An analytical 1D Green's function of a PIC code with non-equidistant grid was given by Tskhakaya at al [7]. Here, each cell has an individual size Δx_i. Integration of the 1D Poisson equation using the Gauss theorem gives

$$E(x_i) = \frac{1}{2\varepsilon_0}\left(\int_{x_0}^{x_i} \rho\, dx - \int_{x_i}^{x_{N_g}} \rho\, dx\right) ,$$

for the absence of external fields. The integrals can be approximated with the Trapezoidal rule

$$E(x_i) = \frac{1}{2\varepsilon_0}\left(\sum_{k=0}^{i-1} \frac{\Delta x_k}{2}(\rho_k + \rho_{k+1}) - \sum_{k=i+1}^{N_g-1} \frac{\Delta x_k}{2}(\rho_k + \rho_{k+1})\right)$$

Assuming charges to be mapped on grid centers, in 1D the volume corresponding to the charge density ρ_i is defined as $\nu_i = \Delta x_i \ \forall i = 1, ..., N_g - 1$ and for the boundary cells of the domain as $\nu_0 = 0.5\Delta x_0$ and $\nu_{N_g} = 0.5\Delta x_{N_g-1}$. Therefore the Green's function as defined in Equ. 8 is given as

$$\hat{g}(x_i, x_k) = g_{ik} = \begin{cases} +\frac{1}{2} & \text{if } i > k \\ \frac{1}{4}\frac{\Delta x_{i-1} - \Delta x_i}{\Delta x_{i-1} + \Delta x_i} & \text{if } i = k \\ -\frac{1}{2} & \text{if } i < k \end{cases} .$$

The different scaling of g_{ik} compared to [7] originates from its definition corresponding to the collective charge instead of charge density. One can see, that the antisymmetry is not violated for $i \neq k$. But for $i = k$, diagonal elements $\hat{g}(x_i, x_i) = g_{ii}$ are non-zero, if the neighbouring cells have different sizes $\Delta x_{i-1} \neq \Delta x_i$. The antisymmetry is broken. As given by Equ. 8, the diagonal element is the proportionality factor to calculate the electric field at a grid point x_i generated by the charge associated with that grid point

$$E_i = g_{ii} q_i \ .$$

For a $g_{ii} \neq 0$, the charge experiences a non-physical self-force $F_{self} = q_i E_i \neq 0$. Therefore, broken antisymmetry of the Green's function results in violation of momentum conservation, if charge is associated with a grid point of different sized neighbouring cells.

In the electrostatic plasma assumption the Green's function is defined by the differential Equ. 3 and therefore by the differential operator ∇. In the PIC code itself, the differential equation is realized by a discrete calculation, namely numerical approximations of the Poisson Equ. 4 and the electric field calculation Equ. 5. If the two calculations have the same solution as the analytic Equ. 3, the numerical schemes are exact and the Green's function is antisymmetric. But if the numerical schemes differ from the analytic solution, antisymmetry is no longer ensured and violation of momentum conservation is possible. Here, the interaction of Poisson solver and electric field calculation is important because single approximation errors in the individual steps can be annihilated or amplified.

For simplicity, an exact Poisson solver is assumed in this work. Therefore, the influence of a non-equidistant grid on the antisymmetry of the Green's function is reduced to the numerical calculation scheme of the electric field. To analyses the generation of a self force, an analytical test case of a single pseudo particle in its own field, located at the grid point $x_p = X_p$, is used. That means, only one grid point is associated with charge. The boundary conditions of the computational domain for a single particle in its own field are

$$E_0 = -E_{N_g} \ ,$$

where E_0 and E_{N_g} denotes the values of the electric field at the first and the last grid point of the domain. In 1D the resulting potential is linear, as sketched in Fig. 1. It can be interpreted as the potential of a charged sheath, with an extension infinite in y and z directions, but infinite small in x direction.

In the following the accuracy of the calculation scheme for the electric field is analysed for a non-equidistant grid.

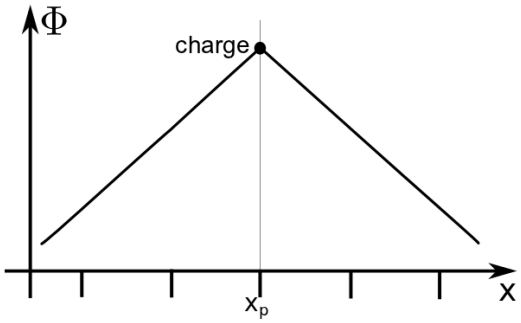

Fig. 1 1D Potential of a charged particle located at $X_p = x_p$.

3.1 Electric field calculation

In the case of an equidistant grid the calculation of the electric field in an electrostatic 1D PIC code is typically done by a two-point central difference scheme. For a non-equidistant grid, it becomes

$$E_i = -\frac{\phi_{i+1} - \phi_{i-1}}{\Delta x_{i-1} + \Delta x_i} \ . \tag{13}$$

This scheme is also applicable for higher dimensional approaches, where it is used for each coordinate. To study its accuracy, the two different regions of the potential, the differentiable region $x_i \neq x_p$ and the particle position x_p, can be analysed separately. At first, it will be proven that E_i is exact for the differentiable region of the potential.

For all grid points in the piecewise linear parts of the potential $x_i \neq x_p$, its accuracy is given by a Taylor series expansion of $\phi(x_{i-1})$ and $\phi(x_{i+1})$ around x_i. One gets

$$\frac{\phi_{i+1} - \phi_{i-1}}{\Delta x_{i-1} + \Delta x_i} = \left.\frac{\mathrm{d}\phi}{\mathrm{d}x}\right|_{x_i} + \sum_{k=2}^{\infty} \left.\frac{\mathrm{d}^k\phi}{\mathrm{d}x^k}\right|_{x_i} \frac{\Delta x_i^k - (-\Delta x_{i-1})^k}{k!(\Delta x_i + \Delta x_{i-1})} \quad \forall x_i \neq x_p \ ,$$

where the sum represents the error of the calculation scheme. Since the right hand side of the Poisson Equ. 4 is zero for all $x_i \neq x_p$, also the second derivative of the potential at x_i is zero. Therefore, all higher derivatives are zero as well and the error vanishes. The two-point central difference scheme is exact for all grid points $x_i \neq x_p$. Therefore, the corresponding entries of the Green's function are antisymmetric $g_{ik} = -g_{ki} \ \ \forall i \neq k$, as shown in the section before.

At the particle grid point the potential has a discontinuity, therefore the Taylor series around x_p is not defined. To determine the accuracy, the symmetry of the potential around x_p can be used. To ensure condition Equ. 12 and therefore to avoid self forces, E_p has to be zero. For neighbouring cells of the same size $\Delta x_{i-1} = \Delta x_i$, the potential ϕ_{i+1} and ϕ_{i-1} have the same values and the electric field is

$$E_p = \frac{\phi_{p+1} - \phi_{p-1}}{2\Delta x_{p-1}} = 0 \quad \text{for} \ \ \Delta x_{p-1} = \Delta x_p \ .$$

No self force is generated. But if $\Delta x_{i-1} \neq \Delta x_i$,the potential values are not equal and the resulting electric field differs from zero

$$E_p = \frac{\phi_{p+1} - \phi_{p-1}}{\Delta x_{p-1} + \Delta x_p} \neq 0 \quad \text{for} \ \ \Delta x_{p-1} \neq \Delta x_p \ .$$

This artificial electric field affects the particle as a self-force, although the calculated potential is correct. The diagonal elements of the Green's function corresponding to the a change of cell size are $g_{ii} \neq 0 \ \forall \Delta x_i \neq \Delta x_{i-1}$. The antisymmetry is broken and the momentum conservation is violated.

To overcome this violation a calculation scheme has to be found which ensures antisymmetry of the Green's function for all grid points. In the next section a modified calculation scheme E_i' is derived.

4 A modified electric field calculation

To illustrate the source of error in the typical electric field calculation in a non-equidistant grid and the idea of the modified calculation scheme, the 1D system is used. In Fig. 2.a and 2.b, the potential of a single particle located at a grid point x_p, with neighbouring grid cells of different size $\Delta x_{p-1} < \Delta x_p$ is shown. The values of the potential on the grid points ϕ_i are marked by a black dot, while the black line represents the analytic solution of ϕ. Since the Poisson solver is assumed to be exact, the dots lie directly on the line. For the conservative and the modified calculation scheme, the electric field at x_p is given by the slope of the red dashed line, respectively of the blue dot-dashed line. While the usual calculation scheme is a two-point central difference scheme Equ. 13, E_p in

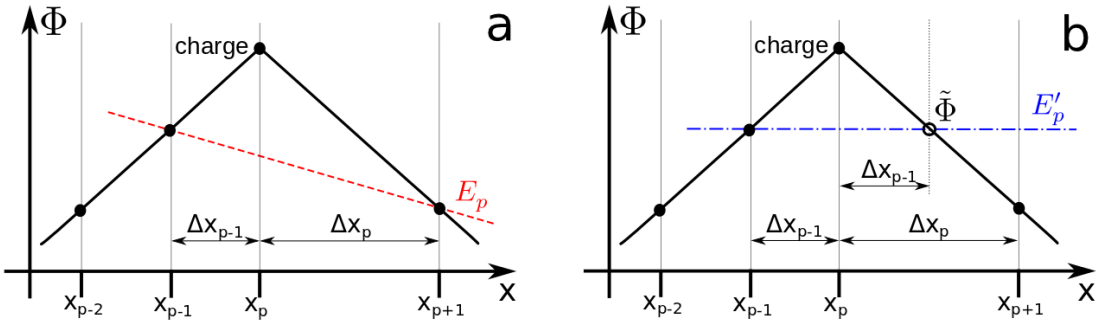

Fig. 2 Electric field calculation for a charged particle located at x_p, in an non-equidistant grid with a change of cell size $\Delta x_{p-1} \neq \Delta x_p$. a: Calculation scheme E_p as for an equidistant grid. b: Modified field calculation E'_p.

Fig. 2.a is non zero and therefore wrong. One can see, that the field inaccuracy has its origin in the unsymmetrical positions of the used neighboring potential values ϕ_{p-1} and ϕ_{p+1} appearing due to the different cell sizes. The idea of the corrected calculation for a non-equidistant grid is to leave the grid at these critical positions and restore the spatial symmetry in the derivation scheme. Therefore, instead of $\phi_{p+1} = \phi(x_p + \Delta x_p)$, an approximated value $\tilde{\phi} \approx \phi(x_p + \Delta x_{p-1})$ is used. The two point central difference scheme gets

$$E'_i = \begin{cases} -\frac{\phi_{i+1}-\phi_{i-1}}{2\Delta x_{i-1}} & \text{if } \Delta x_{i-1} = \Delta x_i \\ -\frac{\tilde{\phi}-\phi_{i-1}}{2\Delta x_{i-1}} & \text{if } \Delta x_{i-1} \neq \Delta x_i \end{cases} . \tag{14}$$

For the system of a single particle at grid point x_p, a linear interpolation between the neighbouring points gives the exact solution for

$$\tilde{\phi} := \phi_p(1 - \frac{\Delta x_{p-1}}{\Delta x_p}) + \phi_{p+1}\frac{\Delta x_{p-1}}{\Delta x_p} = \phi(x_p + \Delta x_{p-1}) . \tag{15}$$

In the sketch in Fig. 2.b the substitution of ϕ_{p+1} by a symmetrical placed $\tilde{\phi}$ is the key element for the correction. Hence $E'_p = E(x_p)$ gives the correct analytical value, as shown by the slope of the blue dot-dashed line.

This modified calculation scheme can also be derived differently. For the single particle system, the potential is piecewise linear, but has a discontinuity in the first derivative at the particle position X_p. That means that the derivative of the potential and therefore the electric field, is not defined at this point is not defined. Therefore, also the electric field at this point is not defined. But since for all position to the left and to the right of X_p the potential is continuously differentiable, right-sided and left-sided derivatives at the particle position are defined as

$$\left.\frac{\mathrm{d}\phi}{\mathrm{d}x}\right|^r_{X_p} := \lim_{\eta\to 0}\frac{\phi(X_p) - \phi(X_p - \eta)}{\eta}$$
$$\left.\frac{\mathrm{d}\phi}{\mathrm{d}x}\right|^l_{X_p} := \lim_{\eta\to 0}\frac{\phi(X_p + \eta) - \phi(X_p)}{\eta} ,$$

with $t \in \mathbb{R}, \eta > 0$. For a 1D system of a single charge, the one-sided derivatives give $\frac{\mathrm{d}\phi}{\mathrm{d}x}\Big|^{r}_{X_p} = -E$ and $\frac{\mathrm{d}\phi}{\mathrm{d}x}\Big|^{l}_{X_p} = +E$, with the analytical value of the electric field $E = const$, generated by the particle.

Although mathematically the electric field at the particle position is not defined, the physics requirement of non-existence of self-force requires $E(X_p)$ to be zero in a system of a single particle in its own field. While for this system, the electric field to the left and to the right of the particle position has the same value but the opposite sign, the analytical calculation of the electric field at X_p can be defined by the average of left-sided and right-sided derivatives

$$\mathcal{E}(X_p) := -\frac{\frac{\mathrm{d}\phi}{\mathrm{d}x}\Big|^{r}_{X_p} + \frac{\mathrm{d}\phi}{\mathrm{d}x}\Big|^{l}_{X_p}}{2} = \lim_{\eta\to 0} \frac{E(X_p-\eta) + E(X_p+\eta)}{2} \ . \tag{16}$$

For a single particle this definition gives an electric field value of 0 at X_p.

$$\begin{aligned}\mathcal{E}(X_p) &= \lim_{\eta\to 0} -\frac{1}{2}\left(\frac{\phi(X_p)-\phi(X_p-\eta)}{\eta} + \frac{\phi(X_p+\eta)-\phi(X_p)}{\eta}\right) \\ &= \lim_{\eta\to 0} -\frac{\phi(X_p+\eta)-\phi(X_p-\eta)}{2\eta} \ = \lim_{\eta\to 0} -\frac{0}{2\eta} \ \to 0\end{aligned}$$

Here, the symmetry of the potential $\phi(X_p-\eta) = \phi(X_p+\eta)\ \forall\eta \in \mathbb{R}$ is used. This definition of the electric field is also valid for the smooth parts of the potential $X \neq X_p$, since right-sided derivatives and left-sided derivatives gives the same value $\frac{\mathrm{d}\phi}{\mathrm{d}x}\Big|^{r}_{X} = \frac{\mathrm{d}\phi}{\mathrm{d}x}\Big|^{l}_{X} \equiv \frac{\mathrm{d}\phi}{\mathrm{d}x}\Big|_{X}$. Therefore, Equ. 16 applied on X is equivalent to $\mathcal{E}(X) = -\frac{\mathrm{d}\phi}{\mathrm{d}x}\Big|_{X}\ \forall X \neq X_p$. From this analytic definition, the modified electric field calculation scheme can be derived. A discrete form of Equ. 16 is

$$\mathcal{E}(x_i) = \frac{E(x_i - \Delta x_{i-1}/2) + E(x_i + \Delta x_i/2)}{2} \ \forall i = 1, ..., N_g - 1 \ . \tag{17}$$

For any isotropic system containing a single charged particle, this form gives the exact value as in Equ. 16. Since the general two point central difference scheme 13 is exact for all $x_i \neq x_p$ also

$$\begin{aligned}E(x_i - \Delta x_{i-1}/2) &= -\frac{\phi(x_i)-\phi(x_{i-1})}{\Delta x_{i-1}} \\ E(x_i + \Delta x_i/2) &= -\frac{\phi(x_{i+1})-\phi(x_i)}{\Delta x_i} \ ,\end{aligned}$$

is exact and can be used in Equ. 17. This gives the modified calculation scheme

$$E'_i = \mathcal{E}(x_i) = -\frac{\Delta x_{i-1}\phi_{i+1} + (\Delta x_i - \Delta x_{i-1})\phi_i - \Delta x_i\phi_{i-1}}{2\Delta x_i \Delta x_{i-1}} \ , \tag{18}$$

which is equivalent to Equ. 14 and Equ. 15.

To ensure antisymmetry of the Green's function Equ. 12, $E'_i = -\frac{\mathrm{d}\phi}{\mathrm{d}x}\Big|_{x_i}\ \forall i \neq p$ and $E'_p = 0$ has to be shown for the analytical test system. Since the electric field to the right and to the left of x_p is constant, $E(x_i) = -E$ for $i < p$ and $E(x_i) = +E$ for $i > p$, the potential is given by

$$\begin{aligned}\phi_{p-k} &= \phi_p - (x_p - x_{p-k}) \cdot E \\ \phi_{p+k} &= \phi_p - (x_{p+k} - x_p) \cdot E\end{aligned}$$

for $k > 0;\ k \in \mathbb{N}$. With this expressions and for a grid point $x_i > x_p$ Equ. 18 gets

$$\begin{aligned}E'_{i,i>p} &= -\frac{(\Delta x_{i-1} - \Delta x_i)(\phi_p - \phi_p + (x_p - x_i)\cdot E)}{2\Delta x_i \Delta x_{i-1}} + E \\ &= E \quad \forall \Delta x_i,\ \Delta x_{i-1} \ .\end{aligned}$$

Using the same procedure $E'_{i,i<p} = E$ can be shown. Therefore, the requirement $E'_i = -\frac{\mathrm{d}\phi}{\mathrm{d}x}\Big|_{x_i} \; \forall i \neq p$ is fulfilled. For the particle position x_p the same calculation gives:

$$E'_p = 0 \quad \forall \Delta x_p,\, \Delta x_{p-1} \; .$$

The modified calculation scheme for the electric field Equ. 18 is therefore exact for all grid points in a 1D system of a single charge with non-equidistant grid as well as for an equidistant grid and does not generate self forces. While also the calculated potential is assumed to be exact for all grid points, the Greens function is antisymmetric and the momentum is conserved.

5 Consequences for energy conservation

Momentum conservation does not guarantee the energy conservation, too. Since the Poisson's equation is solved only at grid points the electric field at particle positions is an approximation and therefore the potential energy of the particle is also not correct. PIC does not conserve energy. In order to prove that not additional error is generated, we compare the kinetic energy obtained from the simulation with the corresponding analytical values.

If a particle "p" with charge Q_p and mass m_p at position $X_p \in [x_p; x_{p+1}]$ is assumed, its kinetic energy is given by $\mathcal{W}_p = 0.5 \cdot m_p V_p^2$ and its kinetic energy change per unit time is

$$\frac{\mathrm{d}\mathcal{W}_p}{\mathrm{d}t} = V_p Q_p (E + \frac{V_p \times B}{B^2}) \; ,$$

where E and B are the electric and magnetic field values at the particle position X_p. Therefore, the numerical error in the energy change per unit time for an electrostatic system is given by

$$\begin{aligned} \delta W_p &:= \frac{\mathrm{d}\mathcal{W}_p^{PIC}}{\mathrm{d}t} - \frac{\mathrm{d}\mathcal{W}_p^{an}}{\mathrm{d}t} = V_p Q_p \left(E(X_p)^{PIC} - E(X_p)^{an}\right) \\ &= V_p Q_p \sum_{i=0}^{N_g} W(X_p, x_i) \left(E_i^{PIC} - E(X_p)^{an}\right) \; , \end{aligned}$$

where E_i^{PIC} denotes the electric field calculated by PIC at the grid point x_i and $E_i^{an}(X_p)$ the analytical electric field at the particle position X_p. Numerically, the error consists of two parts:

$$\delta\mathcal{W}_p = \delta\mathcal{W}_p^0 + \delta\mathcal{W}_p^{self} \; ,$$

the error due to the electric field E_i^0 generated by other particles in the system

$$\delta\mathcal{W}_p^0 = Q_p V_p \sum_{i=0}^{N_g} W(X_p, x_i) \left(E_i^0 - E(X_p)^{an}\right) \tag{19}$$

and the self-field

$$\delta\mathcal{W}_p^{self} = Q_p V_p \sum_{i=0}^{N_g} W(X_p, x_i) E_i^s \; ,$$

which is zero in the case of a uniform grid or a non-uniform grid with correct electric field calculation. For many-particle systems the numerical error due to particle-particle interaction is given by the superposition of the electric fields generated by the charges assigned to other grid cells

$$\delta\mathcal{W}_p^0 = \sum_{k=0}^{N_g} \delta\mathcal{W}_p^k \; ,$$

where

$$\delta\mathcal{W}_p^k = Q_p V_p \sum_{i=0}^{N_g} W(X_p, x_i)\left(E_i^k - E(X_p)^{an,k}\right) \quad . \tag{20}$$

Here the index k indicates the physical quantities generated by the charge q_k. By assuming an exact Poisson solver and extracting the self-field the electric field in 1D is given as (we assume $X_p \neq x_k$)

$$E_i^k = \begin{cases} +\frac{q_k}{\varepsilon_0}, & \text{if } k < i \\ 0, & \text{if } k = i \\ -\frac{q_k}{\varepsilon_0}, & \text{if } k > i \end{cases} .$$

For the corresponding analytical field we have

$$E(X_p)^{an,k} = \begin{cases} +\frac{q_k}{\varepsilon_0}, & \text{if } X_p > x_k \\ -\frac{q_k}{\varepsilon_0}, & \text{if } X_p < x_k \end{cases} .$$

Together with Equ. 20 this results in

$$\delta\mathcal{W}_p^k = \begin{cases} +\frac{Q_p V_p}{\varepsilon_0} q_k \left[W(X_p, x_k) + 2\sum_{i>k} W(X_p, x_i)\right], & \text{if } X_p < x_k \\ -\frac{Q_p V_p}{\varepsilon_0} q_k \left[W(X_p, x_k) + 2\sum_{i<k} W(X_p, x_i)\right], & \text{if } X_p > x_k \end{cases} .$$

In PIC, the weighting function gives each particle a defined size. That means $W(X_p, x_i) \neq 0$ if $x_i \in [X_p - h_p^l; X_p + h_p^r]$, where the left h_p^l and the right boundary h_p^r depends on the cell sizes next to the particle positions. For a second order weighting function like Cloud-In-Cell (CIC) [1], the particle boundaries of particle "p" with $X_p \in [x_p; x_{p+1}]$ are $h_p^l = \Delta x_{p-1}$ and $h_p^r = \Delta x_p$. If a second particle "m" with $Q_m = \sum_{i=0}^{N_g} q_i$ and $X_m \in [x_m; x_{m+1}]$ is introduced, its particle boundaries are $h_m^l = \Delta x_{m-1}$ and $h_m^r = \Delta x_m$. With this set-up the numerical error in the kinetic energy due to interaction of particle "p" and "m" is given by

$$\delta\mathcal{W}_p^0 = \delta\mathcal{W}_p^m + \delta\mathcal{W}_p^{m+1}$$

$$\delta\mathcal{W}_p^0 = \begin{cases} 0, & \text{if } X_p < x_{m-1} \\ +\frac{Q_p Q_m V_p}{\varepsilon_0} W(X_m, x_m) W(X_p, x_m), & \text{if } X_p \in [x_{m-1}; x_m] \\ +\frac{Q_p Q_m V_p}{\varepsilon_0} [W(X_m, x_{m+1}) W(X_p, x_{m+1}) - W(X_m, x_m) W(X_p, x_m)], & \text{if } X_p \in [x_m; x_{m+1}] \\ -\frac{Q_p Q_m V_p}{\varepsilon_0} W(X_m, x_{m+1}) W(X_p, x_{m+1}), & \text{if } X_p \in [x_{m+1}; x_{m+2}] \\ 0, & \text{if } X_p > x_{m+2} \end{cases} .$$

Applying the following Cloud-In-Cell (CIC) weighting function for a non-equidistant grid

$$W(X_p, x_i) = \begin{cases} 1 - \frac{x_i - X_p}{\Delta x_{i-1}} & \text{for } 0 \leq x_i - X_p \leq \Delta x_{i-1} \\ 1 + \frac{x_i - X_p}{\Delta x_i} & \text{for } -\Delta x_i \leq x_i - X_p \leq 0 \\ 0 & \text{else} \end{cases} , \tag{21}$$

one gets

$$\delta\mathcal{W}_p^0 = \begin{cases} 0, & \text{if } X_p < x_{m-1} \\ \frac{Q_p Q_m V_p}{\varepsilon_0} \frac{x_{m+1} - X_m}{\Delta x_m} \frac{X_p - x_{m-1}}{\Delta x_{m-1}}, & \text{if } X_p \in [x_{m-1}; x_m] \\ \frac{Q_p Q_m V_p}{\varepsilon_0} [\frac{X_m - x_m}{\Delta x_m} \frac{X_p - x_m}{\Delta x_m} - \frac{x_{m+1} - X_m}{\Delta x_m} \frac{x_{m+1} - X_p}{\Delta x_m}], & \text{if } X_p \in [x_m; x_{m+1}] \\ \frac{Q_p Q_m V_p}{\varepsilon_0} \frac{x_m - X_m}{\Delta x_m} \frac{x_{m+2} - X_p}{\Delta x_{m+1}}, & \text{if } X_p \in [x_{m+1}; x_{m+2}] \\ 0, & \text{if } X_p > x_{m+2} \end{cases} . \tag{22}$$

An error in the kinetic energy appears only in the region where the particles are overlapping.

In PIC one simulates a large number of particles. Hence, it is important to consider the average energy error of particles of the type P in the given cell p due to interaction with other particles

$$\delta\bar{\mathcal{W}}_P = \sum_{i=0}^{N_g} \sum_{S}^{species} N_S^i \, \delta\bar{\mathcal{W}}_P^{S,i} \; . \tag{23}$$

Here, N_S^i denotes the number of particles of the type S in cell i and $\delta\bar{\mathcal{W}}_P^{S,i}$ the average energy error of particle species P at cell p due to interactions with particles of the type S in the cell i. In order to obtain $\delta\bar{\mathcal{W}}_P^{S,i}$ the average particle position can be set as

$$\bar{X}_p = x_p + 0.5\Delta x_p \; , \qquad \bar{X}_m = x_m + 0.5\Delta x_m \; .$$

Then, introducing an average velocity $\bar{V}_P^p$ from Equ. 22 we obtain

$$\delta\bar{\mathcal{W}}_P^{S,i} = \frac{Q_P Q_S}{4\varepsilon_0} \bar{V}_P^p \left(\delta_{m,p+1} - \delta_{m,p-1}\right) \; ,$$

where $\delta_{i,j}$ is the Kronecker delta. Therefore, the average energy error Equ. 23 becomes

$$\delta\bar{\mathcal{W}}_P = \frac{Q_P \bar{V}_P^p}{4\varepsilon_0} \sum_{S}^{species} Q_S (N_S^{p+1} - N_S^{p-1}) = \frac{Q_P \bar{V}_P^p}{4\varepsilon_0} \, \delta\rho_S^p \; ,$$

where $\delta\rho_S^p = \rho_S^{p+1} - \rho_S^{p-1}$ is the gradient of the charge density of the species S. Typically $\delta\rho^i \ll \rho^i$ and the relative part of the error of energy is negligible even for a non-neutral plasma.

6 Numerical tests

In order to study effect of the modified electric field calculation on the kinetic energy different numerical tests are presented. We compare two field calculation schemes for a non-equidistant grid with an equidistant grid set-up. For an exact Poisson solver, as assumed in this work, the numerical error can only be generated by the pushing routine and by the routine calculating the electric field. The electric field acting on a particle is given by the self field E^{self} and the field E^m generated by all other particles in the system

$$E(X_p) = E^{self}(X_p) + \sum_{m=1}^{N_p} E^m(X_p) \; .$$

To separate these effects separately two different test set-ups are studied. In the first part, a single-particle system is used to analyses self forces. In the second part, additionally the additional influence of other charged particles is studied for a two-particle-system.

6.1 Single-particle tests

To test the modified electric field calculation scheme, a single electron with an initial non-zero velocity is studied in a 1d3v PIC code using a non-equidistant grid. A self force will appear as an artificial acceleration when crossing a cell size change from small cells to larger ones and therefore the kinetic energy will be artificially changed.

In the code, the electron is initialized at $X_e(t=0) = 4\lambda_{D,e}$, in a domain with a length $L = 10\lambda_{D,e}$ length. Since the Debye length $\lambda_{D,e}$ and the plasma frequency $\omega_{p,e}$ are only defined for a many particle system, in this set up they just define an arbitrary length scale and time scale. The corresponding statistical quantities where chosen as $T_e = 6\,\mathrm{eV}$ and $n_e = 1 \times 10^{12}\,\mathrm{cm}^{-3}$, defining a length scale of $\lambda_{D,e} = 1.8 \times 10^{-5}\,\mathrm{m}$ and a time scale of $\omega_{p,e} = 5.64 \times 10^{10}\,\mathrm{s}^{-1}$. The velocities are initialized to $V_e^x = \lambda_{D,e}\omega_{p,e}$ and $V_e^y = V_e^z = 0$. The applied non-equidistant grid consists of two parts but with individually different cell sizes. At $x = 5\lambda_{D,e}$, the cell size

changes from $\Delta x_1 = 0.1\lambda_{D,e}$ to $\Delta x_2 = 5\Delta x_1$. The time step is chosen as $\Delta t = 0.002\,\omega_{p,e}^{-1}$ to guarantee sufficient time resolution of the electron dynamics.

For the Poisson solver a three point central difference scheme for the non equidistant grid

$$\frac{\phi_{i+1}\Delta x_{i-1} - \phi_i(\Delta x_{i-1} + \Delta x_i) + \phi_{i-1}\Delta x_i}{0.5(\Delta x_{i-1} \cdot \Delta x_i)(\Delta x_{i-1} + \Delta x_i)} = -\frac{1}{\varepsilon_0}\frac{\rho_i}{0.5(\Delta x_{i-1} + \Delta x_i)}$$

is applied. Here Δx_i is the length of the grid cell right to the grid point x_i which can be different from the cell size Δx_{i-1} to the left of x_i. For the boundary conditions $\phi_0 = 0$ and $\phi_{N_g} = (L - 2X_e)E$ are set, where E is the electric field generated by the electron. As a weighting function for particles and for the electric field the CIC for non-equidistant grid Equ. 21 is used.

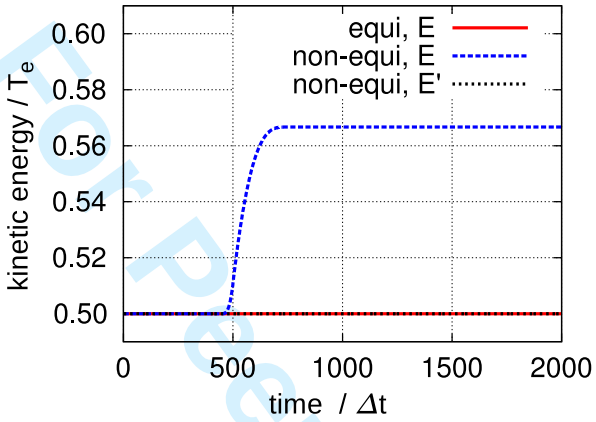

Fig. 3 Kinetic energy of one electron in its own field as a function of time, for an equidistant grid (red solid line) and a non-equidistant grid with (black dotted line) and without E-field correction (blue dashed line). The non-uniform grid boundary is reached at $\sim 500\Delta t$.

Figure 3 shows the dependence of the electron kinetic energy as a function of time, for an E-field calculation without correction (E) and with correction (E') for a non-equidistant grid in comparison with an equidistant grid. One can clearly see that during the crossing of the grid separation boundary, the inaccurate electric field pushes the electron. This is the time period, where the weighting function W assigns the particle to grid points related to different cell sizes. Applying the modified field calculation, no increase of the electron velocity appears at the grid change and kinetic energy and the momentum are conserved.

The simulated electric field as a function of spatial coordinate, x, is shown in Fig. 4. For $t_1 = 200\Delta t$, the electron is in the domain with grid size Δx_1 and for $t_2 = 2000\Delta t$ it is in the domain with grid size Δx_2. The difference of the electric field for t_2 between the corrected and uncorrected run in the non-equidistant grid is due to the different position of the electron. While for the corrected electric field the electron has a constant velocity, it was accelerated for the uncorrected case. The modified field calculation excludes self-forces at a cell size change and therefore conserves the momentum for a single particle.

To quantify the error in the electric field at the grid change, a second test was done. Here, the electron was initialized at the grid point $X_e(t = 0) = 5\lambda_{D,e}$ where the cell size changes. Its velocity was initialized to $\mathbf{V}_e = \mathbf{0}$. According to the analytic solution, the electric field has to be zero at X_e. The calculated electric field as a function of the coarsening of the cell size can be seen in Fig. 5. The error for the corrected field is in the range of the numerical error, while the error of the uncorrected electric field increases with grid coarsening and saturates. For the uncorrected electric field, the error related to the equidistant grid can be derived as

$$||E_p - E_p^{equi}|| = ||\frac{\phi_{p-1} - \phi_{p+1}}{\Delta x_1 + \Delta x_2} - \frac{\phi_{p-1}^{equi} - \phi_{p+1}^{equi}}{2\Delta x_1}|| = \frac{\Delta x_2 - \Delta x_1}{\Delta x_1 + \Delta x_2}\,||E||$$

with the $\phi_{p-1} = \phi_p + E \cdot \Delta x_1$, $\phi_{p+1} = \phi_p + E \cdot \Delta x_2$ and $\phi_{p\pm1}^{equi} = \phi_p + E \cdot \Delta x_1$ for the equidistant grid. The error estimate is shown in Fig. 5 as an orange dashed line. It agrees with the measured field. For a coarser grid,

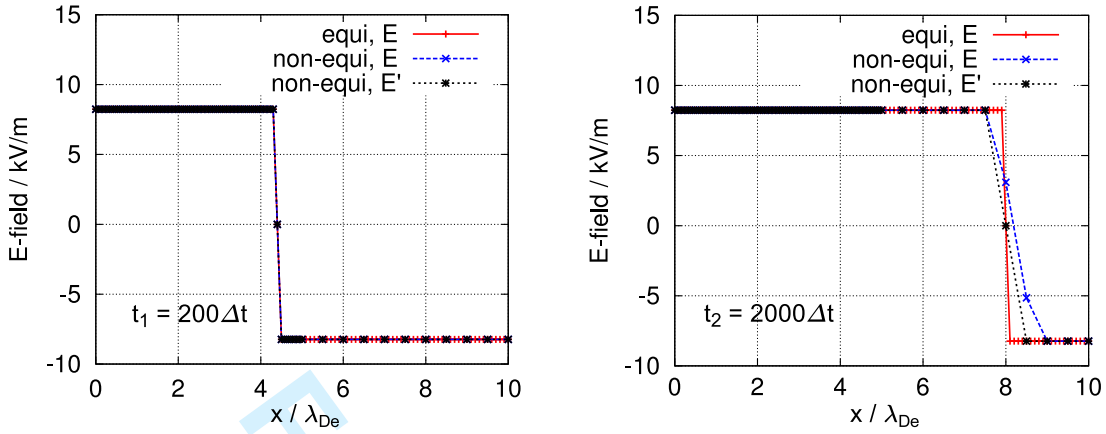

Fig. 4 Electric field as a function of x for different times. At t_1 the electron is in the part of the domain with cell size Δx_1. At t_2 the electron is in the part with Δx_2.

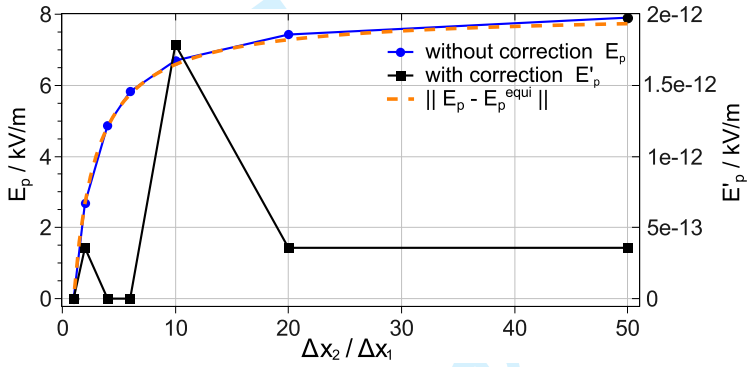

Fig. 5 Error of the electric field calculation for one electron located at the grid change with initial velocity $\mathbf{V} = \mathbf{0}$.

Δx_2 decreases and reduces the influence of Δx_1. The error of the field calculation saturates with

$$\lim_{\Delta x_2 \to \infty} ||E_p - E_p^{equi}|| = ||E|| \,.$$

The same error estimate for the corrected electric field gives

$$||E'_p - E_p^{equi}|| \;=\; ||\frac{\phi_{p-1} - \tilde{\phi}}{\Delta x_1 + \Delta x_2} - \frac{\phi_{p-1}^{equi} - \phi_{p+1}^{equi}}{2\Delta x_1}|| \;=\; 0$$

with the interpolated potential $\tilde{\phi} = \phi_p \frac{\Delta x_2 - \Delta x_1}{\Delta x_2} + \phi_{p+1} \frac{\Delta x_1}{\Delta x_2}$.

6.2 Two-particle test

For a more realistic test-case the interaction of different particles has to be taken into account. Below We consider a two-particle system: one electron interacting with a singly charges Argon ion. Both particles are initialized with a zero initial velocity, so that the total momentum $p_{tot} = 0$. The simulation domain has a length of $L = 10\lambda_{D,e}$, where the same length scale is used as for the single-particle tests. For the equidistant grid, the domain has a cell size of $\Delta x = 0.1\lambda_{D,e}$. In the non-equidistant grid a change in cell size from $\Delta x_1 = \Delta x$ to $\Delta x_2 = 2\Delta x_1$ is implemented at $5\lambda_{D,e} = 50\Delta x_1$. In order to place the zone of particle interaction near the change of cell size, the ion is initialized at $X_i(t = 0) = 49.5\Delta x_1$. The initial position of the electron is taken at $X_e(t = 0) = 39.0\Delta x_1$.

While the ion is nearly "frozen" and does not leave its cell, the electron is oscillating around the ion and therefore crosses the grid change frequently. The time step was chosen according to the average velocity of the ion $\bar{V}_e = 8.3 \times 10^4$ m/s and the minimum cell size Δx_1: $\Delta t = \delta t \cdot \frac{\Delta x_1}{\bar{V}_e}$, where $\delta t = 8.1 \times 10^{-5}$ is a small dimensionless parameter. During the total calculation time of $t_{max} = 10^5 \Delta t$, the electron oscillates 1.2 times around the ion. The same Poisson solver and the weighting function where used, as given in section 6.1. The following boundary conditions have been set: $\Phi(x = 0) = \Phi(x = 10\lambda_{D,e}) = 0$.

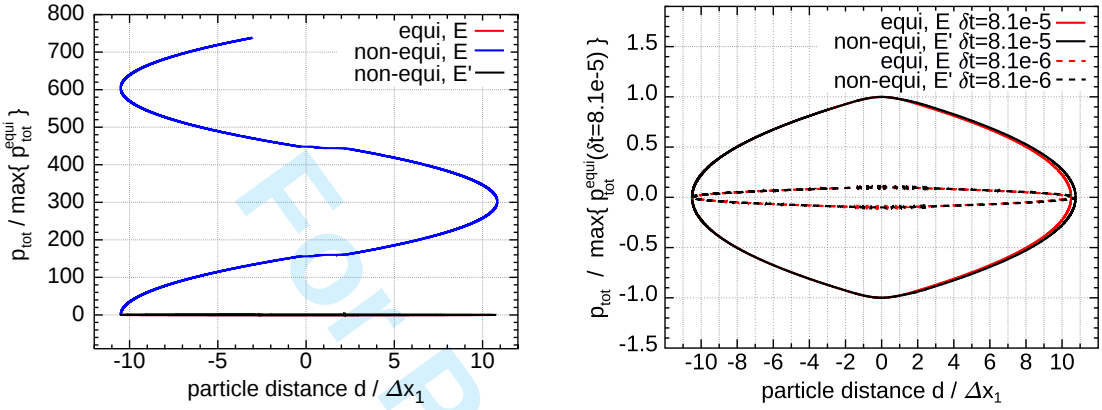

Fig. 6 Total momentum of a two particle system as a function of the particle distance for an equidistant and a non-equidistant grid with and without E-field correction.

In Figure 6, the total momentum is shown for the three cases: equidistant grid, non-equidistant grid and non-equidistant grid with corrected field calculation. It is given normalized to the maximum momentum of the equidistant grid $max\{p_{tot}^{equi}\} = 5.1 \times 10^{-28}$ kg m/s as a function of the distance between particles normalized to Δx_1. The total momentum of the uncorrected non-equidistant grid is continuously increasing (see the left figure), as consequence of the wrong electric field, continuously acting on the ion. For this scheme, the momentum is not conserved. In comparison, the equidistant grid, as well as with the non-equidistant grid with the corrected field calculation have a total momentum is much closer to the analytical value of $p_{tot} = 0$.

For a better comparison, both cases are shown as solid lines at the right hand side in Fig. 6. In dotted lines, the total momentum is given for a 10 times smaller time step $\delta t = 8.1 \times 10^{-6}$. All curves are closed ellipses, therefore the momentum is conserved during the 1.2 oscillations. For both grids the the thickness of the ellipses decreases with the 10 times smaller time step by a factor of 10 and is therefore determined by the numerical error of the solver due to the chosen time step Δt. For the non-equidistant grid a deviation is visible for both time steps, if the electron is located in the coarser grid ($d > 0.5\Delta x_1$). Here, the total momentum is larger than in the equidistant grid. This implies that this error is caused by the numerical error of the solver routine due to the coarser cell size. But it does not affect the conservation of momentum.

As shown in section 5, an error in the kinetic energy appears only in the region where the particles are overlapping. This "overlapping zone" has an extend of 3 grid cells and can be seen in Fig. 7 for $|d| \leq 1.5\Delta x_1$. In this simulation the ion was placed in the middle of the cell with a distance of 4 cells distance from the non-uniform cell boundary. Other parameters were: $X_i(t = 0) = 50.5\Delta x_1$, $X_e(t = 0) = 40.0\Delta x_1$, change of cell size at $56\Delta x_1$ from Δx_1 to $\Delta x_2 = 2 \cdot \Delta x_1$. The total kinetic energy is calculated by the sum of the measured kinetic energy and potential energy

$$\mathcal{E}_{tot}(t) = \mathcal{W}(t) + \mathcal{U}(t) = \sum_{p=1}^{N_p} \frac{m_p \bar{\mathbf{V}}_p(t)}{2} + \sum_{p=1}^{N_p} q_p E(X_p(t)) \quad .$$

For the Boris pusher used in this 1D simulation, the velocities are calculated at half time steps. Therefore, the kinetic energy is calculated from the average velocity

$$\bar{\mathbf{V}}_p(t) = 0.5 \cdot (\mathbf{V}_p(t - 0.5\Delta t) + \mathbf{V}_p(t + 0.5\Delta t)) \quad .$$

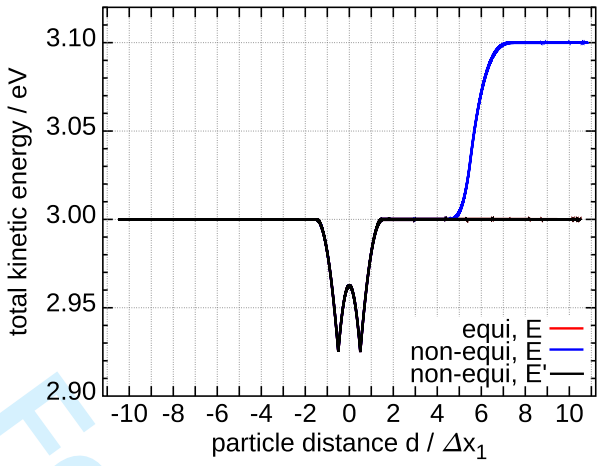

Fig. 7 Total kinetic energy as a function of the particle distance.

For the potential energy of the particles, the electric field at the particle position is calculated by

$$E(X_p(t)) = \sum_{i=0}^{N_g} W(x_i, X_p) E_i - C(x_i, X_p) \quad ,$$

where the function $C(x_i, X_p)$ is a correction of the electric field at particle position. It is necessary due to the fact, that the electric field is given only at grid points and therefore is varying with respect to the distance to the next grid point. For a two particle system with the CIC shape function 21 it is given by

$$C(x_i, X_p) = \frac{Q_p^2}{\varepsilon_0} \frac{(X_p - x_i)(x_{i+1} - X_p)}{\Delta x_i^2} \quad .$$

For the 1D PIC, it can be shown that the calculated potential gives the correct analytical value.

As it was expected, the uniform and non-uniform mesh with correct electric field calculation produces the same error. According to Equ. 22 the error changes the sign when the electron "crosses" the ion, so that the total error after 1.5 cells is zero. If the ion is not placed in the middle of the cell then the positive and negative contributions are different and a residual error appears. This error is known [7] and corrected in many particle systems due to averaging over the particles, as described in section 5. Additional collisions will reduce it further. Contrary to this, the uncorrected code, due to self-field, produces an error when the electron crosses the non-uniform boundary due to self forces.

More critical is the case when the ion is placed next to the non-uniform cell boundary. Also in this case the ion is placed in the middle of the cell with the size Δx_1 and to the left a cell with size $\Delta x_2 = 2\Delta x_1$. The obtained total kinetic energy as a function of the particle distance is given in Fig. 8. For all three cases, equidistant grid, non-equidistant grid with and without field correction, the error in energy is different. The equidistant case is similar to the one shown in Fig. 7. Contrary to this, the non-equidistant case with the field correction produces a residual error caused by the fact that the cell sizes from the left and right hand side of the ion are different and the positive and negative errors do not cancel each other (Equ. 22). In the case of the non-equidistant grid without field correction the error is larger. This is a consequence of a self-force.

As were shown in section 5, in many particle systems the error in the corrected electric field calculation even for a non-neutral plasma is is negligible due to averaging over the particles. Hence, the PIC model with an non-equidistant grid and corrected electric field conserves the average energy with a high accuracy.

7 Conclusions and discussion

In this work effects of non-equidistant grids on conservation of momentum and kinetic energy conservation was studied for simple test cases of an electrostatic 1D PIC code. The aim was to reduce the error for energy and

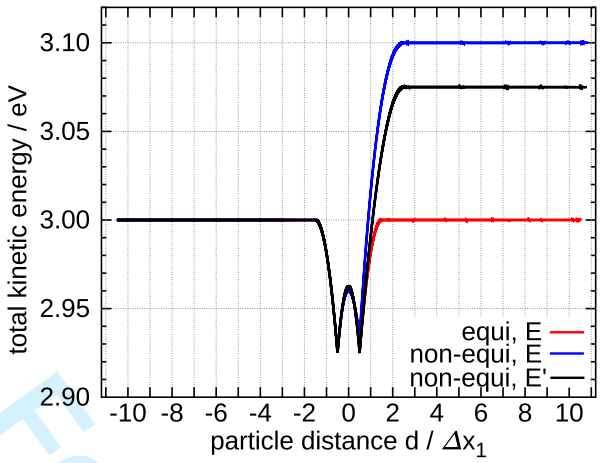

Fig. 8 Total kinetic energy as a function of the particle distance. The change of the cell size is next to the ion.

momentum conservation in PIC. Since an exact Poisson solver was assumed, only numerical errors concerning the particle pusher were analysed. For a standard central difference scheme for electric field calculation, generation of artificial electric fields at the particle position was shown if the particle is situated next to a change of cell size. This generates a self force. With the help of a Green's function theory it was proven that this destroys momentum conservation. To reduce this error a modified electric field calculation scheme was derived.

For non-equidistant grids, violation of kinetic energy conservation independent of the electric field calculation scheme was found for a two-particle system. For a more applicable system of many particles, it was shown that for an average over all particles in one cell scales the error scales with the charge density gradient in the three surrounding cells, which is usually negligible.

To test the accuracy of the two electric field calculation schemes numerical tests were done to compare the results with an equidistant grid set-up. All tests showed an improved behaviour of momentum and kinetic energy conservation for the modified calculation scheme of the electric field. In a first test system only the effects of the self force was studied with respect to momentum conservation. Here, analytical estimates were confirmed. In a second numerical test system the influence of electric fields generated by other particles in the system was investigated. For this case with two particles, momentum conservation and a violated kinetic energy conservation in the so called "overlapping zone" of the particles was shown in agreement with the analytical results.

The presented electric field calculation scheme can be derived in the same way for Cartesian coordinates in higher dimensions. But although numerical errors due to the particle pusher are reduced, for many particle systems an exact Poisson solver is not ensured.

8 Acknowledgments

This work was supported by the German Space Agency DLR through Project 50 RS 1101. This work of D. Tskhakaya was supported by EURATOM and carried out within the framework of the European Fusion Development Agreement. The views and opinions expressed herein do not necessarily reflect those of the European Commission.

References

[1] R. Hockney and J. Eastwood. Computer simulation using particles. Adam Hilger **1981**

[2] C.-D. Munz, R. Schneider, E. Sonnendrücker et al. A finite-volume particle-in-cell method for the numerical treatment of maxwell-lorentz equations on boundary-fitted meshes. International Journal for Numerical Methods in Engineering, 44 461 **1999**

[3] G. Lapenta. Automatic adaptive multi-dimensional particle-in-cell. Advanced Methods for Space Simulations, p. 61 **2007**

[4] T. WESTERMANN. Localization schemes in 2d boundary-fitted grids. Journal of Computational Physics, 101(2) 307–313 **1992**. doi:10.1016/0021-9991(92)90008-M

[5] C. A. FICHTL. An Arbitrary Curvilinear Coordinate Particle In Cell Method. Ph.D. thesis, Nuclear Engineering, University of New Mexico **2010**

[6] P. COLELLA and P. C. NORGAARD. Controlling self-force errors at refinement boundaries for AMR-PIC. JOURNAL OF COMPUTATIONAL PHYSICS, 229(4) 947–957 **2010**. doi:{10.1016/j.jcp.2009.07.004}

[7] D. TSKHAKAYA, K. MATYASH, R. SCHNEIDER et al. The particle in cell method. Contrib Plasma Phys, 47(8-9) 563–594 **2007**

Contrib. Plasma Phys. **46**, No. 0, 1 – 15 (2007) / **DOI** 10.1002/theDOIsuffix

Electrostatic Ion Thrusters - Towards Predictive Modeling

O. Kalentev[1,*], **K. Matyash**[1,**], **J. Duras**[1,***], **K. F. Lüskow**[1,†], **R. Schneider**[1,‡], **N. Koch**[2,§], **M. Schirra**[3,¶], and **B. van Reijen**[3,‖]

[1] Ernst-Moritz-Arndt Universität Greifswald, D-17489, Germany
[2] Technische Hochschule Nürnberg Georg Simon Ohm, Keßlerplatz 12, D-90489 Nürnberg, Germany
[3] Thales Electronic Systems GmbH, Söflinger Straße 100, D-89077 Ulm, Germany

Received XXXX, revised XXXX, accepted XXXX
Published online XXXX

Key words PIC simulation, High Efficiency Multistage Plasma Thruster, Integrated Modeling.

The development of electrostatic ion thrusters so far has mainly been based on empirical and qualitative know-how, and on evolutionary iteration steps. This resulted in considerable effort regarding prototype design, construction and testing and therefore in significant development and qualification costs and high time demands. For future developments it is anticipated to implement simulation tools which allow for quantitative prediction of ion thruster performance, long-term behavior and space craft interaction prior to hardware design and construction. Based on integrated numerical models combining self-consistent kinetic plasma models with plasma-wall interaction modules a new quality in the description of electrostatic thrusters can be reached. These open the perspective for predictive modeling in this field. This paper reviews the application of a set of predictive numerical modeling tools on an ion thruster model of the HEMP-T (High Efficiency Multistage Plasma Thruster) type patented by Thales Electron Devices GmbH.

1 Introduction

Ion thrusters, where the propellant is ionized and the ions are accelerated by electric fields, are of increasing importance for scientific and commercial space missions. Compared to the commonly used chemical thrusters they have a 5 to 10 times higher specific impulse [1]. This results in a considerable reduced propellant budget such that a significant reduction of spacecraft launch mass by some 100 to $1000kg$ can be achieved.
The most straightforward concept of an electric propulsion system is the grid thruster. Here, gaseous propellant is ionized in a low pressure, low temperature gas discharge sustained by DC, radio-frequency or microwave fields, respectively. A biased grid at the thruster exit accelerates and extracts the produced ions. Since ionization and acceleration occurs independent of each other, it is possible to optimize these two processes separately. This yields a high efficiency of the device but also a huge system complexity. Therefore ion propulsion systems based on grid thrusters tend to be expensive and to exhibit reliability issues [2].
An alternative are grid-less ion thrusters which are based on magnetic confinement of the plasma electrons, where the trapped electrons both ionize the propellant and provide the potential drop for ion acceleration. Due to their low complexity in therms of system architecture they are becoming of increasing interest in particular for commercial satellites. In order to achieve reduced development and qualification effort, it is therefore needed to set up and apply a series of different modeling tools which can quantitatively describe the plasma physics within the thruster but also interactions of the thruster with the testing environment and finally the satellite. The integrated modeling strategy should include several modular components in a consistent way in order to provide

* Corresponding author E-mail: kalentevo@uni-greifswald.de, Phone: +49 (0)38 348 61447, Fax: +49 (0)38 348 614 01
** E-mail: knm@ipp.mpg.de
*** E-mail: durasj@uni-greifswald.de
† E-mail: kl081737@uni-greifswald.de
‡ E-mail: schneider@uni-greifswald.de
§ E-mail: Norbert.Koch@th-nuernberg.de
¶ E-mail: Martin.Schirra@thalesgroup.com
‖ E-mail: Benjamin.Reijen@thalesgroup.com

the necessary complexity and accuracy depending on the problem. As an example, results for the grid-less High Efficient Multistage Plasma Thruster (HEMP-T) model DM3a are presented. The outline of the paper is the following: after a general introduction of the HEMP-T the general strategy for predictive modeling is presented. The characteristics of HEMP-T as deduced from 2D Particle-in-Cell (PIC) calculations are reviewed. A first example of 3D PIC results for self-consistent modeling of electrostatic turbulence in a HEMP-like geometry is given. Strategies and results for the simulation of the interaction of the thruster with the satellite in the plume and results on erosions are discussed afterwards, before the paper is summarized in the conclusions.

2 The High Efficient Multistage Plasma Thruster (HEMP-T)

An ion thruster design which has the advantage of an electric field topology similar to grid thrusters at significant reduced thruster complexity is the High Efficient Multistage Plasma Thruster (HEMP), patented by the THALES group in 1998 [3]. As described in [1], HEMP-T's consist of a dielectric, rotationally symmetric discharge chan-

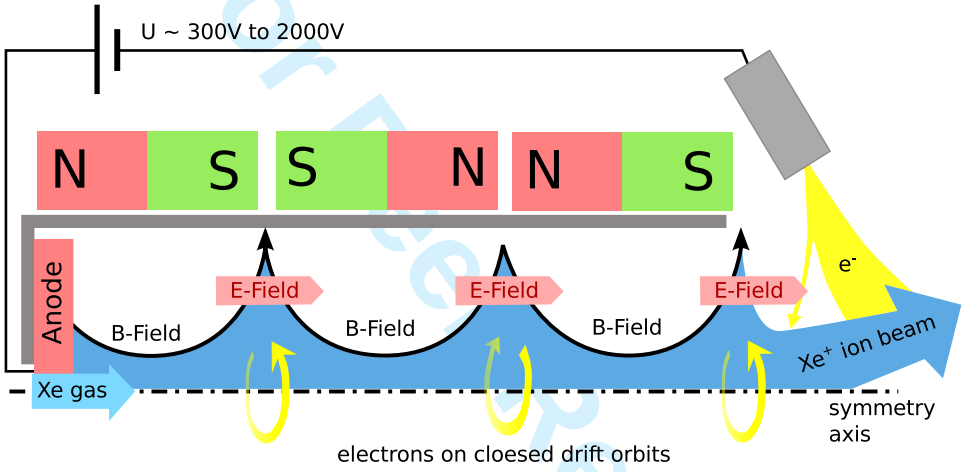

Fig. 1 Schematic view of the High Efficient Multistage Plasma Thruster (HEMP).

nel at the upstream end of which an anode is located. The anode is connected to the power supply and represents the only high voltage electrode in the thruster; it also serves as inlet for the propellant. The discharge channel is surrounded by a system of axially magnetized permanent magnet rings in opposite magnetization, the so-called PPM system. At the downstream end of the discharge channel, the thruster exit, a hollow cathode neutralizer is placed to provide the starter electrons for igniting the discharge and for neutralizing the ion beam emitted by the thruster. A schematic picture of the HEMP-T concept as described above is given in Fig. 1. The PPM system forms a linear magnetic multi-cusp structure inside the discharge channel. The magnetic field periodically changes between predominant axial and predominant radial direction. The level of magnetic induction B at any position within the thruster channel is chosen such that the Larmor radius of the electrons is much smaller than the geometrical dimensions of the discharge channel, whilst the propellant ions are hardly affected by the magnetic field due to their much higher mass. The gradients fulfill $\frac{dB_z}{dz} > 0$ in the axial zones and $\frac{dB_r}{dr} > 0$ in the radial zones, where in addition a strong gradient $\frac{dB_r}{dz}$ is build up. In this way the plasma electrons are efficiently confined along the entire discharge channel and only few electrons are lost to the wall mostly at the cusps. Electron confinement due to cusp mirror oscillations is dominant compared to the Hall current which builds up due to the $E \times B$ drift.

In this work an older prototype model named DM3a is discussed. It has implemented two cusps, the anode and the exit cusp and is described in [4]. In the HEMP thruster the ionization is particularly strong at the cusps regions. Due to the strongly reduced plasma wall contact in the cusp regions and mean energy of impinging ions at these locations below the sputter threshold, HEMP is characterized by a long lifetime of at least $10.000h$ [5].

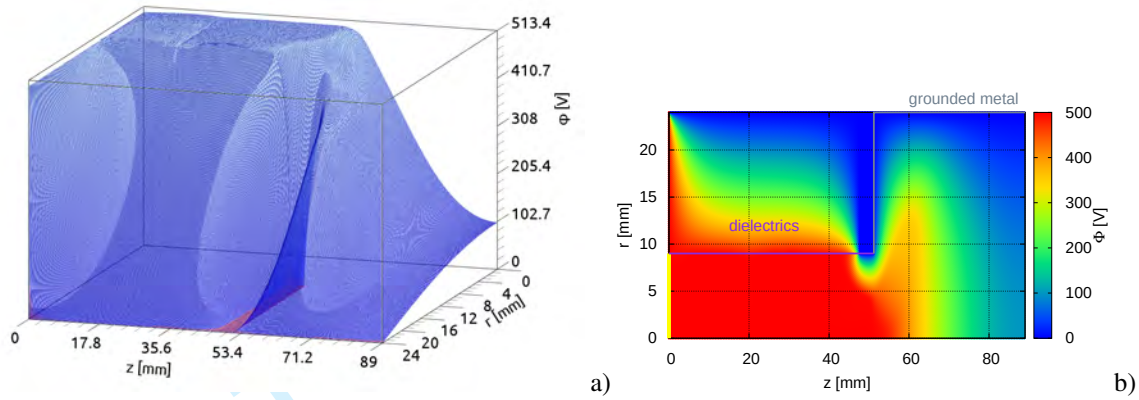

Fig. 2 Potential of the HEMP DM3a thruster with a channel radius of $R = 9mm$ and $L = 51$ length. The anode volatege is set to $500V$. Plotted as a **a)** 3D plot and as a **b)** potential profile.

Potential, densities and plasma species temperatures of the DM3a were calculated with an electrostatic 2d3v Particle in Cell code with Monte Carlo collisions (PIC MCC) [6]. PIC MCC is a simulation method, used for low temperature plasmas [7], [8]. It gives a fully self-consistent microscopic description of a plasma and is able to involve complicated atomic and plasma-surface interactions. In the PIC-MCC simulation we follow the kinetics of so-called Super Particles (each of them representing many real particles), moving in the self consistent electric field calculated on a spatial grid from the Poisson equation. The particle collisions are handled by Monte-Carlo collision (MCC) routines, which randomly change particle velocities according to the actual collision dynamics. All relevant collisional processes are included in the model: electron-neutral elastic, ionization and excitation collisions, ion neutral momentum-transfer and charge exchange collisions. The dynamics of the background neutral gas is self-consistently resolved with direct simulation Monte Carlo. For a reliable plasma simulation, effects on the smallest length scales in a plasma, the Debye-scale $\lambda_{D,e}$ have to be resolved. Therefore, the smallest lateral grid size is $\Delta x = 0.5\lambda_{D,e}$. The simulation has to resolve the fastest process in the system - the electron Langmuir oscillations. Therefore, the time step in the simulation is chosen $dt = 0.2/\omega_{pe}$, where ω_{pe} is the electron plasma frequency. A more detailed description of PIC can be found in [8]. An important ingredient for speeding up the 2D PIC calculations is the use of a similarity scaling [6]. A typical value of the scaling factor is 0.1. Scaling is particularly well applicable for the HEMP-T concept because of the negligible wall effects due to the efficient magnetic plasma confinement.

In Fig. 2 the potential as calculated with an electrostatic 2D PIC code is shown. For the HEMP thruster the potential in the plasma bulk is nearly constant with a steep drop at the thruster exit producing a narrow peak in the ion energy spectrum a high specific impulse. Close to the axis, the mainly axial magnetic field allows the electrons to flow along the electric field. A small perturbation of the electric potential is therefore quickly compensated by fast electrons. The inner surface of the channel walls are made of Boron Nitride based ceramics. Near the thruster walls, the potential is decreasing forming the electrostatic sheath. The maximum potential drops are located at the cusps, where magnetic field is perpendicular to the wall.

The influence of the plasma sheath can also be seen in the electron density in Fig. 3. The electron density is uniformly decreasing towards the channel walls and the cusp regions are clearly visible. The higher electron density in these regions due to electrons confined at the radial magnetic field at cusps can be seen. The transfer of energy from directed into thermal motion heats the electrons [9]. Thus, the density of the electrons in the cusp regions is high and the ionization can take place efficiently. For the HEMP thruster the electron source provides the primary electrons, which defines the operational point for the thruster due to the very strong amplification of it by ionization inside the thruster. The direct connection of anode and exit region close to the axis allows ignition of the thruster even without external source by some free electrons. These electrons can be created e.g. by cosmic radiation and will be accelerated to anode potential starting the ionization avalanche [10]. To characterize the basic physics of HEMP-T the velocity distribution functions resolved spatially along the thruster

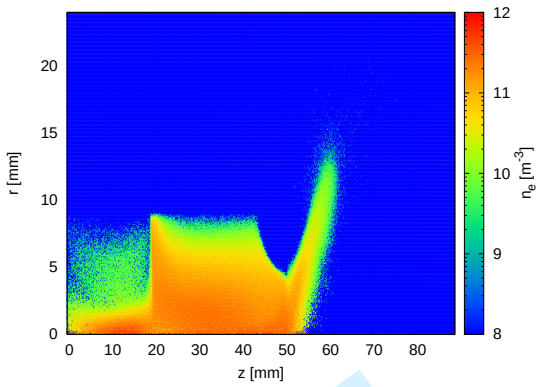

Fig. 3 Electron density profile of the HEMP DM3a thruster.

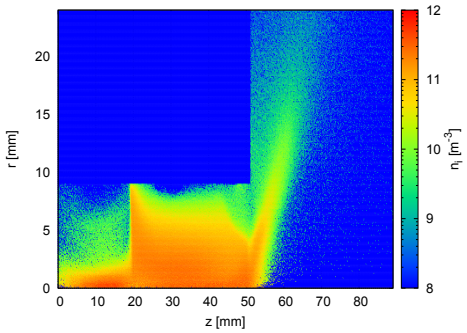

Fig. 4 Ion density profile of the HEMP DM3a thruster.

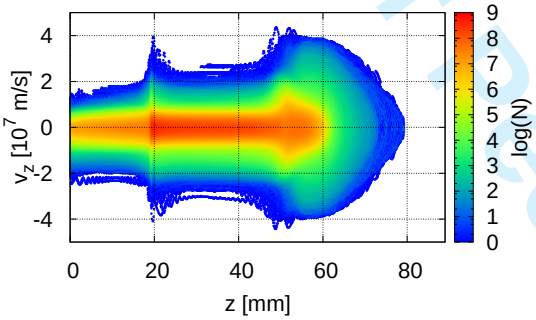

Fig. 5 Electron axial velocity distribution function for $r < R_{thruster}$ as a function of the axial position z

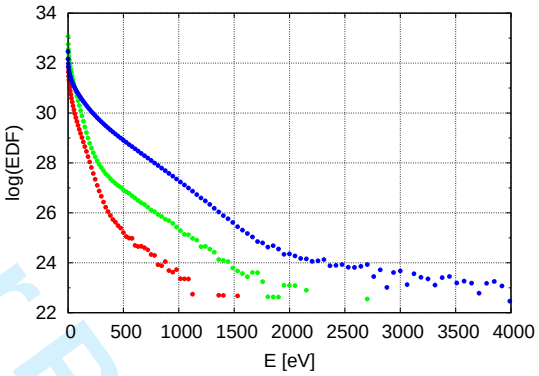

Fig. 6 Electron energy distribution function at different axial positions $10\,mm$ (red), $35\,mm$ (green) and $51\,mm$ (blue)

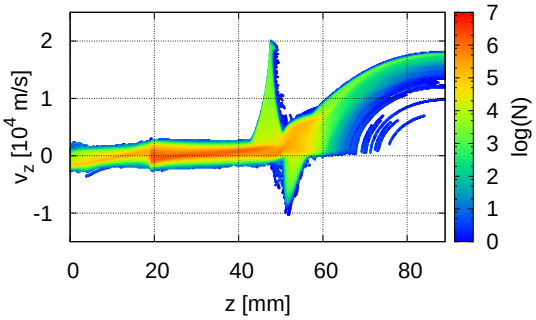

Fig. 7 Ion axial velocity distribution function with $r < R_{thruster}$ as a function of the axial position z

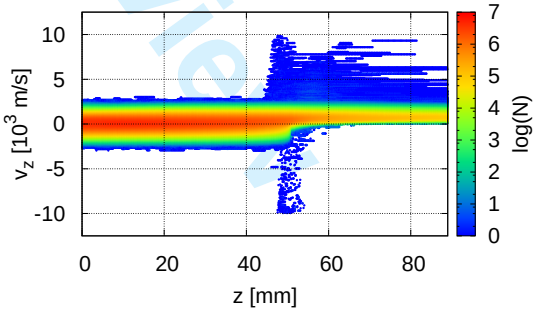

Fig. 8 Distribution of velocity in axial direction for neutrals for $r < R_{thruster}$

axis and averaged in radial direction were calculated. All velocity distribution functions (Fig. 5, 7 and 8) are temporally averaged over 10^6 time steps of a quasi steady-state run. In Fig. 5 the axial velocity distribution function of electrons is plotted. Electron energy distribution functions at different locations are shown in Fig. 6. The distribution functions in the channel are non-Maxwellian, because the mean free paths for electron Coulomb collisions is much longer than the electron path in the system. The axial velocity distribution function shows that the electron axial energy is much higher in the regions about $z = 20\,mm$ and $z = 51\,mm$, since electrons are heated at the cusps. Outside the cusps the velocity distributions are nearly identical within the channel.

The ion density profile is and the corresponding distribution function of the axial velocity are shown in Fig. 4 and 7. Within the channel all ions have rather low velocities due to the nearly constant potential profile. Only at the exit they are accelerated by the strong potential drop. Near the exit cusp and in the plume ions with high energies are existing. The first peak in the distribution at $z = 48\,mm$ with velocities up to $20000\,m/s$ can be explained by the grounded wall after the dielectrics. The right side of the potential structure at this position is very steep and creates a region with large positive velocities. The boundary of this structure is a direct consequence of the potential structure in this region as shown in Fig. 2, because after the grounded wall the potential rises again and ions are slowed down by the counter-acting electric field. Close to the exit cusp inside the channel there are many ions with low velocities. At the exit cusp and afterwards they are accelerated, seen by the shift of the orange color to higher velocities. This acceleration is a consequence of the steep potential drop at the exit. In this acceleration region the ion density decreases. Most of them escape from the region due to their high velocity in radial direction. Further ions are accelerated until the grounded end of the computational domain, due to the continuous drop of the potential. Some of them reach a velocity of about $18000\,m/s$. This explains the trend to higher velocities in Fig. 7 beginning at the exit cusp at $51\,mm$ up to the end of the domain. This structure looks like a quarter of a circle in the velocity distribution function. This is close to a motion with constant acceleration, where the velocity is proportional to the square-root of the distance. Ions are also scattered into the side part of the plume by charge-exchange collisions, where so-called wings can build up.

In Fig. 8 the axial velocity distribution function for neutrals is presented. One can see that charge exchange collisions have an impact on the velocity profile of neutrals. They couple the neutrals to the ions and are responsible for similarities in both distribution functions. Apart from the high-velocity wings the distribution looks quite more regular, since the neutrals are not affected by the magnetic or electric field. Most of the neutrals in the channel have velocities in the range of $-2000\,m/s \ldots 2000\,m/s$, equally distributed in positive and in negative direction. This is again a result of the large neutral density there and their relative low temperature. In the plume the situation for neutrals is different. Neutrals are only flying out of the thruster and negative velocities are not detected.

3 Modeling strategy

The most complete model resolving all time scales would be a direct coupling of a kinetic plasma model with a molecular dynamics model for the walls. This would allow a fully self-consistent analysis of the complete system including plasma dynamics, possible erosion of thruster walls and interaction of the exhausted ions with surrounding satellite surfaces or, during test and qualification, with the testing environment, like the vacuum chamber walls, respectively. Such a solution is not possible due to the tremendous computational costs and high complexity of this combined model. Instead, we propose to use a hierarchical multi-scale set of models in which the parametrization for a lower hierarchy model can be deduced from a higher one (see Fig. 9). For example, a 3D particle-in-cell (PIC) model can deliver a parametrization of turbulence effects by appropriate anomalous transport coefficients. A first proof-of-principle example of a 3D PIC code with a simplified geometry will be presented in section 4. Transport coefficients based on such runs could then be used in a 2D PIC, which is more practical for production runs.

Furthermore, separating the analysis of the thruster from the plume is not adequate, because there exist a strong coupling between thruster and plume plasma. Due to strongly non-Maxwellian characteristics of the distribution functions of both electrons and ions it is not possible to keep any of them in a fluid representation. To get a correct description of both thruster and plume plasma one has to solve a kinetic problem for the whole region of interest including all significant physical processes. These are collisions, turbulence effects, surface driven sheath instabilities and breathing modes. That is why the choice of a PIC model is a natural one for such a problem. In addition, a similarity scaling is applied to further reduce the calculational costs [6].

However, despite the scaling, it is not possible to have a uniform grid for the whole region (thruster and plume) due to extremely different plasma conditions and also physical dimensions of both parts. Therefore, using an equidistant grid will lead to unacceptable grid sizes in terms of computational costs. A possible strategy for the plasma model is a 2D PIC model with a hierarchical grid (see section 5).

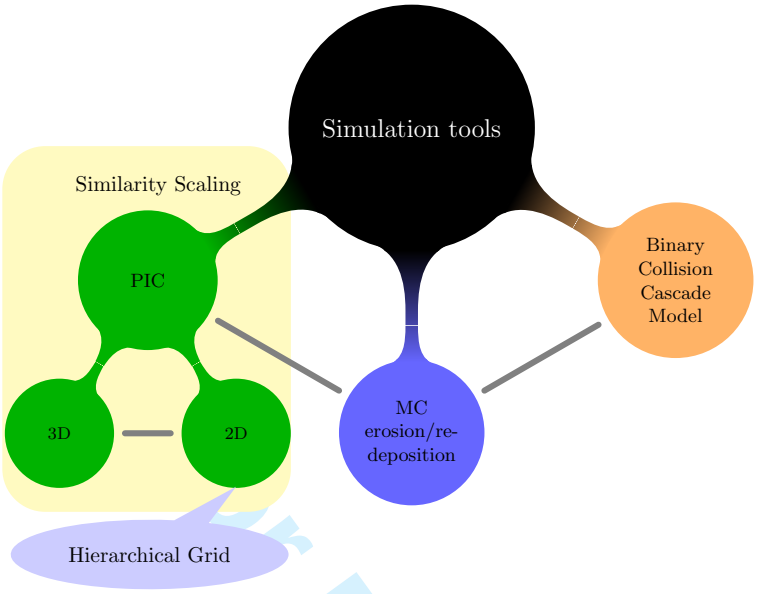

Fig. 9 The concept of a multi-scale modeling for combined thruster-plume models

In order to describe erosion-redeposition processes one can use different approximation levels of the model. The most thorough description is given by the full molecular dynamic model, which would be far too time-consuming because it resolves all individual atoms and their interactions. Next level can be represented by the binary collision cascade model assuming an amorphous target and the interaction of particles with the solid based on heavy particle collisions with ions and additional losses with electrons acting as viscous force. Such a model can use the detailed information about flux distributions provided by the PIC code and calculate then based on this the erosion response of the materials. The most crude approximation is given by a Monte-Carlo (MC) procedure simulating erosion-redeposition based on sputter yield tables calculated from the binary-collision cascade or molecular dynamics model together with the information about plasma fluxes. This model is particular useful due to its simplicity and flexibility allowing to quantify the life time of ion thrusters (see section 6).

4 Anomalous diffusion of electrons

In Hall effect thrusters a radial magnetic field is applied to confine the electrons in the thruster channel and to create the accelerating potential for the ions. The axial electron current towards the anode is possible only because of presence of some diffusion process. There are two major diffusion processes responsible for the electron current across the magnetic field. Classical diffusion due to collisions with neutrals and anomalous diffusion due to azimuthal fluctuations of the electric field.

In classical diffusion, the diffusion coefficient D is proportional to the square of the mean free path λ_{mfp} and one over the average time τ between two collisions

$$D \propto \frac{\lambda_{mfp}^2}{\tau} \quad . \tag{1}$$

Due to the gyration of the electrons, the mean free path in a plasma with an external magnetic field is its Larmor radius $r_{L,e} = \frac{|\vec{v}_{\perp,e}|}{\omega_{c,e}}$. For a strong magnetic field with $\omega_{c,e}\tau >> 1$, the diffusion coefficient due to neutral scattering is given in [11] as

$$D_\perp = \frac{k_B T_e}{m_e \tau \omega_{c,e}} \propto \frac{\vec{v}_{th,e}^2}{v_{\perp,e}^2} \frac{r_{L,e}^2}{\tau} \propto \frac{1}{B^2} \quad . \tag{2}$$

While the Larmor radius is proportional to $1/B$, the diffusion across the magnetic field scales with $1/B^2$. While for diffusion along magnetic field lines collisions are decreasing the mean free path and thus the collision coefficient, here collisions are necessary, therefore $D_\perp$ is proportional to the collision frequency $\nu = 1/\tau$. But in many experiments on the magnetized plasmas, the contribution of classical diffusion is not sufficient to explain the measured electron transport across the magnetic field lines [12]. Another kind of diffusion is the so-called "anomalous" or Bohm diffusion, which is due to electron scattering on the fluctuations of the perpendicular electric field. While in many $E \times B$ experiments $D_\perp$ scales with B^{-1} rather than with B^{-2}, a semi empirical formula was proposed by D. Bohm, E. Burhop, and H. Massey, with a diffusion coefficient [13]:

$$D_\perp = \frac{1}{16}\frac{k_B T_e}{eB} = D_B \quad . \tag{3}$$

A general derivation for $D_\perp \propto B^{-1}$ for this kind of diffusion was given by L. Spitzer in 1960 [12], with

$$D_\perp = 2(K_1 K_2)^2 K_3 \cdot \frac{k_B T_e}{eB} \quad . \tag{4}$$

$K_1,\ K_2,\ K_3$ are empirical constants, determining the strength of the electron perturbation perpendicular to the magnetic field.

To study anomalous diffusion in the HEMP thruster, a three dimensional electrostatic PIC code is used. Because the calculation is extremely time consuming, only a proof-of-principle for studying anomalous transport in a HEMP-like geometry was possible. The HEMP thruster has a cylindrical volume. But in a PIC simulation a cylindrical grid causes self forces. To avoid that, a Cartesian grid is chosen. The HEMP model is set up as a cuboid, based on a Cartesian grid. To be able to obtain a solution in a reasonable run time (one week), the size of the system is scaled down by a factor of 50. In order to preserve the ratio of the charged particles mean free paths and the gyroradii to the system length, the neutral Xenon density and the magnetic field are increased by the same factor 50 [6]. The simulation domain has a height and width of $L_x = L_y = 23mm$, a length of $L_z = 130mm$

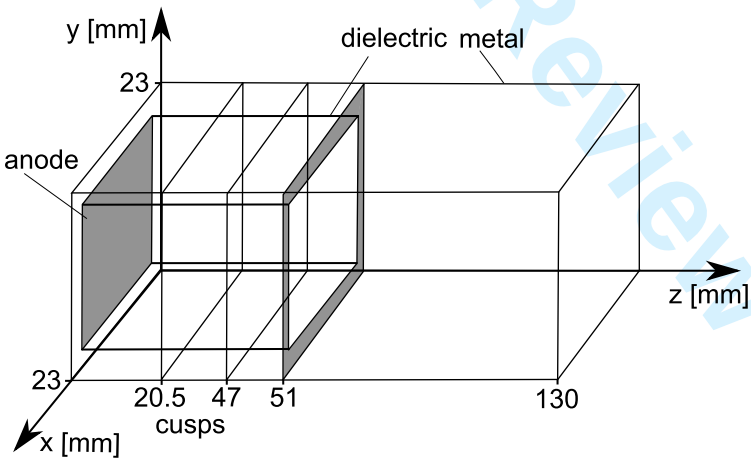

Fig. 10 Schematic view of the computational domain for a HEMP-like thruster model.

and includes the thruster channel as well as the plume region, as shown in Fig. 10. The thruster exit is positioned at $z = 51mm$ and the two cusps at $z = 20.5mm$ (anode cusp) and $z = 37mm$ (exit cusp). The channel walls consist of boron nitride based ceramics. The external domain boundaries consist of metal walls with a potential of $\phi = 0$. The anode voltage, applied at $z = 0mm$ is set to $500V$. Particles which are hitting the metal as well as the dielectric boundaries are absorbed. In the thruster channel, these particles are contributing to the local surface charge. To identify anomalous diffusion driven by turbulence, no secondary electron emission was implemented. For the neutral xenon atoms, the density profile was prescribed by an exponential profile $n_n = n_n exp\{-Z/L\}$, with $L = Z_{max}/2.5$ and $Z_{max} = 65mm$. Such density profile is close to the one obtained from self consistent

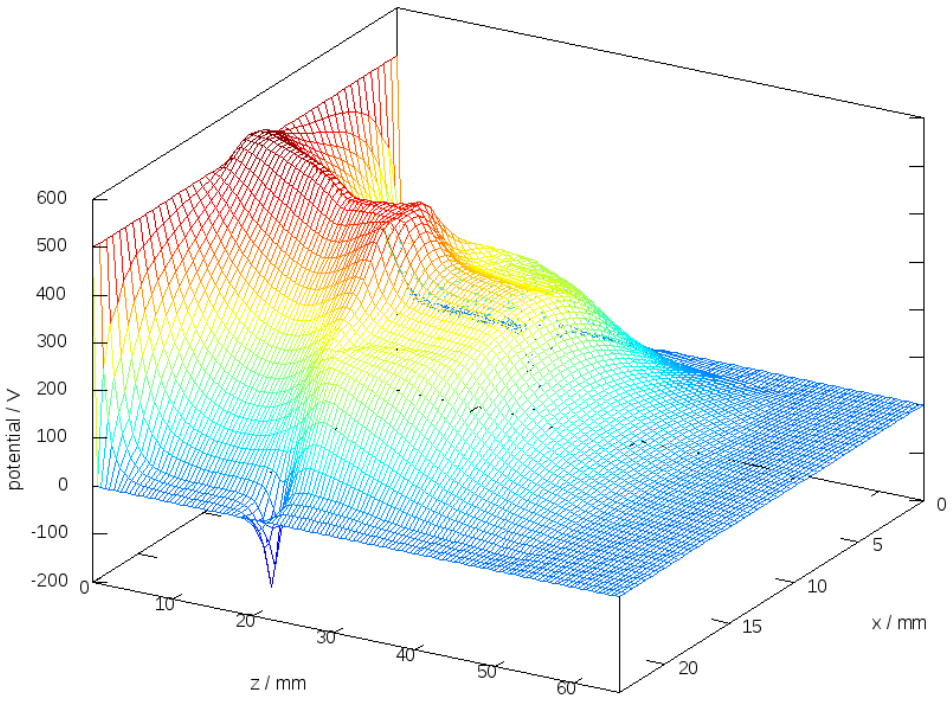

Fig. 11 Plasma potential of a HEMP thruster model, simulated with a 3D Cartesian PIC code, plotted along the y-axis of at $y = 15.5mm$.

models in 2D.

In the following, the three dimensional data is shown in two dimensional cuts. In Fig. 11 a profile of the plasma potential along the y-axis, for $y = L_y/2$, is shown. One can see that the potential has a step-like shape in the z-direction, which is caused by the two cusps. The potential shape is in overall agreement with the 2D results: the main potential drop occurs at the exit cusp, as shown in Fig. 2. At $z = 20.5mm$, the potential gets negative at the wall. This is the anode cusp region, where the magnetic field lines are perpendicular to the wall. The second cusp region can be identified by a potential plateau in the magnetic bottle between $z = 23 - 37mm$.

In Fig. 12 the potential in this cusp is shown in the x-y-plane. The variation of the potential is not purely radial. One can identify a $n = 1$ azimuthal mode at about $R = 3mm$ and a $n = 2$ mode at about $R = 7mm$ with an amplitude of electric field $E \approx 100V/cm$. These fluctuations of the azimuthal electric field are responsible for the anomalous electron transport across the cusps in the simulation.

The electron density is shown in Fig. 13 and 14. The density profile for $y = L_y/2$, Fig. 13, shows a large electron density at the anode ($z = 0$) and at the anode cusp ($z = 20.5$). The density drop between the two regions is due to the electron transport along magnetic field lines. At the exit cusp, practically no electrons can be found, because it is not yet filled with charged plasma particles due to run-time limits of the code. Due to that, no negative wall potential for the exit cusp can be seen in Figure 11. In Fig. 14, the electron density in the x-y-plane at the anode cusp $z = 20.5mm$ is shown. A high electron density in the enter of the model can be seen. Similar to the potential, stretching and compression along the diagonals is visible.

Estimation of the anomalous diffusion coefficient, caused by the fluctuations of the azimuthal electric field following the approach suggested in [12] gives

$$D_\perp \propto 0.4 \cdot \frac{kT}{eB}$$

which is in the order of magnitude of the diffusion coefficient given by Equ.(3). One has to mention, that the presented calculation is only a rough estimate, because of the large scaling factor used in the simulation.

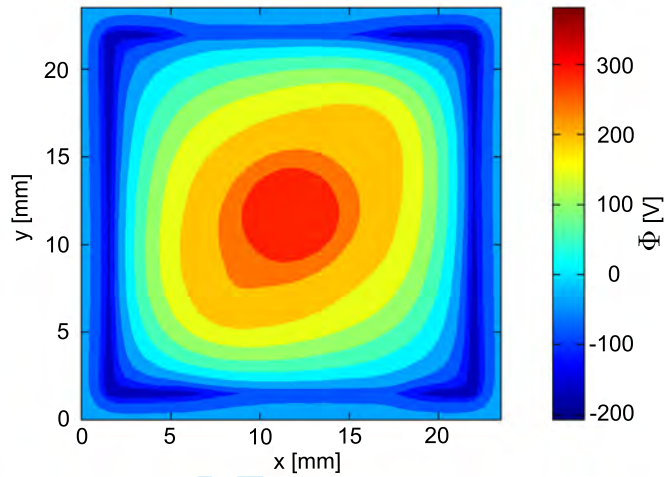

Fig. 12 Plasma potential of a HEMP thruster model in the $x-y-$plane at the cusp region $z = 20.5mm$.

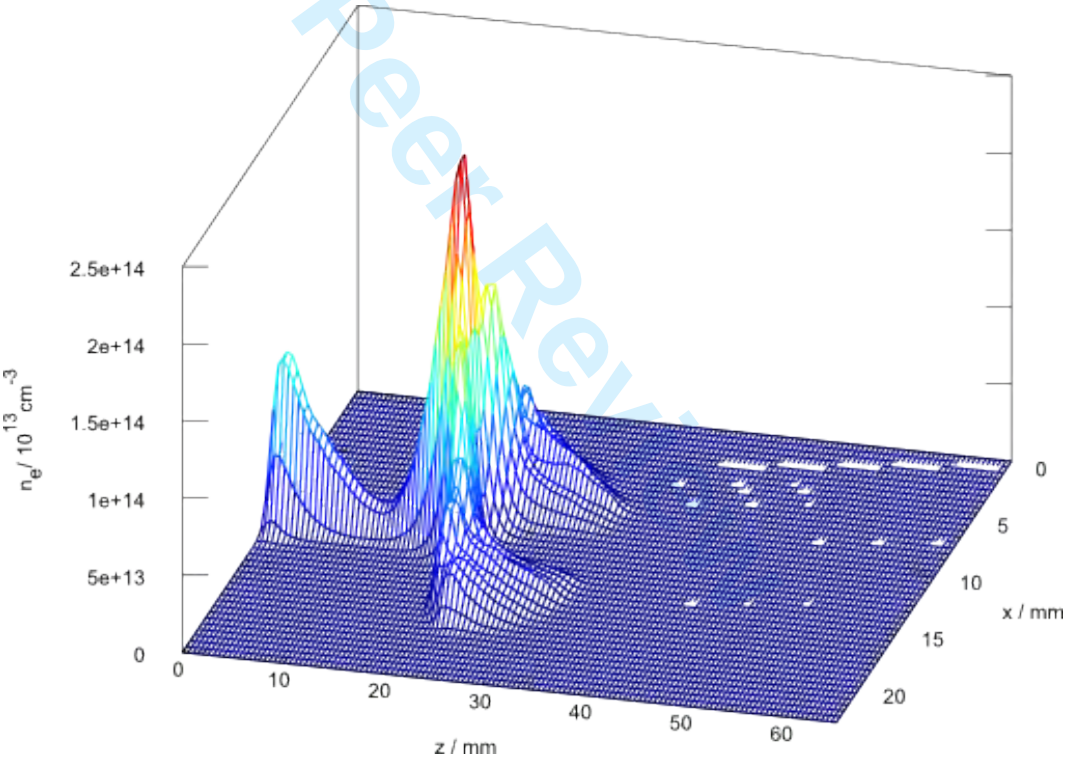

Fig. 13 Electron density along the y-axis of a HEMP thruster model at $y = 15.5mm$.

Due to the geometrical characteristics of the HEMP-T with large parts where the magnetic field is essentially axial and only small zones of radial fields at the cusps, the anomalous transport is only important at the cusps. Here, the anomalous diffusion allows the electrons to overcome the radial magnetic field and to fill the region between cusps. In the region of axial fields the parallel transport along fieldlines dominates. This is different to Hall thrusters, where in the whole acceleration channel the radial magnetic field is applied and the thruster characteristics is determined by anomalous electron transport. As a consequence modeling optimization with a 2D code of HEMP-T is possible, because classical transport dominates.

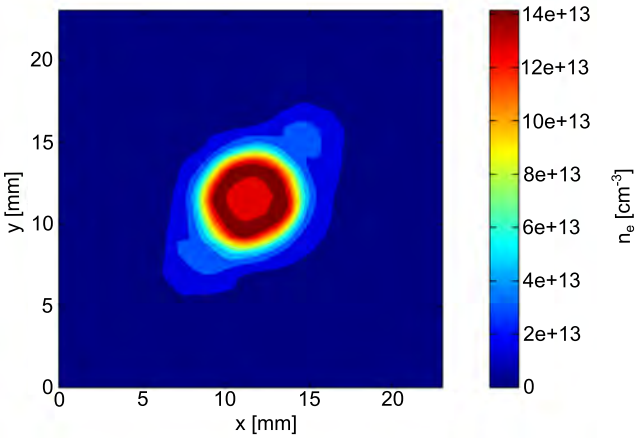

Fig. 14 Electron density of a HEMP thruster model in the $x-y-$plane at the cusp region $z = 20.5mm$.

5 Plume modeling

Up to now, either fluid or hybrid models (with kinetic ions) are used for the plume modeling. However, the plasma in the acceleration channel is already non-Maxwellian [14]. The mean free paths of particles in the plume of about $\sim 10\ m$ does not allow a relaxation of the distributions to a Maxwellian in the plume region. Therefore, a correct model of the plume plasma has to be kinetic. Unfortunately, the well-established Particle-In Cell (PIC) method is momentum conserving and free of artificial self forces only in the case of equidistant meshes [8]. This means that a self-consistent PIC model for an ion thruster including the full plume plasma has to resolve the smallest length scale (usually the Debye scale at the largest electron density inside the thruster) and the fastest time scale (usually the plasma frequency at the largest electron density inside the thruster). A typical thruster size is about $10\ cm$ whereas the typical size of interest for a plume is $1\ m \sim 10\ m$. Electron density inside the thruster is about $\sim 10^{13}\ 1/cm^3$ and for such a density $\lambda_D = 7.43 \cdot 10^{-4}\ cm$ for $T_e = 10\ eV$. In the plume plasma density drops exponentially, such that on a distance of $\sim 5\ cm$ from a thruster nozzle it is around $\sim 10^{10}\ 1/cm^3$ which results in $\lambda_D \sim 10^{-2}\ cm$. This allows only small domains for the plume due to computational time restrictions [6]. Such small domains suffer from the strong influence of the solution from the boundary conditions at the end of the plume, which can lead to results that are not consistent with experimental data, especially in terms of angular ion distribution functions. Fig. 15 demonstrates the influence of boundary conditions on a potential solution in the near-plume region. In addition, non-linear coupling of a plasma inside the thruster with the plume part may influence the operational regime of the thruster, including currents, density distributions and thrust.

The presented method uses a ”matryoshka-like” hierarchy of equidistant grids with different cell sizes. The hierarchy is constructed such, that the most dense grid covers only the thruster and the near-plume region; the next level with a cell size of $2 \sim 4$ times larger extends further to capture more of the plume and so on. Thus, the thruster and the near-plume region is covered with all grids and the most distant from the thruster regions are covered only by the most coarse grid. Furthermore, the density of the charged particles is gathered in all grids independently. The Poisson equation is solved one by one starting from the most coarse and finishing the most dense grid such, that the boundary values for the next level are taken from the coarser mesh obtained on the previous step. Such an approach appears to be not only accurate enough, but also remarkably fast compared with the solution for a single non-equidistant mesh. Such a fast solver is possible due to two reasons. First, the matrix which one gets after the discretization of the Poisson equation for an equidistant grid has a block structure. Such a structuring can be used by specialized solvers, for example [15] or [16]. And second, for such a single mesh one has a larger matrix to solve, rather then for the case of ”matryoshka-like” grids.

However, non-equidistant grids suffer from artifacts [8], like self-forces, and corrections to minimize such errors are needed. To overcome this, a modified two point central difference scheme for calculation of the electric field on non-equidistant grids is implemented [17].

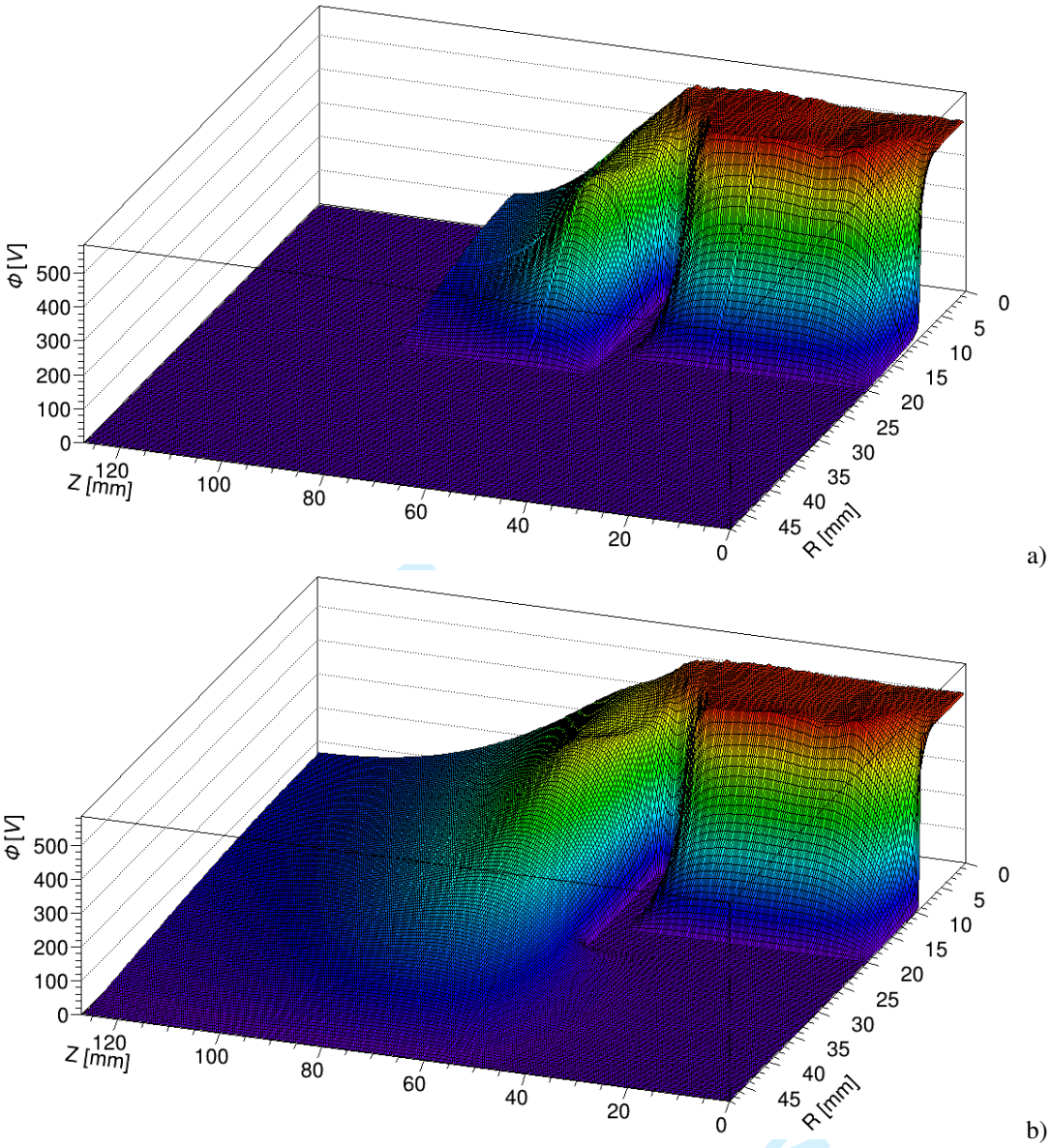

Fig. 15 Influence of boundary conditions on a potential solution for **a)** a small and **b)** a large simulation domain.

6 Effects due to impinging ions

Ions created in the thruster discharge may impinge surrounding surfaces which can induce sputter erosion and re-deposition of eroded material. Depending on the surface region this may affect operational and performance characteristics of the thruster itself, of the ion thruster module or even of the whole satellite, respectively. For the simulation one can distinguish:

a) Impact on inner thruster surface by ions generated in the inner thruster discharge.

b) Impact on exit-sided surface of the thruster and the neutralizing electron source by ions generated in the plasma plume downstream the thruster exit.

c) Impact on satellite surface producing erosion and re-deposition.

d) Impact on vacuum chamber walls during testing and life-time qualification creating redeposition onto thruster and thruster module surface.

The proposed multi-scale modeling strategy is well suited to address the above mentioned ion impingement effects. A good approximation of a plasma surface interaction are binary collisions between the impinging ion, which gets neutralized next to the surface, and the target atoms, producing collisional cascades in the solid. When a part of the collided particles get enough energy to leave the surface, the target emits them as sputtered particles. Sputtered particles are impurities in a plasma, values of sputter yields are important for plasma experiments and simulations. A tool for simulating binary collisions in matter is the SD.Trim.SP (Stationary/Dynamic Transport of Ions in Matter, with the calculation mode Serial or Parallel) code.

The SD.Trim.SP computer program simulates sputtering, backscattering and transmission effects of ion bombarded material and can additionally take the modification of the target into account, when it runs in the dynamic mode. It applies the Monte-Carlo Binary Collision Approximation (BCA) and assumes therefore an amorphous (randomized) material with a infinite lattice size and a temperature of $0K$. In SD.Trim.SP the particle movement in matter is approximated as a series of inelastic binary collisions between atoms, the BCA and a continuous friction, to simulate the interactions of moving atoms with electrons. For additional information about the use of SD.Trim.SP, see [18]. The domain of SD.Trim.SP, is a one dimensional simulation space, where the Cartesian x-component is perpendicular to the surface. Also two dimensional simulations are possible A negative x-component indicates the space above the surface, while a positive one shows the position in the solid. Also layers of different materials can be implemented. SD.Trim.SP in static mode proceeds in the following way. At first a projectile is initialized with the kinetic energy E_0 and the direction $\vec{r_0}$. After a distance of λ, a collision partner is determined by the stochastic choice of an impact parameter p. While SD.Trim.SP assumes an amorphous structure of the material, no lattice structure has to be taken in account and therefore λ and p are determined by their distribution functions given by the BCA. Both are implemented with inverse Monte-Carlo sampling. The azimuthal angles between two collisions are chosen randomly between $[0; 2\pi]$. The BCA gives the energies of the particles after the collision and the scattering angle ϑ_1 as well as the recoil angel ϑ_2, which are determining the new direction of the projectile and the target atom. The energy loss of atoms traveling through matter, due to interactions with electrons, is simulated as a continuous friction in between two collisions. Three scenarios are possible for each particle. If the energy is smaller than the binding energy of the matter $E < E_b$ the particle sticks and is not followed any more. If $E > E_b$ and the particle is close enough to the surface, it gets emitted as a sputtered atom and is also not followed any more. In the third case the particle moves through the matter and produces a collision cascade through several collisions, proceeded as described above. Reflection at the surface is realized with different binding energies for particles coming from inside or outside the target. To determine the dynamics of the target thickness, SD.Trim.SP has a dynamic mode. Here, the material is resolved one dimensional and the target is segmented into slabs. These slabs have an initial thickness, which changes during the calculation due to collisional transport. For many particles, the calculation as well as the memory occupation of every collisional cascade becomes very costly. Therefore, for large fluence pseudo particles which are representing a number of real particles are introduced to minimize the numerical costs. For an entire dose of Φ_0 the material should be exposed with, pseudo particles with a differential fluence of $\Delta\Phi = \Phi_0/N_d$ are followed in N_d simulation steps. Moreover, the physical sputter yield rapidly decreases for energies lower than a threshold energy E_{thr}.

Although the coupling of the BCA and the PIC models is promising in terms of analyzing erosion of a thruster during its operation, it is in practice inapplicable for other above mentioned tasks (c and d). That is why a Monte-Carlo model, which uses sputter yield tables pre-calculated with a binary collision cascade model is developed [18]. Coupling the plasma model with this erosion module an integrated model can be set up. The plasma fluxes impinging on the walls from PIC are used in a Monte-Carlo procedure for erosion re-deposition simulations, where the erosion fluxes are determined from the tables. Application of this model is discussed in [19].

A terrestrial qualification of a thruster has a significant difference from outer space exploitation in that it is held in a limited vessel, which can create different artifacts on the measured thruster properties. For example, the back scattered flux from vessel walls can be deposited on the walls of the thrusters and by that create a conducting layer influencing the thruster operating regimes. The quantitative characterization of such an influence is possible by means of a self-consistent coupling between the PIC code modeling of the plasma and the Monte-Carlo (MC) erosion-deposition code modeling of erosion of the thruster walls due to plasma-wall interaction and of deposition

of the eroded particles both from vessel and thruster walls. Due to large size difference of a thruster and a vessel it is possible to parametrize the back-scattered flux from vessel walls as an effective source for the MC erosion-deposition code. The primary distribution of ions with respect to energies, angles and species is specified and pseudo-particles are followed interacting with the vessel walls. Hitting a wall, based on sputter rates calculated by a binary collision cascade code, the back-flow of eroded particles from vessel walls towards the ion thruster acceleration channel is calculated [20]. In case of metal walls large erosion is appearing, whereas for carbon walls much smaller physical sputtering happens. However, in the case of carbon the release of hydrocarbons is a major problem linked to the sponge-like characteristics of carbon with respect to its interaction with hydrogen. This means that every time the vessel is opened a large amount of hydro-carbons are created due to the interaction of air with carbon. Due to the porous structure of graphite air molecules can diffuse quite deep into the bulk of such graphite tiles and produce there hydro-carbons. The ions bombarding these tiles release this large reservoir and create back-flow to the thruster. Co-deposited layers of hydro-carbons are created in the acceleration channel. These layers are getting conductive hence changing the potentials and produce sub-sequent problems. The result is a different performance of the thruster in the vessel compared to the one in space. Using instead of carbon metal walls the rates of physical sputtering are larger, but the evaporation at hot channel parts will prevent deposition inside the thruster.

Strategies to overcome this limitations by additional baffles are studied with the help of the Monte-Carlo erosion code. In Fig.17 the influence of a baffle on the back flow towards the thruster channel is sketched. Particles, accelerated by the thruster, impinge on the vessel walls and sputter its surface. Due to micro roughness of the surface, the distribution function of the sputtered particles follows a cosine function [21]. Its orientation is mainly vertical to the surface, but nearly independent on the incident angel of the accelerated particles. For baffles tilted away from the thruster, this cosine distribution results in a reduced amount of back-scatted particle towards the thruster channel.

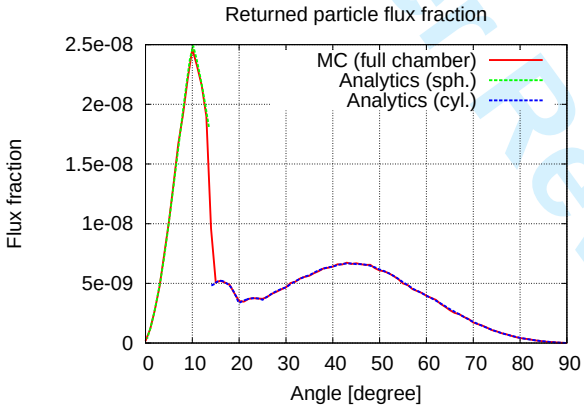

Fig. 16 Particle flux fraction at the thruster exit due to backscattering at vacuum vessel wall.

The calculated angular distribution of the back scattered particles by the Monte-Carlo simulation and from an analytical model are shown in Fig. 16. Due to the larger intersection of the solid angle with the thruster exit plane, the particle flux is larger for small angles of incidence. The returned particle flux consists of two parts, due to the vessel geometry. Sputtered particles from the spherical end are giving the contribution of small angles between 0 and 15 degrees, while for larger angles the sputtered particles are from the cylinder walls. The Monte-Carlo simulation (full line) agrees to the analytical calculations (dashed lines).

In further simulations these results can be used to verify structure of co-deposited layers inside the thruster channel and its impact on the measured thrust.The advantage of the shown simulation is its flexibility to analyze different vessel geometries. In spite of the low back-flowing fraction of emitted particles ($< 1\%$), these particles are producing co-deposited layers during the long test runs causing artifacts in the thrust. A strategy for avoiding this is to implement baffles in the vessel. While the $cos(\theta)$ distribution of the sputtered particles does not depend on the angle of incidence of the impinging ion, tilted baffles are turn the direction of the distribution and reduce the back-flow to the thruster exit, as sketched in Fig. 17. A implementation of baffles in the whole vessel, as

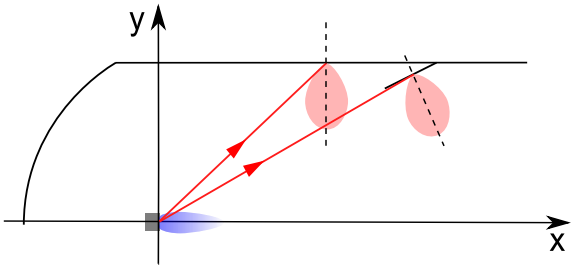

Fig. 17 Effect of a baffle on the distribution of sputtered particles.

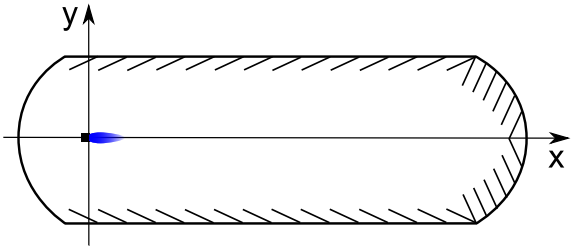

Fig. 18 Sketch of a vacuum vessel with implemented baffles.

sketched in Fig. 18 can reduce the back flow by $40\% - 66\%$. The results of this analysis have entered directly the preparation of the life-time qualification set-up for the HEMP-T system foreseen for the SGEO satellite [5]. The vacuum vessel was equipped with baffles tilted by about 20° to reduce artifacts due to sputtered particles from the vessel walls.

7 Conclusions

An integrated, modular approach is suggested to address the multi-scale problem of combined thruster-plume models. This approach covers ion-thruster plasma, plume and plasma wall interaction. A hierarchical multi-scale set of models in which the parametrization for a lower hierarchy model is deduced from a higher one is proposed. In the frame of such an approach the 3D PIC model could be used to parametrize turbulence effects on the electron mobility in the 2D PIC model. Due to the non-Maxwellian characteristics of plasma the 2D PIC is chosen as the core of the approach for analyzing both in-thruster and plume plasmas. The idea of the "matryoshka-like" set of grids is utilized to reach acceptable length scales with the capability to resolve even the plume kinetically. Furthermore, the modified central different scheme is used to obtain the electric field in order to minimize the error in the momentum conservation introduced by the use of the non-equidistant grid.

For the erosion, re-deposition analysis a direct coupling of the kinetic PIC model with binary-collision codes allows a detailed analysis of sputtering inside the thruster. To address longer scales including the plume and its interaction with the satellite Monte-Carlo approaches offer the best perspective, allowing even studies of the interaction of ion thrusters with the walls of the testing facilities and the development of strategies to minimize back-flows from vessel walls to the thruster by using appropriate baffle designs.

8 Acknowledgement

The authors would like to thank the German Space Agency DLR, specially Ralf Dittmann, Norbert Püttmann, Jürgen Schulze and Klaus Ruf for continuous support throughout Thales HEMP thruster system development.

References

[1] N. Koch, H. P. Harmann, and G. Kornfeld (eds.), Status of the THALES High Efficiency Multi Stage Plasma Thruster Development for HEMP-T 3050 and HEMP-T 30250, No. IEPC-2007-110, Florence, Italy, September 17-20, 2007.
[2] PANAMSATANNOUNCEMENT, Galaxy 10r satellite suffers propulsion system failure, Tech. rep., August 2004, http://www.spaceflightnow.com/news/n0408/05galaxy10r/.
[3] G. Kornfeld, H. Seidel, and J. Wegener, Plasma accelerator arrangement, 1999, Priority: Germany No. 198 28 704.6, filed 26 June 1998.
[4] G. Kornfeld, N. Koch, and H. P. Harmann, 30'th International Electric Propulsion Conference(IEPC-2007-108) (2007).
[5] A. Lazurenko, A. Genovese, S. Weis, M. Schirra, B. van Reijen, J. Haderspeck, P. Holtmann, K. Ruf, N. Püttmann, and N. Koch, Space Propulsion Conference(SP2012_2366197) (2012).
[6] K. Matyash, R. Schneider, A. Mutzke, O. Kalentev, F. Taccogna, N. Koch, and M. Schirra, IEEE Transactions on Plasma Since **38**(9, Part 1), 2274–2280 (2010).
[7] C. K. Birdsall and A. B. Langdon, Plasma physics via computer simulation (McGraw-Hill, New York, 1985).
[8] D. Tskhakaya, K. Matyash, R. Schneider, and F. Taccogna, Contrib. Plasma Phys. **47(8-9)**, 563–594 (2007).

[9] J. Bittencourt, Fundamentals of Plasma Physics, third edition (Springer Verlag, 2004).
[10] N. Koch, M. Schirra, S. Weis, A. Lazurenko, B. van Reijen, J. Haderspeck, A. Genovese, P. Holtmann, R. Schneider, K. Matyash et al., Proceedings of the 32nd International Electric Propulsion Conference (2011).
[11] F. F. Chen, Introduction to Plasma Physics and Controlled Fusion (Springer Verlag, 1984).
[12] L. Spitzer, Physics of fluids **3**(4), 659–661 (1960).
[13] D. Bohm, E. Burhop, and H. Massey, The characteristics of electrical discharges in magnetic fields (New York: McGraw-Hill, 1949).
[14] F. Taccogna, S. Longo, M. Capitelli, and R. Schneider, Contributions to Plasma Physics **47**(8-9), 635–656 (2007).
[15] P. Kravanja and M. Van Barel, Calcolo **33**(1-2), 147–164 (1996).
[16] E. Chow and Y. Saad, SIAM Journal on Scientific Computing **18**(6), 1657–1675 (1997).
[17] D. Tskhakaya et al., Self-force in 1d electrostatic particle-in-cell codes for non-equidistant grids, to be published, 2013.
[18] W. Eckstein, R. Dohmen, A. Mutzke, and R. Schneider, SDTrimSP: A Monte-Carlo Code for Calculating Collision Phenomena in Randomized Targets (Max-Planck-Institut für Plasmaphysik, 2007).
[19] J. Duras, O. Kalentev, A. Mutzke, K. F. Lüskow, and R. Schneider, Interactions between ion thruster plumes and vessel walls, to be published at 33'IEPC, October 2013.
[20] O. Kalentev, L. Lewerentz, J. Duras, K. Matyash, and R. Schneider, Journal of Propulsion and Power **29(2)**, 495–498 (2013).
[21] W. Eckstein, Springer Series in Materials Science **10** (1991).

J. Plasma Phys. (2017), *vol.* 83, 595830107
doi:10.1017/S0022377817000125

Ion angular distribution simulation of the Highly Efficient Multistage Plasma Thruster

J. Duras[1,2,†], D. Kahnfeld[2], G. Bandelow[2], S. Kemnitz[3], K. Lüskow[2], P. Matthias[2], N. Koch[1] and R. Schneider[2]

[1]Nuremberg Institute of Technology, D-90489 Nuremberg, Germany

[2]Institute of Physics, University of Greifswald, D-17498 Greifswald, Germany

[3]Institute of Computer Science, University of Rostock, D-18059 Rostock, Germany

(Received 18 July 2016; revised 16 January 2017; accepted 16 January 2017)

Ion angular current and energy distributions are important parameters for ion thrusters, which are typically measured at a few tens of centimetres to a few metres distance from the thruster exit. However, fully kinetic particle-in-cell (PIC) simulations are not able to simulate such domain sizes due to high computational costs. Therefore, a parallelisation strategy of the code is presented to reduce computational time. The calculated ion beam angular distributions in the plume region are quite sensitive to boundary conditions of the potential, possible additional source contributions (e.g. from secondary electron emission at vessel walls) and charge exchange collisions. Within this work a model for secondary electrons emitted from the vessel wall is included. In order to account for limits of the model due to its limited domain size, a correction of the simulated angular ion energy distribution by the potential boundary is presented to represent the conditions at the location of the experimental measurement in 1 m distance. In addition, a post-processing procedure is suggested to include charge exchange collisions in the plume region not covered by the original PIC simulation domain for the simulation of ion angular distributions measured at 1 m distance.

Key words: plasma applications, plasma simulation

1. Motivation

For ion thrusters, the angular ion distribution in terms of ion current, charge state and energy is an important parameter since it determines the thrust efficiency of the propulsion system. It is also one of the few thruster characteristics that can be accessed experimentally to validate numerical plasma simulations.

In the present study, numerical simulations are performed for the Highly Efficient Multistage Plasma Thruster (HEMP-T), patented by the THALES group in 1998 (Kornfeld, Seidel & Wegener 1998). As described in Koch, Harmann & Kornfeld (2007), HEMP-Ts consist of a dielectric, rotationally symmetric discharge channel with an anode and a propellant inlet located at the upstream end and a hollow cathode neutraliser placed at the thruster exit. The discharge channel is surrounded

† Email address for correspondence: julia.duras@th-nuernberg.de

by a system of axially magnetised permanent magnet rings in opposite magnetisation, forming a multi-cusp structure. The level of magnetic induction at any position within the thruster channel is chosen such that the Larmor radius of the electrons is much smaller than the geometrical dimensions of the discharge channel. While the propellant ions are hardly affected by the magnetic field due to their much higher mass, electrons are efficiently confined and only few electrons are lost to the wall, mostly at the cusps. In this work an older prototype model named DM3a is discussed. It has three cusps, the anode, the central and the exit cusp and is described in Kornfeld, Koch & Harmann (2007). An anode potential of $U_a = 500$ V is applied.

Numerical simulations show a typical neutral particle density in the channel is $n_n = 10^{20}$ m^{-3} with a neutral temperature of $T_n = 700$ K. Typical plasma parameters are a plasma particle density of $n_{e,i} = 10^{18}$ m^{-3}, with a temperature of approximately $T_e = 4$ eV and $T_i = 1$ eV. While the ions in the channel are nearly thermalised, the electrons have an additional drift velocity of approximately 10^4 m s^{-1} towards the anode. Inside the thruster channel the electron Debye length is $\lambda_{D_e} = 7.4$ μm, the electron plasma frequency is $\omega_{p,e} = 1.8 \times 10^{11}$ Hz and the electron mean free path is in the range of the channel length of 50 mm. This motivates kinetic simulations rather than a fluid approach for the electrons. The electrostatic approximation can be used, because the magnetic fields connected with the internal plasma currents are negligible compared to the static magnetic fields from the magnets. A strong coupling of the channel and plume plasma requires a simulation of both regions. In the plume, the plasma densities are decreased by at least 4 orders of magnitudes and the ion kinetic energy is increased to $E_{kin,i} = 500$ eV, as a consequence of the accelerating potential drop close to the exit.

A widely applied kinetic method is the particle-in-cell (PIC) scheme with Monte Carlo collisions (PIC-MCC), simulating the trajectories of super-particles consisting of many real particles. It requires the resolution of the smallest length scale of the system, usually the Debye scale, and the shortest time scale of the system, usually the plasma frequency, resulting in small domain sizes in the mm range and short simulated run times of approximately some μs. Since angular ion distributions are typically measured at a distance of tens of centimetres to some metres from the thruster exit, it is necessary to introduce proper mapping functions to transfer the results of the kinetic model to these positions. The computational requirements for such a fully kinetic model are quite demanding in memory and run time. Therefore, after a short description of the PIC-MCC code, a possible parallelisation strategy is discussed in § 2. Afterwards, the simulated angular distribution of ion current and energy is described in detail in § 3 and compared with experimental data.

2. Code description and parallelisation strategy

The non-Maxwellian characteristics of the electron distribution function in the thruster requires a kinetic method (Kalentev *et al.* 2014). Due to the rotational symmetry of the system, the spatial domain was reduced to r–z (radial and axial coordinate) and an electrostatic 2d3v PIC code (2-D in position space and 3-D in velocity space) with Monte Carlo collisions (Matyash *et al.* 2010; Kalentev *et al.* 2014) was used. In this PIC-MCC simulation we follow the kinetics of so-called super-particles (each of them representing many real particles), moving in the self-consistent electric field calculated on a spatial grid by solving Poisson's equation

$$\Delta \Phi = -\frac{\rho}{\varepsilon}. \tag{2.1}$$

Here, Φ indicates the electric potential, ρ the plasma density and ε the absolute permittivity. The relevant collisions: electron–electron Coulomb, electron–neutral elastic, ionisation and excitation collisions, ion–neutral momentum transfer and charge exchange collisions are included. For Coulomb collisions a binary collision routine, as suggested by Takizuka & Abe (1977), is used. Collisions with neutrals are simulated by a Monte Carlo routine similar to Vahedi *et al.* (1993), using cross-sections for xenon from Hayashi (2003), Phelps (2000) and Phelps (2002). A detailed description of the applied collision models can be found in Tskhakaya *et al.* (2007). The dynamics of the background neutral gas is self-consistently resolved by Direct Simulation Monte Carlo (Procassini *et al.* 1987). As can be seen from three-dimensional (3-D) simulations of a similar HEMP thruster model, classical transport along magnetic field lines is dominant (Kalentev *et al.* 2014). Only in the narrow cusp regions, where $\boldsymbol{B}$ turns from the axial to radial direction, fluctuations of the azimuthal electric field allow the electrons to overcome. In the 3-D simulations the anomalous fluxes are calculated self-consistently (Kalentev *et al.* 2014). Using these results, an effective anomalous transport coefficient of $D_\perp \propto 0.4 \times k_B T/eB$ following Bohm, Burhop & Massey (1949) can be determined. This coefficient is then used in the 2-D model, which does not allow us to calculate electrostatic turbulence self-consistently. The anomalous transport fluxes are implemented by a diffusive model using the calibrated transport coefficient deduced from the 3-D simulation for a random walk model in velocity space in all three velocity components (radial, axial and poloidal). Information of all three velocity components exists in the 2-D code due to the Monte Carlo collisions (Bronold *et al.* 2007; Tskhakaya *et al.* 2007). The isotropic characteristics of turbulence is well represented by this procedure. Dominant transport contributions in two dimensions will be perpendicular to the magnetic field lines, as discussed previously. With respect to the channel plasma parameters, an equidistant grid with a spacing of $\Delta r = \Delta z = 1.3\,\lambda_{D,e} = 0.01$ mm is used, including both the thruster channel and the near-field plume. In order to reduce the computational time, a similarity scaling is applied with a factor of 10 (Taccogna *et al.* 2005). For the time resolution a time step of $\Delta t = 0.2\,\omega_{p,e}^{-1} = 1$ ps is chosen. In the channel around the propulsion exhaust, the neutral particle density is two orders of magnitude higher than for the plasma particles. For a correct treatment of MCC of neutrals with plasma particles, the same weighting of plasma and neutral super-particles is required. This results in a number of simulated super-particles which is 100 times higher than for ions and electrons. In total, the high resolution in space, time and particles results in a long run time. For the serial PIC-MCC code, typically one month of calculation is needed on a desktop system in order to simulate a run time in the range of some micro seconds. With access to parallel computing clusters, the best chance of gaining a speed up of the simulation is an efficient parallelisation.

Dependent on the simulated system, a domain decomposition according to number of particles in each subdomain is applied; collision probability or grid cells per rank. In this work, a domain decomposition according to number of particles was used. With the help of the Message Passing Interface (MPI), particle arrays as well as the electric field computed on the grid are distributed to the different subdomains. Each subdomain is either located at different nodes or cores. This allows the parallel execution of the particle pusher. In a second step, the MC collisions routine is planned to be parallelised by using the Open Multi-Processing (OpenMP), suitable for shared memory parallelisation on a single node.

To calculate the electric field on the grid, Poisson's equation (2.1) is solved using a finite difference scheme for the spatial second-order derivatives creating a system of

linear equations

$$\boldsymbol{A}\boldsymbol{\Phi} = \boldsymbol{b}. \tag{2.2}$$

Here, the vector $\boldsymbol{\Phi}$ and $\boldsymbol{b}$ indicate the electric potential ϕ and the plasma density $-\rho/\varepsilon$ respectively, on the grid points. For a two-dimensional $M \times N$ grid, this gives a matrix $\boldsymbol{A}$ of dimension $(M \cdot N) \times (M \cdot N)$. In order to reach reasonably low computing time, the calculation of $\boldsymbol{\Phi}$ within one time step has to be faster than one second $t_{max} \leqslant 1$ s.

A standard sparse matrix solver is the LU decomposition. The matrix is decomposed into a product of an upper triangular matrix $\boldsymbol{U}$ and a lower triangular matrix $\boldsymbol{L}$. By this, in each time step the calculation of $\boldsymbol{L}(\boldsymbol{U}\boldsymbol{\Phi}) = \boldsymbol{b}$ can be done easily. While the decomposition is rather time consuming, the so-called back solve has a complexity of $\sim(M \cdot N)^2/2$ (Stoer 2005*a*), making it very efficient. Therefore, the decomposition is calculated only at the beginning of the simulation, as the matrix does not change throughout the execution of the code, and only the back solve has to be computed every PIC cycle, hence giving a complexity of $\sim(M \cdot N)^2$ per PIC cycle. A parallelisation of this method is problematic, as each line within a back-solve step depends on the results of the previous lines, limiting its application to one computational core. Parallel methods are only available for the calculation of the LU decomposition but not for the back solve (Li 2005).

In order to reduce the number of grid points, a 'matryoska-like' hierarchy of equidistant grids can be used for the simulation of the HEMP thruster (Kalentev *et al.* 2014). The hierarchy is constructed such that a coarse grid, given by the electron Debye length in the plume, covers the whole domain, while a fine grid with a mesh spacing of $\lambda_{D,e}$ in the channel, covers in addition the channel and the near-field plume. The solution of Poisson's equation (2.1) is obtained by first solving the equation on the coarse grid and then using the interpolated coarse grid values as boundary values for the fine grid solution. This approach appears to be not only accurate enough, but also remarkably fast compared with the solution for a single equidistant mesh. Alternatively, non-equidistant meshes could be used, but these suffer from artefacts (Tskhakaya *et al.* 2007), such as self-forces, and corrections to minimise such errors are needed. A reduction can be achieved by a modified two point central difference scheme for calculation of the electric field on a non-equidistant grid (Duras *et al.* 2014). In the case of thruster simulations, a transition from a fine to a coarser grid can be done in the plume region, since here the coupling with the channel plasma is lower and the influence of artificial forces is reduced.

Instead of using the fast, but serial back solve, the advantage of a slower but parallelisable method can be facilitated (Kahnfeld *et al.* 2016). A standard iterative solver is the successive over-relaxation (SOR) method which is often applied to solve the finite difference discretisation of the Poisson equation (2.1). It is a variation of the Gauss–Seidel algorithm with a relaxation factor $\omega > 1$. The matrix $\boldsymbol{A}$ is represented by the sum of $\boldsymbol{A}$'s diagonal matrix $\boldsymbol{D}$ (with $a_{ii} \neq 0$ for all i) and it's strictly lower and upper triangular matrices $\boldsymbol{L}$ and $\boldsymbol{R}$ (not to be confused with the matrix used in the LU decomposition) with $\boldsymbol{A} = 1/\omega(\boldsymbol{D} + \omega\boldsymbol{L}) + \boldsymbol{R}$. The expected number of iteration steps is $\sim(M \cdot N)$, giving the entire SOR method a complexity of $\sim(M \cdot N)^3$ (Stoer 2005*b*). This is much higher compared to the back solve of the LU decomposition which scales quadratically, however the algorithm allows for easy parallelisation as the calculation of each point's iterate depends only on the surrounding points. Only the boundary points have to be exchanged during each iteration step.

In this work, compared to a serial run, parallelisation of the particle pusher gained a speed up of 2.6, running on 2 nodes with 4 cores each node. Here, mainly the serial solver limits the total simulation speed up.

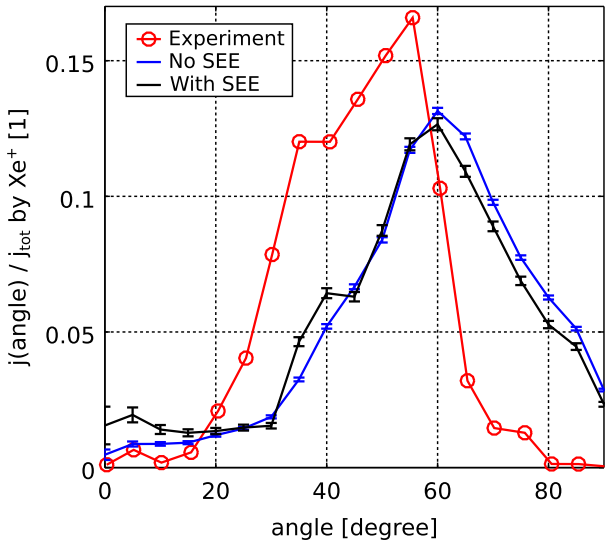

FIGURE 1. Angular ion current distribution with respect to the thruster exit at $r = 0$ mm, measured in experiment (Matyash *et al.* 2009) and simulated with SEE and without. Simulation results are given with statistic error bars.

3. Ion angular distributions

The angular distributions of ion current and energy are among the key parameters of an ion thruster and are also directly accessible to experiments. Within experiments, ion angular distributions are typically measured with a Retarding Potential Analyzer (RPA) at approximately 1 m distance from the thruster exit (van Reijen *et al.* 2013). In the PIC simulation, the simulated plume has a size of several centimetres, limited by the high computational costs. In the plume, the potential distribution and ion–neutral collisions are the important physical mechanisms for current and energy distribution of the ions. Also, secondary electron emission (SEE) at vessel walls, generated by accelerated ions, influences the potential at the thruster exit. These low energetic electrons are magnetised in the thruster near-field plume and follow the magnetic field lines.

In the following the angular ion current distribution, as well as the angular energy distribution, will be discussed in detail. Within the simulation, these distribution functions are diagnosed along a diagnostic surface at the plume domain boundary. The angle is defined with respect to the thruster exit at the symmetry axis ($r = 0$ mm), assuming a point source. In experimental measurements the same assumption is applied. The angular resolution is chosen to be 5°. For the current diagnostics, the current passing the diagnostic surface is calculated and for the energy distribution, the kinetic energy of the ions crossing this surface is detected.

3.1. *Angular ion current distribution*

In figure 1, the calculated angular ion current distribution is given in blue. It shows contributions for all angles with a maximum current at 60°. In the same figure a measured angular ion current distribution for the DM3a HEMP model is given in red. It shows two maximums at 35° and 55°, respectively. For a better understanding, the origin of the detected ions was diagnosed and analysed with respect to the angle. It indicates a correlation of the respective cusp, in which an ion is generated, and the

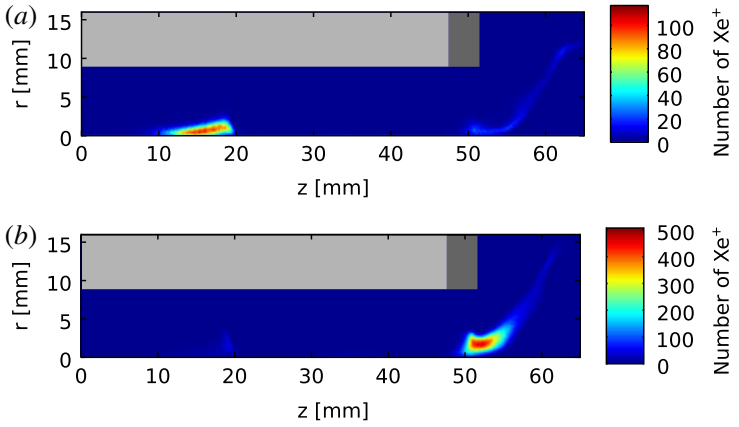

FIGURE 2. Ionisation distribution for ions detected at the diagnostic surface at $40 \pm 2.5°$ (*a*) and $60 \pm 2.5°$ (*b*). The dielectric channel wall is shown in light grey and the grounded pole piece is shown in dark grey.

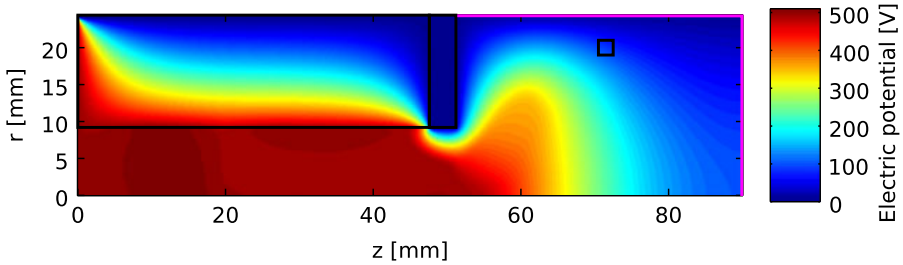

FIGURE 3. Potential of thruster channel and plume, given in *V*. In magenta, the diagnostic surface for the ion angular distributions is given at the plume domain boundary. The small black box in the plume indicates the position of the electron source.

angle into which it is emitted, as can be seen in figure 2, which shows the ionisation distribution for ions detected at 40° and 60°. While for angles between 30° and 50°, ions are mainly generated in the central cusp, for angles larger than 55° the exit cusp apparently is the place of origin. Due to a low contribution of the ionisation in the central cusp, the second maximum around 40° is not well accentuated. Therefore, the simulated ion angular current distribution can be seen as qualitatively matching the experimental data, shifted by 5° towards higher angles.

An important effect on the angular ion distribution is the potential drop in the plume, accelerating the ions towards different angles. In the simulation, it is also sensitive to the potential at the boundary of the simulation domain due to its limited size. In figure 3, the resulting potential is shown and in magenta, the diagnostic surface is indicated. The black rectangle at $r = 20$ mm and $z = 75$ mm indicates the position of the primary electron source with a source current of $I_{src,1} = 0.3$ mA. It represents the real neutraliser, which is located outside the computational domain. The position was chosen in order to provide sufficient starter electrons for the thruster channel. In experiments, the HEMP-T can operate even without the neutraliser because even a very small amount of free electrons are sufficient for successful start up. Corresponding ion and electrons distributions can be found in Duras *et al.* (2016). For the boundary condition at the right-hand side of the domain $E_z = 0$ is chosen. The potential at the left-hand side is fixed to the anode potential U_a. At the

upper boundary $\Phi = 0$ V is used. This fixed potential can squeeze or stretch the potential solution in the radial direction, which results in shifted angular distributions. To prevent this, it is reasonable to use, for the area of the simulated plume, a similar aspect ratio as the vessel in which the experiments were taking place. What constitutes a sufficient domain size to reduce the influence of this defined potential boundary remains to be investigated.

An indirect influence on the potential is induced by the emission of secondary electrons from the vessel walls. These low energetic electrons are attracted by the anode potential and become magnetised by the magnetic field of the thruster acting as additional primary source of electrons. A study of different external electron sources and their positions showed strong influence of the magnetic field on the near-field plume (Duras *et al.* 2016). To represent the possible contributions of secondary electrons created by ions at the vessel walls, an electron source is placed close to the symmetry axis. This changes the potential distribution in the channel, while external electron sources at other places in the plume hardly influence the potential structure. The main reason for this is that the magnetic field, close to the symmetry axis, points directly into the thruster. At other radial positions the field lines are curved and electrons are trapped between a magnetic mirror movement, pushing them away from the thruster, and the potential drop forcing them towards the exit. Electrons emitted close to the symmetry axis have higher energies due to the direct guidance into the channel. This increases the probability of ionisation which expands the potential drop out of the thruster channel.

SEE at the aluminium vessel walls can act as an additional electron source. Secondary electrons created at the vessel walls by impinging ions fly towards the thruster. Rosenberg & Wehner (1962) measured sputter yields for singly charged ions impinging on aluminium which have been published for ion energies of 100, 200, 300 and 600 eV. With the help of an empirical fitting formula by Yamamura, Matsunami & Itoh (1983), an emission coefficient of $\gamma = 0.6$ can be approximated for singly charged xenon ions impinging with an energy of 500 eV.

Approaching the thruster entrance such electrons experience an increasing magnetic field, which directs them mostly towards the axis. In the small simulation domain of this work, the electron influx from this process is parametrised as an additional surface source close to the axis. Electrons are injected at the right domain boundary close to the symmetry axis at $r \in (0; 2\ \text{mm})$ and $z \in (88\ \text{mm}; 90\ \text{mm})$, with a directed drift velocity towards the thruster based on an energy of 100 eV corresponding to the potential at this location and a thermal broadening of the source distribution assuming a temperature of 0.45 eV. Of the total emitted ion current of $I_{tot} = 142$ mA, 10 % were chosen as an effective electron source close to the axis, representing SEE. This contribution is a factor of approximately 5 times higher than the primary electron source. This value was chosen because it induced a visible effect in the solution without affecting strongly the integral ion current.

The resulting angular current distribution with SEE can be seen in black in figure 1. It shows a higher ion contribution close to the symmetry axis (0°), which is the direct effect of the additional electron source in this region. At approximately 40° the second ion beam becomes more pronounced, which is in qualitative agreement with the experimental data.

3.2. *Angular ion energy distribution*

The simulated angular ion energy distribution calculated at the domain boundary is shown in figure 4. At the left-hand side the calculated ion flux is colour coded in

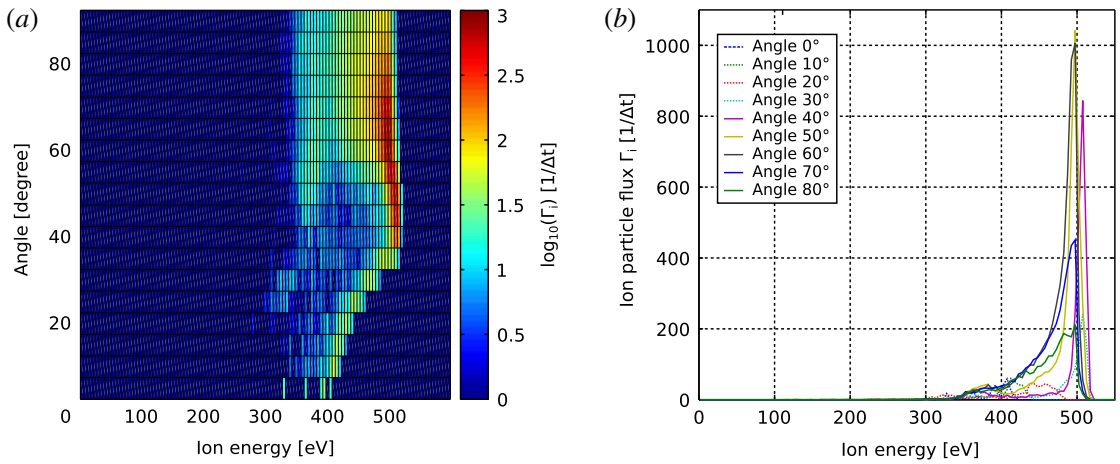

FIGURE 4. Angular ion energy distribution at the domain boundary. (*a*) Contour plot of the ion particle flux Γ_i in logarithmic scale as a function of angle and ion energy. (*b*) Γ_i in linear scale as a function of ion energy shown for nine angles.

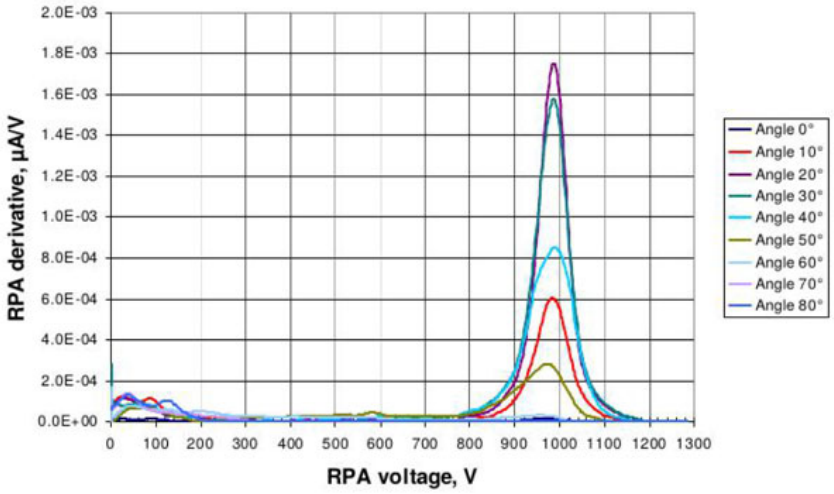

FIGURE 5. Angular ion energy distribution for the HEMP thruster model HEMPT 3050, derived from RPA measurements. The applied thruster anode voltage was $U_a = 1000$ V (Koch *et al.* 2011).

logarithmic scale and the angle is defined with respect to the thruster exit at the symmetry axis. The right-hand side of figure 4 shows the same result in linear scale as line plots for nine angles. As expected, the maximum ion energy is 500 eV, given by the anode potential. The dominant contribution of ions originates from ions at approximately 60°.

An experimentally measured energy distribution for the HEMP thruster model HEMPT 3050 is shown in figure 5 for nine different angles (Koch *et al.* 2011). It is characterised by a maximum close to the anode potential $U_a = 1000$ V, with an opening angle of 20°. While the simulated energy distribution shows a peak, smeared out to lower energies, the measured data show a Gaussian distribution around U_a.

In the numerical diagnostic, the limited domain size causes differences between the simulated and measured ion energy distributions. In order to make the simulated ion distribution comparable to the experimentally measured one, a transfer function $g(f)$,

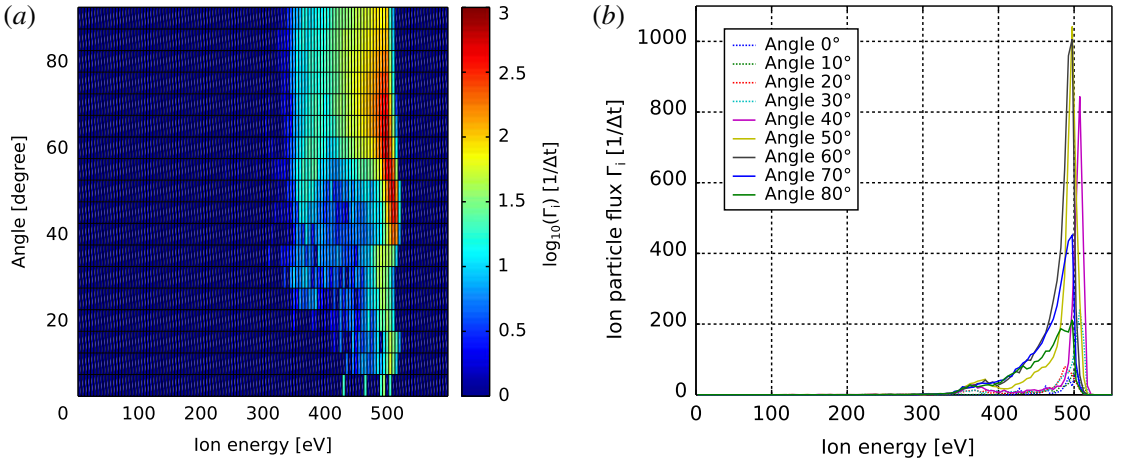

FIGURE 6. Mapped angular ion energy distribution to the location of the experimental detector position. (*a*) Contour plot of the ion particle flux Γ_i in logarithmic scale as a function of angle and ion energy. (*b*) Γ_i in linear scale as a function of ion energy shown for nine angles.

similar to the detector function in Reiter (2009), is used to transfer information from the domain boundary to the detector position in the experiment

$$g : f(\text{domain boundary}) \mapsto f(\text{detector position}). \tag{3.1}$$

Here f stands for the angular ion energy distribution. This correction is used to represent effects which are not included in the current PIC simulation. One artefact caused by the limited domain size originates from the von Neumann boundary condition at the right-hand side of the domain. Ions reaching the diagnostic surface at this location have not yet reached the maximum kinetic energy of U_a. For small angles, 0°–30°, one can clearly see in figure 4 a reduction of the maximum energy, which is decreasing with the angle. At the detector position 1 m distant from the thruster exit, the potential will have relaxed to values close to ground potential and the additional acceleration by this potential drop has to be taken into account. Therefore, the transfer function $g(f)$ of the angular ion energy distribution corrects the ion energies of the detected ions by adding the additional potential at the domain boundary

$$f(\text{detector position}) = f(\text{domain boundary}) + q_i \Phi(\text{domain boundary}), \tag{3.2}$$

with the ion charge q_i. In figure 6, the corrected angular ion energy distribution can be seen. For angles $<35°$, the correction results in a shift to higher energies, so that for all angular bins the maximum energy corresponds to the anode potential U_a. This improves the qualitative agreement between simulation and measured ion energy distribution (see figure 5).

Another discrepancy between experiment and simulation are the missing ion charge exchange (CX) collisions during the 1 m of flight within the plume. Within the PIC simulation, domain charge exchange collisions between ions and neutrals are fully included. While within the acceleration channel the mean free path of these collisions is smaller than the channel length, the decreasing neutral density increases this mean free path to approximately 1 m, which is larger than the simulated domain size. Therefore, CX collisions appearing between the domain boundary of the simulation

and the position of the experimental measurement of the ion energy distribution are not represented within this simulation due to the latter's limited domain size and require special corrections. This is visible in the missing low energetic part of the ion energy distribution of the simulation (figure 4), which clearly appear in the experimental measurements at about 0–200 eV (figure 5). Here the idea of the transfer function, trying to map the information from the boundary of the simulated domain to the location of the experimental measurement, can be improved using a Monte Carlo post-processing procedure including CX collisions for a pre-defined neutral background gas density in the vessel.

4. Conclusions

Although angular ion distributions are important parameters in experiments and the validation of ion thruster simulations, measurements and simulations are difficult to compare. Especially for PIC simulations, the measurement distance of these distributions is much larger than the possible domain size. Therefore, a parallelisation strategy is necessary in order to increase the domain size. With a parallel particle pusher, using a particle weighted domain decomposition, a speed up of a factor 2.6 was achieved for 2 nodes with 4 cores, compared to a serial simulation.

Ion angular distributions are sensitive to the plume potential. Secondary electron emission at vessel walls due to impinging fast ions can modify the potential structure in the near-field region of the plume and by this the ion angular distributions. As shown in previous studies (Duras *et al.* 2016), only near-axis electron sources are able to change the plume potential. In addition the magnetic field of the thruster guides most of the emitted secondary electrons towards the channel axis. Therefore a near-axis surface source was implemented at the domain boundary, which affects only the small angles in the ion angular current distribution as expected.

The small domain size leads to artefacts at the domain boundary, because the potential does not drop to zero within this domain size. The concept of a transfer function was introduced to map the simulated ion angular distribution from the computational boundary to the location of the experimental measurement at approximately 1 m. For this, the potential energies of the ions were corrected, shifting them by the potential at the domain boundary. This improves the qualitative agreement between simulation and measured ion energy distribution. In the future, a further improvement of the transfer function is possible including the effect of charge exchange collisions in the plume plasma by a Monte Carlo module, following the ions from the domain boundary to the location of the detector.

Acknowledgements

This work was supported by the Bavarian State Ministry of Education Science and the Arts and the German Space Agency DLR. We also like to thank R. Heidemann from THALES Electron Devices GmbH for interesting and stimulating discussions.

REFERENCES

Bohm, D., Burhop, E. H. S. & Massey, H. S. W. 1949 *The Characteristics of Electrical Discharges in Magnetic Fields*. McGraw-Hill.

Bronold, F. X., Matyash, K., Tskhakaya, D., Schneider, R. & Fehske, H. 2007 Radio-frequency discharges in oxygen: I. particle-based modelling. *J. Phys.* D*: Appl. Phys.* **40** (21), 6583–6592.

DURAS, J., MATYASH, K., TSKHAKAYA, D., KALENTEV, O. & SCHNEIDER, R. 2014 Self-force in 1d electrostatic particle-in-cell codes for non-equidistant grids. *Contrib. Plasma Phys.* **54** (8), 697–711.

DURAS, J., SCHNEIDER, R., KALENTEV, O., KEMNITZ, K., MATYASH, K., KOCH, N., LÜSKOW, K., KAHNFELD, D. & BANDELOW, G. 2016 Influence of electron sources in the near-field plume in a multistage plasma thruster. *Plasma Physics and Technology* **3** (3), 126–130.

HAYASHI, M. 2003 Bibliography of electron and photon cross sections with atoms and molecules published in the 20th Century – Argon –. *Res. Rep. NIFS-Data Series*, NIFS-DATA-072.

KAHNFELD, D., BANDELOW, G., DURAS, J., LÜSKOW, K., KEMNITZ, K. & SCHNEIDER, R. 2016 Solution of poisson's equation in electrostatic particle-in-cell simulations. *Acta Polytech*; (submitted).

KALENTEV, O., MATYASH, K., DURAS, J., LÜSKOW, K. L., SCHNEIDER, R., KOCH, N. & SCHIRRA, M. 2014 Electrostatic ion thrusters – towards predictive modeling. *Contrib. Plasma Phys.* **54**, 235–248.

KOCH, N., HARMANN, H.-P. & KORNFELD, G. 2007 Status of the THALES high efficiency multi stage plasma thruster development for HEMP-T 3050 and HEMP-T 30250. In *Proceedings of the 30th International Electric Propulsion Conference,* vol. IEPC-2007-110. Electric Rocket Propulsion Society.

KOCH, N., SCHIRRA, M., WEIS, S., LAZURENKO, A., VAN REIJEN, B., HADERSPECK, J., GENOVESE, A., HOLTMANN, H.-P., SCHNEIDER, R., MATYASH, K. *et al.* 2011 The hempt concept – a survey on theoretical considerations and experimental evidences. In *Proceedings of the 32nd International Electric Propulsion Conference,* vol. IEPC-2011-236. Electric Rocket Propulsion Society.

KORNFELD, G., KOCH, N. & HARMANN, H.-P. 2007 Physics and evolution of HEMP-Thrusters. In *Proceedings of the 30th International Electric Propulsion Conference,* vol. IEPC-2007-108. Electric Rocket Propulsion Society.

KORNFELD, G., SEIDEL, H. & WEGENER, J. 1998 Plasma accelerator arrangement. *Patent* PCT/DE99/01708.

LI, X. S. 2005 An overview of superlu: Algorithms, implementation, and user in- terface. *ACM Trans. Math. Softw.* **31**, 302–325.

MATYASH, K., KALENTEV, O., SCHNEIDER, R., TACCOGNA, F., KOCH, N. & SCHIRRA, M. 2009 Kinetic Simulation of the stationary HEMP thruster including the near-filed plume region. In *Proceedings of the 31st International Electric Propulsion Conference,* vol. IEPC-2009-110. Electric Rocket Propulsion Society.

MATYASH, K., SCHNEIDER, R., MUTZKE, A., KALENTEV, O., TACCOGNA, F., KOCH, N. & SCHIRRA, M. 2010 Kinetic simulations of SPT and HEMP thrusters including the near-field plume region. *IEEE Trans. Plasma Sci.* **38** (9, Part 1), 2274–2280.

PHELPS, A. V. 2000 Nitrogen atoms and molecules. Retreved from http://jila.colorado.edu/avp/collision_data/neutralneutral/atomatom.txt (January 2015).

PHELPS, A. V. 2002 Nitrogen atomic and molecular ions. Retreved from http://jila.colorado.edu/avp/collision_data/ionneutral/IONATOM.TXT (January 2015).

PROCASSINI, R., BIRDSALL, C., MORESE, E. & COHEN, B. 1987 A relativistic monte carlo binary collision model for use in plasma particle simulation codes. *Mem. No.* UCB/ERL M87/24, University of California, Berkeley.

VAN REIJEN, B., WEIS, S., LAZURENKO, A., HADERSPECK, J., GENOVESE, A., HOLTMANN, P., RUF, K. & PTTMANN, N. 2013 High precision thrust vector determination through full hemispherical rpa measurements assisted by anguar mapping of energy charge state distribution. In *Proceedings of the 33nd International Electric Propulsion Conference,* vol. IEPC-2013-284. Electric Rocket Propulsion Society.

REITER, D. 2009 The EIRENE code user manual. Retreved from http://www.eirene.de (September 2016).

ROSENBERG, D. & WEHNER, G. K. 1962 Sputtering yields for low energy He+-, Kr+-, and Xe+-Ion Bombardment. *J. Appl. Phys.* **33** (5), 1842–1845.

STOER, J. 2005*a* *Numerische Mathematik*, vol. 1. Springer.

STOER, J. 2005*b* *Numerische Mathematik*, vol. 2. Springer.

TACCOGNA, F., LONGO, S., CAPITELLI, M. & SCHNEIDER, R. 2005 Self-similarity in hall plasma discharges: Applications to particle models. *Phys. Plasmas* **12**, 053502.

TAKIZUKA, T. & ABE, H. 1977 A binary collision model for plasma simulation with a particle code. *J. Comput. Phys.* **25**, 205–219.

TSKHAKAYA, D., MATYASH, K., SCHNEIDER, R. & TACCOGNA, F. 2007 The particle-in-cell method. *Contrib. Plasma Phys.* **47** (8–9), 563–594.

VAHEDI, V., DIPESO, G., BIRDSALL, C. K., LIEBERMAN, M. A. & ROGNLIEN, T. D. 1993 Capacitive RF discharges modelled by particle-in-cell Monte Carlo simulation. I. Analysis of numerical techniques. *Plasma Sources Sci. Technol.* **2** (4), 261.

YAMAMURA, Y., MATSUNAMI, N. & ITOH, N. 1983 Theoretical studies on an empirical formular for spittering yiels at normal incidence. *Radiation Effects* **71**, 65–86.

Plasma Physics and Technology **3**(3):126–130, 2016

INFLUENCE OF ELECTRON SOURCES ON THE NEAR-FIELD PLUME IN A MULTISTAGE PLASMA THRUSTER

Duras J.[a,b,*], Schneider R.[a], Kalentev O.[d], Kemnitz S.[c,e], Matyash K.[c], Koch N.[b], Lüskow K.[a], Kahnfeld D.[a], Bandelow G.[a]

[a] *Institute of Physics, Ernst-Moritz-Arndt University of Greifswald, D-17498 Greifswald, Germany*

[b] *Department of Applied Mathematics, Physics and Humanities, Nürnberger Institute of Technology, D-90489 Nürnberg, Germany*

[c] *Computing Center, Ernst-Moritz-Arndt University of Greifswald, D-17498 Greifswald, Germany*

[d] *Biomedizinische NMR Forschungs GmbH am Max-Planck-Institut für biophysikalische Chemie, D-37077 Göttingen, Germany*

[e] *University Rostock, Institute of Informatics, D-18059 Rostock, Germany*

[*] julia.duras@uni-greifswald.de

Abstract. In order to obtain a better understanding of the near-field plume of a multistage plasma thruster, the influence of an external electron source is investigated by Particle-In-Cell simulations. The variation of the source position showed a strong influence of the magnetic field configuration on the electron distribution and therefore on the plume plasma. In the second part of this work, higher energetic electrons were injected in order to model collision-induced diffusion in the plume. This broadens the electron distribution, which leads to a more pronounced divergence angle in the angular ion distribution.

Keywords: Multistage plasma thruster, near-field plume, external electron source, Particle-In-Cell.

1. Motivation

Ion thrusters with magnetic plasma confinement can be optimized by modifying magnetic field configuration, anode potential, neutral gas source and neutralizer properties. In the case of neutralizer adjustment, mainly the plume behavior is influenced. For a better understanding of the near-field plume physics, the influence of an external electron source on its properties is studied. Here, position and source distribution are varied and the interaction between magnetic field, potential and plasma densities are investigated.
For this purpose a multistage plasma thruster similar to the HEMP thruster [1], [2] was simulated with the Particle-In-Cell method.

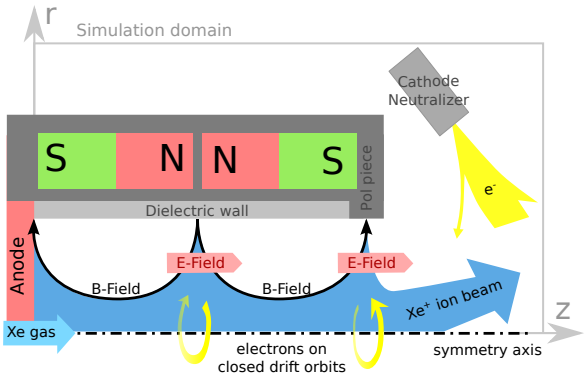

Figure 1. Scheme of HEMP-like thrusters, similar to [3].

2. Physics of a multistage plasma thruster

A multistage plasma thruster consists of a rotationally symmetric discharge channel with an anode and an inlet for the propellant at the upstream end, as shown in figure 1. The discharge channel is surrounded by axially magnetized permanent magnet rings with opposite magnetization. Inside the thruter channel a dielectric wall is facing the plasma. At the exit a grounded pole piece is placed. Outside the thruster channel a hollow cathode neutralizer is placed. It provides the thruster with starter electrons for igniting the discharge and neutralizes the out-going ion beam. The permanent magnets generate a magnetic field which points mainly in axial direction especially in the channel region next to the symmetry axis. In the so-called cusp regions, the magnetic field next to the channel wall is mostly directed in radial direction. In figure 1 three cusps are shown, an anode cusp, an inner cusp and an exit cusp. The magnetic field strength B is chosen such that the Larmor radius of the electrons is much smaller than the radius of the discharge channel, while for the ions it is larger $r_{\mathrm{L,e}} \ll R < r_{\mathrm{L,i}}$. Therefore, in the thruster channel electrons are magnetized while ions are not. Electrons are created by the neutralizer acting as cathode and experience close to the axis a magnetic field nearly parallel to the axis which directs them towards the anode.
The cusp-structure of the magnetic field builds up

a magnetic mirror in front of the thruster exit. In combination with the potential drop, this magnetic mirror lets the electrons oscillate in a confined electron cloud in the plume originating from the electron source pointing towards the thruster's exit. In the cusp regions, the perpendicular electric and magnetic fields induce a $\vec{E} \times \vec{B}$-drift to the electrons in poloidal direction. In addition the magnetic field configuration builds up a magnetic mirror in radial direction and the electrons are reflected before they reach the channel wall. The strong radial magnetic field in these regions separate the different thruster regions. Only few electrons can overcome these regions by collisional and anomalous transport, which is caused by electrostatic turbulence [4]. By this, electron density is increased in the respective downstream cusp region and allows for efficient ionization of the propellant. In the channel regions between the cusps, the electron transport is determined in axial direction by the fields and in radial direction by collisional transport. Therefore, in the regions where no cusps are existing electron losses at the dielectric wall are low and the non-magnetized ions can generate a positive surface charge. The dominance of the axial transport along the magnetic field lines quickly compensates small perturbations of the electric potential and results in a flat potential inside the discharge channel with only small steps at the regions with large radial transport, namely at the cusps. Xenon ions follow the potential gradients and are getting accelerated mostly in the potential drop of the thruster exit. Within the acceleration channel the radial potential gradients towards the wall are rather small and the ion energies are kept below the sputter threshold, hence minimizing erosion. The different dynamics for electrons and ions lead to a spatial separation of ionization in the channel and acceleration at the thruster exit. In order to produce an ion beam with small divergence angle, a grounded magnetic pole piece is placed at the exit cusp. The magnetic field lines are focused in this region and the grounded potential produces in radial direction a large potential drop of $\Delta\phi = eU_\mathrm{a}$. This guides the electrons to enter the thruster channel and get confined only close to the symmetry axis, which creates an ion lens. The resulting ion beam is strongly affected by the potential structure in this region as well as in the near-field plume region. Here, the magnetized electrons are determining the potential and therefore influencing the ion trajectories.

Therefore, the thruster magnetic field topology and the potential in the plume are important for optimization of the ion beam divergence. Different external electron source positions might change the electron distribution in the plume and therefore potential and angular ion distribution.

3. Code description and simulation set-up

The non-Maxwellian characteristics of the electron distribution function in the thruster requires a kinetic method [5]. Due to the rotational symmetry of the system, the spatial domain was reduced to r-z and an electrostatic 2d3v Particle-In-Cell code with Monte Carlo collisions (PIC MCC) [6], [4] was used. In this PIC-MCC simulation we follow the kinetics of so-called Super Particles (each of them representing many real particles), moving in the self-consistent electric field calculated on a spatial grid by solving Poisson's equation. The particle collisions are treated by Monte Carlo Collision (MCC) routines. All relevant collisions are included in the model: electron-electron Coulomb, electron-neutral elastic, ionization and excitation collisions, ion-neutral momentum transfer and charge exchange collisions. The dynamics of the background neutral gas is self-consistently resolved by Direct Simulation Monte Carlo [7]. Plasma surface interactions are provided by a Monte Carlo erosion module. For electrons an anomalous transport model is applied [8]. In order to reduce the computational time a similarity scaling is applied with a factor of 10 [9].

In figure 1, the simulation domain and the thruster geometry are shown. The thruster has a channel radius of $R = 9\,\mathrm{mm}$ and length of $L = 51\,\mathrm{mm}$. The main part of the channel wall is dielectric, at the exit a grounded magnetic pole piece terminates the thruster channel. At the anode a potential of $U_\mathrm{a} = 500\,\mathrm{V}$ is applied. The simulated domain consists of a fine grid of 890×240 cells with a grid spacing of $\Delta r = \Delta z = 0.5\lambda_{D,e} = 0.01\,\mathrm{mm}$ containing the thruster channel and the near field plume. It is overlaid by a courser grid of four times larger cell size, covering the whole domain. The potential boundary condition at the symmetry axis and at the right hand side of the domain is set to zero radial electric field, while at other domain boundaries Dirichlet boundary conditions with $\phi = 0\,\mathrm{V}$ or $\phi = U_\mathrm{a}$ are applied. For the grounded magnetic pole piece the potential is set to zero. The solution at the domain boundary between fine and coarse mesh is transferred explicitly by boundary conditions between the two meshes.

4. Results

4.1. Influence of the electron source position

Within PIC ion thruster simulations, the resolved domain is usually too small to simulate the neutralizer at the position of the experiment. Due to the magnetization of the electrons the usage of an effective source, placed at the same magnetic field line as the neutralizer is used. The external source is simulated as a volume source of size $4\,\mathrm{mm} \times 4\,\mathrm{mm}$ with Maxwellian distributed electrons of a temperature of $T_\mathrm{e} = 2\,\mathrm{eV}$ and a cathode current of $I_\mathrm{cath} = 1.5\,\mathrm{mA}$.

Four different source positions were chosen in order

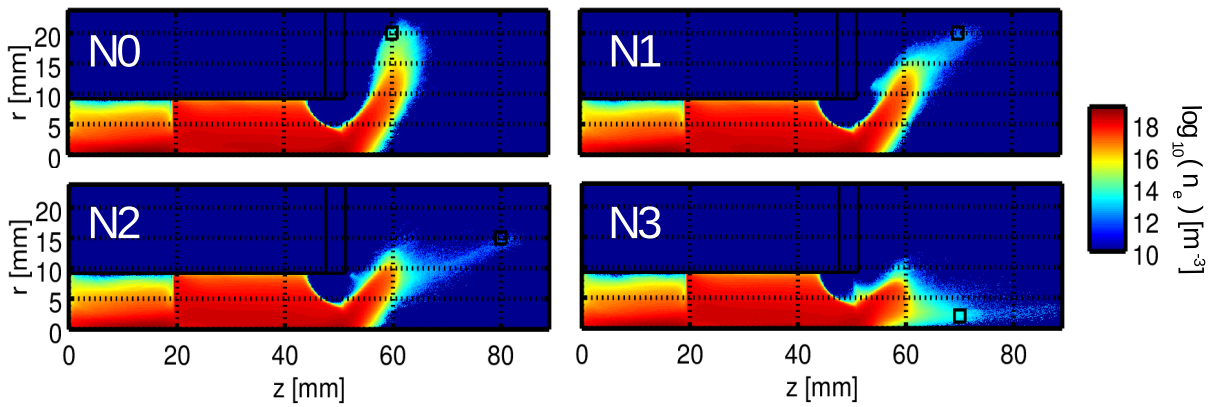

Figure 2. Electron density in logarithmic scale for different source positions.

to study its influence on the plume plasma. In figure 2 the resulting electron density is shown and the black box in the plume indicates the electron source position. The magnetic field lines where the sources N0 and N1 are located, are connected to the front of the metal cap. Sources N2 and N3 aim at the thruster exit. The positions where also chosen to represent different magnetization strengths of the source electrons. While the B-field strengths at positions N1 and N3 are similar, it is nearly doubled at N0 and nearly the half at N2.

In figure 2 the electron density for the different source position is shown in logarithmic scale. The simulated time to reach steady state was in the range of 2–6 µs, which corresponds to a computation time of 20 up to 60 days. For the four cases the channel plasma is practically not changing. At 20 mm the central cusp is clearly visible, as well as the dominant axial transport by the magnetic field lines close to the z-axis, which produces a higher density. Due to the electron loss at the anode, the region between anode and central cusp is less filled than the region between the central and exit cusp, where both cusps act as sources of energetic electrons.

For the sources N0–N2, the electron distribution in the near-field plume and close to the exit is changing only in the low density range. The electron density in the range of $10^{18}\,\mathrm{m}^{-3}$, shown in red, is nearly constant. This distribution is built up by trapped electrons, oscillating between the magnetic mirror and the potential drop. For N2, with lowest magnetic field strength at its source position, electrons are getting accelerated by the potential, which results in a lower density. It increases in the region of higher B due to oscillation in the magnetic trap. In the case of N0, with highest magnetic field strength at the source position, this appears already in the source region and increases with increasing B. The electron distribution formed by source N1 shows a mixture of these two cases. Electrons injected by source N3 fill in a wider area due to the magnetic field configuration in this region.

Since the differences of the electron distribution generated by sources N0, N1 and N2 are only visible in the low density range, the resulting potentials are quite similar. Only the source position of N3 close to the axis shows an electron distribution expanded towards the symmetry axis. Therefore, the resulting potential, in the first row in figure 3, is given for N0 and N3. It clearly shows a flat potential in the channel, which drops in the plume. At the thruster exit the metal wall is forming a potential drop in radial direction which acts as a lens for the non-magnetized ions. For N3, in comparison to N0, the potential distribution in the plume is compressed in radial direction and stretched in axial direction. This is a result of the broader electron distribution close to the symmetry axis.

Since the ions are not magnetized they follow the potential gradient which determines their angular distribution. At the bottom row in figure 3 the corresponding ion densities for electron source N0 and N3 are shown in logarithmic scale. Within the channel the distribution satisfies very well quasi-neutrality, as expected for a plasma. At the thruster exit the potential drop accelerates the ions into the plume. Due to the different electron distributions in the plume, for N0 the distribution of higher ion density is expanding deeper into the plume than for N3. For the angular ion distribution, the influence of the different electron sources is minor, since in both cases ions show a broad distribution. Only close to the symmetry axis the contribution is higher for N3.

The magnetic field configuration in front of the thruster exit determines the distribution of electrons in the plume, whereas the source position influences the ion distribution in the plume only slightly.

4.2. Thermal versus beam-like electron source

Due to the long run time of PIC simulations, it is not possible to represent the full electron dynamics. In the plume electron and neutral density are two orders lower than in the channel with a typical Coulomb collision time of about 50 µs. Typically, for a runtime of

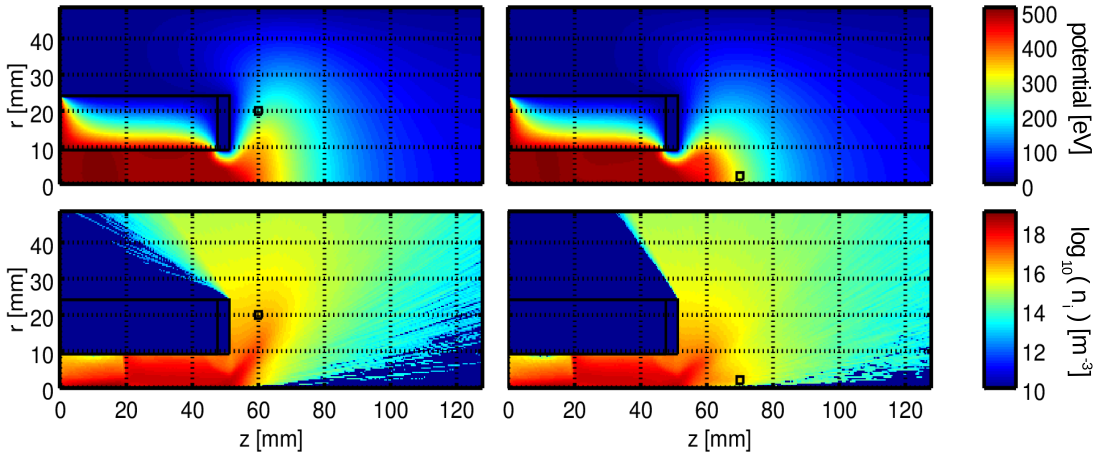

Figure 3. Potential and ion density generated by electron source N0 and N3. The ion density is given in logarithmic scale.

1 month a simulated time in the range of some micro seconds is possible, which does not resolve collision-induced electron diffusion. Therefore, the filling of the plume with electrons guaranteeing quasi-neutrality is not appearing as observed experimentally, as this happens only on the time-scale of collisional transport.
In order to investigate this effect an electron beam directed away from the thruster is used as external source. Electrons with a higher velocity have a larger Larmor radius, which broadens their distribution in the plume. To further reduce the influence of the magnetic mirror the source is placed in a region of low magnetic field strength, similar to the one at the source position of N2. The injected electron beam has a thermal energy of 0.1 eV and a drift velocity of 20 eV. It is directed down-stream the thruster plume, with an angle of 55° with respect to the symmetry axis. As before the cathode current is set to $I_{\mathrm{cath}} = 1.5\,\mathrm{mA}$. The resulting electron density, potential and ion density are shown in figure 4. Densities are given in logarithmic scale. The black box in the plume indicates the electron source position.

As in the previously studied cases, the shape of the electron distribution in the plume remains very similar. But due to the higher probability to cross magnetic field lines, the distribution is broader. Since the magnetic field lines guide the plume electrons into the thruster this results in a higher density at the thruster exit, which increases the collisional rate, filling up the channel volume. As can be seen in the potential plot in figure 4, the increased electron density in the plume extends the potential drop. This affects the ions, which just follow the potential gradients, and a beam with a more pronounced shape and a dedicated peak at around 60° divergence angle is developing. Due to the higher electron density in the channel and close to the exit, the ionization rate increases which increases the ion density, as can be seen in the bottom plot in figure 4.

In figure 5 the angular current distribution with respect to the symmetry axis is given for the two thermal sources N0 and N3 as well as for the beam-like electron source. This distribution is calculated at the outer domain boundary and the angle vertex refers to the thruster exit $z = 51\,\mathrm{mm}$ at $r = 0\,\mathrm{mm}$. It is given in ion current density within 5° normalized to the total measured ion current density. Both thermal sources produce a flat angular distribution, where for source N3, the higher ion density close to the symmetry axis contributes more at low angles. The more extended electron distribution in the plume generated by the beam-like source directed away from the thruster produces a clear ion beam. This is a characteristics which is also seen in experiments [8].

5. Conclusion

In this work the influence of external electron sources on the plume in a multistage plasma thruster was studied. A strong impact of the magnetic field on the electron distribution in the near field plume was observed, especially due to the magnetic mirror effect. The electron distribution was insensitive to the source position in case of a thermal electron source. Only an effective source close to the symmetry axis increases the electron density close to the axis, which leads to higher contribution in the angular current distribution at small angles. In order to overcome calculation time limits and to represent electron diffusion in the plume by collisions, a source of higher energetic electrons directed away from the source was simulated. This produces a broader distribution in the plume, its shape determined by the magnetic field lines. The broader filling produces a more extended potential drop, which generates a pronounced ion beam.
In the experiment this effect might be further increased due to a higher neutral background pressure. Also, secondary electrons produced by impinging ions at the vacuum vessel walls can influence the electron

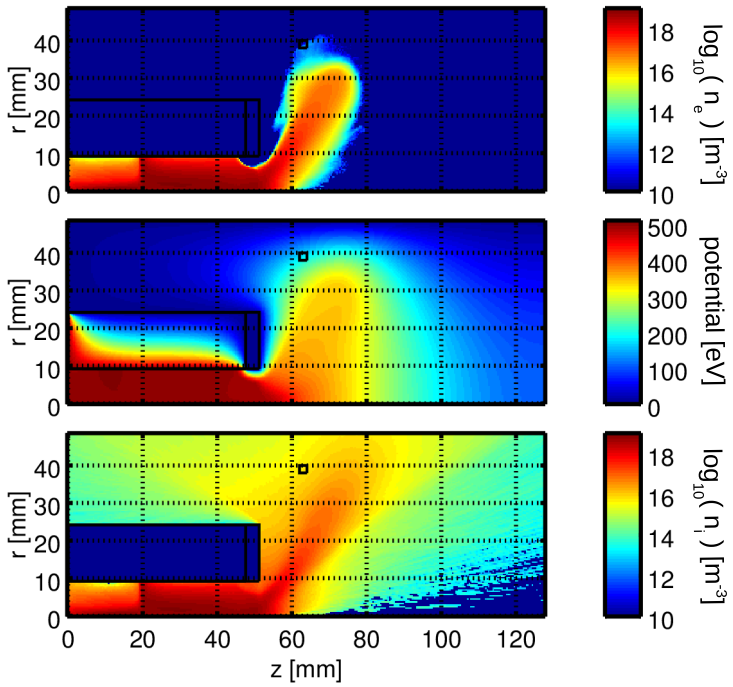

Figure 4. Electron density, potential and ion density for a beam-like electron source directed away from the thruster.

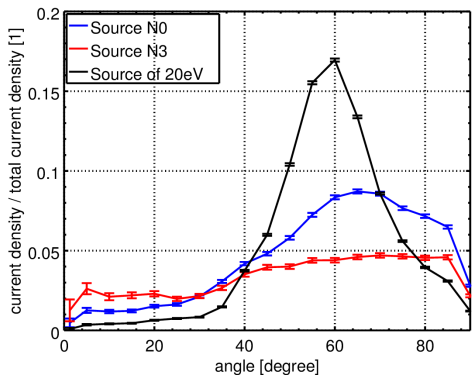

Figure 5. Angular current distribution with statistic error bars and angle given with respect to the symmetry axis.

distribution in the plume acting as additional near-axis source. Due to the magnetic field lines such electrons are guided towards the symmetry axis and would rise the angular current distribution at lower angles.

Acknowledgements

This work was supported by the "ITSim - Skalierung von Ionentriebwerken mittels numerischer Simulation" project of the Bavarian State Ministry of Education Science and the Arts and the German Space Agency DLR.

References

[1] G. Kornfeld, H. Seidel, and J. Wegener et al. Plasma Accelerator Arrangement, 1999. Priority: Germany No. 198 28 704.6, filed 26 June 1998.

[2] N. Koch, M. Schirra, and S. Weis et al. The HEMPT Concept - A Survey on Theoretical Considerations and Experimental Evidences . In *Proceedings of the 32nd International Electric Propulsion Conference*, number IEPC-2011-236, 2011.

[3] N. Koch, H.P. Harmann, and G. Kornfeld. Development and Testing Status of the THALES High Efficiency Multistage Plasma (HEMP) Thruster Family. In *Proceedings of the 29nd International Electric Propulsion Conference*, number IEPC-2005-297, 2005.

[4] O. Kalentev, K. Matyash, and J. Duras. Electrostatic Ion Thrusters - Towards Predictive Modeling . *Contributions to Plasma Physics*, 54:235–248, 2014.

[5] Karl Felix Lüskow. Physics of Ion Thrusters' Plumes . Master's thesis, University of Greifswald, July 2013.

[6] K. Matyash, R. Schneider, and A. Mutzke et al. Kinetic Simulations of SPT and HEMP Thrusters Including the Near-Field Plume Region. *IEEE Transactions on Plasma Since*, 38(9, Part 1):2274–2280, 2010.

[7] R. Procassini, C. Birdsall, E. Morese, and Cohen B. A relativistic monte carlo binary collision model for use in plasma particle simulation codes. *Memorandum No. UCB/ERL M87/24, University of California, Berkeley*, 1987.

[8] K. Matyash, O. Kalentev, and R. Schneider et al. Kinetic Simulation of the stationary HEMP thruster including the near-filed plume region. In *Proceedings of the 31st International Electric Propulsion Conference*, number IEPC-2009-110, September 2009.

[9] F. Taccogna, S. Longo, M. Capitelli, and R. Schneider. Self-similarity in Hall plasma discharges: Applications to particle models. *Phys. Plasmas*, 12:053502, 2005.

Acta Polytechnica **55**(1):7–13, 2015
doi:10.14311/AP.2015.55.0007

available online at http://ojs.cvut.cz/ojs/index.php/ap

MONTE-CARLO RE-DEPOSITION MODEL DURING TERRESTRIAL MEASUREMENTS OF ION THRUSTERS

Julia Duras[a,*], Oleksander Kalentev[a], Ralf Schneider[a,b], Konstantin Matyash[b], Karl Felix Lüskow[a], Jürgen Geiser[a]

[a] *Institute of Physics, Ernst-Moritz-Arndt University Greifswald, Felix-Hausdorff-Str.6, D-17498 Greifswald, Germany*

[b] *Computing Center, Ernst-Moritz-Arndt University Greifswald, Felix-Hausdorff-Str.12, D-17498 Greifswald, Germany*

[*] corresponding author: julia.duras@physik.uni-greifswald.de

Abstract. For satellite missions, thrusters have to be qualified in large vacuum vessels to simulate the space environment. One caveat of these experiments is the possible modification of the beam properties due to the interaction of the energetic ions with the vessel walls. Impinging ions can produce sputtered impurities or secondary electrons from the wall. These can stream back into the acceleration channel of the thruster and produce co-deposited layers. Over a long operation time of thousands of hours, these layers can modify the optimized geometry and induce changes in the ion beam properties, e.g., broadening of the angular distribution and thrust reduction. A Monte Carlo code for simulating the interaction of ion thruster beams with vessel walls was developed to study these effects. Back-fluxes of a SPT-like ion thruster for two different test-setups and vessel geometries are calculated.

Keywords: Ion thruster, Monte-Carlo method, terrestrial testing of thrusters, interaction with vessel walls.

1. Introduction

Ion thrusters, where the propellant is ionized and the ions are accelerated by electric fields, are of increasing importance for scientific and commercial space missions. Compared to commonly used chemical thrusters they have a 5 to 10 times higher specific impulse [1]. This results in a considerably reduced propellant budget, and a significant reduction of spacecraft launch mass by some 100 to 1000 kg can be achieved. One concept for this electric propulsion involves grid-less ion thrusters, which are based on magnetic confinement of the plasma electrons, where the trapped electrons both ionize the propellant and provide the potential drop for ion acceleration. Due to their low complexity in terms of system architecture, they are becoming of increasing interest in particular for commercial satellites.

In order to reduce the development and qualification costs, it is therefore necessary to set up and apply a series of different modeling tools which can quantitatively describe the plasma physics within the thruster, and also the interactions of the thruster with the testing environment and finally with the satellite. The integrated modeling strategy should include several modular components in a consistent way in order to provide the complexity and accuracy required for the problem [2].

Ions created in the thruster discharge may impinge on the surrounding surfaces, which can induce sputter erosion and redeposition of eroded material. Depending on the surface region, this may affect the operational and performance characteristics of the thruster itself, of the ion thruster module, or even of the whole satellite. For the simulation, one can distinguish:

(a) The impact on the inner thruster surface by ions generated in the inner thruster discharge.

(b) The impact on the exit-sided surface of the thruster and the neutralizing electron source by ions generated in the plasma plume downstream the thruster exit.

(c) The impact on the satellite surface producing erosion and redeposition.

(d) The impact on the vacuum chamber walls during testing and life-time qualification, creating redeposition onto the thruster and thruster module surface.

The proposed multi-scale modeling strategy is well suited to address these ion impingement effects.

The outline of the paper is as follows: the modeling strategy is described and the problems of artifacts during terrestrial qualifications are outlined. As one example of this modeling, the influence of the test-setups on particle back-fluxes towards the ion thruster channel is studied with a Monte Carlo model for an SPT-like ion thruster. Finally, the results are summarized.

2. Modeling strategy

The most complete model resolving all time scales of ion thrusters would be a direct coupling of a kinetic plasma model with a molecular dynamics model for the walls. This would allow a fully self-consistent

analysis of the complete system, including plasma dynamics, possible erosion of the thruster walls and the interaction of the exhausted ions with the surrounding satellite surfaces or, during testing and qualification, with the testing environment, like the vacuum chamber walls. This type of solution is not feasible, due to the tremendous computational costs and the high complexity of this combined model. Instead, we propose to use a hierarchical multi-scale set of models, in which the parameterization for a lower hierarchy model can be deduced from a higher level model.

For example, a 3D particle-in-cell (PIC) model can deliver a parameterization of turbulence effects by appropriate anomalous transport coefficients. Transport coefficients based on these runs could then be used in a 2D PIC, which is more practical for production runs.

To get a correct description of both the thruster and the plume plasma, one has to solve a kinetic problem for the whole region of interes,t including all significant physical processes. These are collisions, turbulence effects, surface driven sheath instabilities and breathing modes. A PIC model is therefore a natural choice for this problem. In addition, similarity scaling is applied to further reduce the calculation costs [3].

In order to describe erosion-redeposition processes, one can use various approximation levels of the model. The most thorough description is given by the full molecular dynamic model. However, this would be far too time-consuming, because it resolves each individual atom and their interactions. The next level can be represented by the binary collision cascade model, which assumes an amorphous target and the interaction of particles with the solid based on heavy particle collisions with ions, and additional losses with electrons acting as a viscous force. This model can use the detailed information about flux distributions provided by the PIC code, and can then, on the basis of this, the erosion response of the materials. The most crude approximation is given by a Monte-Carlo (MC) procedure simulating erosion-redeposition on the basis of sputter yield tables calculated from the binary-collision cascade or molecular dynamics model together with information about the plasma fluxes. This model is particular useful due to its simplicity and flexibility for the quantifying the lifetime of ion thrusters.

3. Artifacts during terrestrial measurements of an ion thruster

Terrestrial qualification of a thruster differs significantly from outer space exploitation, in that it is held in a limited vessel, which can create various artifacts on the measured thruster properties. For example, the back scattered flux from the vessel walls can be deposited on the walls of the thrusters, and can in that way form a conducting layer influencing the thruster operating regimes. These measurements are taken in large vacuum vessels, up to 10 times larger than the thruster itself, in order to provide a space-like environment. Despite these dimensions, however interactions of exhausted particles with residual gas and vessel walls still take place and can modify the measurements. One source of differences between measurements in space and during terrestrial testing is the re-deposition of sputtered particles inside the thruster channel or for the grid thruster at the thruster walls. The accelerated ions impinge on the vessel walls and produce sputtered impurities. These can stream back towards the acceleration channel of the thruster and produce co-deposited layers. Over a long operation time of thousands of hours, these layers can modify the optimized geometry of the thruster channel or grids and the inner wall surface. This induces changes in the ion beam properties, e.g., broadening of the angular distribution and thrust reduction, as observed in the test campaigns of HEMP-T [4] and the NEXT grid thruster [5]. A reduced back-flux is therefore important to minimize artifacts in the plume measurements.

Due to the large size difference between the thruster and the vessel, it is possible to parameterize the back-scattered flux from the vessel walls as an effective source for the MC erosion-deposition code. This paper will show that the position of the thruster inside the vessel, the wall material and the vessel geometry play important roles and can influence the plume measurement results.

4. Description of the Monte Carlo model

The Monte Carlo (MC) method is a common approach for plasma-wall problems, for example MC simulations of sputtering and re-deposition are well established in fusion-oriented studies [6] as is magnetron sputtering [7, 8]. The idea of the Monte Carlo model is to sample the primary distribution of the ions with respect to energies, angles and species. These pseudo-particles are followed hitting the vessel walls and generating sputtered particles, based on sputter rates calculated by a binary collision cascade code. Their angular distributions are sampled and the back-flow of the eroded particles from the vessel walls towards the ion thruster acceleration channel is calculated.

In this work, we assume that particles move along rays according to their source distribution. In this 3D model, the vacuum chamber is assumed to be a cylinder with two spherical caps attached to its ends. The angular source distributions of the mean ion energy, the current and the species fraction were generated with respect to the emission angle θ, see Fig. 3. As an example, ion current and energy distributions similar to those published for SPT-100 [9] are used. The fraction of Xe^{2+} to Xe^{+} ions is taken

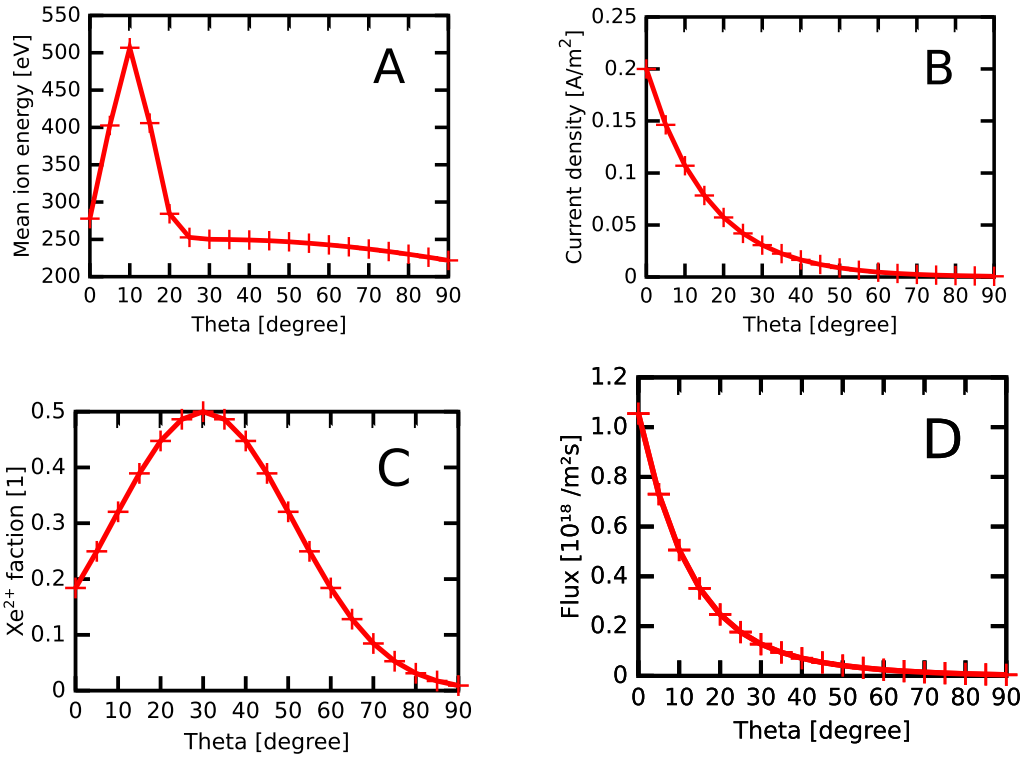

FIGURE 1. Distribution of mean ion energy (A), current density (B), Xe^{2+} faction (C) and the resulting emitted flux (D) similar to SPT-100.

arbitrarily. All used source distributions used here are shown in Fig. 1(A)–(C), sampled as a point source at the thruster exit, within angular steps of $\Delta\theta = 5°$. The resulting emitted flux

$$\Gamma(\theta) = \frac{j(\theta)}{e \cdot (1 + f^{\mathrm{em}}(\theta))}$$

is shown in Fig. 1(D), where $j(\theta)$ is the current density, e is the elementary charge and $f^{\mathrm{em}}(\theta)$ is the emitted Xe^{2+} fraction. Equal distribution of the poloidal angle is used. This distribution represents an emitted beam of Xenon ions with a mean emission angle of $\theta^{\mathrm{em}} = 0°$. The sputter yield for the impinging ions on the vessel walls is taken from SDTrimSP [10] simulations. While the thruster is operating, ions with energies larger than the sputter threshold form a micro roughness on the thruster surfaces. Due to shadowing, this micro-roughness modifies the real angle of incidence, effectively reducing its range to values between 20° and 50°. For this angular range, the sputter yields vary only slightly with angle. We therefore assume that the sputter yields depend only on the energy of the impinging ions. It is also assumed that the sputtered particles obey a cosine law [11] for their angular distribution. Due to their low energies, the sputtered particles are assumed to have a sticking coefficient of 1. Therefore, only particles with direction towards the thruster exit are followed. A detailed description of the Monte Carlo model and its validation with analytic calculations can be found in [12].

In the following, the influence of the thruster position inside the vessel is studied. This is important, since ion thrusters are qualified within various test-setups.

5. Back-flux for two different test-setups

Measurements of plume parameters are taken in two different test-setups: a 'performance test', where a single thruster is placed in the center of the circular cross-section of the vesse,l and an 'end-to-end test', where four thrusters are assembled as a cluster. Performance tests are typically carried out to test and qualifying single thrusters, while end-to-end tests give the characteristics of a whole cluster of thrusters, as it is applied on satellites where only one of the thrusters is operating. The following comparison of the two test setups shows strong dependency of the back-flux on this thruster position.

For the performance test, the ion thruster is placed co-axially in the vessel. In the following, the LVTF-1 vessel at Aerospazio [13] in Siena, Italy was taken as a reference. It has a cylinder length of $Z_c = 7.7\,\mathrm{m}$ and a radius of $R_c = 1.9\,\mathrm{m}$. The spherical cap at the end has a radius of $R_{sp} = 2.7\,\mathrm{m}$. For simplicity, the ion thruster is approximated by a cylinder with a length of $L = 9.0\,\mathrm{cm}$ and a diameter of $D = 9.0\,\mathrm{cm}$. In most test chambers, graphite-coated walls are used in order to reduce the back-fluxes of sputtered par-

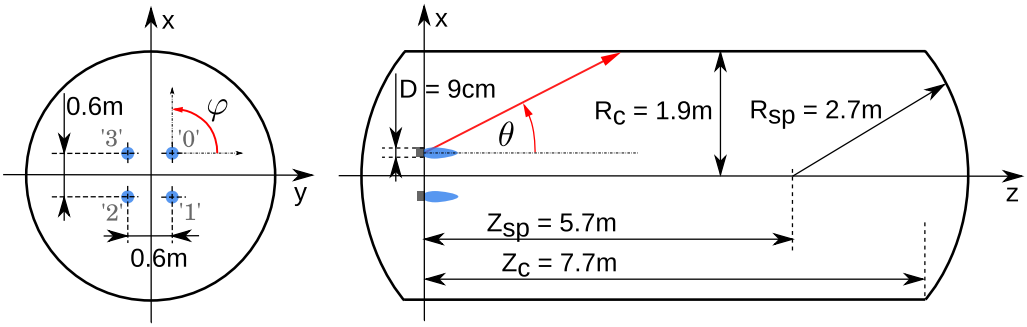

Figure 3. Sketch of a thruster cluster assembled in the LVTF-1 vessel within an end-to-end test set-up. '0' to '3' indicate the different thrusters.

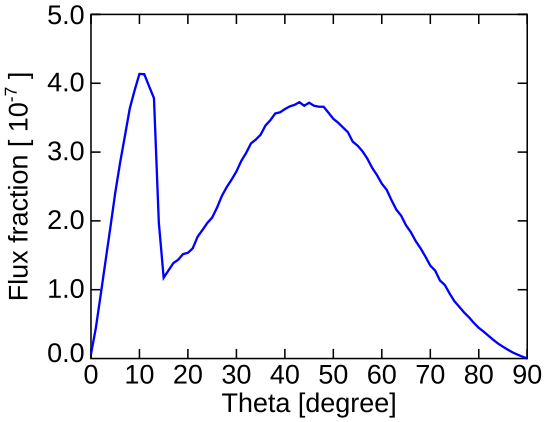

Figure 2. Calculated back-flux towards the thruster exit in total (total flux fraction of $1.97 \cdot 10^{-5}$).

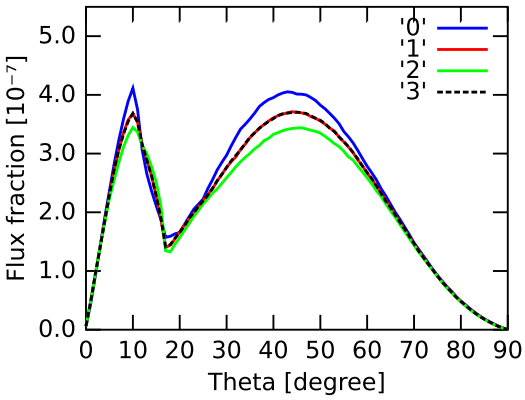

Figure 4. Calculated back-flux to four thruster channels with a total flux fraction of $f = 8.0 \cdot 10^{-5}$.

Thruster	$\int f(\theta)\, d\theta$
'0'	$2.11 \cdot 10^{-5}$
'1'	$2.00 \cdot 10^{-5}$
'2'	$1.91 \cdot 10^{-5}$
'3'	$2.00 \cdot 10^{-5}$

Table 1. Calculated back-flux to four thruster channels with a total flux fraction of $f = 8.0 \cdot 10^{-5}$.

ticles, since graphite has a lower sputter yield than aluminum. However, in the case of carbon the release of hydrocarbons is a major problem linked to the sponge-like characteristics of carbon with respect to its interaction with hydrogen. The sputtered hydrocarbons produce a co-deposited layer inside the thruster channel, which can become conductive and can therefore change the potentials and can produce subsequent problems. When carbon is replaced by metal walls, the rates of physical sputtering are larger, but the evaporation in the hot parts of the channel will prevent deposition inside the thruster [2]. Aluminum walls are therefore studied with the Monte-Carlo model.

Within this model, the back-flux is collected on a circle, which represents the thruster exit. The calculated back-flux fraction towards the source is shown by a blue line in Fig. 2. It is given by the number of particles hitting the thruster exit in a certain angular range $[\theta; \theta + \Delta\theta]$, with $\Delta\theta = 1°$, divided by the total number of source particles. For the chosen parameters of the vessel, the back-flux for $\theta = [0; 14°]$ originates from the spherical cap, while for $\theta = [14°; 90°]$ it comes from the cylindrical walls of the vessel. The flux fraction shows a pronounced peak at around 10° and a broader peak at about 45°. These structures are determined by the combination of the mean ion energy distribution of the emitted Xenon ions, the sputter yield and the cosine distribution of the sputtered particles. The first peak at 10° is dominated by the maximum of the mean ion energy which takes place at the same emitting angle. The second peak is given by the combination of decreasing mean ion energy, with increasing θ and increasing back-flow as given by the cosine law. For zero degree emission angle less flux is seen, due to the small number of emitted particles in this angular region, because of its small circular area for $\theta \in [0; 1°]$.

For the 'end-to-end' simulations the same vacuum chamber was taken as a reference. A sketch of the implemented geometry is shown in Fig. 3. In order to reduce the artifacts further, all thrusters are pointing

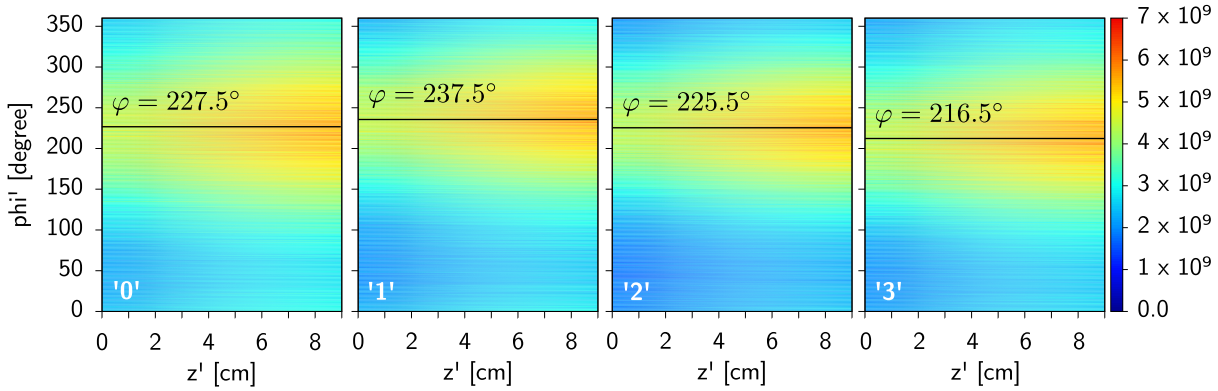

FIGURE 5. Re-deposited flux in $s^{-1}m^{-2}$ inside the four 9 cm long thruster channels within an end-to-end test setup at the LVTF-1 vessel. Total re-deposited flux $\Gamma = 4.3 \cdot 10^{+12}\,m^{-2}s^{-1}$

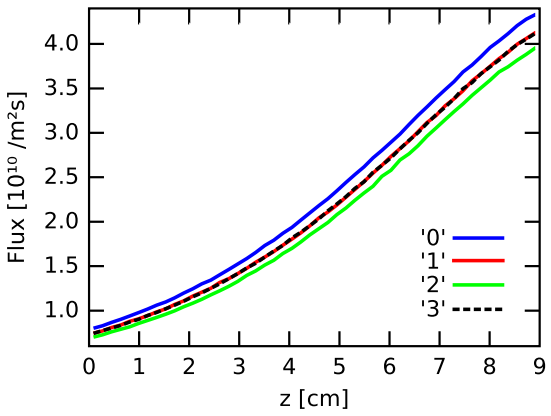

FIGURE 6. Re-deposited flux along the four thruster channels.

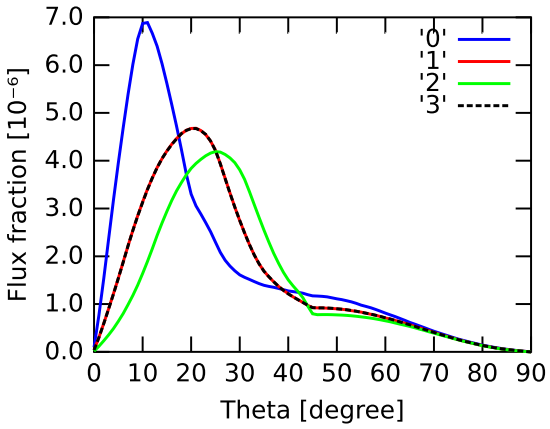

FIGURE 7. Calculated back-flux to four thruster channels with total flux fraction of $f = 5.7 \cdot 10^{-4}$ at the ULAN vessel.

Thruster	$\int f(\theta)\,d\theta$
'0'	$1.61 \cdot 10^{-4}$
'1'	$1.42 \cdot 10^{-4}$
'2'	$1.26 \cdot 10^{-4}$
'3'	$1.42 \cdot 10^{-4}$

TABLE 2. Calculated back-flux to four thruster channels with total flux fraction of $f = 5.7 \cdot 10^{-4}$ at the ULAN vessel.

in the same direction. Thruster '0' was chosen as the operating thruster.

The computed back-flux fractions towards the thruster exit planes of all four thrusters are shown in Fig. 4. The integral flux fraction for each thruster is given in Table 1. Most of the back-flux is measured for thruster '0', since it is the emitting source. One can see that the integral deposited flux decreases with distance to the source. Therefore, equal flux distribution for symmetrically placed thrusters '1' and '3' is reasonable. Since the emitting source is not placed co-axially in the vessel one cannot deduce, where the sputtered particles originate from. In addition, the back-flux is no longer equally distributed in poloidal direction. In Fig. 5, the back-flux on the simplified inner thruster channel wall is given with respect to the depth z' and the poloidal angle φ of the thruster. Here the z'-axis is the symmetry axis of the cylinder, where $z' = 0$ cm is at the anode and $z' = 9$ cm is at the thruster exit. As expected, the flux is slightly higher in the thruster exit region and decreases towards the thruster bottom, see Fig. 6. It shows the measured flux summed over the poloidal angle. In poloidal direction, the distribution varies and the angle with maximum flux

$$\varphi = \max_{\varphi} \int n(\varphi, z')dz'$$

along the z-axis is given in each plot. Thrusters '0' and '2' show approximately the same maximum angle, while for the others the angle is shifted by ±10°. This can be explained by the symmetric thruster positions within the vessel with respect to the emitting source. In total, the re-deposition distribution pattern is nearly the same for all four thrusters, due to the

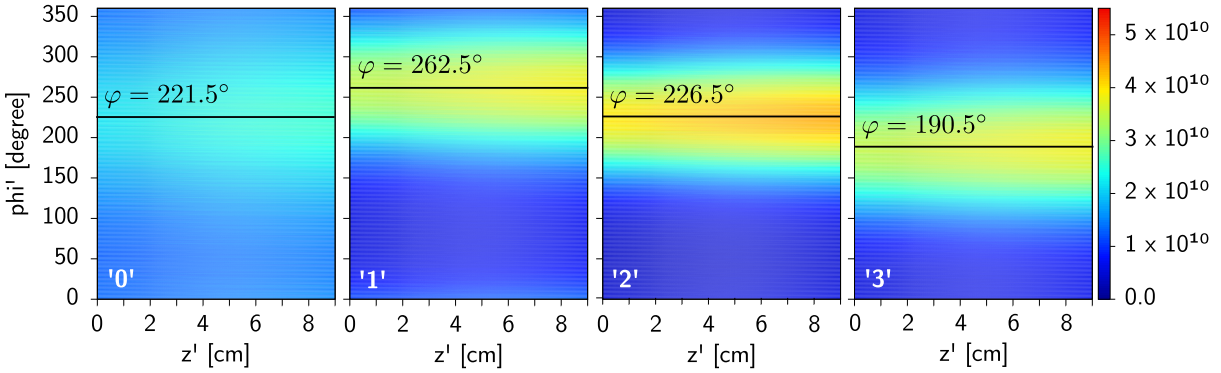

Figure 8. Re-deposited flux in $s^{-1}m^{-2}$ inside the four 9 cm long thruster channels within an end-to-end test setup at the ULAN vessel. Total re-deposited flux $\Gamma = 2.4 \cdot 10^{+13}\,m^{-2}s^{-1}$

large vessel geometry in comparison with the thruster size, and the narrow beam-like emission distribution.

For the purposes of comparison, the same simulation was carried out for a smaller vessel. The ULAN facility [14] in Ulm was modeled. It has a cylinder length of $Z_c = 2.9\,m$ and a radius of $R_c = 1.2\,m$. As in Aerospazio, the thruster cluster is placed co-axially in the vessel. In Fig. 7, the back-flux fraction at the exit planes and the integral flux fraction are given in Table 2. The total back-flux fraction $f = 5.7 \cdot 10^{-4}$ is about 14 times higher than for the larger Aerospazio vessel $f = 8.0 \cdot 10^{-5}$. A clearer distinction between the four thrusters and a different back-flux pattern develop. The maximum back-flux is measured for the emitting thruster '0', while it decreases with distance from the source, as can be seen in Tab. 2. These differences can be explained by the thruster position closer to the cylinder walls of the vessel. The back-flux for each channel is given in Fig. 8. Here, too, the re-deposition decreases with channel depth, as expected, but more pronounced re-deposition areas with parts of practically no re-deposition build up. In comparison with the larger vessel, the maximum peak is approximately one order higher. While for thruster '0' the re-deposition is almost equally distributed within the channel, a peak builds up with increasing distance from the emitting source, resulting in the highest maximum flux for thruster '2'. Also, the position of the maximum back-flux varies more in poloidal angles φ. Here, the symmetric thruster positions within the vessel with respect to the emitting source is important. These distribution characteristics correspond to observations during testing of the HEMP-T (B.van Reijen, personal communication, June, 2014).

Summarizing these results, a complex re-deposition profile appears due to the non-central position of the source within the vessel. Therefore, the source particles do not hit the vessel walls equally distributed in φ, which destroys the poloidal symmetry of the emitted flux hitting the vessel walls. In addition, the distribution of the sputtered particles is overlying, which gives no poloidal symmetry of the re-deposited particles, although the test-setup has such a simple geometry. The size of the vessel not only influences the amount of re-deposited particles but also gives a more pronounced re-deposition pattern.

6. Conclusion

A Monte Carlo model using a ray approximation for the particles allowsus to calculate the back-flux towards the thruster exit generated by sputtered particles at the vessel walls. It has shown the influence of the test set-up and the vessel size, which affects the re-deposition pattern inside the thruster channels. A non-centered emitting source leads to a complex re-deposition profile within the thruster channels. This effect can be diminished with a larger vacuum vessel which reduces the back-flux and smoothes the re-deposition patterns inside the channel. The emission distribution of the thruster itself also plays an important role. The results represent a worst case scenario, since the emission distribution of the thruster was assumed to be beam-like and aluminum was taken as the vessel wall material. For broader emission distributions and back-flux reducing modifications, e.g., carbon walls or baffles [2], the effects are reduced.

Effects like secondary electron emission at the vessel walls, which influence the plume potential, collisions of propellant ions with residual gas, regions of magnetized electrons in the plume and changes in the thruster potential due to re-deposited layers inside the channel are not considered within this model. In a future modeling step, the estimated back-flux distribution can be used for simulating the erosion and re-deposition on the thruster surfaces. This could clarify more precisely how terrestrial conditions influence the thrust measurements in total.

Acknowledgements

This work was supported by the German Space Agency DLR through Project 50 RS 1101.

References

[1] N. Koch, H.-P. Harmann, G. Kornfeld (eds.). *Status of the THALES High Efficiency Multi Stage Plasma Thruster Development for HEMP-T 3050 and HEMP-T*

30250, IEPC-2007-110. 30th International Electric Propulsion Conference, 2007.

[2] O. Kalentev, K. Matyash, J. Duras, et al. Electrostatic Ion Thrusters - Towards Predictive Modeling. *Contributions to Plasma Physics* **54**:235–248, 2014. DOI:10.1002/ctpp.201300038.

[3] K. Matyash, R. Schneider, A. Mutzke, et al. Kinetic Simulations of SPT and HEMP Thrusters Including the Near-Field Plume Region. *IEEE Transactions on Plasma Since* **38**(9, Part 1):2274–2280, 2010. DOI:10.1109/TPS.2010.2056936.

[4] A. Genovese, A. Lazurenko, N. Koch, et al. (eds.). *Endurance Testing of HEMPT-based Ion Propulsion Modules for SmallGEO*, IEPC-2011-141. 32th International Electric Propulsion Conference, 2011.

[5] R. Shastry, D. A. Herman, G. C. Soulas, M. J. Patterson (eds.). *Status of NASA's Evolutionarry Xenon Thruster (NEXT) Long-Duration Test as of 50,000 h and 900 kg Throughput*, IEPC-2013-121. 33th International Electric Propulsion Conference, 2013.

[6] R. Behrisch, W. Eckstein. Springer-Verlag.

[7] V. Serikov, K. Nanbu. Monte Carlo numerical analysis of target erosion and film growth in a three-dimensional sputtering chamber. *Journal of Vacuum Science & Technology A: Vacuum, Surfaces, and Films* **14**(6):3108–3123, 1996. DOI:10.1116/1.580179.

[8] C. Shon, J. Lee. Modeling of magnetron sputtering plasmas. *Applied Surface Science* **192**(1–4):258–269, 2002. Advance in Low Temperature RF Plasmas, DOI:10.1016/S0169-4332(02)00030-2.

[9] L. King. *Transport-property and mass spectral measurements in the plasma exhaust plume of a Hall-effect space propulsion system.* Ph.D. thesis, University of Michigan, 1998.

[10] A. Rai, A. Mutzke, R. Schneider. Modeling of chemical erosion of graphite due to hydrogen by inclusion of chemical reactions in SDTrimSP. *Nuclear Inst and Methods in Physics Research, B* **268**(17-18):2639–2648, 2010. DOI:10.1016/j.nimb.2010.06.040.

[11] W. Eckstein. *Computer Simulation of Ion-Solid Interaction*, vol. 10 of *Springer Series in Material Science*. Springer, 1991.

[12] O. Kalentev, L. Lewerentz, J. Duras, et al. Infinitesimal Analytical Approach for the Backscattering Problem . *Journal of Propulsion and Power* **29**(2):495–498, 2013. DOI:10.1002/ctpp.201300038.

[13] AEROSPAZIO Tecnologie s.r.l. `http://www.aerospazio.com` [2014-02-01].

[14] H.-P. Harmann, N. Koch, G. Kornfeld (eds.). *The ULAN Test Station and its Diagnostic Package for Thruster Characterization*, IEPC-2007-119. 30th International Electric Propulsion Conference, 2007.

Simulation for an improvement of a down-scaled HEMP thruster

By Tim BRANDT[1,3,4], Ralf SCHNEIDER[2], Julia DURAS[2], Daniel KAHNFELD[2], Holger KERSTEN[4], Frank JANSEN[1] and Claus BRAXMAIER[1,3]

[1] *DLR, Institute of Space Systems, Bremen, Germany*
[2] *Institute of Physics, Ernst-Moritz-Arndt University Greifswald, Greifswald, Germany*
[3] *Center of Applied Space Technology an Microgravity, University of Bremen, Bremen, Germany*
[4] *Institute of Experimental and Applied Physics, University of Kiel, Kiel, Germany*

(Received August 21th, 2016)

Abstract: We present an electrostatic Particle-in-cell simulation of a downscaled High Efficiency Multistage Plasma Thruster (HEMPT). The purpose of downscaling the HEMPT design is to reach the requirements of missions which have a need for low thrust (0.1...150 μN) and low noise (root of the noise spectral density $\leq 0.1\ \mu\mathrm{N}/\sqrt{\mathrm{Hz}}$). These are upcoming formation flying space missions like eLISA (evolved Laser Interferometer Space Antenna) or NGGM (Next Generation Gravity Mission). The aim of the here presented numerical simulations is to get an improved understanding of the thruster's physics especially in its downscaled configuration, in order to reach the design goals.

Key Words: HEMPT, Cusped Field Thrusters, Magnetized Plasmas, Plasma Simulation, Particle-in-Cell Method

Nomenclature

HEMPT	:	High Efficiency Multistage Plasma Thruster
FEMM	:	Finite Element Method Magnetics
SCCM	:	Standard Cubic Centimeters per Minute
PIC	:	Particle-In-Cell
MCC	:	Monte-Carlo Collisions

1. Introduction

Upcoming formation flying space missions like eLISA (evolved Laser Interferometer Space Antenna) [1] or NGGM (Next Generation Gravity Mission) [2] create a new demand for highly precise attitude control. In eLISA, three satellites form a space based interferometer. For this interferometer to work properly these satellites must keep the test masses in a drag free environment. The demands lie in the micro-Newton regime for thrust and noise levels with continued operation for several years. One promising candidate to reach these goals is the High Efficiency Multistage Plasma Thruster (HEMPT). This is a new type of grid less thruster with a magnetic field topology which reduces plasma-wall contact. Both being grid less and minimising wall contact enables long live-time, which has been demonstrated in experiments [3] . The latest models show stable operation over a wide range of parameters. The simple and robust design, due to the use of permanent magnets and direct current, makes it applicable to miniaturization. An effort to downscale this thruster into the demanded thrust and noise regime is undertaken in cooperation of Airbus Defence and Space, the Center of Applied Space Technology and Microgravity (ZARM) of the University Bremen, the Workgroup Plasma Technology of the University of Kiel and the German Aerospace Center (DLR). This campaign consists of a breadboard level model of the thruster [4] , a highly precise thrust balance [5] , and computer modeling to support the development [6] . The first models of the downscaled HEMPT reach the higher μN regime, however, a better understanding of the thrusters inner working is required to reach the low thrust required for e.g. eLISA. The aim of the modeling part of the campaign is to gain this understanding. We present results of the first simulations of a downscaled HEMPT, including its discharge chamber and its near exit region.

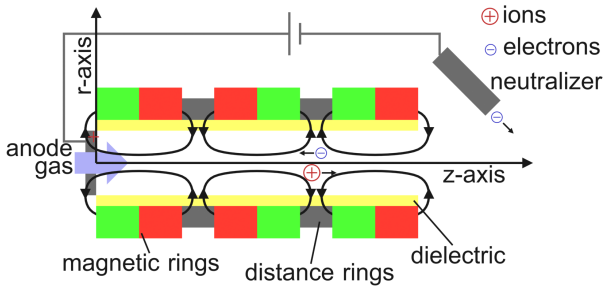

Fig. 1. HEMP thruster principle.

2. Model setup

The HEMPT uses a direct current discharge for ion generation, where electron confinement is improved by a static magnetic field with cusps [7] . Fig. 1. shows the thrusters principle. Fig. 2. describes the simulation domain in the HEMPT thruster.

A typical HEMPT, like the DM3a thruster, has a discharge channel length of $Z_{thr} = 51\ mm$ and inner radius of $R_{thr} = 9\ mm$. With the micro HEMPTs parameters of $Z_{thr} = 14\ mm$ and $R_{thr}1.5\ mm$, its length is scaled down by a factor of 3.6 and its inner radius by 6. Due to the inverse dependence of the gyroradius on the strength of the magnetic field, the magnetic field must be increased by the scaling factor to obtain the same magnetization for electrons in the micro HEMPT as in the origi-

nal HEMP. However, the possibilities of such an increase are limited for permanent magnets. For the same permanent magnet geometry, the maximum flux density stays the same when scaling down. The maximum flux density inside the micro HEMPTs discharge channel (e.g. at $Z = 11\ mm$, $R = 0\ mm$, with Z being counted from the anode surface) is about $0.6\ T$. For a $12.5\ eV$ electron the gyroradius is $0.02\ mm$, which is only about 1 % of the accelaration channel radius of $1.5\ mm$). This indicates that the magnetic confinement is still effective even in this downscaled HEMPT. Near the magnetic cusps the flux is about $0.2\ T$ and lower, the increase in gyration radii enables the electrons to overcome the cusp structure [8) 9)] and reach the anode. At the exit cusp outside the channel the flux is also low (e.g. $0.05\ T$ at $Z = 17\ mm$, $R = 0\ mm$), and the strong electric field drags the electrons inside. When entering the channel, electrons have already a significant portion of the anode potential of 400 eV by accelaration of the potential drop forming at the thruster exit.

The domain for the simulation of the downscaled thruster investigated here is a $r-z$ plane which corresponds to a cylinder with the radius $R = 5.12\ mm$ and the length $Z = 20.48\ mm$. It includes not only the thruster's discharge chamber, but also its near exit region. The $Z = 0$ position lies at the anode surface. The discharge chamber extends beyond that into a section, which is mostly occupied by the neutral gas inlet and is not modeled in detail. The static magnetic field within this domain is imported from a finite element simulation using the software FEMM (Finite Element Method Magnetics), based on the geometric and material properties of the permanent magnet arrangement. Its $r-z$ simulation domain consists of a triangular mesh. The resulting flux density in $r-$ and $z-$ direction is than interpolated to the regular grid of the plasma simulation.

The result of a DSMC (Direct Simulation Monte Carlo) [10)] simulation of the neutral gas for an inflow of $0.27\ SCCM$ (Standard Cubic Centimeters per Minute) Xenon is imported to create the neutral gas distribution inside the simulation domain. The neutral gas inlet of the thruster redirects the gas so that it directly hits the interior of the discharge chamber wall. This is done to thermalize the neutral atoms. By this, their axial momentum and thus neutral thrust is reduced. Since this section is not part of the simulation, a small volume source was inserted near the place where the actual inlet is. This source inserts the neutrals with a thermal velocity according to the Maxwell-Boltzmann distribution. The neutrals are reflected at the dielectric walls of the discharge channel. In reality the way the particles are reflected depends on the surface roughness and is supposed to lie somewhere between total reflection and diffuse reflection. This value is not known by experiments and can change over time due to ion sputtering. The assumption of solely diffuse reflection gave good agreement between simulated and measured neutral gas thrust. The simulated thrust was calculated by the mass flow and the exhaust velocity, which lies roughly at the average thermal velocity of the neutrals at 500 K. The experiments showed that the overall reduction of neutral gas due to ionization was around 25 %. Considering this relatively low value, and because the timescale of the simulation is too short for significant changes in the neutral gas, it is kept as a static background.

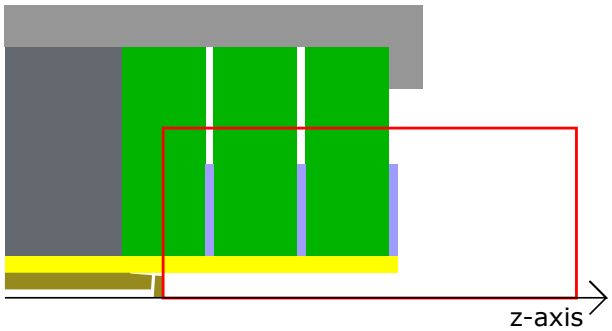

Fig. 2. Simulation domain (red) in comparison to the real thruster. Dielectric (yellow), distance rings (blue-gray), magnets (green), neutral gas inlet (brown), thruster housing (grey).

For an average neutral gas density inside the discharge channel of about $2 \cdot 10^{20}\ m^{-3}$, the ionization mean free path for an electron at $12.5\ eV$ is $4.76\ m$. At $100\ eV$, which is about the energy for the maximum of the ionization cross section [11)], the mean free path becomes $0.086\ m$, which is still several times larger than the discharge channel length ($0.014\ m$). This shows the necessity of magnetic confinement.

For the downscaled system to stay the same as the original, additional to the magnetic field strength the neutral gas density must be increased. Only then the Knudsen number, which is the ratio of the mean free path to system length, stays constant. However, for the micro HEMPT the neutral gas flow should be kept low in order to reduce thrust fluctuations caused by non-ionized gas outside the thruster.

For the plasma simulation, a fully self-consistent kinetic electrostatic Particle-In-Cell (PIC) [12)] modeling code is needed, as this enables to properly represent non-local effects and accurate energy distributions function for all plasma particles. The PIC method is combined with Monte-Carlo collisions (PIC-MCC). In plasma physics PIC is a widely accepted method to obtain a better understanding of the basic physics mechanisms in various systems, because PIC-MCC provides full insight for all (microscopic and macroscopic) parameters. A more detailed description of the PIC-MCC method itself can be found in several reviews [13) 14)] . The principle of PIC is to follow so-called super-particles. Each of them represents the same number of physical particles following the same trajectory as single particles due to their identical mass-to-charge ratio resulting in the same Lorentz force. The electric field for the Lorentz force is calculated self-consistently on a spatially equidistant grid from the Poisson equation. In the electrostatic approximation, magnetic field effects are included in the Lorentz force, but are determined just by their external sources (e.g. magnets). Corrections from plasma currents are neglected. Particles experience collisions according to Monte-Carlo collision algorithms. This allows to implement all relevant collision types. For this work electron-neutral elastic, ionisation, excitation, coulomb and charge exchange collisions are implemented. Neutrals are treated as plasma particles with zero charge.

As fully kinetic methods are computationally expensive, an efficient use of MPI (Message Passing Interface) for parallel computing was considered necessary. A number ratio of 1 : 2618 for the so-called super particles to real particles is applied to the Xenon ions and electrons. This is to ensure that in the cells at the symmetry axis, for the maximum assumed plasma

density, there are no less than six super particles, in order to keep numerical noise low.

Long range electrostatic interactions are resolved on the simulation grid, which has 1024×256 cells. The volume $0\ mm \leq z \leq 14\ mm$, $2.5\ mm \leq r \leq 5.12\ mm$ is grounded, in order to represent the magnets and their distance rings. The remaining upper domain boundary ($14\ mm \leq z \leq 20.48\ mm$) and the right side ($0\ mm \leq r \leq 5.12\ mm$) has a potential fixed at $0\ V$.

The anode lies at $z = 0\ mm$ (left side) in the range from $0\ mm \leq r \leq 1.5\ mm$ on a potential of $400\ V$. It should be noted that in the real experimental setup the grounded boundaries are the walls of the vacuum vessel, who are much further away from the thrusters exit. The chosen domain size and thus the position of the boundaries is a compromise between saving computational time and simulation accuracy.

The cell size of $\Delta r = 2 \cdot 10^{-5}\ m$ and the timestep $\Delta t = 3.17 \cdot 10^{-12}\ s$ are chosen in order to resolve the Debye lengths and the electron cyclotron frequency. The spatial domain is two-dimensional (axial and radial), but due to collisions three components in velocity space need to be resolved.

The size of the domain is scaled down by a factor of four to overcome spatial resolution limits. One applies a self-similarity scaling keeping the relevant non-dimensional parameters constant, namely the ratio of system length to gyroradii and to mean free path. The first represents the influence of the magnetisation by the external magnetic field, the second one the collisional effects. In order to preserve the ratio of both the charged particles mean free paths and their gyration radii to the system length, the electron source strength and neutral gas inflow is reduced by the same factor, while the magnetic field strength is increased by this factor. This ensures the physical correctness of the simulation as proven by [15] . However, as soon as surface processes and sources get important the scaling derived for infinite plasmas deviates from the real solution, because the surface to volume ratio changes with system size. The results have to evaluated carefully for possible surface-dominated effects. For the densities and currents presented in this work, their values are scaled back for the original sized system.

It has been shown [16] that turbulence in a plasma can be created or at least be enhanced by magnetic fields. The nonlocal effect is also observed in systems like the cylindrical Hall thruster from PPPL [17] . According to this [16] , anomalous diffusion is implemented in velocity space to account for this cross-field transport linked with varying magnetic field. A value of $1 \approx m^2 s^{-1}$ is used, based on diffusion coefficients from magnetic fusion [18] .

At $r = 1.5\ mm$ over the distance $0\ mm \leq z \leq 14\ mm$, surface charge accumulation on the ceramic tube, that forms the discharge chamber, is taken into account. A surface with equal properties is at $z = 14\ mm$, $1.5\ mm \leq r \leq 2.5\ mm$, which forms the top end of the ceramic tube. The accumulated charge densities are taken into account in the potential calculation. Also a simple secondary electron emission model is implemented, where 50 % of the electrons are re-emitted with 90 % of their incident energy. All other boundaries for the charged particles are that they are completely absorbed. In the real thruster, the electron source (neutralizer) is located relatively far outside, approximately $z = 14\ mm$, $r = 40\ mm$. This is far beyond the simulation domain. Strictly following the magnetic field lines, the electrons would not reach the discharge channel from this position, yet the experiments suggest they do. The magnetic field so far outside is weak, hence the electrons gyration radii are large, therefore it is reasonable to assume that they are evenly distributed before they reach the close proximity of the discharge channel exit. Therefore, an approximation is a spatially even distributed source at the maximum r and maximum z boundary. The electrons are injected with a thermal energy of $1\ eV$, enough to give them some initial movement, yet negligible towards the energy they will gain from the $400\ V$ potential drop.

In order to speed up the plasma discharge ignition, an additional electron source was inserted at the discharge channels exit. This source was shut down after $1.5 \cdot 10^6$ time steps. The complete simulation was run over $1.1 \cdot 10^7$ time steps.

3. Results

Even for larger systems a direct experimental access to the plasma parameters in a thruster is rather difficult. Due to the small size of the HEMP thruster studied in this work it is rather impossible to receive detailed experimental information about profiles inside the thruster. Here, this simulation offers the only possibility to get an improved understanding of the profiles and physical principles in downscaled HEMPTs. Using the PIC-MCC code one is able to calculate all relevant parameters of the device.

Fig. 3. shows the profile of the electric potential for a quasi steady-state condition after a simulated time of $3.487 \cdot 10^{-5}\ s$ (averaged over $1 \cdot 10^6$ time steps). The potential is mostly flat throughout the discharge channel, with a value close to the anode potential.

The potetial is determined by the competition of parallel and perpendicular transport of the electrons. The dynamics of the heavy ions is then a consequence of the quasi-neutrality of the plasma, that means that the overall distribution of electron and ion density minimizes charge separation. Therefore, like in the case of this device, magnetization of the electrons is already sufficient to actively control the dynamics and density of the plasma by magnetic fields. Because the ions just follow the electrons to avoid large electric fields, which anyhow would counteract charge separation on the characteristic length scales larger than a Debye length. The magnetic field structure determines then, like in the case of the larger HEMPT, the electron density, shown in Fig. 9. .

Close to the z axis the magnetized electrons move practically parallel to it towards the anode and tend to create a rather smooth potential in z-direction due to the very large parallel transport. Only in the cusp regions electrons are directed towards the dielectric channel wall and produce pronounced maxima of the particle fluxes hitting the surface. In the other regions radial transport has to overcome the magnetic confinement. This is only possible by collisons [19] or anomalous turbulent transport. In comparison to the larger HEMPT models the electron density fills up the accelaration channel more uniformly, which is a consequence of the larger radial transport in the smaller device studied here. The ratio of gyroradii of the electrons to discharge radius is larger in this smaller device as discussed before and this induces larger transport in radial direction. The ions have nearly the same density distribution as

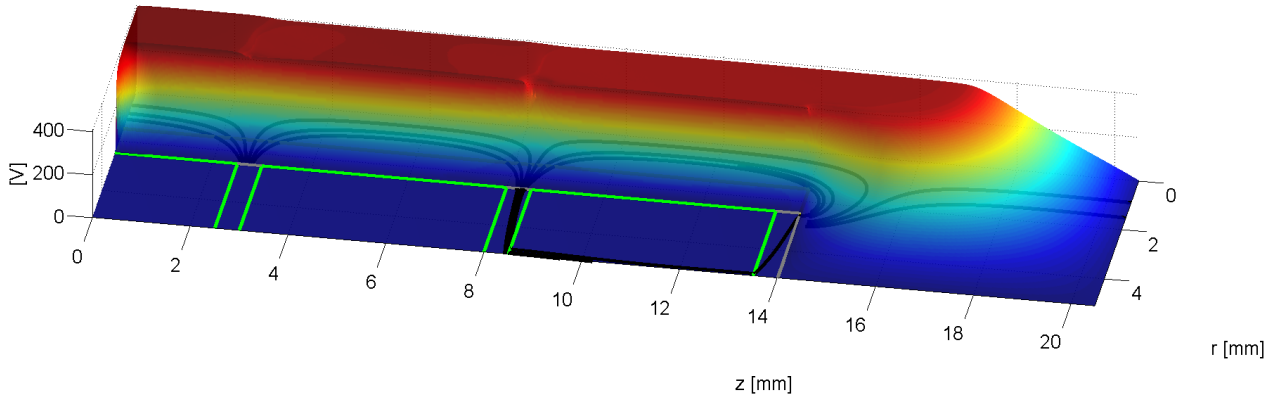

Fig. 3. Electric potential. Dielectric surface (yellow), distance rings (gray), magnets (green), magnetic field lines (black).

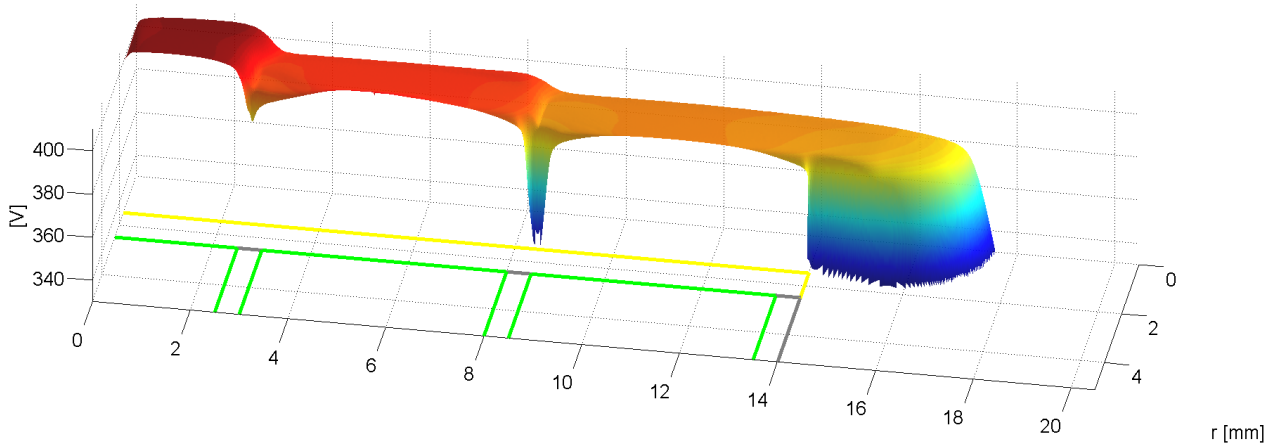

Fig. 4. Electric potential 330 - 410 V (potential inside the dielectric not shown).

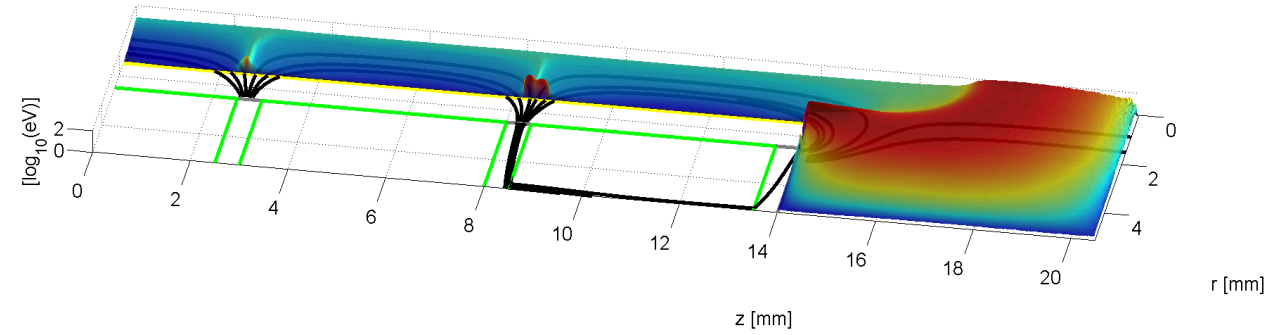

Fig. 5. Electrons energy.

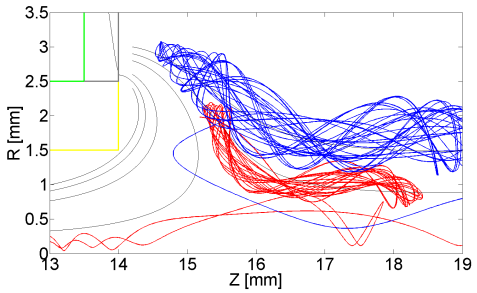

Fig. 6. Particle traces.

the elctrons to satisfy the quasi-neutrality constraint. The dielectrics produces a radial structure of the potential by the formation of a sheath, which is quite narrow as expected (typically 5 to 10 Debye lengths). In contrast to a metallic wall, the dielectrics is not enforcing a constant potential along its surface, but is determined by the surface charge collected locally, but affecting the potential non-locally as determined by the Poisson equation. The dielectrics is not requiring any explicit boundary condition in the solver, just the change of the dielectric constant and the accounting of surface charges in the boundary cell in front of the dielectrics. The dielectrics in this model is quite narrow (1 *mm*) and then grounded elements are forcing the potentail to 0 *V*. Fig. 4. highlights the potential at 330–410 *V*. Near the anode the plasma potential is about 10 *V* (relative to the anode potential of 400 *V*). At the first magnetic cusp, the potential undergoes a drop of about 20 V. At the second cusp inside

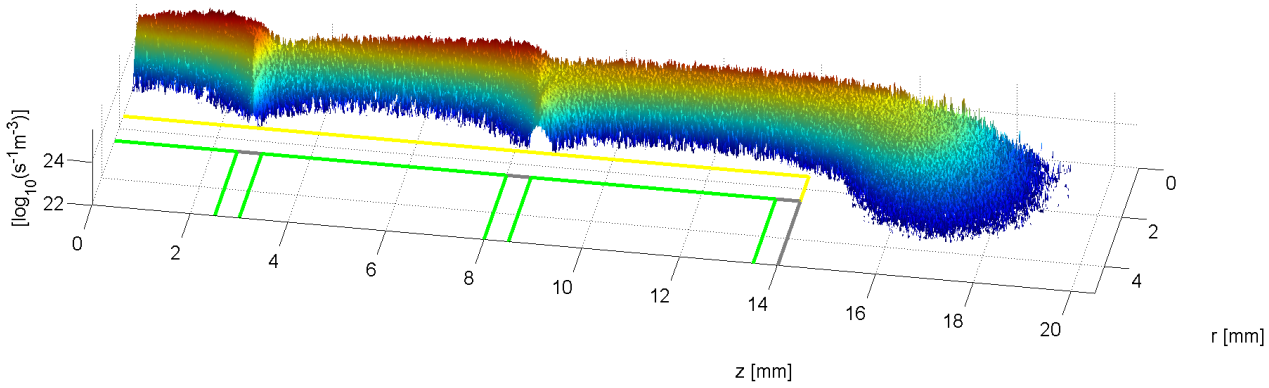

Fig. 7. Ionization rate.

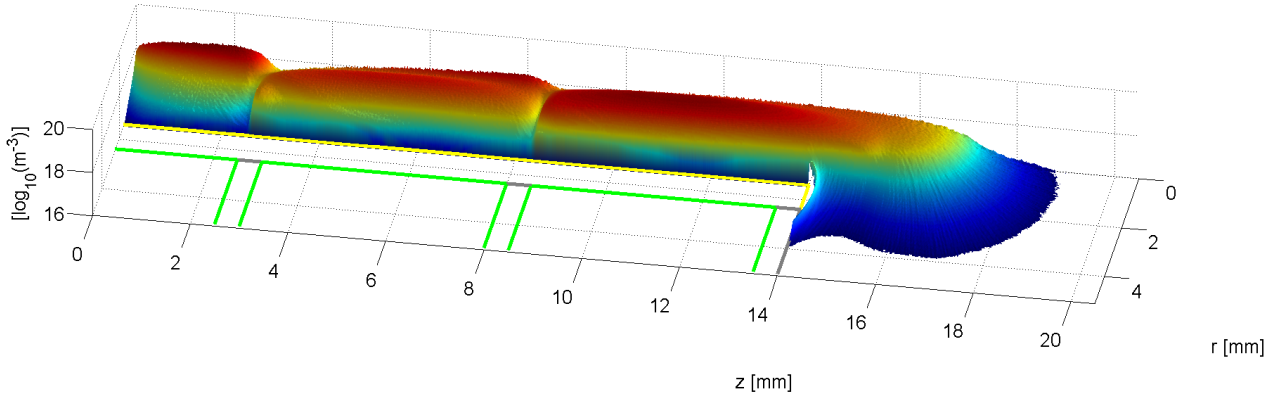

Fig. 8. Ion density.

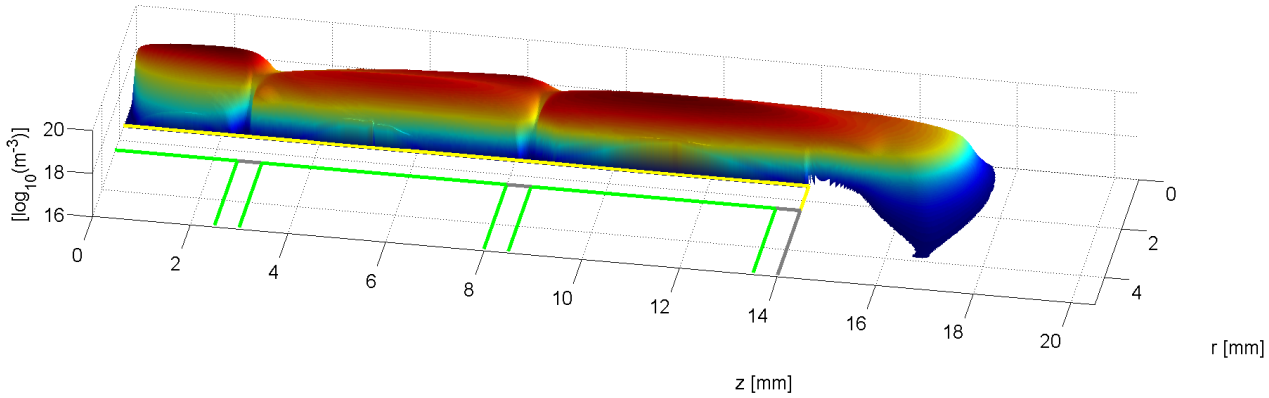

Fig. 9. Electron density.

the channel, the potential drop is significantly lower, with only about 10 V. At the cusps, the axial movement of the electrons in regions not close to the axis is strongly hindered by the radially directed magnetic field, reducing by this their axial transport and allowing by this axial potential changes. The ions are not magnetized and just follow the electrons. The smaller drop of the potential at the second cusp can be explained, because electrons have here a higher energy and consequently higher gyration radii, which make it easier for them to overcome the cusp. The main potential drop occurs at the exit cusp, beyond the positive 'anchor' of the dielectric. Therefore, the overall potential structure is very similar to a grid thruster, but without the life time limitaion of ion sputtering at the grid.

Retarding potential analyzer measurements for the downscaled HEMPT that is modeled here also suggest a single, major potential drop for most of the ions [20] .

The main potential drop near the thruster's exit forms a 'bulge'. This accelerates the ions obliquely away from the symmetry axis, showing the reason for the hollow cone shaped plume which is typical for HEMP thrusters.

The ion density of the entire simulation domain is presented in Fig. 7. (averaged over $1 \cdot 10^6$ time steps). It illustrates, that the ions just follow the structure of the elctron density. Ions have mostly a density of about $1 \cdot 10^{19}\ m^{-3}$, which results in a Debye length in the order of magnitude of $1 \cdot 10^{-2}\ mm$. With a typical size for a plasma sheath of ten Debye lengths, its size would be

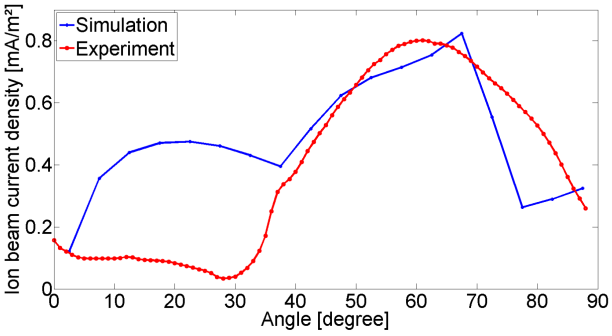

Fig. 10. Angular ion beam current distribution.

$1 \cdot 10^{-4}$ m. This is still significantly smaller than the channel diameter of $1.5 \cdot 10^{-3}$ m. Therefore, even in its downscaled configuration, the HEMPT is still not wall-effect dominated and an application of the self-similarity is possible.

The ionization rate is shown in Fig. 6. . The dominant ionization appears close to the axis and in the cusps, where the electrons are trapped, and at the thruster's exit, where the source electrons gets accelerated by the potential drop into the thruster, very similar to the larger HEMP. There is a peak in the ionization rate upstream of each cusp, which can be explained by the electrons gaining additional energy as they are kinetically heated in the cusp traps and then move towards the anode. In the simulation the electron current at the anode is 4.9 mA, which is close to the measured value of 4.5 mA. This means that in the simulation the value of ions who are generated and not lost to the wall ('recycled' after wall contact as neutrals), is $3.2 \cdot 10^{16}$ particles per second. Compared to the neutral gas influx of $1.1 \cdot 10^{17}$ particles per second, this gives an ionization rate of 29 %, which is close to the value of 25 % derived from the measurements. The ratio of neutral to ion densities inside the channel is significantly different, with about 50 times more neutrals. This is due to the relatively slow moving neutral gas, by design of the neutral gas inlet. The primary electron source in the simulation has a value of 0.6 mA, with 0.4 mA passing the maximum-r boundary. The electrons from this source do not reach the thruster. From the remaining $0,2$ mA, it is estimated that half of them reach the thruster. This gives a ratio from anode current to primary current of about 50, far lower than for non-downscaled HEMPTs, which means a more linear response to the electron source. It should be investigated by experiments, whether this results in better system control possibilities.

The electrons energy is displayed in Fig. 5. . There is a high energy region of around 100 eV near the exit cusp, where the electrons gain energy through the main potential drop. Inside the thruster the trapping of electrons in the magnetic mirror-like cusp configurations produce a kinetic heating of the elctrons. By this and the trapping of electrons in between the cusps an increased ionization is obtained.

Electron trajectories in Fig. 8. show that the electrons spent a significant amount of time in the cusp outside the thruster, before they are able to enter. For electrons with higher energies their gyration radii are comparable to the cusps size, which enables them to overcome the exit cusp. If this would not be the case, filling of the thruster by source electrons would be very difficult. As the electrons enter the thruster, they have sufficient energy after being accelarated by the potential drop close to the exit to cause ionization.

For long-term operation the sputtering of the dielectrics has to be analysed. For this, the particle flux and mean energies of the ions hitting the dielectric surface is shown in Fig. 11. and Fig. 12. . The maxima in particle fluxes and mean energy appear as expcted at the cusp locations. The most critical area for sputtering is the cusp inside the accelaration channel close to the exit of the thruster, with ion energies up to 70 eV. For a worst case estimate experimental values for sputter yields one gets from experimental measurements a value of $1,3E-3mm^3/C$ [21] . At this location one gets a current flux density of $380A/m^2$. For an operation time of 100 hours that gives a maximum erosion of $0,178$ mm. At all other locations the erosion is practically zero due to the much lower mean energies.

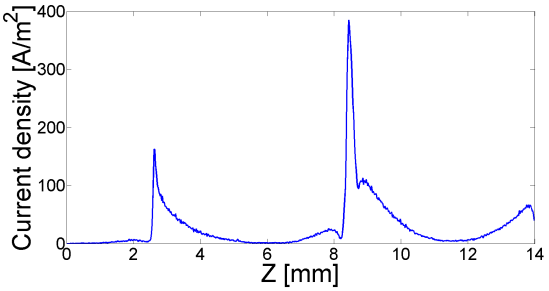

Fig. 11. Ion flux to the channel wall.

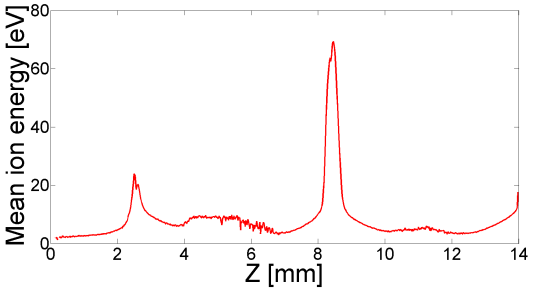

Fig. 12. Mean ion energy the channel wall.

Another important quantity for ion thrusters is the angular distribution of the ion current. For this, the boundary cells are used to count the ions reaching them. From the location of the cells the angle with respect to the axis at the thruster exit is calculated and the ion flux is determined in 5 degree steps. The simulated values can be compared to Faraday cup measurements [22] . The Faraday cup is moved in a radius of 40 cm around the discharge chamber exit in one degree steps. Fig. 10. shows the results for both measurements and simulations. The peak of the simulated ion current is about the same height, while there are deviations at lower angles, the angular profile shows similarity with the measurements at higher angles. In both cases, the maximum lies at about 60 degrees. The deviations between simulation and experiment are expected, because the outer simulation domain is still too small, as was tested changing the potential boundary conditions from Dirichlet (potential set to 0 V) to von-Neumann (electric field set to zero V/m) conditions. In case of a sufficient large domain this should not change the results, but here the potential distribution close to the boundary is still strongly affected. One should

note that overall structure is not changing, but the ratio between ion currents at smaller and larger angles and the exact location of the maximum will vary. Further simulations with larger domain size will resolve this problem. From the angular distributions the overall ion beam current can be calculated, resulting in 3.1 *mA* for the experiment [22] and 3.1 *mA* for the simulation, which agree quite well.

4. Conclusions and Outlook

The electrostatic Particle-in-Cell simulation of this downscaled HEMP thruster shows a flat potential inside the thruster, which is typical for normal sized HEMPTs with a strong potential drop at the exit, very similar to a grid thruster. The electron density distribution inside the accelaration channel is radially broader than in the normal HEMPT due to the larger ratio of gyroradii of the electrons to discharge radius, which induces larger transport in radial direction. The ion density follows the electron density due to the quasi-neutrality constraint in plasmas.

The angular distribution of the ion beam in the simulation reproduces the hollow cone seen in the experiment, with some deviations due to the limitesd size of the plume region. The simulated ion beam current value agrees quite well with experiment. As in the larger HEMPT systems erosion is minimized by the rather small mean energies of the ions reaching the dielectrics. Only at the second internal cusp close to the exit some erosion can happen, without limiting the operational scenarios. A better model will need an extension of the simulation domain including larger plume volumes. The simulation time was sufficient to reach steady state. Thrust oscillations as observed in the experiment appear on a timescale where the neutral dynamics interact with the plasma dynamics through ionization, resulting in breathing modes. To resolve this an increase of the simulation time by about one order of magnitude is needed. As an alternative the possibility will be investigated to run charged and neutral particles on alternating different time scales, in a similar fashion as it is done with the electrons and ions in the F3MPIC [23] code.

Acknowledgments

The main Author would like to thank Franz Georg Hey (Airbus D & S, Friedrichshafen), who provided the experimental data for the thruster. Additional thank is to Rodion Groll (ZARM), whos neutral gas simulation of this thruster provided a valuable reference.

References

1) M. Vallisneri: Low-frequency gravitational-wave science with eLISA/NGO, *arXiv:1202.0839 [gr-qc]*.
2) P. Silvestrin, M. Aguirre, L. Massotti, S. Cesare: Next Generation Gravity Mission: a Step Forward in the Earth's Gravity Field Determination, *Conference Paper, EGU General Assembly 2009, Volume: Vol. 11, EGU2009-2184, 2009.*
3) G. Kornfeld, N. Koch, G. Coustou: The highly efficient multistage plasma (HEMP) thruster, a new electric propulsion concept derived from tube technology, *4th IEEE International Conference on Vacuum Electronics, 2003*.
4) A. Keller, P. Köhler, F. G. Hey, M. Berger, C. Braxmaier, D. Feili, D. Weise, U. Johann: Parametric Study of HEMP-Thruster, Downscaling to μN Thrust Levels, *in proceeding of: 33rd International Electric Propulsion Conference, At The George Washington University, Washington, D.C., USA*.
5) F. G. Hey, A. Keller, D. Papendorf, C. Braxmaier, M. Tajmar, U. Johann, D. Weise: Development of a Highly Precise Micro-Newton Thrust Balance, *in proceeding of: 33rd International Electric Propulsion Conference, At The George Washington University, Washington, D.C., USA*.
6) T. Brandt, T. Trottenberg, R. Groll, F. Jansen, F. G. Hey, U. Johann, H. Kersten, C. Braxmaier: Particle-in-Cell simulation of the plasma properties and ion acceleration of a down-scaled HEMP-Thruster, *4th International Spacecraft Propulsion Conference, May 19th - 22th, 2014, Cologne, Germany*.
7) K. N. Leung, N. Hershkowitz, K. R. MacKenzie: Plasma confinement by localized cusps, *Physics of Fluids (1958-1988) 19, 1045 (1976); doi: 10.1063/1.861575*.
8) R. Van Norton: The motion of a charged particle near a zero field point, *New York: New York University: Courant Institute of Mathematical Sciences, 1961*.
9) Kuniz Shinano, and Hiroshi It: Behavior of a Charged Particle in a Cusp Field, *J. Phys. Soc. Jpn. 21, pp. 1822-1829 (1966)*.
10) J.Spanier, E.M.Gelbard: Monte Carlo Principles and Neutron Transport Problems, *Addison Wesley 1969*.
11) S. T. Perkins, D. E. Cullen, S. M. Seltzer: Tables and graphs of electron-interaction cross sections from 10 eV to 100 GeV derived from the LLNL Evaluated Electron Data Library (EEDL), Z = 1 to 100, *November 12, 1991*.
12) R.W. Hockney, J.W. Eastwood: Computer Simulation Using Particles, *Adam Hilger, 1988*.
13) C.K. Birdsall, A.B Langdon: Plasma Physics via Computer Simulation; Series in Plasma Physics, *CRC Press, 2004*.
14) Tskhakaya D., Matyash K., Schneider R., Taccogna F.: The Particle-In-Cell Method, *CONTRIBUTIONS TO PLASMA PHYSICS. 2007; 47:563-594*.
15) Francesco Taccogna, Savino Longo, Mario Capitelli, Ralf Schneider: Self-similarity in Hall plasma discharges: Applications to particle models, Physics of Plasmas (1994-present) 12, 053502 (2005); doi: 10.1063/1.1877517.
16) A. Guthrie and R. K. Wakerling (eds.), New York: McGraw-Hill: The characteristics of electrical discharges in magnetic fields, *New York: McGraw-Hill.*
17) C. L. Ellison, Y. Raitses, and N. J. Fisch: Cross-field electron transport induced by a rotating spoke in a cylindrical Hall thruster, *2012 American Institute of Physics. [doi:10.1063/1.3671920].*
18) Nuclear Fusion, *Volume 39 Number 12, December 1999*.
19) J. P. Wright: Diffusion of Charged Particles across a Magnetic Field Due to Neutral Particles, *Physics of Fluids (1958-1988) 3, 607 (1960); doi: 10.1063/1.1706095*.
20) A. Keller, P. Köhler, D. Feili, M. Berger, C. Braxmaier, D. Weise, U. Johann: Feasibility of a down-scaled HEMP-Thruster, *IEPC-2011-138*.
21) Michael Tartz, Thomas Heyn, Carsten Bundesmann and Horst Neumann: Measuring sputter yields of ceramic materials, *Presented at the 31st International Electric Propulsion Conference, University of Michigan,Ann Arbor, Michigan,USA, September 20 24, 2009*.
22) A. Keller, P. Köhler, F. G. Hey, M. Berger, C. Braxmaier, D. Feili, D. Weise, U. Johann: Parametric Study of HEMP-Thruster Downscaling to μN Thrust Levels, *IEEE TRANSACTIONS ON PLASMA SCIENCE, VOL. 43, NO. 1, JANUARY 2015*.
23) A. Lucca Fabris, C. V. Young, M. Manente, D. Pavarin, and M. A. Cappelli: Ion Velocimetry Measurements and Particle-In-CellSimulation of a Cylindrical Cusped Plasma Accelerator, *IEEE TRANSACTIONS ON PLASMA SCIENCE, VOL. 43, NO. 1, JANUARY 2015*.

A. Appendix

A.1. Plasma parameters of the DM3a HEMP-T model

Channel plasma property	for electrons	for ions
Density	$n_e = 10^{18}\,\mathrm{m}^{-3}$	$n_i = 10^{18}\,\mathrm{m}^{-3}$
Temperature	$T_e = 4\,\mathrm{eV}$	$T_i = 2\,\mathrm{eV}$
Debye length	$\lambda_{D,e} = 14.9\,\mu\mathrm{m}$	$\lambda_{D,i} = 19.5\,\mu\mathrm{m}$
Plasma frequency	$\omega_{p,e} = 9.0\,\mathrm{GHz}$	$\omega_{p,i} = 18.4\,\mathrm{MHz}$
Larmor radius	$r_{L,e} = 47.6\,\mu\mathrm{m}$	$r_{L,i} = 1.7\,\mathrm{cm}$
Cyclotron frequency	$\omega_{c,e} = 2.8\,\mathrm{GHz}$	$\omega_{c,i} = 11.6\,\mathrm{kHz}$
Hall parameter	$\omega_{c,e}/\nu_{e-e} = 18.7$	$\omega_{c,i}/\nu_{i-i} = 0.5$

Table A.1.: Plasma parameters of the DM3a HEMP thruster model inside the channel.

Plume plasma property	for electrons	for ions
Density	$n_e = 10^{14}\,\mathrm{m}^{-3}$	$n_i = 10^{14}\,\mathrm{m}^{-3}$
Temperature	$T_e = 4\,\mathrm{eV}$	$T_i = 500\,\mathrm{eV}$
Debye length	$\lambda_{D,e} = 1.5\,\mathrm{mm}$	$\lambda_{D,i} = 1.7\,\mathrm{cm}$
Plasma frequency	$\omega_{p,e} = 0.9\,\mathrm{MHz}$	$\omega_{p,i} = 0.2\,\mathrm{MHz}$

Table A.2.: Example plasma parameters of the DM3a HEMP thruster in the plume region at about 5 cm distance from the thruster exit.

A.2. Collision parameters of the DM3a HEMP-T channel plasma

The following calculations are done for the DM3a HEMP thruster channel plasma except the cusp region. Chosen parameters are:

- for electrons: $n_e = 10^{18}\,\mathrm{m}^{-3},\ T_e = 4\,\mathrm{eV},\ v_{th,e} = 8.4 \times 10^5\,\mathrm{m/s}$
- for Xenon ions: $n_i = 10^{18}\,\mathrm{m}^{-3},\ T_i = 2\,\mathrm{eV},\ v_{th,i} = 1.2 \times 10^3\,\mathrm{m/s}$
- for Xenon neutrals: $n_n = 10^{21} - 3 \times 10^{19}\,\mathrm{m}^{-3},\ T_n = 800\,\mathrm{K} = 0.07\,\mathrm{eV},\ v_{th,n} = 2.2 \times 10^2\,\mathrm{m/s}$

where the thermal velocity corresponds to $v_{th,s} = \sqrt{k_B T_s m_s^{-1}}$, assuming a Maxwell- Boltzmann velocity distribution. The mean free path of test particle A colliding with a particle B can be approximated by [Lieberman and Lichtenberg, 2005]

$$\lambda_{A\Rightarrow B}^{mfp} = \frac{\int_0^\infty v \cdot f_B(v)\,dv}{n_B \int_0^\infty \sigma_{A\Rightarrow B}(v) \cdot v \cdot f_A(v)\,dv} \approx \frac{v_{th,B}}{n_B \cdot \sigma_{A\Rightarrow B}(v_{th,A}) \cdot v_{th,A}}\ ,$$

where $f(v)$ indicates the velocity distributions and σ the cross section. The corresponding collision frequency can be given as

$$\nu_{A\Rightarrow B} = n_B \int_0^\infty \sigma_{A\Rightarrow B}(v) \cdot v \cdot f_A(v)\,dv \approx n_B \cdot \sigma_{A\Rightarrow B}(v_{th,A}) \cdot v_{th,A}\ .$$

For collisions with neutrals, the tabulated cross sections are used. For Coulomb collisions ν is given by the slowing down relaxation process, calculated after [Huba et al., 2016]. In Table A.3, calculated mean free paths and collision frequencies are given for the most important collision processes.

With the help of these mean free paths, the behaviour of the channel plasma can be estimated. While electron Coulomb collisions are much larger than the channel dimensions ($L = 5.1\,\mathrm{cm},\ R = 0.9\,\mathrm{cm}$) and elastic collisions with neutrals does not change the velocity distribution of the electrons, electrons in the channel are non Maxwellian. For neutrals the mean free path of elastic neutral neutrals collisions is in the range of the channel radius. Therefore, neutrals are thermal and have a Maxwellian velocity distribution. Ions are coupled to neutrals, due to ionisation. Also the charge exchange collisions, with a mean free path lower than the channel radius couples the ions with the slow propellant atoms. But for the plasma parameters of the HEMP channel plasma, the ion-ion Coulomb collisions have a

collision process	$\lambda^{mfp}_{A\Rightarrow B}$	$\nu_{A\Rightarrow B}$
$e^- + Xe$ elastic [Hayashi, 2003]	$0.001 - 0.04\,\mathrm{cm}$	$2 - 0.06\,\mathrm{GHz}$
$Xe^+ + Xe$ charge exchange [Phelps, 2002]	$0.01 - 0.4\,\mathrm{cm}$	$204 - 6.1\,\mathrm{MHz}$
$Xe + Xe$ elastic [Phelps, 2000]	$0.02 - 0.6\,\mathrm{cm}$	$126 - 3.8\,\mathrm{MHz}$
$Xe^+ + Xe^+$ Coulomb	$5.8\,\mathrm{cm}$	$21\,\mathrm{kHz}$
$e^- + e^-$ Coulomb	$10.3\,\mathrm{cm}$	$8.2\,\mathrm{MHz}$
$Xe^+ + e^-$ Coulomb	$5 \times 10^6\,\mathrm{cm}$	$17.2\,\mathrm{Hz}$

Table A.3.: Collision mean free path within the thruster channel of the DM3a HEMP thruster. Cross-sections are taken from the references.

mean free path which is larger than the channel dimensions. That means, ions are not able to thermalise in the thruster channel. Therefore, the ion velocity distribution differs from a Maxwellian.
Since there are also mean free path which are larger than the thruster channel length, the channel and plume plasmas are coupled.

Due to the higher threshold energies of ionisation and excitation of neutrals $\mathcal{E}^{INZ}_{thr} = 12.13\,\mathrm{eV}$ [Hayashi, 2003] and $\mathcal{E}^{EX}_{thr} = 8.32\,\mathrm{eV}$ [Hayashi, 1983], electrons with thermal energy does not take part in these collision process. Only for high energetic electrons from the tail of the energy distribution these collisions appear. The mean free path for such ionisation can be estimated by considering a high energetic electron with a velocity of $v_e = 2.9 \times 10^6\,\mathrm{m/s}$, which corresponds to a kinetic energy of $\mathcal{E}_{e,kin} = 24\,\mathrm{eV}$. With the above given neutral properties for the channel region ($n_n = 7 \times 10^{19}\,\mathrm{m^{-3}}$), one get

$$\lambda^{INZ}_{e,n} \approx \frac{v_{th,n}}{n_n \cdot \sigma^{INZ}_{e,n}(\mathcal{E}_{e,kin}) \cdot v_e} = 0.4\,\mathrm{cm} \quad < R \ ,$$

where the cross-section $\sigma^{INZ}_{e,n}(\mathcal{E}_{e,kin}) = 3.1 \times 10^{-16}\,\mathrm{cm^2}$ is taken from [Hayashi, 2003]. The resulting ionisation mean free path is smaller than the thruster radius, which means for fast electrons ionisation takes place inside the thruster channel, as it is indicated in experiments. Analogue, the mean free path of propellant excitation by fast electrons can be estimated as

$$\lambda^{EX}_{e,n} \approx \frac{v_{th,n}}{n_n \cdot \sigma^{EX}_{e,n}(\mathcal{E}_{e,kin}) \cdot v_e} = 0.3\,\mathrm{cm} \quad < R \ ,$$

with $\sigma^{EX}_{e,n}(\mathcal{E}_{e,kin}) = 3.8 \times 10^{-16}\,\mathrm{cm^2}$ [Hayashi, 1983].

A.3. Similarity scaling

The aim of similarity scaling is to change the system parameters but keeping the system physical characteristics similar. For this purpose scaling laws have to be found which conserve the important physical parameters of the system. In the context of this work, the similarity scaling is applied to the system size L and the simulated time t. This approach corresponds to [Taccogna et al., 2005]. For the HEMP thruster magnetic confinement and collisions with neutrals are crucial. To make sure that the down-scaled system is identical concerning these physical properties, the following parameters are preserved: the electron Hall parameter

$$\beta_{Hall} = \frac{r_{L,e}}{L} = \frac{m_e v_{e,\perp}}{eBL} = const.$$

and the Knudsen number

$$Kn = \frac{\lambda_{s,n}}{L} = \frac{1}{n_n \sigma_{s,n} \langle v_s \rangle L} = const. \qquad s \in \{e, i, n\} \quad .$$

For a down-scaled system of length $L^* = L/\xi$ and simulated time $t^* = t/\xi$, where $\xi > 1$, particle velocities are preserved $L/t = v = v^*$. For the Hall parameter, this results in a scaled magnetic field $B^* = \xi B$. Due to the smaller system collisions with neutrals are underestimated since their mean free path is larger than the new system dimensions ($\lambda_{e,n},\ \lambda_{n,n},\ \lambda_{i,n}^{CX} > L^*$). This changes the velocity distributions of all species and lower electron and ion densities compared to the experiment, due to less ionisation. To preserve these collisions the Knudsen number, has to be preserved for all species. One possibility is to increase the collision cross-section $\sigma_{s,n}^* = \xi \sigma_{s,n}$ and keep the neutral density n_n constant. This results in a down-scaled mean free path and therefore in a better representation of collisions with neutrals. Another possibility to conserve the Knudsen number is to increase the neutral density $n_n^* = \xi n_n$ while keeping the collision cross-section constant. This is used only if details of the neutral dynamics are not of interest, as e.g. in [Matyash et al., 2010]. Also particle source current I_{src}, used e.g. to simulate a neutraliser, has to be adapted. In the down-scaled system the amount of particles is injected within shorter time, therefore $I_{src}^* = I_{src}/\xi$. In table A.4 the applied scaling laws are summarised.

Since velocities are not scaled, temperatures and kinetic energies are remaining as well. Also the anode voltage U_a is not changed therefore electric potential and potential energy stay constant. Comparing with [Taccogna et al., 2005], no scaling of collision probability

Length	$L^* = L/\xi$
Time	$t^* = t/\xi$
Magnetic field	$B^* = \xi B$
Cross section	$\sigma^*_{s,n} = \xi\sigma_{s,n}$
Source current	$I^*_{src} = I_{src}/\xi$

Table A.4.: Scaling laws for similarity scaling of the system size and the simulated time.

is necessary, since this is done automatically within the used PIC-MCC method by the implementation of collisions via cross-sections. For the resulting system the number of cells and time steps is reduced due to down-scaled system size and system time.

B. Bibliography

[Bird, 1994] Bird, G. A. (1994). Molecular Gas Dynamics and the Direct Simulation of Gas Flows. Oxford (U.K.): Clarendon Press.

[Birdsall and Langdon, 1985] Birdsall, C. K. and Langdon, A. B. (1985). Plasma physics via computer simulation.

[Bohm et al., 1949] Bohm, D., Burhop, E., and Massey, H. (1949). The characteristics of electrical discharges in magnetic fields. New York (U.S.A.): McGraw-Hill.

[Boyd, 2005] Boyd, I. D. (2005). Numerical modeling of spacecraft electric propulsion thrusters. Progress in Aerospace Sciences, 41:669 – 687.

[Bronold et al., 2007] Bronold, F. X., Matyash, K., Tskhakaya, D., Schneider, R., and Fehske, H. (2007). Radio-frequency discharges in oxygen: I. particle-based modelling. Journal of Physics D: Applied Physics, 40(21):6583.

[Courant et al., 1967] Courant, R., Friedrichs, K., and Lewy, H. (1967). On the Partial Difference Equations of Mathematical Physics. IBM Journal of Research and Development, 2(11):215–234.

[Dreissigacker, 2013] Dreissigacker, O. (2013). Einer kommt runter, drei gehen rauf. Physik Journal, 12:7–8.

[Duras et al., 2013] Duras, J., Kalentev, O., Matyash, K., Schneider, R., and Kemnitz, S. (2013). Interactions between ion thruster plumes and vessel walls. In Proceedings of the 33rd International Electric Propulsion Conference. IEPC-2013-059.

[Eckstein, 1991] Eckstein, W. (1991). Computer Simulation of Ion-Solid Interaction (10th ed.). Springer Series in Material Science. Springer Verlag.

[Eckstein et al., 2007] Eckstein, W., Dohmen, R., Mutzke, A., and Schneider, R. (2007). Sdtrimsp: A monte-carlo code for calculating collision phenomena in randomized targets. IPP Report, 12(3):40.

[ESA, nd] ESA (n.d.). ESA's gravity mission GOCE. Retreved, Jan. 2015, from `http://www.esa.int/Our_Activities/Observing_the_Earth/GOCE`.

[Francis, 1982] Francis, C. (1982). Electrostatic charging problems of spacecraft. Journal of Electrostatics, 11(3):265 – 280.

[Gamero-Castano and Katz, 2005] Gamero-Castano, M. and Katz, I. (2005). Estimation of hall thruster erosion using hphall. In Proceedings of the 29th International Electric Propulsion Conference. IEPC-2005-303.

[Genovese et al., 2011] Genovese, A., Lazurenko, A., Koch, N., Weis, S., Schirra, M., Haderspeck, J., and Holtmann, P. (2011). Endurance testing of hempt-based ion propulsion modules for smallgeo. In Proceedings of the 32nd International Electric Propulsion Conference. IEPC-2011-141.

[Harmann et al., 2007] Harmann, H.-P., Koch, N., and Kornfeld, G. (2007). The ulan test station and its diagnostic package for thruster characterization. In Proceedings of the 30th International Electric Propulsion Conference. IEPC-2007-119.

[Hayashi, 1983] Hayashi, M. (1983). Determination of electron-xenon total excitation cross-sections, from threshold to 100 eV, from experimental values of Townsend's alpha. Journal of Physics D: Applied Physics, 16(4):581.

[Hayashi, 2003] Hayashi, M. (2003). Bibliography of Electron and Photon Cross Sections with Atoms and Molecules Published in the 20th Century - Argon.

[Hoskins et al., 2013] Hoskins, W. A., Cassady, R. J., Morgan, O., Mayers, R. M., Wilson, F., King, D. Q., and deGrys, K. (2013). 30 years of electric propulsion flight experience at aerojet rocketdyne. In Proceedings of the 33th International Electric Propulsion Conference. IEPC-2013-439.

[Huba et al., 2016] Huba, J., Naval Research Laboratory, and United States Office of Naval Research (2016). NRL Plasma Formulary. NRL publication. Washington (U.S.A.): Naval Research Laboratory.

[Janes and Lowder, 1966] Janes, G. S. and Lowder, R. S. (1966). Anomalous Electron Diffusion and Ion Acceleration in a Low-Density Plasma. The Physics of Fluids, 9(6):1115–1123.

[Kalentev et al., 2013] Kalentev, O., Lewerenz, L., Duras, J., Matyash, K., and Schneider, R. (2013). Infinitesimal analytical approach for the backscattering problem. Journal of Propulsion and Power, 29(2):495–498.

[King, 1998] King, L. (1998). Transport-property and mass spectral measurements in the plasma exhaust plume of a Hall-effect space propulsion system. PhD thesis, University of Michigan.

[Koch et al., 2003] Koch, N., Kornfeld, G., and Coustou, G. (2003). The hemp thruster - an alternative to conventional ion sources? Symposium conducted at the 10th Erfahrungsaustausch Oberflächentechnologie mit Plasma- und Ionenstrahlprozessen, Mühlleithen, Germany.

[Koch et al., 2011] Koch, N., Schirra, M., Weis, S., Lazurenko, A., van Reijen, B., Haderspeck, J., Genovese, A., Holtmann, P., Schneider, R., Matyash, K., and Kalentev, O. (2011). The hempt concept - a survey on theoretical considerations and experimental evidences. In Proceedings of the 32nd International Electric Propulsion Conference. IEPC-2011-236.

[Kornfeld et al., 2003] Kornfeld, G., Koch, N., and Coustou, G. (2003). First test results of the hemp thruster concept. In Proceedings of the 28th International Electric Propulsion Conference. IEPC-2003-212.

[Kornfeld et al., 2007] Kornfeld, G., Koch, N., and Harmann, H.-P. (2007). Physics and evolution of hemp-thrusters. In Proceedings of the 30th International Electric Propulsion Conference. IEPC-2007-108.

[Kornfeld et al., 1999] Kornfeld, G., Seidel, H., and Wegener, J. (1999). Plasma accelerator arrangement. Patent, priority: Germany No. 198 28 704.6, filed 26 June 1998.

[Lazurenko et al., 2012] Lazurenko, A., Genovese, A., Weis, S., Schirra, M., van Reijen, B., Haderspeck, J., Holtmann, P., Ruf, K., Püttmann, N., and Koch, N. (2012). Progress in the endurance testing of hempt ion propulsion system for smallgeo. In Lazurenko, A., editor, Space Propulsion Conference. SP2012_2366197.

[Lieberman and Lichtenberg, 2005] Lieberman, M. A. and Lichtenberg, A. J. (2005). Principles of Plasma Discharges and Materials Processing (2nd ed.). Hoboken (U.S.A.): John Wiley & Sons, Inc.

[Liu et al., 2010] Liu, H., Wu, B., Yu, D., Cao, Y., and Duan, P. (2010). Particle-in-cell simulation of a hall thruster. Journal of Physics D: Applied Physics, 43(16):165202.

[Matyash, 2003] Matyash, K. (2003). Kinetic Modeling of Multi-Component Edge Plasmas. PhD thesis, Ernst-Moritz-Arndt-Universität Greifswald.

[Matyash et al., 2009] Matyash, K., Kalentev, O., Schneider, R., Taccogna, F., Koch, N., and Schirra, M. (2009). Kinetic simulation of the stationary hemp thruster including the near-filed plume region. In Proceedings of the 31st International Electric Propulsion Conference. IEPC-2009-110.

[Matyash et al., 2010] Matyash, K., Schneider, R., Mutzke, A., Kalentev, O., Taccogna, F., Koch, N., and Schirra, M. (2010). Kinetic simulations of spt and hemp thrusters including the near-field plume region. IEEE Transactions on Plasma Since, 38(9, Part 1):2274–2280.

[Messerschmid and Fasoulas, 2009] Messerschmid, E. and Fasoulas, S. (2009). Raumfahrtsysteme, Eine Einführung mit Übungen und Lösungen (3rd ed.). Berlin (G.): Springer Verlag.

[Monetti et al., 2017] Monetti, F., Bonelli, E., Pulcinelli, F., Scortecci, F., Lazurenko, A., and Genovese, A. (2017). Performance of aerospazio lifetest facilities and diagnostic tools for the hempt qualification programme. In Proceedings of the 35th International Electric Propulsion Conference. IEPC-2017-483.

[Neumann et al., 2009] Neumann, P. R. C., Bilek, M. M. M., Tarrant, R. N., and McKenzie, D. R. (2009). A pulsed cathodic arc spacecraft propulsion system. Plasma Sources Science and Technology, 18(4):045005.

[Phelps, 2000] Phelps, A. V. (2000). Nitrogen atoms and molecules. Retreved, Jan. 2015, from `http://jila.colorado.edu/~avp/collision_data/neutralneutral/atomatom.txt`.

[Phelps, 2002] Phelps, A. V. (2002). Retreved, Jan. 2015, from `http://jila.colorado.edu/~avp/collision_data/ionneutral/IONATOM.TXT`.

[Rayman, nd] Rayman, M. (n.d.). Deep Space 1. Retreved, Jan. 2015, from `http://nmp.jpl.nasa.gov/ds1`.

[Rosenberg and Wehner, 1962] Rosenberg, D. and Wehner, G. (1962). Sputtering Yields for Low Enregy He+-, Kr+-, and Xe+-Ion Bombardment. J. Appl. Phys., 33(5).

[Shastry et al., 2013] Shastry, R., Herman, D. A., Soulas, G. C., and Patterson, M. J. (2013). Status of nasa's evolutionarry xenon thruster (next) long-duration test as of 50,000 h and 900 kg throughput. In Proceedings of the 33rd International Electric Propulsion Conference. IEPC-2013-121.

[Sovey et al., 2001] Sovey, J. S., Rawlin, V. K., and Patterson, M. J. (2001). Ion propulsion development projects in u.s.: Space electric rocket test into deep space 1. Journal of Propulsion and Power, 17(3):517 – 526.

[Szabo et al., 2000] Szabo, J., Martinez-Sanchez, M., and Batishchev, O. (2000). Numerical modeling of the near-anode region in a tal thruster. In 36th AIAA/ASME/SAE/ASEE JointPropulsion Conf. and Exhibit.

[Taccogna et al., 2005] Taccogna, F., Longo, S., Capitelli, M., and Schneider, R. (2005). Self-similarity in hall plasma discharges: Applications to particle models. Phys. Plasmas, 12:053502.

[Tskhakaya et al., 2007] Tskhakaya, D., Matyash, K., Schneider, R., and Taccogna, F. (2007). The Particle-In-Cell Method. Contrib. Plasma Phys., 47(8-9):563–594.

[Turner, 2006] Turner, M. J. (2006). Rocket and Spacecraft Propulsion (2nd ed.). Springer-Verlag.

[Vahedi et al., 1993] Vahedi, V., DiPeso, G., Birdsall, C. K., Lieberman, M. A., and Rognlien, T. D. (1993). Capacitive RF Discharges modelled by Particle-In-Cell Monte Carlo simulation. I. Analysis of numerical techniques. Plasma Sources Science and Technology, 2(4):261.

[Wise, nd] Wise, J. (n.d.). Dawn - a journey to the beginning of the solar system. Retreved, Jan. 2015, from `http://dawn.jpl.nasa.gov`.

C. Scientific Contributions

Reviewed Publications

- Lüskow, K. F., Neumann, P. R. C., Bandelow, G., Duras, J., Kahnfeld, D., Kemnitz, S., Matthias, P., Matyash, K., and Schneider, R. (2018). Particle-in-cell simulation of the cathodic arc thruster. Physics of Plasmas, 25(1):013508

- Duras, J., Kahnfeld, D., Bandelow, G., Kemnitz, S., Lüskow, K., Matthias, P., Koch, N., and Schneider, R. (2017). Ion angular distribution simulation of the highly efficient multistage plasma thruster. Journal of Plasma Physics, 83

- Brandt, T., Schneider, R., Duras, J., Kahnfeld, D., Hay, F. G., Kersten, H., Jensen, J., and Braxmaier, C. (2016). Particle-in-cell simulation of a down-scaled hemp thruster. Transaction of the Japan Society for Aeronautical and Space Sciences, Aerospace Technology Japan, 14(ists30):Pb_235–Pb_242

- Lüskow, K. F., Kemnitz, S., Bandelow, G., Duras, J., Kahnfeld, D., Matthias, P., Schneider, R., and Konigorski, D. (2016b). Electrostatic particle-in-cell simulation of heat flux mitigation using magnetic fields. Journal of Plasma Physics, 82(5)

- Duras, J., Schneider, R., Kalentev, O., Kemnitz, S., Matyash, K., Koch, N., Lüskow, K., Kahnfeld, D., and Bandelow, G. (2016). Influence of electron source on the near field plume in a multistage plasma thruster. Plasma Physics and Technology, 3(3):126–130

- Kahnfeld, D., Bandelow, G., Duras, J., Lüskow, K., Kemnitz, K., and Schnieder, R. (2016). Solution of poisson's equation in electrostatic particle-in-cell simulations. Plasma Physics and Technology Journal, 3(2):66–71

- Lüskow, K., Kemnitz, S., Bandelow, G., Duras, J., D., K., Schneider, R., and Konigorski, D. (2016a). Simulation of heat-flux mitigation using electromagnetic fields. Plasma Physics and Technology Journal, 3(3):110–115

- Duras, J., Kalentev, O., Schneider, R., Matyash, K., Lüskow, K., and Geiser, J. (2015). Monte-carlo re-deposition model during terrestrial measurements of ion thrusters. Acta Polytechnica, 55(1):7–13

- Duras, J., Matyash, K., Tskhakaya, D., Kalentev, O., and Schneider, R. (2014). Self-force in 1d electrostatic particle-in-cell codes for nonequidistant grids. Contributions to Plasma Physics, 54(8):697–711

- Kalentev, O., Matyash, K., Duras, J., Lüskow, K. F., Schneider, R. E., Koch, N., and Schirra, M. (2014). Electrostatic ion thrusters - towards predictive modeling. Contributions to Plasma Physics, 54(2):235–248

- Kalentev, O., Lewerenz, L., Duras, J., Matyash, K., and Schneider, R. (2013b). Infinitesimal analytical approach for the backscattering problem. Journal of Propulsion and Power, 29(2):495–498

Non-reviewed Conference Proceedings

- Koch, N., Duras, J., Kahnfeld, D., Matthias, P., Bandelow, G., Lüskow, K., Schneider, R., Kemnitz, S., and Schirra, M. (2017). Particle-in-cell simulation of a hemp thruster digital prototype optimized for future satellite applications. In Proceedings of the 35rd International Electric Propulsion Conference. IEPC-2017-329

- Kahnfeld, D., Schneider, R., Cichocki, F., Merino, M., Ahedo, E., Duras, J., and Koch, N. (2017). Hempt thruster discharge and plume simulation with a 2d3v-pic-mcc and a 3d hybrid fluid-pic code. In Proceedings of the 35rd International Electric Propulsion Conference. IEPC-2017-309

- Bandelow, G., Schneider, R., Duras, J., Koch, N., and Kalentev, O. (2017). A fast estimate tool for redeposition caused by sputtering during terrestrial testing. In Proceedings of the 35rd International Electric Propulsion Conference. IEPC-2017-300

- Duras, J., Kalentev, O., Matyash, K., Schneider, R., and Kemnitz, S. (2013). Interactions between ion thruster plumes and vessel walls. In Proceedings of the 33rd International Electric Propulsion Conference. IEPC-2013-059

- Lüskow, K. F., Duras, J., Kalentev, O., Geiser, J., Schneider, R., and Tskhakaya, D. (2013). Non-equidistant particle-in-cell for ion thruster plumes. In Proceedings of the 33rd International Electric Propulsion Conference. IEPC-2013-067

- Kalentev, O., Duras, J., Lüskow, K. F., Matyash, K., and Schneider, R. (2013a). Strategy of multiscale modelling for combined thruster-plume models. In Proceedings of the 33rd International Electric Propulsion Conference. IEPC-2013-126

Oral and Poster Presentation

Invited Talks

- Duras, J. (2017, March a). Kinetic modeling of electrostatic ion thrusters. Symposium conducted at the Workshop on Ion Propulsion and Accelerator Industrial Applications, Bari, Italy

- Duras, J. (2016, May b). Simulationen von ionenantrieben - zwischen numerik und experiment -. Symposium conducted at the Mathematische Physikalisches Kolloquium der TH Nürnberg, Nürnberg, Germany

Talks and Poster Presentations

- Duras, J. (2017, October b). Particle-in-cell simulation of a hemp thruster digital prototype optimized for future satellite applications. Symposium conducted at the 35rd International Electric Propulsion Conference, Washington D.C., USA. IEPC-2017-329

- Duras, J. (2016, June). Influence of electron sources on the near- field plume in a multi-stage plasma thruster. Symposium conducted at the 27th Symposium of Plasma Physics and Technology, Prague, Czech Republic

- Duras, J. (2014, November a). Modeling tools for optimizing design and performance of thrusters. Symposium conducted at the Electric Propulsion Innovation and Competitiveness Stackholder Workshop, Brussels, Belgium

- Duras, J. (2014, March b). Non-equidistant particle-in-cell for ion thruster plume simulation. Symposium conducted at the DPG-Frühjahrstagung, Berlin, Germany

- Duras, J. (2013, October a). Interaction between ion thruster plumes and vessel walls. Symposium conducted at the 33rd International Electric Propulsion Conference, Washington D.C., USA. IEPC-2013-059

- Duras, J. (2013, November b). Plume simulation of ion thrusters. Symposium conducted at the 5th German Electric Propulsion Workshop, Göttingen, Germany

- Duras, J. (2012, January). Particle simulation of ion thrusters. Poster presented at the Joint ICTP-IAEA Workshop on Fusion Plasma Modelling Using Atomic and Molecular Data, Triest, Italy

- Duras, J. (2011, May a). Interactions between ion thruster plume and vessel walls. Symposium conducted at the national qualification for the International Studentconference of the Internationale Astronautische Föderation (IAF), Würzburg, Germany

D. Acknowledgement

First of all I want to thank Prof. Dr. Ralf Schneider for being an excellent supervisor, who always took time to explain all my questions and guiding me in the correct direction many times. I also want to thank him for reading and discussing this thesis so frequently. Due to his friendly and warmhearted manner he fosters a collegian and productive atmosphere, which makes it a pleasure to work with him.

I am also thankful to Dr. Konstantin Matyash for the many discussions and valuable comments, which were always very helpful. Dr. Oleksander Kalentev I want to thank for providing me with a running PIC-MCC code and for his technical support. Furthermore, I did appreciate the friendly cooperation with Dr. David Tskhakaya.

I express my gratitude to Prof. Dr. Norbert Koch for the many inspiring discussions about the HEMP-T experiment. The THALES group from Ulm I want to thank for the friendly cooperation. I also want to thank the German Space Agency without whose founding this work would not have been feasible.

Special thanks I dedicate to my colleagues and friends Lars Lewerentz, Gunnar Bandelow, Stefan Kemnitz, Karl Lüskow, Daniel Kahnfeld, Paul Matthias and Marc Marschall. This work would not have been possible without all the discussions about physical and numerical problems as well as their practical and mental support. I am grateful to work with such a good team and I enjoyed all the funny coffee breaks, parties and group excursions.
I also would like to thank Thomas Kramer and Uwe Bittermann for the daily life advises.

My parents Annette and Jochen Duras, my grandmother Dr. Helga Pulkow and the rest of my family I want to thank for their patience and emotional support. Due to their example I always found the strength and persistence to follow my own way. Finally, I want to thank Tobias Latzel who always cheered me up and supported me with a well-balanced amount of motivation and diversion. I excuse for the deferred holidays and I promise we will have to make up for it soon.